DEVELOPMENT, CHARACTERIZATION AND DURABILITY OF SWITCHABLE INFORMATION CARRIERS BASED ON SHAPE MEMORY POLYMERS

Inaugural-Dissertation

to obtain the academic degree

Doctor rerum naturalium (Dr. rer. nat.)

submitted to the Department of Biology, Chemistry and Pharmacy

of Freie Universität Berlin

by

MELANIE ECKER

from Hamburg

2014

This work was carried out between July 2011 and September 2014 under the supervision of **Dr. Thorsten Pretsch** at BAM Federal Institute for Materials Research and Testing, Division 6.5 – Polymers in Life Science and Nanotechnology.

1st Reviewer: **Dr. Thorsten Pretsch**

Project manager of the BMBF project EtiFGPTech at BAM Federal Institute for Materials Research and Testing, Division 6.5, Polymers in Life Science and Nanotechnology
Berlin, Germany

2nd Reviewer: **Prof. Dr. Rainer Haag**

Professor of Organic and Macromolecular Chemistry at Freie Universität Berlin, Institute of Chemistry and Biochemistry
Berlin, Germany

Date of defense: January 28, 2015

„Die ersten sind gescheitert, die ersten was geworden

Die ersten wurden Eltern, die ersten sind gestorben

Bob Dylan gab mir einst einen Kompass ohne Norden

So treibe ich verloren in ein unbekanntes Morgen“

Prinz Pi

ACKNOWLEDGEMENTS

First of all, I would like to express my deep gratitude to my supervisor Dr. Thorsten Pretsch for providing this interesting topic and for his support and advice in all concerns. I am especially grateful for his professional and scientific support. Moreover, I am very thankful to him for giving me the opportunity to attend national and international conferences in order to present my work and to become a member of the SMP community.

Furthermore, I would like to thank Prof. Dr. Rainer Haag, from Freie Universtität Berlin for taking the academic responsibility for this thesis, his support and for reviewing my thesis.

I am grateful to the Federal Ministry of Education and Research (BMBF) for the funding of my research project (project funding reference number 03V0043) and to Bayer MaterialScience AG for kindly providing the PEU.

My thanks and appreciations also go to my colleagues of the SMP group: Martin Bothe and Nikolaus Fritzsche for their daily support, coffee breaks and enjoyable discussions. I also want to thank all the interns and student coworkers who accompanied me during my PhD work and who provided me with various time-consuming measurements: Josefine Buschke, Maren Erdmann, Jan Hüttig, Mitesh Kumar Patel, Chloé Mendre, Daffne Pilga Vaca, Arbel Sisso and Boonya Thongrom.

Furthermore I would like to thank Dr. Volker Wachtendorf for facilitating weathering test machines, equipment for spectral analysis and for fruitful discussions about artificial weathering. Sigrid Benemann is acknowledged for providing me with SEM images and Edelgard Lorenz for support with the cryomicrotome, the optical microscopes and the camera. I also want to thank Sebastian Chruscicki for helping me with colorimetric measurements and for providing the measuring equipment. Next, I want to thank Dietmar Neubert and Tina Garchow for conducting DSC measurements and Petra Fengler for DMA experiments. Besides that, I want to thank the staff from the workshop for prompt and diligent construction and repair of lab-equipment.

I also want to thank my other colleagues and all former doctoral students from BAM 6.5 for their general support, useful scientific discussions and for making my working time enjoyable.

Finally, I want to thank my family and friends for supporting me throughout my PhD thesis, in particular Dörte for all the conversations over a cup of coffee. Deepest thanks to my parents who provided me with support and understanding. Most of all, I appreciate my husband for his great patience, love, trust and faithful support for accomplishing my goals.

PREFACE

This dissertation is a cumulative work based on four peer-reviewed and published articles and one peer-reviewed conference paper published as a book section. The articles are presented separately as independent chapters with their own introduction, experimental section, results, discussion, conclusions and reference part. To ensure consistency and to fit to the layout of this thesis, the formatting of already published manuscripts was modified.

The following manuscripts are enclosed in this thesis:

I. T. Pretsch, **M. Ecker,** M. Schildhauer and M. Maskos, Switchable information carriers based on shape memory polymer, *J. Mater. Chem.*, **2012,** *22* (16), 7757-7766

II. **M. Ecker** and T. Pretsch, Durability of switchable QR code carriers under hydrolytic and photolytic conditions, *Smart Mater. Struct.*, **2013**, *22* (9), art. no. 094005

III. **M. Ecker** and T. Pretsch, Freely configurable functionalization tool for switchable information carriers. In *Materials Challenges and Testing for Manufacturing, Mobility, Biomedical Applications and Climate*, Udomkichdecha, W.; Böllinghaus, T.; Manonukul, A.; Lexow, J., Eds. Springer Berlin Heidelberg, **2014**, ch. 3, pp. 25-35

IV. **M. Ecker** and T. Pretsch, Multifunctional poly(ester urethane) laminates with encoded information, *RSC Adv.*, **2014**, *4* (1), 286-292

V. **M. Ecker** and T. Pretsch, Novel design approaches for multifunctional information carriers, *RSC Adv.*, **2014**, *4* (87), 46680-46688

The thesis also contains a general introduction, discussion and conclusion part. References of these parts are combined in a separate chapter.

SUMMARY

The aim of this thesis was the development of switchable information carriers based on shape memory polymers (SMPs) and the investigation of their durability. Deployed as a new kind of security label, such technology may be an effective tool to prevent counterfeiting and product piracy.

Thermoplastic as well as thermoset SMPs turned out to be applicable as a specific substrate for the fabrication of switchable information carriers. In particular, a physically cross-linked and semi-crystalline poly(ester urethane) (PEU), and a chemically cross-linked epoxy-based polymer were investigated. Both SMPs were able to undergo distinct changes in shape upon triggering, which is commonly known as the shape memory effect (SME).

A key step for the fabrication of switchable information carriers was the development of a suitable technique for a surface-specific coloring of the polymeric base material. In particular, it was necessary to have a thin coat of paint in order to assure sufficient surface contrasts within the subsequently laser-engraved barcodes (*e.g.* quick response (QR) codes). In detail, coloring was conducted by diffusion of staining solutions, based on organic dyes, into the polymeric matrix. As a result of properly selected exposure times, homogenous layers of paint having thicknesses of about 100 µm, could be produced.

In order to obtain room temperature stable, temporary shapes with non-decipherable code information, various programming procedures were applied to the information carriers. These were either based on tensile or on compressive deformation. For instance, when using plane steel plates in the course of compressive deformation, code areas were randomly distorted. By contrast, selective distortions could be achieved using a steel ball type indenter. However, the triggering of the SME resulted in almost complete shape recoveries. As a result, the information carriers could reliably be switched back to readable states.

Before the developed information carriers can be brought onto the market, it is important to evaluate their durability against various environmental impacts. Artificial weathering was conducted exemplarily on blue and black colored QR code carriers based on PEU. Various scenarios were selected: exposure to UVA irradiation and aging in aqueous solution. In both cases, the durability was investigated at temperatures below and above the switching temperature of the employed SMP. It turned out, that the

limiting factor for the usage of switchable information carriers was a lack of contrast and thus was dye-related. In the case of UV irradiation, the color of the dyes started fading, culminating in unreadable QR codes. For hydrolytic degradation, the non-colored code regions were stained in the course of aging. This originates from the fact that the organic dyes used for coloring were soluble in water. As a consequence, they were able to diffuse easily in and out of the swollen polymeric matrix. For both scenarios, aging at elevated temperature caused acceleration of the observed effects. However, the shape memory properties of the PEU were only slightly influenced by the applied aging scenarios.

Next, an additional thermo-responsive security feature was added to the information carriers. Therefore, thermochromic pigments (T-PIGs) were embedded into a PEU matrix. However, in contrast to the organic dyes, the size of the thermochromic microcapsules was too large to diffuse into the polymeric matrix. Thus, another procedure for a surface-specific coloring of the PEU was developed. This mainly included the preparation of a PEU-paste doped with T-PIG by solution mixing. The thermochromic paste was deposited by means of a solvent casting technique as thin layer atop the PEU plaque. After solvent evaporation, tightly connected PEU/PEU-T-PIG laminates were obtained. Beyond that, the layer thickness was adjustable by using a doctor blade for the paste deposition. Subsequent laser ablation finalized the QR code carriers. These were readable at room temperature, but unreadable above the color switching temperature of the employed T-PIGs due to a lack of contrast. Hence, the obtained multifunctional information carriers were characterized by distinct shape memory properties and tunable color switching performances. Furthermore, the combination of several T-PIGs having different colors and switching temperatures resulted in surfaces with multiple and unique temperature-dependent changes in color. Besides that, information carriers with temporarily concealed information could be obtained by covering the QR code with an additional layer doped with T-PIG.

ZUSAMMENFASSUNG

Ziel der Arbeit war es, schaltbare Informationsträger aus Formgedächtnispolymer (FGP) zu entwickeln, und diese auf ihre Beständigkeit gegenüber unterschiedlichen Umwelteinflüssen zu untersuchen. Eingesetzt als neuartige Etiketten könnten diese zur fälschungssicheren Kennzeichnung von Waren verwendet werden.

Sowohl thermoplastische als auch duroplastische FGPs waren geeignete Ausgangsmaterialien für solche Informationsträger. Im Speziellen wurde sowohl ein physikalisch quervernetztes, semikristallines Poly(ester urethan) (PEU), als auch ein chemisch quervernetztes, amorphes FGP auf Epoxidbasis näher untersucht.

Ein wichtiger Schritt für die Entwicklung von schaltbaren Informationsträgern aus FGP war die Entwicklung eines Färberverfahrens, bei dem das Polymer nur oberflächennah eingefärbt wird. So konnten ausreichend hohe Kontraste in den anschließend mittels Lasergravur eingebrachten Barcodes (z.B. QR engl. *quick response* Codes) erreicht werden. Die Färbung der Polymeroberflächen durch Diffusion von organischen Färbelösungen in die Polymermatrix stellte sich als probate Methode heraus. Dabei konnte die Eindringtiefe der Farbstoffe durch die Einwirkzeit auf etwa 100 µm eingestellt werden.

Um die Informationsträger in stabile, temporäre Formen mit unlesbarer Information zu überführen, wurden unterschiedliche thermomechanische Programmierungsmethoden angewendet. Sowohl Druck- als auch Zugverformung stellten sich hierfür als geeignet heraus. In beiden Fällen waren die Informationen im programmierten Zustand aufgrund zu großer Verzerrungen der QR Codes unlesbar. Durch den Einsatz von konfigurierbaren Stempelwerkzeugen während der Druckverformung war es darüber hinaus möglich, selektive Verformung der Oberfläche zu erreichen. Nach dem Auslösen des Formgedächtniseffektes kehrten die Etiketten nahezu in ihre ursprüngliche Form zurück, sodass die Information dann in jedem Fall wieder lesbar war.

Um die Haltbarkeit der neu entwickelten Informationsträger gegenüber Umwelteinflüssen besser beurteilen zu können, wurden gefärbte Etiketten aus PEU künstlich bewittert. Hierfür wurden zwei Alterungsszenarien gewählt: die Degradation durch UVA-Strahlung und die Beständigkeit in wässrigem Medium. In beiden Fällen wurde die Bewitterung unterhalb und oberhalb der Schalttemperatur des Polymers durchgeführt. Die UV-Alterung führte zum Ausbleichen der Farben und somit zum

Verlust der Lesbarkeit durch die Abnahme des QR Code Kontrastes. Während der Alterung in Wasser wurden die anfangs ungefärbten Domänen innerhalb des QR Codes nach und nach gefärbt, was ebenfalls zu einem Kontrastverlust führte. Das rührte daher, dass die organischen Farbstoffe wasserlöslich waren und somit in das gequollene Polymer hinein- und hinausdiffundieren konnten. Lagerung bei erhöhter Temperatur führte in beiden Fällen zu einer Beschleunigung der beobachteten Phänomene. Im Gegensatz dazu wurde während der untersuchten Alterungszenarien die Formgedächtnis-Funktionalität des Polymers kaum beeinflusst.

Anschließend wurden die Informationsträger mit einem weiteren thermoresponsiven Sicherheitsmerkmal kombiniert. Die hierfür verwendeten thermochromen Pigmente (T-PIGs) waren im Vergleich zu den vorher verwendeten Farbstoffen jedoch zu groß, um in die Polymermatrix hineinzudiffundieren. Daher wurde eine weitere Methode zur oberflächenspezifischen Einfärbung von Polymeren entwickelt. Hierzu wurde zunächst eine viskose PEU-Lösung hergestellt, die im Anschluss mit den T-PIGs vermengt wurde. Die so erhaltene Paste wurde mittels der sogenannten „solvent cast“ Technik als dünner Film auf die Polymeroberfläche aufgebracht. Dabei konnte die Schichtdicke durch den Einsatz eines „doctor blades“ eingestellt werden. Nach dem vollständigen Abdampfen des Lösungsmittels wurden fest verbundene PEU/PEU-T-PIG Laminate erhalten. Die anschließende Lasergravur führte zu Informationsträgern, die bei Raumtemperatur lesbar waren. Oberhalb der Farbumschlagstemperatur der eingesetzten T-PIGs wurden diese jedoch aufgrund von Kontrastverlusten unlesbar. Die so erhaltenen multifunktionalen Informationsträger waren demzufolge neben ihren Formgedächtniseigenschaften durch einstellbare, temperaturabhängige Farbänderungen charakterisiert. Darüber hinaus war es möglich, Informationsträger mit mehreren Farbumschlägen zu erhalten, indem T-PIGs mit unterschiedlichen Farben und Farbumschlagstemperaturen während der Herstellung eingesetzt wurden. In einem weiteren Szenario wurden Informationsträger mit einer Schicht aus thermochromer Paste überdeckt. Als Folge war der Barcode bei Raumtemperatur unter dieser Schicht verborgen und wurde erst beim Erwärmen oberhalb der Schalttemperatur sichtbar und lesbar.

TABLE OF CONTENTS

1. INTRODUCTION

1.1. INTRODUCTION TO POLYMERS

Polymers are substances composed of macromolecules (IUPAC definition),[1] which in turn are built by repeated subunits, the so-called monomers.[2-5] Polymers range from natural biopolymers,[6,7] such as DNA and proteins to synthetic plastics[8,9] like polyethylene (PE), as used in the manufacture of carrier bags.[10]

One common way to classify a polymer is depicted in **Figure 1.1**. Therein the polymers are divided into three major classes depending on their structure and the nature of their cross-links.[3]

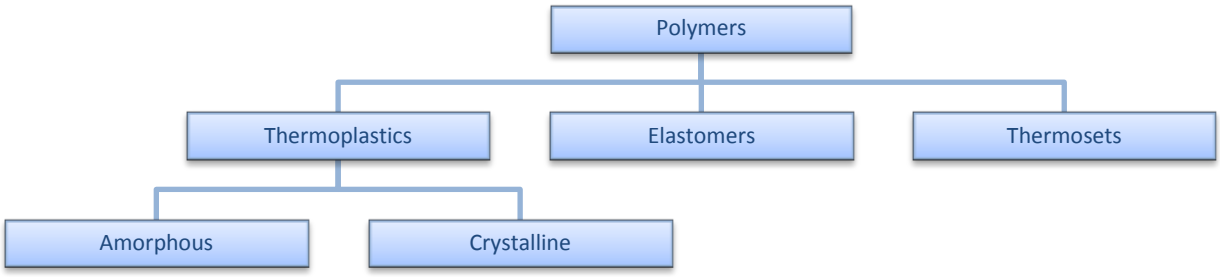

Figure 1.1 Classification of polymers.

On the one hand polymer chains can be physically cross-linked forming thermoplastics and thermoplastic elastomers; on the other hand they can be chemically cross-linked forming elastomers and thermosets. But before the polymer classes are considered in more detail, various architectures and states of matter will be discussed.

1.1.1. Architecture

When macromolecules are composed of one sort of monomer, the resulting polymer is called homopolymer. Prominent examples are PE[11] and polystyrene[12]. In turn, if the long chain molecules derive from more than one species of monomers, the polymer is called a copolymer. By the variation of the monomer fractions, the physical, chemical and processing behavior can be strongly influenced. Depending on the arrangement of the subunits, *i.e.* segments, copolymers can be separated into several types, such as statistical, alternating, block or grafted polymers.[4,5]

The skeletal structure of polymers depends on the arrangement of the monomers and can be divided into linear, branched and network polymers.[5,13] In linear polymers, the macromolecules simply consist of a long chain, in which all of the monomers exist in a single line. However, the chains are not straight and stiff, they are rather flexible. Thus, the macromolecules are able to twist and bend and can become entangled.[14] Commonly, the degree of entanglement has an impact on the physical properties of the polymer. In general one can say, the higher the number of entanglements per chain, the higher the polymer strength, toughness, and the glass transition temperature (T_g).

In branched polymers, the macromolecules have side chains, interconnected with the main chain. They can be further categorized by how they branch off from the main chain.[15] The categories include star-, comb-, and brush-shaped polymers, as well as dendronized and ring polymers. In addition, the branching affects the ability of chains to slide past one another and thus influences the chain entanglement.

Network polymers have three-dimensional (3D) structures. Therein the chains are interconnected with each other, for example, through the formation of covalent bonds and are thus prevented from sliding off each other.[15] Such polymers are said to be chemically cross-linked. Depending on the chain length, cross-link density, degree of cross-linking and nature of the cross-links one can adjust the phase transition temperature, rigidity and crystallinity of the polymer.[3,15] When polymers are characterized by a dense network, they are very rigid whereas network polymers containing long, flexible branches connected at only a few sites along the chains exhibit elastic properties. In particular, post-polymerization cross-linking of chemically active sites of the polymeric chains by curing[16] or electron beam irradiation[17] are appropriate methods to set the thermal and mechanical properties of network polymers.

1.1.2. States of Matter and Thermal Transitions

The bulk state of polymers, sometimes called the condensed or the solid state, may include both amorphous and crystalline domains.[18,19] Amorphous polymers have often a glass-like, transparent appearance. In contrast to that, semi-crystalline polymers are often opaque because the crystallites may scatter light.

Long chain linear and branched macromolecules tend to be in an amorphous state. The atoms rotate around the axis of covalent bonds and thereby the polymer chain adapts various conformations. Statistically, the most probable arrangement of a single

macromolecule is randomly coiled and entangled.[14] Disordered chains are more probable than stretched, ordered ones, due to entropic forces. The thermal transition of amorphous polymer domains is the glass transition, which is also called glass-liquid or glass-rubber transition.

As a result of vitrification, *i.e.* supercooling, of a viscous liquid into the glassy state, the amorphous domains of the polymer become rigid and brittle. The micro-Brownian motion of the (network) chains is reduced and the polymer is in a persistent non-equilibrium state. The relaxation times associated with such hindered motions are usually long compared to the time of their observation. The phase transition occurs over a given temperature range, the glass transition region, and can be quantified by differential scanning calorimetry (DSC) and dynamic mechanical analysis (DMA). Differential scanning calorimetry monitors heat effects associated with phase transitions and chemical reactions as a function of temperature. In the DSC experiment, the glass transition is manifested by a drastic shift of the baseline, indicating a change in the heat capacity C_p (**Figure 1.2**).

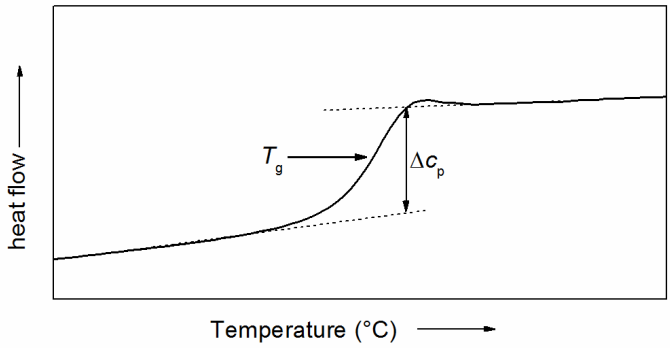

Figure 1.2 Typical DSC scan showing a glass transition of an amorphous polymer.

The temperature at the midpoint of the transition from the glassy to the rubbery state is often defined as the glass transition temperature T_g. No enthalpy is associated with such a second-order transition.[20]

When passing the glass transition, the polymer undergoes a smooth increase in the viscosity accompanied by a decline in Young´s modulus.[21] Typically, the modulus drops by a factor of about 1000 in a 20 to 30 °C range.[22] In other words, the conformational freedom permits viscous flow as well as elastic behavior. Thus, the polymer reversibly switches from a brittle to a rubber-like material. This change in behavior can be studied by means of DMA (**Figure 1.3**).

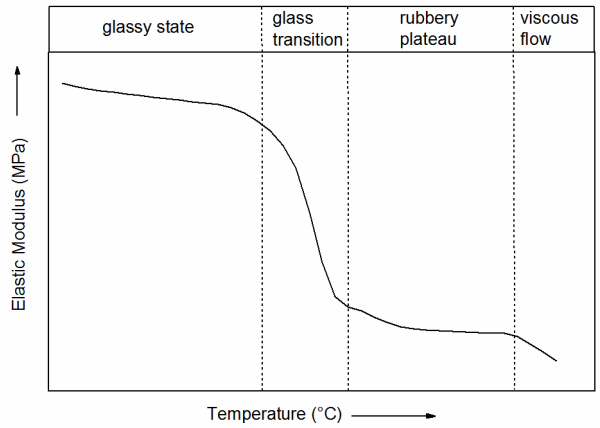

Figure 1.3 Typical DMA measurement of an amorphous polymer.

Apart from that, polymers like linear homopolymers and block-copolymers may crystallize when their chains adopt regular arrangements. This is favored, if the macromolecules are of low molecular weight. On the other hand, long chain and branched polymers are difficult to crystallize due to their high degree of entanglement. This is particularly true when the polymer melt is very viscous, which means that the individual chains do not flow very easily. However, polymers do not form perfect crystalline materials, but instead form semi-crystalline polymers, consisting of crystalline domains and amorphous regions. The degree of crystallinity can be estimated by analytical methods such as DSC,[23] density measurements[24] and X-ray diffraction[25,26] and typically ranges between 10 and 80%. Semi-crystalline polymers are characterized by very high toughness due to strong intermolecular forces associated with close chain packing in the crystallites.

Crystalline segments exhibit a first-order transition, known as melting.[27] Herein, the volume-temperature dependence, and the heat of transition show discontinuity. The associated transition temperatures are the melting temperature T_m when heating, and the crystallization temperature T_c when cooling the polymer (**Figure 1.4**). The respective heat transitions are the melting ΔH_m and crystallization enthalpy ΔH_c. The melting temperature is always higher than T_g. As a result, a semi-crystalline polymer is amorphous in the melt.

The structural modifications of polymeric crystals can be various, ranging from granular crystallites and lamellae, over spherulites, to row-nucleated structures ("Shish-kebab" structures).[28]

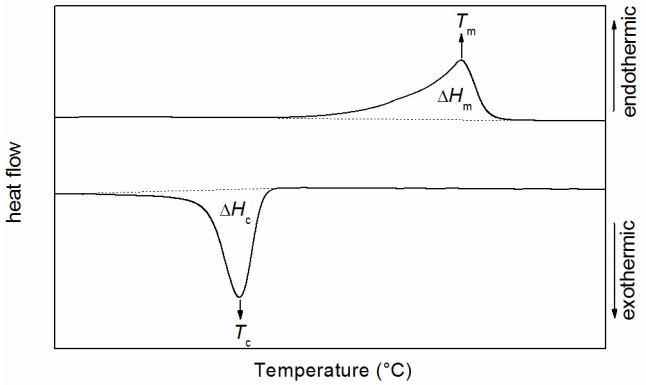

Figure 1.4 Typical DSC thermogram of a polymer with a crystalline phase.

Besides cooling the polymer below T_c, crystallization can also be induced by deformation (stretching), which causes the chains to line up.[29-31] This effect is known as strain-induced crystallization. As a consequence of drawing, the polymer becomes much harder to break because the crystallites formed have a pronounced reinforcing effect.

1.1.3. Thermoplastics

Thermoplastics are physically cross-linked polymers, consisting of linear or branched macromolecules. The cross-links arise from physical interactions between the chains like entanglement,[14] hydrogen bonding, dipole-dipole interaction and van der Waals forces. These interactions hold the polymer segments together and support the formation of crystal structure.[32] As a consequence, thermoplastics may be completely amorphous or semi-crystalline. Besides that, thermoplastics can be molded and remolded into virtually any shape in the course of processing. This includes techniques such as extrusion, injection molding and blow molding.

The subgroup of thermoplastic elastomers is characterized by reversible cross-links acting as netpoints.[33] These can be resolved by heat or solvation and reform on subsequent cooling/desolvation. Such systems are typically comprised of thermodynamically incompatible blocks and thus they reveal a phase segregated microstructure.[34-36] The block with the highest thermal transition T_{perm}, the so-called hard segment, sets the netpoints that function both as physical cross-links and as reinforcing fillers. Therefore, the mechanical strength of the polymer is provided by the hard segments. Above T_{perm}, the polymer forms a homogenous viscous melt that can be processed as described above. In turn, the block with the lower thermal transition temperature, the so-called soft segment, is acting as a mobile (switching) phase and

gives the elastic properties of the polymer. The behavior of thermoplastic elastomers below T_{perm} is similar to that of elastomers and will be described in more detail in the following chapter.

The thermal properties and functional performance of thermoplastics and thermoplastic elastomers can be tailored by varying synthesis and manufacturing strategies. Some of the tunable key parameters are in the polymer architecture including the molecular weight of the different segments,[37-40] microphase separation[41,42] and cross-link density.[43]

Prominent examples for phase segregated polymers are thermoplastic polyurethanes (TPUs). Typically three building blocks are necessary for their synthesis: polyols, polyisocyanates and chain extenders (**Figure 1.5**).[33,44]

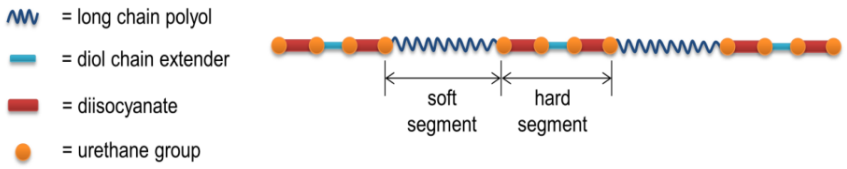

Figure 1.5 Schematic representation of a TPU.

The first building block is supposed to be a long-chain difunctional, hydroxy-terminated oligoester or -ether, determining the soft segment. Examples of polyester polyols are polyadipates synthesized *via* esterification (**Scheme 1.1**) of adipic acid and access of ethylene glycol, diethylene glycole, propylene glycol, 1,4-butanediole, 1,6-hexanediole or mixtures of these diols.

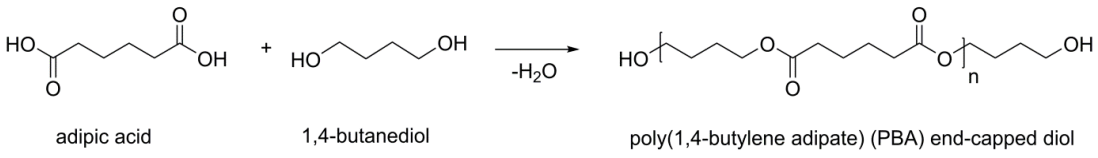

Scheme 1.1 Synthesis of a polyadipate *via* esterification.

Other polyesters of commercial interest are polycaprolactones and aliphatic polycarbonates. The former are based on ε-caprolactone and a bifunctional initiator such as 1,6-hexanediole. The latter are made from polyols by transesterification with low molecular weight carbonates such as diethyl or diphenyl carbonate.

The second building block (hard segment) could either be an aliphatic or aromatic diisocyanate such as hexamethylene diisocyanate, 1,4-cyclohexane diisocyanate, 4,4′-methylene diphenyl diisocyanate or 2,4-toluene diisocyanate.

Finally, a short chain (low molecular weight) diol or diamine such as ethylene glycol, 1,6-hexanediol, 1,4-butanediol, ethylene diamine or hydrazine is required as chain extender.

In principle, a TPU can be synthesized by two methods, namely a one-shot-[45-47] or pre-polymer[48-50] method. In the one-shot method, the polymer is synthesized in a single step by simultaneous addition of polyol, diisocyanate and chain extender. Applying the pre-polymer method, the polymerization is initiated by the reaction of linear polyols, having molecular weights of 500 to 5000 g mol^{-1} with excess of diisocyanate (**Scheme 1.2**).[48] Thus, an intermediate polymer called pre-polymer is formed. In a second step, the pre-polymer is converted into the final high molecular weight polymer by further reaction with a diol chain extender.

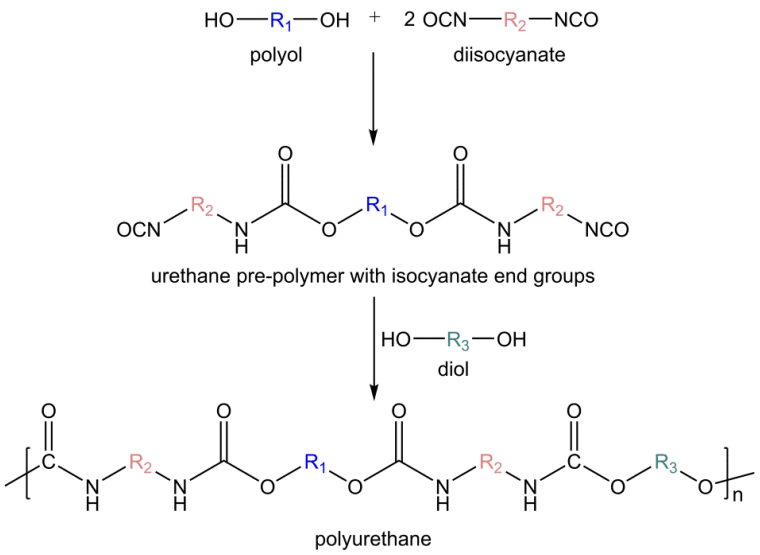

Scheme 1.2 Synthesis of polyurethane *via* pre-polymer method.

In a modified pre-polymer method, the so-called soft segment pre-extension method,[51,52] the first step comprises of the reaction of the linear polyol with just a part of the diisocyanate. Thus, a higher molecular weight isocyanate pre-elongated soft segment is formed. In a second step, the latter is mixed with the remaining amount of diisocyanate to form the pre-polymer. Finally, the TPU is formed by the addition of a diol chain extender.

All synthesis methods have in common, that other substances like components or additives can be admixed during the processing. Some of them are: stabilizers against hydrolysis[53] and radiation,[54,55] flame retardants,[56,57] dyes and pigments for coloring,[58] and reinforcing fibers.[59,60]

The advantage of two- and multi-step polymerization is that it allows a better control of the reaction itself and the resulting block lengths. This is because the competing reaction, the addition of polyol and diol to the diisocyanate, is strongly suppressed during the gradual growth reaction. At the same time one has a better control over the resulting properties of the polymer, including the processing behavior, melting/crystallization temperatures and the rigidity.[51,61]

The urethane bonds that are linked through the chain extender molecules are entities with high polarity.[62] Thus, they have the possibility of extensive hydrogen bonding. As a result of their strong intermolecular interaction, they form the hard segments, which are embedded in the amorphous or semi-crystalline matrix of the elastic soft segments.

1.1.4. Elastomers

This class of polymers is characterized by wide-meshed chemical cross-links. Since their working temperature is above T_g they show a rubbery behavior. In contrast to physically cross-linked polymers, the cross-linking takes place during the processing. As a consequence, the network is irreversibly cross-linked and tends to be non-recyclable. Thus, these polymers cannot be re-processed into different shapes by means of hot forming or welding without chemical degradation.

The 3D networks are usually formed during a curing process, in which chemically active sites of the polymeric chains react. One prominent example for chemical cross-linking is the vulcanization of rubber, which changes the property of elastic rubber to the hard, durable material associated with car and bike tires.[63] Here, the cross-linking is usually achieved by the addition of sulfur, which reacts with allylic hydrogen atoms of the poly(isoprene) chains.[4,64] This results in sulfur "bridges" between neighboring polymeric chains. The physical properties of the rubber and other elastomers are strongly dependent on the cross-linking density and the length of the bridges.

Elastomers can be stretched easily to high extensions (five to ten times of their original length)[65] applying comparatively small stresses, exhibiting a loss of entropy S.[66] The distance between the netpoints increases during stretching and the chains become aligned. When the applied stress is released, the material subsequently recovers to its original dimensions and gains back the entropy lost before. This phenomenon is known as entropy elasticity. Interestingly, the coefficient of thermal expansion is negative for a stretched elastomer above T_g, while it is conventional (positive) when unloaded. Besides

that, the elastic modulus increases upon heating when stretched. Another characteristic of ideal elastomers is that the inner energy will not change if it is stretched. They warm up when they are stretched and cool down when contracting.

1.1.5. Thermosets

Thermosets are network polymers with a high degree of chemical cross-linking. As a consequence, the chain mobility is greatly restricted and the material is rigid.[67]

One class of widely used thermoset polymers is epoxy, which is the cured end product of epoxy resins.[68-71] The latter are low molecular weight pre-polymers or higher molecular weight polymers which normally contain at least two epoxide groups. Usually, they are built up by the reaction of epichlorohydrin with aromatic and aliphatic diols, polyols or dicarboxylic acids. Examples are: bisphenol A and F, novolacs, 1,4-butanediol, 1,6-hexanediol and hexahydrophtalic acid.[72] Although a number of different types are commercially available, one of the most widely used epoxy resin is composed of epichlorohydrin and bisphenol A (**Scheme 1.3**).

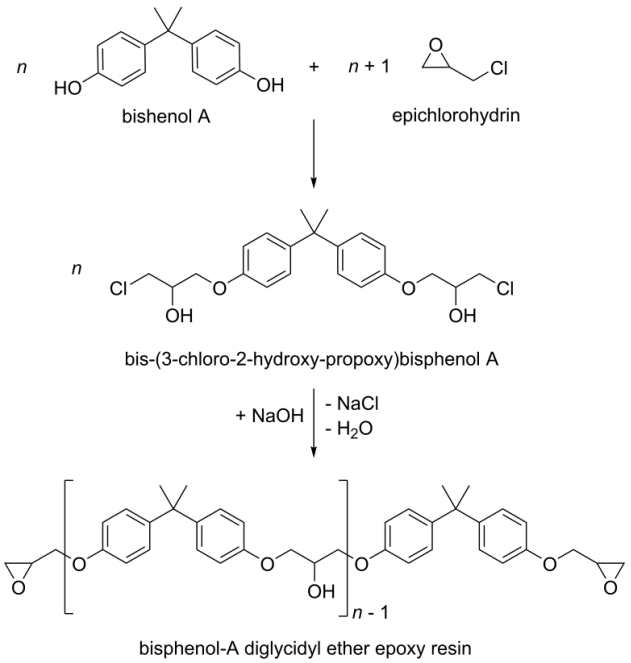

Scheme 1.3 Synthesis of expoxy resin based on bisphenol A and epichlorohydin.

The repeating units *n* are usually between 0 and 12. Cross-linking under the influence of heat is not sufficiently or rapid enough and thus a curing agent must be added. Common classes of hardeners for epoxy resins include amines, acids, acid anhydrides, phenols, alcohols and thiols. Some of them will cross-link the resins at ambient temperature, but

many of them require heat, with temperatures between 120 and 150 °C. When polyamines are used for cross-linking, the curing involves the base catalyzed opening of the epoxide groups. On the contrary, when using anhydrides, the hyperbranching occurs primarily through the hydroxyl groups.

Chemical cross-linking can also be induced in materials that are normally thermoplastic, for example through exposure to a radiation source,[73] such as electron beam exposure,[17] gamma-radiation,[74] or UV light.[75]

1.2. Fundamental Aspects of Shape Memory Polymers

Shape memory polymers (SMPs) are stimuli-responsive "smart" polymers that can remember a primary (permanent) shape after having been stabilized in a secondary (temporary) shape by heating.[76-79]

The shape memory effect (SME) is a result of the structure and morphology of the polymer together with the applied processing and programming procedure.[76] In general, an SMP consists of cross-links or netpoints, which determine the permanent shape. This is because the polymer is required to remain in a stable network structure so as to recover to its permanent shape. On the other hand, an SMP consists of switching segments which are used to create and maintain the temporary shape.

On the basis of the nature of their network structure, SMPs can be subdivided into physically and chemically cross-linked (**Figure 1.6**).[76,78]

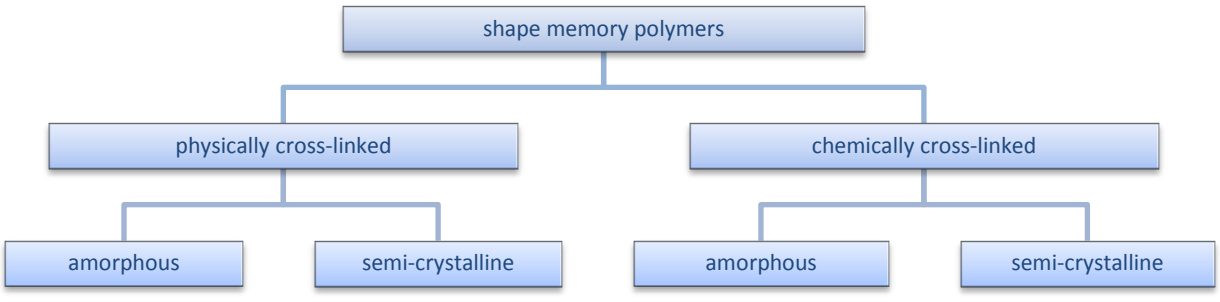

Figure 1.6 Categorization of shape memory polymers.

Further separation can be made according to the thermal transition T_{trans} of the particular switching segment on which the triggering of the SME is based. Either the

transition temperature T_{trans} is the glass transition temperature T_g or the melting temperature T_m.

The permanent shape of the polymer is set during the processing. The programming of an SMP from the permanent shape into a temporary shape typically consists of heating up, deforming and cooling the sample (**Figure 1.7**). When heated above the transition temperature T_{trans}, the viscoelasticity of the SMP increases. Thus, the sample can easily be deformed into the desired temporary shape through application of an external force. The new shape can then be fixed by cooling the polymer below T_g or T_c, respectively. Subsequently, the remaining stress can be released and the polymer remains stable in that new shape until the SME is triggered by re-heating the sample above T_{trans}. Hence, the polymer almost recovers its permanent shape. No recovery to the temporary shape can be observed on subsequent cooling, thus the described effect is termed one-way SME.

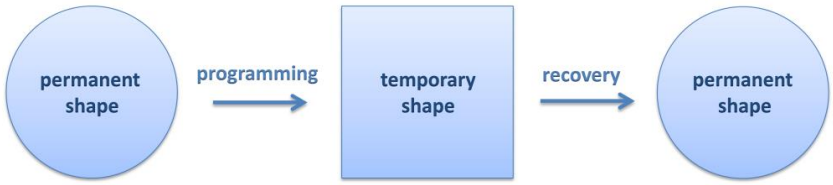

Figure 1.7 Schematic representation of the thermally induced one-way shape memory effect.

The thermally induced SME may either be triggered *via* direct or indirect heating. In the case of the latter, the polymer is doped with suitable fillers, which enable selective heating of the polymer by electric current,[80-82] magnetic fields[83,84] or irradiation with light.[85-87] These stimuli methods will be discussed in more detail in chapter 1.5.1.

SMPs have advantages compared to other shape memory materials, such as alloys. Particular highlights are their ability to sustain high elastic deformation (strains >200%) and their tailorable switching temperature.[78,88] Besides that, SMPs are characterized by low density, low cost, easy processability, and high shape recoverability as well as by potential biocompatibility and biodegradability. One limitation of SMPs is, that their recovery stresses are comparatively low (between 1 and 3 MPa). In return, shape memory alloys achieve values of about 150–300 MPa, but recover only up to 8% of elongation.

1.2.1. Physically Cross-linked SMPs

In this section SMPs are presented that form part of the class of physically cross-linked polymers. Consequently, they belong to the class of thermoplastics and thermoplastic elastomers, too.[76] In these materials the soft segment acts as a molecular switch. It is interconnecting the netpoints and enables the fixation of the temporary shape. On the contrary, the hard segment provides the physical cross-links and sets the permanent shape of the polymer.

One example for a chemically cross-linked polymer with shape memory properties is Desmopan DP 2795A SMP, a poly(ester urethane) (PEU) from Bayer MaterialScience AG. Therein, the rigid hard segments are composed of 4,4′-methylene diphenyl diisocyanate (MDI) and 1,4-butanediol (BDO) as chain extender (**Scheme 1.4**). The elastomeric soft segments are based on PBA (Scheme 1.1).[89-91] The synthesis is usually performed *via* a soft segment pre-extension method,[52] as described in section 1.1.3.

4,4'-methylenediphenyl diisocyanate (MDI) 1,4-butanediol (BDO)

Scheme 1.4 Chemical structures of the building blocks for the hard segment synthesis of DP 2795A SMP.

The room-temperature semi-crystalline DP 2795A SMP is characterized by the following thermal transitions: T_g (PBA) at −49 °C and broad DSC signals with peak maxima for T_m (PBA) at 45 °C and T_c (PBA) at −4 °C.[92] The PBA phase is polymorphic and tends to crystallize in a thermodynamically stable α crystal form (monoclinic) or metastable β crystal form (orthorhombic).[39] The polymorphic mixture is affected by crystallization conditions like the cooling rate, whereas a polymorphic β to α transition may either be promoted or inhibited by the storage conditions (**Figure 1.8**).

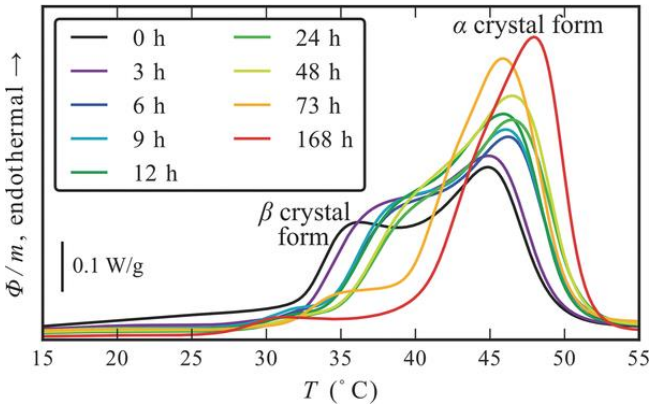

Figure 1.8 DSC thermograms of PEU, showing the first heating run after thermal pretreatment and different times of room temperature annealing, including the assignment of the PBA melting peaks to the β and α crystal form. Reproduced from Ref.[39] with permission from Wiley.

1.2.2. Chemically Cross-linked SMPs

A second class of SMPs consists of chemically cross-linked polymers. In these materials the cross-links are formed by covalent bonds, thus they belong to the thermosets. The chemically interconnected structures determine the original macroscopic shape of the SMPs. The switching segments are generally the network chains between the netpoints. Again, the SMPs can be divided into two categories, according to the thermal transition of their switching segments. Some examples of chemically cross-linked SMPs are shown in **Table 1.1**.

Table 1.1 Examples of shape memory thermosets with shape recovery either triggered by T_g or T_m. Adopted from Ref.[78]

Material	switching segment	T_{trans} (°C)
epoxy	amorphous	50–80
polynorbonene		40
PMMA–PBMA copolymers		20–110
PET–PEG copolymer		up to 80
poly(caprolactone)	semi-crystalline	54–58
polyethylene		~120
poly(cyclooctene)		45

Another example of a thermoset polymer with distinct shape memory properties is Veriflex® E2, an epoxy-based SMP from Cornerstone Research Group, Inc.[93] The Veriflex® E2 is a two-part, fully formable thermoset SMP resin mixture. It consists of the base resin Veriflex® E2a, and the curing agent Veriflex® E2b.

The cured, amorphous resin is characterized by a T_g of 61 °C and thus changes from a rigid glassy state to an elastic rubber upon heating past the transition temperature.[94,95]

1.3. Molecular Mechanism of the Shape Memory Effect

Polymers exhibit shape memory functionality, when a deformed shape can be stabilized in a temperature range relevant for the particular application. It is mandatory, that the flexibility of a network polymer is a function of temperature.

The principle of the shape memory functionality is initially shown for a physically cross-linked and phase segregated block-polymer like the above-described PEU (**Figure 1.9**).

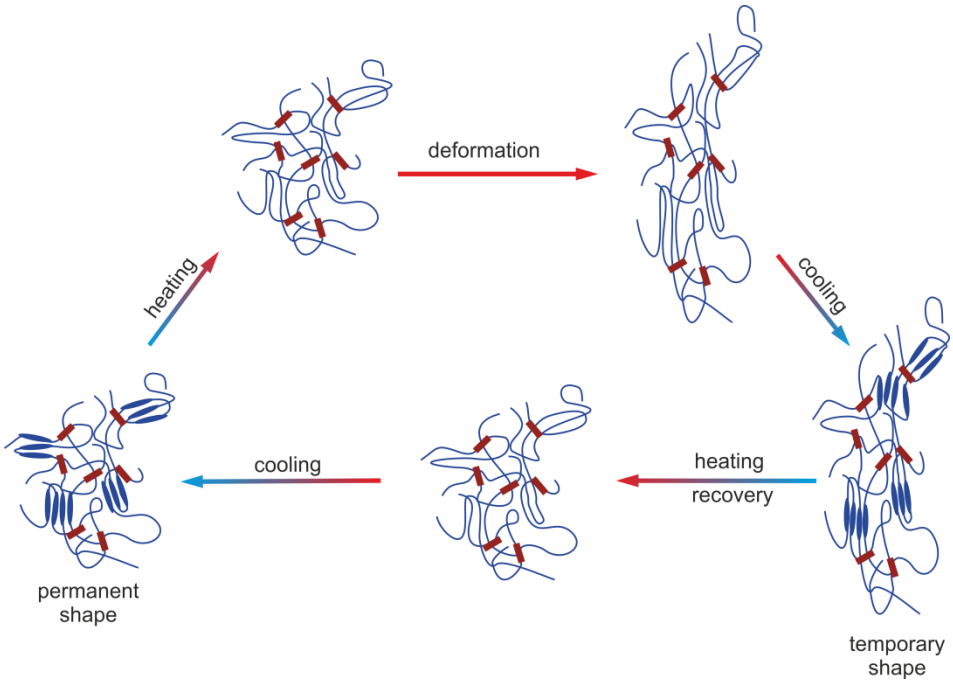

Figure 1.9 Molecular mechanism of programming and recovering a physically cross-linked SMP. Red blocks represent the netpoints formed by hard segments; blue lines represent soft segment.

Herein, the T_{trans} is T_m of the soft segments. In the permanent shape, the polymer chains prefer to be in a randomly coiled arrangement. Upon heating the polymer above T_{trans}, the soft segment (blue lines in **Figure 1.9**) becomes viscoelastic and shows entropy elasticity. When subsequently stretched, the distance between the netpoints increases and the molecular chains become oriented. The deformed shape can then be fixed by introduction of reversible physical cross-links such as crystalline segments, *i.e.* by cooling the polymer below T_c of the soft segment. The formed crystals stabilize the new shape and prevent the macromolecules from their attempt to spontaneously return to the random coil structure. As a result, the temporary shape is stable until the SME is

thermally triggered. By heating above T_m, the crystals melt and the polymer recovers almost its permanent shape. The thermodynamic reason is the entropic gain to recover the random structure. The physical cross-links in the hard segments (red blocks in **Figure 1.9**) act as netpoints and help the polymer to memorize its permanent shape.

Chemically cross-linked SMPs exhibit viscous flow above their T_g, as described in chapter 1.1.5. As a consequence, the SMP can be deformed elastically in the rubbery state. The fixation of the temporary shape is accomplished by kinetically freezing the motion of the chains through cooling below T_g. In other words, in the glassy state the polymeric chains do not possess sufficient thermal energy to retract to their preferred orientation. When thermal energy is brought into the system *via* heating above $T_{trans} = T_g$, the permanent shape is recovered.

1.4. MACROSCOPIC SHAPE MEMORY EFFECT

1.4.1. One-way Shape Memory Effect

In the following, the macroscopic SME is described in more detail. Most prominent and widely employed is the dual-shape one-way SME. After programming, the polymer is able to recover once into its original shape under stress-free conditions. An additional shape memory cycle requires an extra programming step.

Commonly, the shape memory performance of a polymer is quantified by means of cyclic thermo-mechanical measurements (CTMs) using a tensile testing machine equipped with a thermochamber (**Figure 1.10**).

Figure 1.10 MTS tensile testing machine equipped with a thermochamber.

With this setup the measuring parameters such as the temperature (T), strain (ε) and stress (σ) as well as the respective rates for heating/cooling, deformation and loading/unloading can be adjusted. The MTS Insight 10 electromechanical testing system from MTS System Corporation was used for conducting the experiments. The detailed setup is described in the experimental parts of the respective chapters. The load cell was chosen in accordance with the required tensile forces (100 or 250 N load cell) and compressive forces (10 kN load cell).

Typically, CTMs are performed on dog-bone shaped tensile bars (EN ISO 527-2:1996) and consist of four distinct steps in which the first three involve the programming and the last one the recovery (**Figure 1.11**).

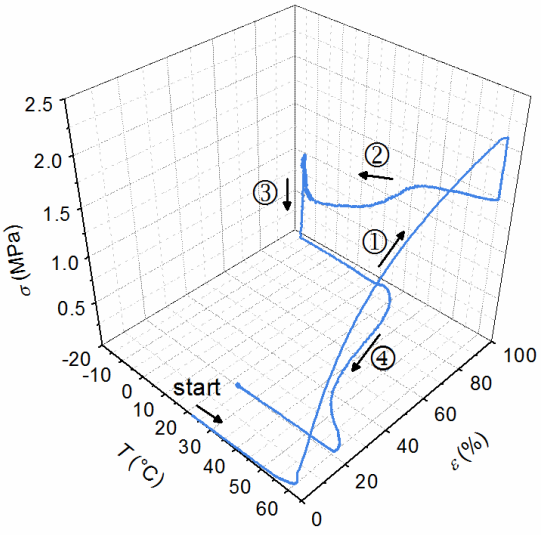

Figure 1.11 Cyclic thermo-mechanical measurement of a PEU, showing one cycle including elongation ①, strain fixing ②, unloading ③ and strain recovering ④.

The first step of a protocol of a thermo-mechanical procedure consists of deformation of the SMP at $T_d > T_g$ or T_m (① in **Figure 1.11**), for example by drawing the specimen to a strain of $\varepsilon_m = 100\%$. As a result of the growing deformation, the stress is also increasing. This originates from the entropy-elasticity.

The second step of programming comprises of the fixation of the new shape (② in **Figure 1.11**). Therefore, the specimen is cooled under constant strain ε_m to $T_{fix} < T_g$ or T_c. During fixation, the stress also decreases. This originates from differences of the coefficient of thermal expansion of the stretched polymer at temperatures above and below T_{fix} as a result of entropy-elasticity.[76] In addition, the volume of semi-crystalline SMPs decreases upon crystallization due to an increase in density.[96]

The last programming step consists of unloading of the specimen at T_{fix} (③ in **Figure 1.11**) and heating to room temperature.

Finally, recovery of the SMP is induced by heating the specimen again to T_d. Two different procedures are possible. Recovery can be measured in free (④ in **Figure 1.11**) or constraint recovery. In other words, when the stress is kept constant upon recovery, the polymer responds with a change in strain and *vice versa*.

After cooling the specimen back down to room temperature, the first cycle of a thermo-mechanical procedure is completed and a second cycle can be run.

After at least two subsequent cycles of the above-mentioned CTM, the shape memory related properties can be determined. These include the strain fixity ratio $R_f(N)$, strain recovery ratio $R_r(N)$ and the total strain recovery ratio $R_{r,tot}(N)$, which are calculated using the following equations:

$$R_f(N) = \frac{\varepsilon_u(N)}{\varepsilon_m} \cdot 100\% \tag{1}$$

$$R_r(N) = \frac{\varepsilon_m - \varepsilon_p(N)}{\varepsilon_m - \varepsilon_p(N-1)} \cdot 100\% \tag{2}$$

$$R_{r,tot}(N) = \frac{\varepsilon_m - \varepsilon_p(N)}{\varepsilon_m} \cdot 100\% \tag{3}$$

The strain fixity ratio $R_f(N)$ quantifies the ability of the material to fix the mechanical deformation applied in the course of the deformation. The strain recovery ratio $R_r(N)$ describes the ability of the polymer to memorize its permanent shape, whereas the total strain recovery ratio $R_{r,tot}(N)$ is defined as the strain recovery after N passed cycles with respect to the original shape of the sample. Herein, the fixed strain ε_u is the strain after programming and the residual strain ε_p is the strain after recovering a permanent shape. Both values can be determined after holding the unconstrained specimens for 5 min at room temperature.

Typical shape memory related values are exemplarily shown for a PEU, which was a precursor of Desmopan DP 2795A SMP in **Table 1.2**.

Table 1.2 Values for the shape fixity, strain recovery and total strain recovery ratio of PEU from Ref.[89] Deformation was applied at 60 °C and fixation at −15 °C

N	R_f (%)	R_r (%)	$R_{r,tot}$ (%)
1	98.8	76.5	–
2–5	99.2±0.4	97.7±1.5	72.0±1.5

The first cycles of CTMs may differ significantly from the following ones. That is why usually five subsequent cycles of programming and recovering are conducted in order to characterize the shape memory properties. With increasing number of cycles the stress-strain-temperature behavior becomes more similar and the process of deformation and recovery becomes highly reproducible. The discrepancy of the first cycles can be explained by different thermal histories for various samples, including processing and storage conditions. Besides that, the polymer chains align in the direction of deformation in the course of the programming. Thereby, some of the chains may be disrupted.

Apart from this, the shape memory performance of a polymer is strongly dependent on the measuring parameters such as T_d and T_{fix}, heating and cooling rates, deformation rate, maximum strain, holding times and number of testing cycles. On the other hand, the thermal and mechanical properties of the polymer itself play also an important role. Thus, it is important to set the testing parameters carefully in accordance with the materials thermal and mechanical properties.

The chemical composition and structural characteristics of the polymer have a strong influence on the thermal and mechanical properties of the material and thus on the shape memory performance as well. In TPUs for instance, the SME is strongly affected by the hard to soft segment ratio.[39,40] It was found that as the crystallinity of soft segments increased, the ability of the samples in the fixation of temporary shape was higher. On the other hand, the shape recovery performance is dependent on the hard segment content. In other words, the samples with higher soft segment content show higher values of shape fixity and the specimens containing higher hard segment content show increased shape recovery.

Besides the dual-shape effect, some polymers and polymer composites are also able to perform multiple-shape changes, such as triple-shape[97-100] changes. Here the polymer may recover from a temporary shape A to a second intermediate shape B back to the permanent shape C. A physically cross-linked PEU, for instance, can be transformed

from the original to a first temporary shape B, fixed by cooling below T_c (PBA).[92] Subsequently, a second programming step can be applied by an additional deformation B ⇨ C, fixed by cooling below T_g (PBA). The shape A remains stable as long as the polymer is kept at temperatures below T_g (PBA). In return, the programmed PEU may recover twice upon gradual heating, A ⇨ B above T_g and B ⇨ C above T_m.

More than two intermediate shape changes can be achieved by stepwise programming and recovering of polymers having broad thermal transitions (T_g or T_m), similar to the procedure described for triple-shape procedure.[101-103]

1.4.2. Two-way Shape Memory Effect

The two-way shape memory effect of polymers is characterized by thermoreversible actuation.[104-107] In contrast to the one-way SME, the polymer may switch reversibly between two different shapes upon temperature variation without the requirement for deformation by external thermomechanical programming.

When SMPs have crystallizable switching domains, they show distinct actuation when the temperature is cycled above T_m and below T_c while the stress is maintained constant. A common procedure for the thermoreversible two-way SME was recently shown for a PEU by Bothe *et al.*[108]. Herein, the first step comprised a pre-conditioning of the specimen. In detail, the polymer was heated above T_m (PBA) and stretched applying an initial stresses σ_i of 0.75 to 3 MPa, followed by unloading to $\sigma_c = 2/3\,\sigma_i$. The respective stress σ_c after pre-conditioning were kept constant during the following actuation, which was achieved by cooling the polymer to −20 °C < T_c (PBA) and subsequent heating to 60 °C > T_m (PBA). In dependence of the applied stress, the PEU showed different actuation behavior as depicted in **Figure 1.12**. During cooling, the PBA soft segment started crystallizing and induced thereby an elongation of the specimen (crystallization-induced elongation). In reverse, heating the polymer induced melting and thus initiated the recovery of the specimen almost to the pre-elongated strain (melting-induced contraction). As long as the load was kept constant, the actuation was thermo-reversible and cyclically not limited. Most distinct actuation was detected when the maximum applied stress during the pre-conditioning approached the point where the deformation-induced crystallization of the soft segments sets in.

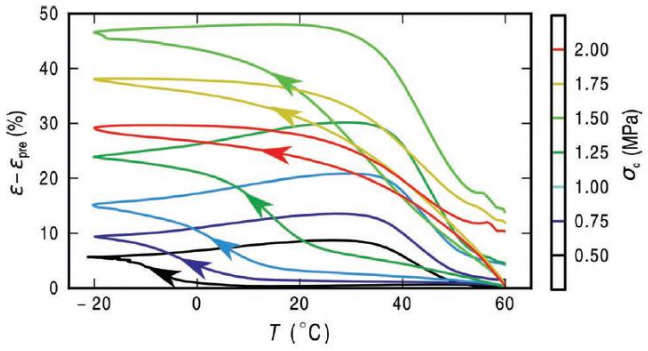

Figure 1.12 Strain–temperature protocol for PEU at different constant stresses σ_c (every color constitutes a separate measurement as defined by the table of colors, provided by the right vertical axis). The actuation behavior within the first thermo-mechanical cycle ($N = 1$), corresponding to the strain changes $\varepsilon - \varepsilon_{pre}$, is plotted. The isotonic measurements started after thermo-mechanical pretreatment at ε_{pre} values of 15% (0.5 MPa), 27% (0.75 MPa), 47% (1.0 MPa), 79% (1.25 MPa), 199% (1.5 MPa), 326% (1.75 MPa), and 362% (2.0 MPa). Reproduced from Ref.[108] with permission from Wiley.

Recently, it was shown that it is also possible to reversibly actuate a semi-crystalline SMP just by heating and cooling the polymer, without any load.[109-111] In the case of the so-called free standing actuation, the shape changes are enabled by a specific pre-conditioning procedure, the so-called training.[111] Such training consists of extensive tensile deformation in the viscoelastic state. Hence, deformation-induced crystallization is initiated. After subsequent unloading, pronounced thermo-reversible shape changes including expansion on cooling and contraction on heating could be verified as visible in **Figure 1.13**.

Other possibilities to achieve reversible changes in shape are provided by composite material. Therein, the actuation can be accomplished, for example, through lamination of two different polymer types.[112-114] The deformation of such systems is induced by a large disparity between the coefficients of the thermal expansion of the different composite materials. Tamagawa[112] for example, fabricated a polymeric laminate simply by attaching a resin plate to the fiber-reinforced polymer plate with instant glue. Another approach is the lamination of two stripes of the same polymer, where one is in the permanent shape and the other in a pre-elongated (programmed) state.[105,115] That way, bending upon heating and reverse bending upon cooling can be achieved. Westbrook *et al.*[116] demonstrated a transversal actuation of ~10% of the specimen length by an SMP composite, where a pre-stretched SMP was embedded in an elastomeric matrix.

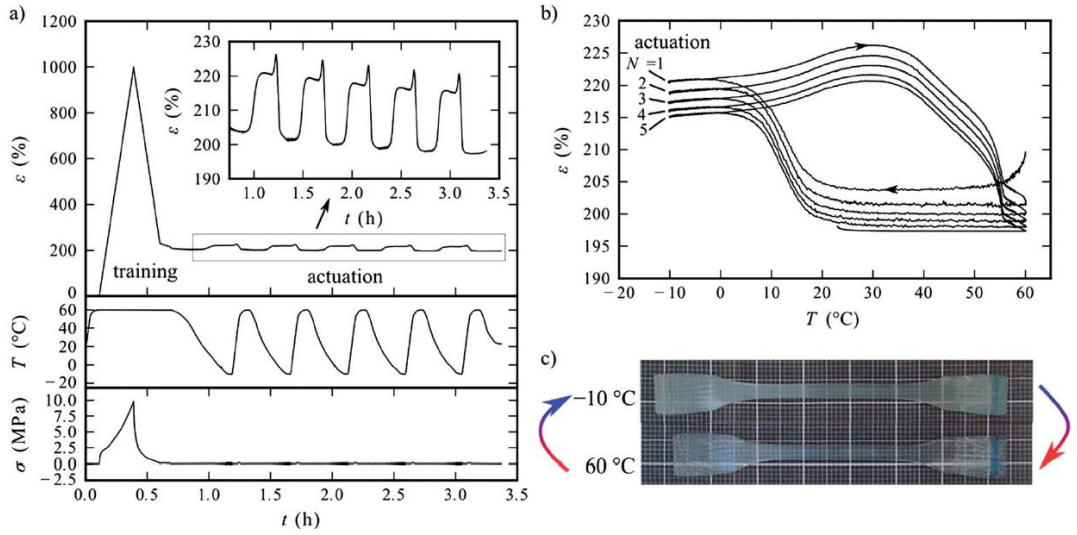

Figure 1.13 Actuation of PEU after training. (a) Evolution of tensile strain ε, temperature T and stress σ above time t in five cooling–heating cycles. The inset enlarges the actuation strains. (b) Cyclic evolution of strain *versus* temperature in five thermal cycles. (c) Trained PEU specimen in the sixth cycle at −10 and 60 °C. Reproduced from Ref.[111] with permission from The Royal Society of Chemistry.

1.5. MULTIFUNCTIONAL SHAPE MEMORY POLYMERS

Multifunctionality may be given by the combination of SMPs with additional functionalities.[88,117,118] Such materials consist either of one-component polymers or multi-material systems, such as composites or hybrid structures.

Composite materials are often realized by reinforcing SMPs with particles or fibers. As a result, these materials do not only exhibit the SME but also show tailor-made physical properties, such as high electrical conductivity,[80-82] magnetic response[83,84] or light sensitivity.[85-87] Thus, the SME of the polymer can be triggered *via* indirect heating. This effect may not only be used as a specific trigger, but also as a sensor for the particular stimulus.

1.5.1. Advanced Stimuli Methods

Electro-induced shape recovery could be realized by incorporation of conductive fillers like carbon fibers,[119-121] carbon nanotubes[122-124] or carbon black.[80,82,125,126] When a voltage is applied, the programmed polymer recovers due to Joule heating. In other words, electric energy is converted to heat through resistive losses in the material. Inductive heating can be accomplished by magnetic fillers like terfenol-D[127,128] or magnetite particles[129-131] and application of alternating magnetic fields.[132,133] Thus, electromagnetic energy is transformed from an external high frequency field into heat. Photothermal

induced shape recovery may be obtained for SMPs doped with selectively absorbing dyes or pigments.[134-137] Hence, indirect heating can be accomplished by illumination with radiant thermal energy of infrared light or by irradiation with laser light. For example, Leng *et al.*[138] demonstrated that SMPs filled with carbon black show infrared light induced SME.

Apart from the thermally-induced SME, the recovery of a programmed polymer can be achieved through chemical reaction,[139] pH sensitivity[140] and solvent effects.[141] In the latter, the solvent lowers T_g *via* disruption of hydrogen bonds and plasticization.[142-144]

1.5.2. Additional Multifunctional Systems

Another approach is to introduce additional functionalities which are not in connection with the trigger for the shape recovery. Promising examples are SMPs which are biodegradable or have advanced color changing properties. If applied for biomedical purposes, SMPs need to be biocompatible and biodegradable,[145-149] which requires them to be of low cytotoxicity, thrombogenicity and inflammatory response. This can be achieved through careful selection of the chemical composition of the polymer and by the choice of appropriate additives.

The change in color can indirectly be caused by a change in orientation of the polymer chains. Recently, Kunzelman *et al.*[150,151] introduced a novel type of shape memory material with reversible temperature sensing capabilities. They incorporated excimer-forming, chromogenic dyes into cross-linked poly(cyclooctene) (PCO) *via* guest diffusion. The exposure of this material to temperatures above T_m caused dispersion of the dye molecules, accompanied by color changes (**Figure 1.14**). Subsequent crystallization of the PCO was accompanied by aggregation of the dye and a return to the original color. In other words, the effect allows monitoring whether the set/release temperature of the material is attained. Thus, the conformational change could be visualized macroscopically as well.

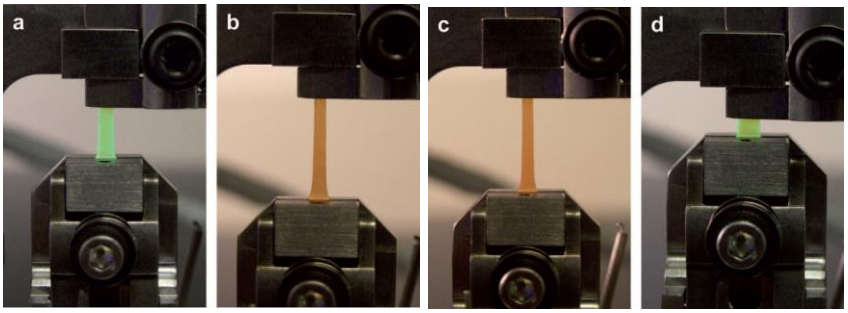

Figure 1.14 Photographs of the one-way shape memory cycle for a 1.5 mg mL^{-1} PCO/C18-RG sample (illuminated with 365 nm UV light) during (a) deformation (75 °C, 600 kPa), (b) cooling/fixing (5 °C, 600 kPa), (c) unloading (5 °C, 4 kPa), and (d) recovery (75 °C, 4 kPa). Reproduced from Ref.[151] with permission of The Royal Society of Chemistry.

1.6. ADVANCED TECHNOLOGICAL APPLICATIONS

There are manifold areas for potential application of SMPs, ranging from biomedical[152,153] over aerospace[154-156] to textile applications.[157-160]

Proposed biomedical applications for SMPs are diverse and comprise drug delivery systems,[161,162] devices for minimal invasive surgery such as blood clot removal devices,[134] aneurysm occlusion devices,[163] vascular stents,[164] orthopedics,[165] orthodontics[166] and sutures for wound closure (**Figure 1.15**).[146]

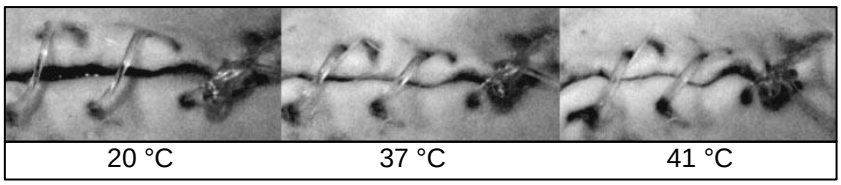

Figure 1.15 Degradable shape-memory suture for wound closure. Reprinted from Ref.[146] with permission of AAAS.

Vascular stents, for example, are small tubes or mesh-tubes, which may be inserted into the human body to maintain the patency of blood vessels or ureters. Such implants can be delivered *via* a catheter to the desired target in a compressed temporary shape. The functional permanent shape may be released *in situ* upon heating through the surrounding tissue to body temperature or *via* indirect thermal stimulus from outside of the body. Besides that, such stents may be coated with drug eluting agents in order to facilitate healing processes for example.[167]

SMPs are also attractive for aerospace applications due to their light weight.[156] Applied as deployable hinges or booms[168,169], they are space saving upon transportation into space and allow self-unfolding of different devices such as solar arrays[170,171] or antennas. The

restriction for the applicability in aerospace industry is that the polymers need to be stable against space environment. That includes resistance against low pressure conditions, ultra-high or low temperature cycle effects and ultraviolet (UV) radiation.[156]

Textile industry is another emerging field for potential shape memory applications.[157-160,172,173] Incorporated as fibers into textiles, SMPs may yield smart functionalities, such as moisture/temperature management,[174,175] controlled release of drugs and odor, wound monitoring, smart wetting properties, protection against extreme climatic conditions and wrinkle free fabrics.[160]

1.7. COLOR VISION AND COLORIMETRY

The science of color includes the perception of color by the human eye and brain, the origin of color in materials and the physics of electromagnetic radiation in the visible range.[176-179] Generally, light can be absorbed (completely or partially) by gases, liquids and solids. Besides that, it can be reflected at the surface of liquids and solids or transmitted through gases, liquids and transparent solids. Materials, that have the ability to absorb or to emit light in the visible range (λ = 400–800 nm), such as dyes and pigments are termed colorants. In dyes, for example, the color has its origin in the absorption of discrete wavelengths, resulting in excited electronic states.[180] A quantitative way to describe colors is called colorimetry.[181,182]

By defining a color space, colors can be identified numerically by their coordinates. Depending on the purpose, different color spaces are used.[183] For example, when colors are displayed on a computer monitor, one uses the so-called RGB (red, green and blue) color space[184] (**Figure 1.16**a). Here, the individual intensity of the colors can be considered as a vector in a 3D space with unique positions for every possible color. The RGB color model uses additive color mixing, since the color is given by emitted light of the respective colors. In contrast, the color space used for printing is CMYK (cyan, magenta, yellow and key/black),[185] which uses subtractive color mixing (**Figure 1.16**b). Here, the resulting color is given by the light reflected through the printed ink.

The color space used in connection with the enclosed manuscripts is the CIE 1976 ($L^*a^*b^*$) (CIELAB), which is a color-opponent space.[181,186] The dimensions of the 3D model are defined by the lightness *(L^*)*, the position between red and green (a^*) and the position between yellow and blue (b^*) (**Figure 1.16**c).

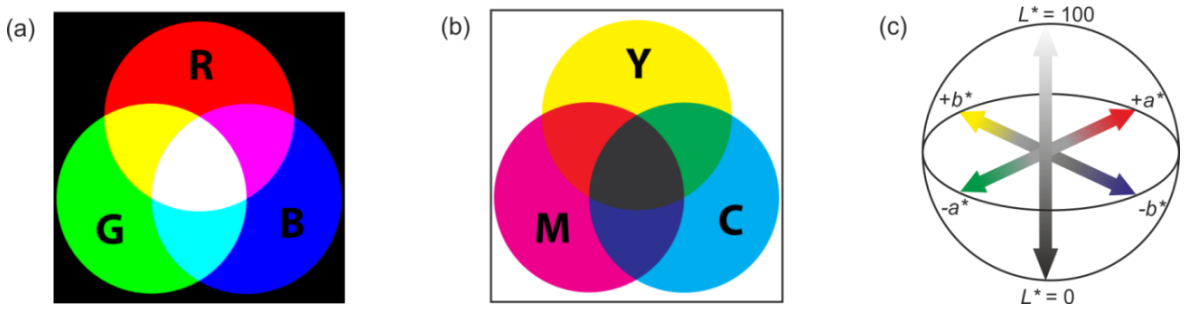

Figure 1.16 Different color spaces: RGB (additive color mixing, a),[187] CMY without black (subtractive color mixing, b)[188] and CIELAB (c).

The advantage of the CIELAB, which was specified by the International Commission on Illumination, is that this color space was developed in order to approximate human vision. It describes all the colors visible by human eye. Besides that, the CIELAB was created to serve as a device-independent model to be used as reference. It can be easily converted from spectral data by the application of a specified measuring geometry and light source.[189] Often used measuring geometries are 45°/0° or 0°/45°, where the first angle represents the angle between light source and sample and the second the angle between the sample and the reflected light collected by a spectrometer, respectively. Commonly, the D65 standard illuminant, simulating natural daylight at midday in Central Europe[190] is used as light source.

Another advantage of CIELAB is that it allows defining color differences ΔE by determining the distance between colors in the 3D color space. The color difference enables the definition of tolerances. This is of great importance to those whose work is color critical such as in the paint and coatings industry. Commonly values of $\Delta E < 1$ are not perceived by the human eye.[191]

1.8. TRIARYLMETHANE DYES

Triarylmethane dyes are part of an important class of commercial dyes and belong to the first developed synthetic dyes.[192-194] They are known since the 19th century. The first commercial dye was Phenolphthalein, which was synthesized in 1871 by Baeyer.[195,196] Commonly, they are characterized by brilliant and intense colors. These dyes often serve as pH indicators since many of them undergo reactions in response to acids and bases.[197,198] Besides that, they were also used in the textile industry, for cosmetics, food[199] and as printing inks.[200]

The color of triarylmethane dyes arises from their structure.[201,202] Their backbone is consisting of triphenylmethane, thus they are sometimes referred to as triphenylmethane dyes. The sp^2-hybridized central carbon atom of the positively charged system carries three aryl groups having at least one auxochromic group, such as $–NH_2$, $–NHR$, $–NR_2$, $–OH$ or $–OR$ in *para* position. Due to the electron donating groups, the conjugated system is extended by resonance, resulting in a bathochromic shift of λ_{max} to visible light. Some simple representatives of triarylmethane dyes, such as malachite green (*Basic Green 4*) and crystal violet, are shown in **Scheme 1.5**. In the ground state the conformation of the molecules is propeller-like with out-of-plane rotated phenyl rings due to steric hindrance of the six *ortho* hydrogen atoms.[180] In this conformation, the positive charge is located at the central carbon atom, forming a carbenium ion. As a result, the π-systems of the phenyl rings are not interconnected with each other and the molecule is achromatic.

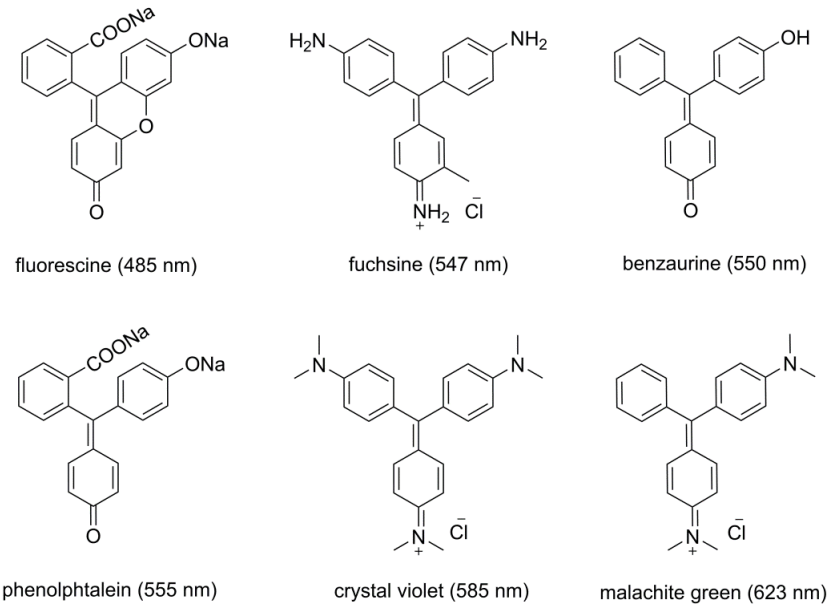

Scheme 1.5 Structural conformations of different triarylmetheane dyes. The numbers in the brackets represent the wavelength of maximum absorption λ_{max}, respectively.

The strong spectral absorption of triarylmethane dyes in their excited states arise from $\pi \rightarrow n^*$ transitions. The conjugated π-bonds act as chromophore, and the electron donating substituents in *para*-position act as an auxochrome.

In the first excited state of malachite green, for example, the two substituted phenyl rings are in-plane whereas the unsubstituted phenyl ring is out-of-plane. The π-electrons are conjugated and the positive charge is delocalized within the in-plane rings and the central carbon atom. The major band at $\lambda_{max} = 623$ nm corresponds to a polarization

along the *x*-axis of the molecule, whereas the minor band at λ_{max} = 427.5 nm corresponds to the polarization along the *y*-axis.[192]

1.9. THERMOCHROMISM

In general, thermochromism describes the characteristic of a material to change its optical properties in response to a change in temperature. Different types of thermochromic materials include, but are not limited to inorganic pigments,[203] liquid crystals[204-207] and conjugated polymers as well as leuco dye-developer-solvent systems[208-210] and inorganic-organic hybrid materials.

Thermochromic behavior can occur in organic and inorganic compounds, in monomers or polymers and in single- or multi-component systems. The color can change reversibly or irreversibly[211] with temperature variation due to changes of the light reflection, absorption or scattering.[212,213] It may be abrupt at a distinct temperature or gradually on heating.

In solid inorganic materials, such as metal salts and metal oxides, the thermochromic behavior can have its origin in lattice expansion. One example is ruby, a regular Al_2O_3 α-crystal with small content of Cr^{3+}, with a continuous color change from red to violet to green.[214] The color change temperatures strongly depend on the Cr^{3+} content. Another way to obtain reversible color changes in inorganic materials has its origin in changes of the crystal modification. In $[Cu_2(HgI_4)]$ for example, the low-temperature modification of the tetrahedral holes of the face-centered cubic cell is ordered whereas the high-temperature modification is disordered.[215] Besides that, the change in color can also be due to the increase of the band gap of semi-conductors on increasing temperature, such as in ZnO.[203]

Different behavior is observed for solutions of inorganic materials, such as of transition metal complexes, or of metal-organic hybrid materials. Therein the change in color has its origin in changes of the number of the solvent molecules in the coordination sphere or in changes in the ligand geometry.[203,216] As a result, the crystal field splitting of the *d*-orbitals is changing, which causes also a change in the absorbed wavelength. One example is $CoCl_2$, which is pink in aqueous solutions at room temperature due to the formation of octahedral $[Co(H_2O)_6]^{2+}$ complexes. Upon heating to 100 °C the color switches to violet because the formation of tetrahedral $[Co(H_2O)_4]^{2+}$ is favored.

Liquid crystals, which are compounds having a distinct phase of matter between the crystalline (solid) and isotropic (liquid) states, also show thermochromism.[207,217] Herein, the thermochromic effect results from temperature-dependent reflection of certain wavelengths by the crystalline structure of the anisotropic chiral or twisted nematic phase.[207] Here, the color change can be highly temperature sensitive and range over the colors of a rainbow. Popular applications for thermochromic liquid crystals are mood rings or thermometers.[218]

Another interesting class of thermochromic colorants is consisting of leuco dye-developer-solvent systems.[209] Such systems are composed of an electron donating chromogenic compound (leuco dye), an electron acceptor (developer) and a matrix component (solvent). Often, the three components are embedded in polymeric microcapsules and thus form thermochromic pigments (T-PIGs, **Figure 1.17a**).[219] These may turn colorless when heated above the color switching temperature (CST) and regain color upon cooling below that temperature (**Figure 1.17b**).[220-222] The advantage of microencapsulation is that the color forming components are protected against the environment by the highly mechanical and thermal stress resistant spherical membrane. Established polymeric shell materials are styrene[223] and melamine based resins.[224-228] The first step of encapsulation process usually consists of emulsification of the core components leuco-dye, the developer and the solvent in aqueous solution.[229] Subsequently, the shell formation is carried out by *in situ* interface polymerization. Thereby, the size of the capsules and the thickness of the walls can be set by the reaction conditions, such as the mixing speed, pH value and temperature.[230] Typically, the mean particle sizes are ranging between 1–100 µm in diameter.

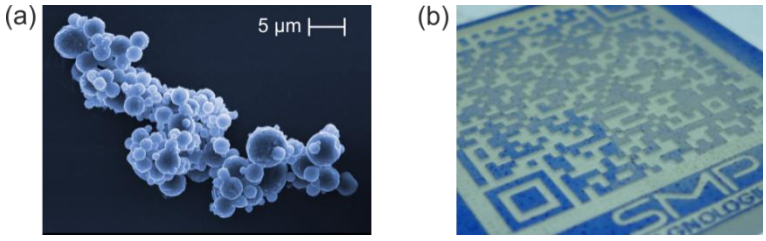

Figure 1.17 Colorized scanning electron micrograph of thermochromic microcapsules (T-PIG blue-43 from Sintal Chemie AG, a) and partially decolorized QR code carrier surface-colored with the same kind of T-PIG (b).

The thermochromic effect of leuco-dye-developer solvent systems is dependent on the transition between the solid and the liquid state of the solvent. In the solid state, the system is colored due to electronic interaction between dye and developer which form an

extended conjugated π-electron system.[231,232] On the contrary, the color-forming components get separated from each other when the solvent starts melting because both the leuco-dye and the developer, are solvated separately. As a consequence, electronic interactions are inhibited and the microcapsules become achromatic.[208,233] A common example for a leuco-dye in a thermochromic system is crystal violet lactone (CVL, **Scheme 1.6**).

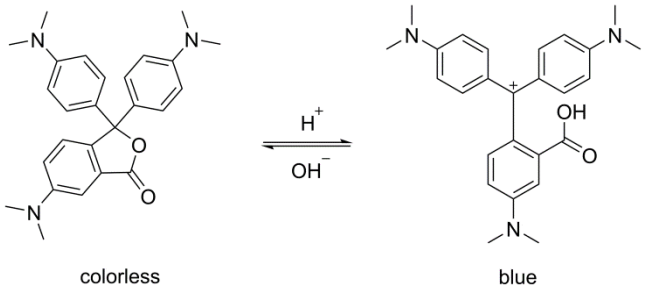

Scheme 1.6 Chemical structure of CVL with closed lactone ring (left) and with opened lactone ring (right).

Here, the ground state of the dye is colorless due to a π-π* interaction having λ_{max} at 280 nm.[208,232,234] In the presence of weak acids or electron acceptors, the lactone ring can be opened and the formation of a triphenylmethane system (chapter 1.7) is favored. At the same time, the length of the conjugated system increases and thus the energy of the π-π* transition decreases to λ_{max} = 620 nm. As a result, the dye appears intensely blue.[234-236]

Although the color forming process is well known, the mechanism is still under discussion.[234,235] Many efforts have been made to investigate the role of the developer, especially for solid state colored leuco-dye-developer systems. One example consists of CVL with bisphenol A (BPA) or lauryl gallate (LG) as developer. It was observed, that leuco-dye-developer complexes of the ratio CVL:BPA of 1:4[237] and CVL:LG of 1:3[234] are formed in the colored state.

Suitable solvents for thermochromic microcapsules are long chain alkyl alcohols, esters or acids having a minimum chain length of six carbon atoms. Since the solvent concentration typically is about 70–90 mass percent, the thermochromic transition temperature is largely controlled by the solvent melting temperature. Thus, the CST is easily adjustable by varying the chain length of the solvent.

The pigments can be incorporated into dyes for fabrics to produce clothing, which changes color with temperature.[238] Incorporated in inks, they can also be used for

printing on to clothing and food packaging. Thermochromic materials can also be found in safety applications in kettles and baby spoons. The pigments inside the products change color to warn if the liquid or food is too hot for drinking or feeding respectively. Baby spoons for example are designed to change color at 38 °C.

1.10. BARCODES

A barcode is an optically machine-readable label that encodes any kind of information. Originally, barcodes were linear and one-dimensional (1D), systematically represented by varying the width and spacing of parallel lines. Their emerging history began in 1974, where the first Universal Product Code (UPC)[239] (**Figure 1.18a**) from a retail product was scanned by a supermarket checkout system instead of manually keying in the price of the good being sold.[240] Today, barcodes appear on nearly all manufactured goods, letters and parcels.

By now, various two-dimensional (2D) or matrix codes exist, such as quick response (QR),[241] Data Matrix,[242] Maxi[243] or Aztec codes[244] (**Figure 1.18**). Herein, the information is encoded into rectangles, dots, hexagons or other geometric patterns in a 2D matrix. Many industrial sectors and large organizations have developed their own particular forms of barcodes. Aztec codes, for example, can be found on online tickets of different European railway companies such as Deutsche Bahn.[245]

Figure 1.18 Different 1- and 2D barcode types. UPC with encoded information: 001234567895 (a), QR code (b), Data Matrix code (c) and Aztec code (d). All 2D codes have the encoded information: http://www.bam.de.

This work mainly focuses on QR codes since they are now one of the most often used types of 2D codes. They can easily be read by most smartphone devices using their camera and suitable application software.

The advantage of 2D codes is that they are not restricted to numerical information; they can also encode alphanumerical, binary/byte information and kanji (**Table 1.3**).

Table 1.3 Possible data which can be stored within QR codes.

Mode	max. number of characters	possible characters
numeric	7,089	0, 1, 2, 3, 4, 5, 6, 7, 8, 9
alphanumeric	4,296	0–9, A–Z (upper-case only), space, $, %, *, +, –, ., /, :
binary/byte	2,953	8-bit single-byte coded graphic character sets (ISO/IEC 8859–1:1998)
kanji/kana	1,817	7-bit and 8-bit double byte coded KANJI sets (JIS X 0208)

The amount of data that can be stored varies with the mode and code version (size). For QR codes for example, the character storage capacity for alphanumerical information can amount to a maximum of 4,296 characters (**Table 1.4**).[241]

Another important advantage of 2D codes is their ability of error code correction (ECC), which enables the decodability of a code, even if it is damaged. In the case of QR codes four levels of ECC exist, namely L, M, Q and H, which means that 7, 15, 25 or 30% of the encoded data can be restored. The ECC is enabled by 8 bit code words and the use of a Reed-Solomon error correction algorithm,[246] which is a non-binary cyclic error-correcting code invented by Irving S. Reed and Gustave Solomon.[247] The downside of error correction is, that the higher the ECC level is, the less storage capacity is left for the information.

QR codes were invented in 1994 by Denso Wave Inc. for the automotive industry.[248] Today they are very popular in consumer advertising, since they can be decoded very fast and easily by smartphones and have a high data capacity. A user may receive a text, a vCard, a link to a webpage or to a video after QR code scanning. Besides that, a QR code can be dynamic. If a code links to an URL and the web address changes, it is possible to revise the underlying data without altering the image of the code. Another point for the overall success of QR codes is, that their use is free of any license and that they are clearly defined as an ISO standard.[241] Denso Wave Inc. still owns the patent rights[249] on QR codes, but has chosen not to exercise them.

The fast decodability of QR codes can be achieved through the position detection pattern. These are squares positioned in the upper right and left, and in the lower left corner of the code. **Figure 1.19** displays the arrangement of the characters within the QR code. The message starts at the right lower corner and follows the arrow.

Table 1.4 List of data capacity of different QR code versions.[241]

Version	modules	ECC Level	data bits	numeric	alphanumeric	binary	kanji
1	21 × 21	L M Q H	152 128 104 72	41 34 27 17	25 20 16 10	17 14 11 7	10 8 7 4
2	25 × 25	L M Q H	272 224 176 128	77 63 48 34	47 38 29 20	32 26 20 14	20 16 12 8
3	29 × 29	L M Q H	440 352 272 208	127 101 77 58	77 61 47 35	53 42 32 24	32 26 20 15
40	177 × 177	L M Q H	23,648 18,672 13,328 10,208	7,089 5,596 3,993 3,057	4,296 3,391 2,420 1,852	2,953 2,331 1,663 1,273	1,817 1,435 1,024 784

At the beginning, information about the encoding mode and the length of encoded information is positioned. The message itself is encoded as 8 bits per character, where the dark squares are 0 on even rows and 1 on odd rows, followed by an end-of-message marker. Finally, the ECCs are placed within the code matrix. Besides that, format information is provided by the red zones besides the position detection pattern.

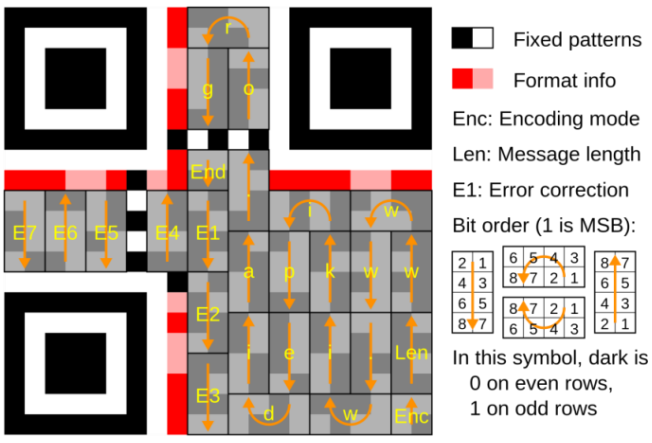

Figure 1.19 This diagram illustrates the placement of the message characters within a QR code. Reprinted from Ref.[250]

QR codes can be printed with all common procedures, such as inkjet, offset or laser printing.[248] Important for the reliable readability is to have a preferably high contrast, ideally the code is printed as black on white. Besides that, the QR Code symbol area

requires a margin or "quiet zone" around it to be used. The margin is a clear area around a symbol where nothing is printed and is usually four-modules wide.

1.11. MOTIVATION

Nowadays, almost every product category is affected by counterfeiting and piracy. It is no longer restricted to high quality products and brands, which causes immense financial damage for the industry.[251] The number of counterfeits, which were detained by customs at the European external borders, achieved nearly 40 million articles in almost 91,000 cases in 2012 (**Figure 1.20**).[252]

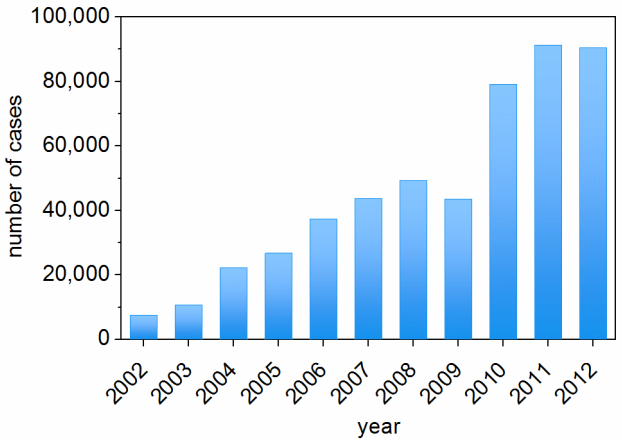

Figure 1.20 Number of cases of counterfeited goods at the European border. Adapted from Ref.[252]

The coverage of counterfeit products ranges from pharmaceuticals[253-255] to banknotes[256] and identity cards[257] and even product packaging.[258] The top categories of counterfeit goods include watches, bags, wallets, purses, sport shoes, sunglasses, clothing, perfumes and cosmetics.[252] To respond to that problem, a lot of strategies against counterfeiting have been developed during the last decades.[251,258-261] In order to reduce counterfeiting, the following protective responses were identified: communication, legal, government, direct contact, labeling, strong proactive marketing and piracy as promotion.[262]

However, in connection with this thesis, the focus is set on labeling. Generally, the aim of a security label is to enable the authentication of a product by government, supplier or even the consumer. Besides that, a security label may serve as deterrent for counterfeiters due to complex and difficult-to-copy characteristics, such as visible (overt) and hidden (covert) security features, forensic techniques and serialization/track and trace opportunities.[263]

The category of overt security features comprises holograms,[264,265] optically variable devices,[257] color shifting security inks and films[266,267] and security graphics. These features enable consumers to verify the origin of a product, but are often attractive for counterfeiters to mimic them.

Hidden security features are usually not noticed by users and aimed to identify a product as original or counterfeit for the brand owner. These characteristics should not be detectible without special knowledge. Examples for covert security features include invisible printing, such as UV active inks,[268] embedded images, digital watermarks,[269,270] hidden marks,[271] laser coding,[272,273] as well as micro-encapsulated odors and specific substrates.[256,274]

The third category, the forensic markers, requires laboratory testing or special test kits to be identified. They comprise chemical, biological and DNA taggants[275] as well as specific isotope ratios.[276] These markers are usually incorporated into the material of the good itself or the packaging.

Serialization and track and trace technologies enable the identification of each stock unit from their fabrication until their consumption. The identity of a product can comprise information such as the product number, expiry date, or details about the manufacturer. Additionally, a product can be tracked during the delivery process for data capture or traceability. Prominent examples are bar codes,[277,278] radio-frequency identification (RFID) tagging[279-281] and unique surface topographies.[282]

Protection against product piracy is becoming increasingly important. Generally it can be said that the more widely a security feature is used, the more attractive it is for counterfeiters to mimic it. This resulted in the idea to develop a new kind of security label. The more complex such a security label is, the more difficult it is to copy it. Thus, it is particularly recommendable to combine several of the above mentioned strategies against counterfeiting in one and the same system.

As part of this work, which was founded by the Federal Ministry of Education and Research (BMBF, project funding reference number 03V0043), the development of switchable information carriers based on shape memory polymers (SMPs) will be presented.

The concept of switchable information carriers is based on a SMP with decipherable information in the permanent shape. Such information can be codified, *e.g.* in a quick response (QR) code. As a result of thermo-mechanical programming (functionalization), the information carrier is converted into a stable, temporary shape with an indecipherable QR code. By heating the information carrier above the transition temperature T_{trans} of the selected SMP, the barcode becomes decipherable again as a result of recovering the original polymer shape (**Figure 1.21**).

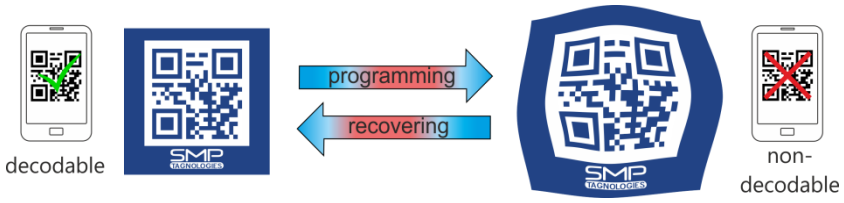

Figure 1.21 Working principle of switchable information carriers based on SMP.

Deployed as smart labels, switchable information carriers may serve as valuable technology for anti-counterfeit product verification and identification.

The proof of concept comprised the development of appropriate information carriers, including different fabrication and programming methods as well as their characterization by means of thermal, mechanical and spectrometric methods. Beyond that, the durability of QR code carriers against different aging scenarios like hydrolytic degradation and UVA irradiation will be shown. Further developments, such as the introduction of additional security features will be presented as well.

2. SWITCHABLE INFORMATION CARRIERS BASED ON SHAPE MEMORY POLYMER

The article: T. Pretsch, M. Ecker, M. Schildhauer and M. Maskos, *J. Mater. Chem.*, **2012**, *22* (16), 7757-7766 and the journal cover (**Figure 2.1**) are reproduced by permission of The Royal Society of Chemistry. The original article is available at: http://dx.doi.org/10.1039/C2JM16204K

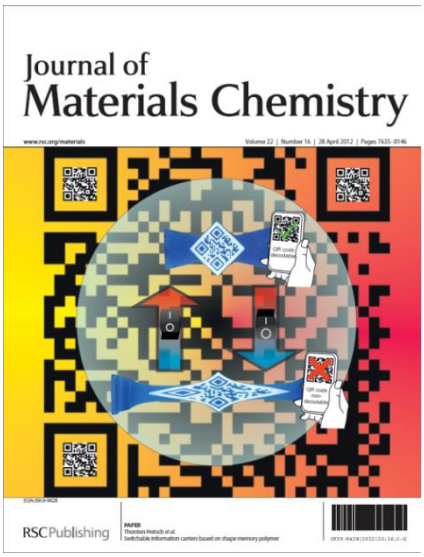

Figure 2.1 Cover of the *Journal of Materials Chemistry* issue 22, 2012.

2.1. EXPERIMENTAL CONTRIBUTION

My contribution for this manuscript comprises:

Conducting the experiments and data analysis including development of surface-specific dyeing process, tag preparation, visible absorption spectroscopy, thermal analysis and microscopic investigations, preparation of figures and the design of the journal cover image.

Contributions of co-authors:

T. Pretsch: Conception and writing of the manuscript.

M. Schildhauer: Development of tag design, programming of tags and preparation of figures.

M. Maskos: Conception of the manuscript.

2.2. PUBLICATION

2.2.1. Abstract

Herein we demonstrate the realization of a new technological concept, which enables the use of shape memory polymers (SMPs) as switchable information carriers. At first, we applied a surface-specific dyeing process based on "guest-diffusion" on two sophisticated polymeric host materials, including a thermoplastic poly(ester urethane) SMP and a thermoset epoxy-based SMP. Upon drying, selfassembly of the dye molecules inside the polymer surfaces occurred, resulting in homogeneous color penetration depths of about 100 µm. Subsequently, the colored surfaces were patterned with quick response (QR) codes. For this purpose, laser ablation was used. The resulting cavity depth was exceeding the color penetration depth. This assured sufficient surface contrast and rendered the QR codes machine-readable. In a progressive approach, two thermo-mechanical functionalization protocols were designed in accordance with the thermal properties of the polymers. As a result of programming, the tag prototypes were converted into stable, temporary shapes with non-decodable QR code information. When thermally triggering the shape memory effect on the functionalized tags, we verified the mostly complete recovery of the polymer surface and the associated restoration into the almost original shape. As such, the QR code could again precisely be read out. We anticipate that tagging products with these information carriers is helpful for the purpose of secure one-time identification.

2.2.2. Introduction

Shape memory polymers (SMPs) are stimuli-responsive materials. Their structural prerequisite is the coexistence of netpoints and switching segments.[1,2] In those chemically or physically cross-linked network structures,[3] the cross-links set the permanent shape and the switching segments serve as mobile phase, having a thermally "reversible" phase transition. In a polymer functionalization process, which is typically called "programming", the blocking of the restoring force after deforming the polymer in its elastic state is achieved by crystallizing or vitrifying the switching segment. Adjacently, the functionalized polymer is available for "on demand" movements. Depending on the nature of the switching segment, these can be initiated by melting or devitrification. The ensuing response of the polymer and thus the shape memory effect (SME) is known to be predominantly entropically driven.[1]

Meanwhile, plenty of innovative concepts have taken advantage of the notable polymer functionality, including textile applications,[4,5] self-deployable structures,[6] self-sufficient thermoprogrammable releasing systems,[7] polymer transformers,[8] display devices[9] and smart adhesives.[10-12] Beyond this, one remarkable discovery came from DiOrio *et al.*,[13] who elegantly functionalized SMP labels for continuous monitoring of a polymer's exposure conditions. However, plenty of applications still seem to lie in the biomedical field.[14-22]

Inspired by gecko footpads, researchers started controlling adhesion properties by micro-structuring SMP surfaces.[10,23,24] Further research efforts, which aimed at the surface modification of SMPs, were devoted to the realization of protrusive shapes through indentation and polishing,[25,26] the formation of protrusive bumps on pre-compressed SMP surfaces,[27] the modification of micro/nano-sized wrinkles in SMP surfaces[28] and the analysis of bending and stretching actuation through surface-initiated polymerization.[29] More in-depth coverage of the overall technological progress in this field has been provided by Huang *et al.*[30,31] Limitations have also been identified, *e.g.* by Schmidt *et al.*,[32] who elucidated the phenomenon of functional fatigue for an SMP by applying a multiple-cycling strategy. As a result, significant changes in surface geometry were found as exemplified by surface conversion from flat to wavy.

Our particular interest in this contribution lies in the proof of concept for using SMPs as information carriers. We investigated two SMP prototypes, which were strongly differing in chemical composition, nature of cross-links, phase morphologies, mechanical characteristics and thermal properties. Motivated by the aim to bring in quick response (QR) codes as specific information, the surfaces of a thermoplastic poly(ester urethane) (PEU)[33-35] and a thermoset epoxy-based polymer (EBP, Veriflex® E2) were identically treated by the CO_2-laser ablation technique. QR codes had been selected due to their relevance as presently ubiquitous technology for machine-readable data and, among others, including their decodability by means of widely used mobile devices such as smartphones. At first glance, our results did not meet the expectations, indicating that SMPs with engraved QR codes unveiled a lack of surface contrast, thus rendering the QR code difficult to decode. A way out of this dilemma turned out to be surface-specific dyeing *via* "guest diffusion". Considering the use of a triarylmethane dye as staining agent, we developed a concept which later proved to be universally applicable to both of the herein investigated polymeric materials. In a different sense, a process of "guest-diffusion" of a fluorescent, chromogenic oligo(p-phenylene vinylene) dye into a cross-

linked poly(cyclooctene) matrix with distinct shape memory properties has been effectively realized by Kunzelman *et al.*,[36] but for later monitoring the switching transition. By contrast, the present dye diffusion method was developed for the enhancement of surface contrast when combined with the CO_2-laser marking technique. Samples, which were subjected to local surface dyeing, QR code-patterning and laser cutting, will hereafter be uniformly termed "tags". In a combinatorial approach, two "programming procedures" (tag functionalization methods) were implemented. As a result of tensile or compressive deformation-determinated functionalization (TDDF/CDDF), the tags were transformed in almost all cases from an originally QR code decodable state into a temporary QR code non-decodable state. Later, the SME was exploited to recover the permanent shape to the greatest possible extent. It will be demonstrated that by virtue of the initially applied surface coloring, the contrast in the marked region was sufficient enough so that the QR code was accurately decodable again, even after triggering the SME on strongly distorted tags.

2.2.3. Experimental Section

2.2.3.1. Materials

The synthesis of a thermoplastic poly(ester urethane) was done by Bayer MaterialScience AG according EP 0571830. The hard segments were composed of 4,4′-methylene diphenyl diisocyanate (MDI) and a 1,4-butanediol (BDO) chain extender; the soft segments were based on poly(1,4-butylene adipate) (PBA) (**Scheme 2.1**).

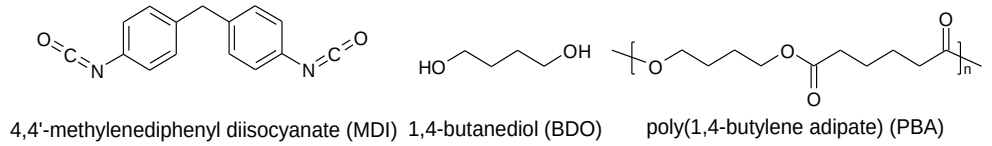

Scheme 2.1 Chemical structures of 4,4-methylenediphenyl diisocyanate, 1,4-butanediol and poly(1,4-butylene adipate).

The second polymer investigated was Veriflex® E2, a cured thermoset, epoxy-based SMP from Cornerstone Research Group, Inc. The as-received polymers were obtained as plaques; their geometry was length × breadth × thickness of 126 × 52 × 2 mm^3 (PEU) and 300 × 450 × 3.5 mm^3 (Veriflex® E2), respectively.

2.2.3.2. Thermal and mechanical analysis

Dynamic mechanical analysis (DMA) was conducted with a Netzsch DMA 242 under dynamic oscillatory mode at a frequency of 10 Hz. The relaxation spectrum was scanned under nitrogen from −150 to 100 °C (PEU) and 23 to 150 °C (EBP) at a linear ramp rate of 1 °C min^{-1}. The tensile storage modulus E', the loss modulus E'' and the phase angle tan $\delta = E''/E'$ were determined as a function of temperature. The investigated test specimens exhibited rectangular geometries with thicknesses of 2 mm (PEU) and 3.5 mm (EBP), respectively.

The thermograms obtained from differential scanning calorimetry (DSC) were recorded with a DSC 204 F1 Phoenix® from Erich Netzsch GmbH & Co. Holding KG. A specimen, weighing approximately 10 mg, was sealed in a DSC aluminum pan, before it was placed inside the calorimeter. When investigating PEU, the sample was cooled down to −80 °C and heated to 90 °C. After 5 min at 90 °C, the sample was recooled to −80 °C, before it was heated for a second time to 90 °C. In case of EBP, the sample was cooled down to −20 °C and then heated to 150 °C. After 5 min at 150 °C, the sample was recooled to −20 °C, before it was heated for a second time to 150 °C. Both for PEU and EBP, consistent heating and cooling rates of 10 °C min^{-1} were selected.

The DMA-related glass transition temperature of PEU and EBP was assigned according to the peak in the tan δ curve. For PEU, a second tan δ peak occurred and was taken as hint for strong morphological changes associated with the melting transition of PBA. The inflectional tangent method was used as part of the standard procedures of the software Proteus Thermal Analysis from Netzsch to determine the DSC-related glass transition temperature T_g. In case of PEU, further information obtained from DSC measurements included the melt peak crystallization temperature T_c (first cooling scan) and the melting peak temperature T_m of PBA (second heating scan).

2.2.3.3. Surface dyeing and characterization

Different concentrations of dye solutions were prepared. To obtain a concentration of 3.2×10^{-2} mol l^{-1}, 1 g of N-[4-[[4- (dimethylamino)phenyl] [4-(phenylamino)-1-naphthyl]methylene]-2,5-cyclohexadien-1-ylidene]-N-methyl-methanaminium chloride (*Victoria Blue B*, C.I. 44045; CAS 2580–56–5, Sigma- Aldrich) was completely dissolved in 30 ml of acetone (98%, AppliChem) and 30 ml of ethanol (96%, Merck). For a lower dye concentration of 7.8×10^{-3} mol l^{-1}, 250 mg of *Victoria Blue B* were dissolved in the same volume of solvent mixture.

The chemical structure of the triarylmethane dye *Victoria Blue B* shows a conjugated system of three linked aromatic units, acting as chromophore (**Scheme 2.2**).

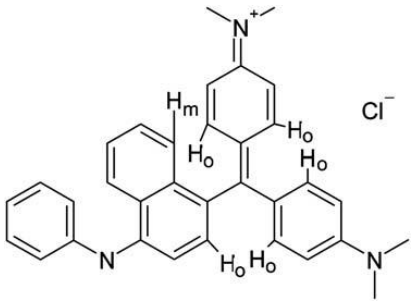

Scheme 2.2 The molecular structure of *Victoria Blue B* with drawn in *ortho*-hydrogen atoms H_o and *meta*-hydrogen atom H_m.

The polymer surface was briefly treated with acetone, before the dye solution was pipetted and uniformly distributed onto the dye-absorbing polymer surface. Adjacently, the surface was cleaned with water and dried with lint-free cloth, which resulted in consistent blue surface coloring.

In order to microscopically explore the influences of guest diffusion and CO_2-laser ablation, the polymer surfaces were treated with a cryomicrotome CM1950 from Leica. The slices were prepared at −20 °C (PEU) and 23 °C (EBP); the direction of the cuts was perpendicular to the colored, engraved polymer surface. The obtained polymer slices had a thickness of 20 µm. Samples of PEU were studied with a Leica DM EP microscope at a 10 times optical zoom; for EBP a WILD M5A stereomicroscope with 25 times optical zoom was utilized. The diffusion depth of the guest molecules into the polymer matrices was determined together with the depth of ablation by means of the Dieterman & Heuser Solution GmbH (dhs) software (version 13).

2.2.3.4. Visible spectroscopy

The visible absorption spectra of homogeneous solutions containing acetone/ethanol (50:50) and *Victoria Blue B* were recorded with a Varian's spectrophotometer Cary 300 Scan, which was equipped with a Czerny-Turner pre-monochromator, a high performance R928 photomultiplier tube and a tungsten halogen visible source containing a quartz window. The employed quartz cuvette had a thickness of 10 mm. The visible absorption spectra of surface-colored polymer samples were recorded with the same optical spectrophotometer, at which the uncolored backside of the samples pointed towards the light source and the colored surface towards the detector. Labsphere DRA–CA–30I was used as the integrating sphere to collect the lost light and to direct it onto

the detector. All visible absorption spectra were recorded at 23 °C with a scan rate of 60 nm min^{-1} in the range between 800 and 400 nm.

2.2.3.5. QR code dimensioning and scanning

The dimensions of the tags, including the size of the QR code area and its position within the polymer surface, were defined by manual input in Corel Draw X5 (version 15.2.0.661). For TDDF (described in Section 2.2.3.7), a specific tag dimensioning was developed (**Figure 2.2**), assuring the strong non-affine distortion of the QR code in course of tensile deformation.

The change Δa of the clamping distance $a_0 = 30$ mm was used to determine the tag elongation after tensile deformation. The QR code diagonals served as measure for the QR code distortion compared with the initial state ($b_0 = c_0 = 25.3$ mm). For CDDF (described in Section 2.2.3.7), squarish tags (**Figure 2.2**b) were selected. Their consistently chosen dimensions were corresponding exactly to the QR code field. Likewise, deformation-related changes in the area A and thus in the boundary edges of the QR code were defined through deviations from $A_0 = ½ b_0^2 = 320.1$ mm². The QR code area of deformed tags was determined by using the computer aided design (CAD) tool Solid Edge ST3 (version 103 from Siemens PLM Software) through manually fitting polygons to the QR code boundary edges in real-size scaled photographs. Solid Edge enabled the computation of the polygon areas.

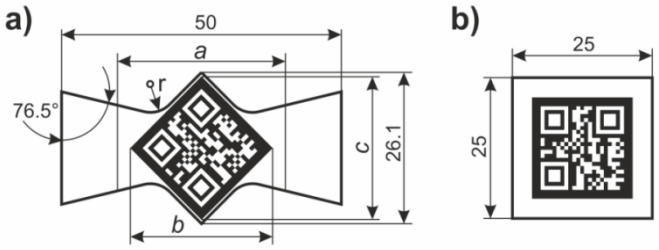

Figure 2.2 Sketches of smart tags as developed for TDDF (a) and CDDF (b). When passed to the laser engraver and cutting machine for tag preparation, the boundary edges were cut and the black areas were engraved into the surface-colored polymer. The sketches contain inversed QR codes, which were generated by means of a free application accessible through the website http://goQR.me, using the error correction level "M". The latter enabled the reading software to restore about 15% of the contained QR code information in case of wrongly detected pixels. The QR codes are identical in (a) and (b) and carry the information "BAM QRM-Label". PEU and EBP tags exhibited a thickness t_0 of 2.0 and 3.5 mm, respectively. All dimensions given within the sketches are in millimeters (radius $r = 5$ mm).

A Samsung Galaxy S I9000 smartphone (5.0 megapixel camera, 2560 × 1920 pixel) with integrated autofocus function, Android 2.3.3 operating system and barcode scanner version 3.6 (Zxing Team[37]) was exemplarily selected as QR code scanning and decoding

device. The evaluation of the decodability of the QR code information was conducted on raw tags (prior to their functionalization) and on functionalized (temporarily fixed) and recovered tags. The standard reading software was applied to deskew the QR code mapping in order to prepare it for its decoding algorithms. Therefore, the software shows some tolerance, not only towards optical distortion effects, but also towards real code distortion. To gain validity, the readability of each tag was tested at various camera angles of around 90° and distances of about 10 cm. All tests were run under varying daylight entrance angles.

2.2.3.6. Tag preparation

For engraving the exemplarily selected QR code information "BAM QRM-Label" into surface-colored SMP and cutting plaques into "tag-size", an Epilog Zing 16 laser engraver and cutting machine, equipped with a continuous wave 30 W CO_2-laser (spot size: 0.0762–0.127 mm; wavelength: 10.6 µm), was used. The laser engraver was operated in raster mode with a resolution of 1000 dpi and vector mode at a frequency of 500 Hz, both for engraving and cutting, respectively. An air compressor unit, operating with a pressure of 2.1 bar, was employed to direct a constant stream of compressed air over the work surface. In the end, the dimensions of the tags were verified with a digital caliper gauge from American General Tools (AGT).

2.2.3.7. Tag functionalization and recovering

The functionalization and recovering of the tags was conducted with an electromechanical testing system (MTS Insight 10), which was equipped with a thermochamber (Thermcraft). The thermochamber operated with a temperature controller (Eurotherm). The heating was achieved through two electrical heating elements in the back of the thermochamber. The cooling was done by injecting liquid nitrogen from a tank into the thermochamber. The liquid nitrogen flow was controlled *via* a solenoid valve at its nitrogen entrance. An electric motor-driven fan behind a baffle provided diffused convection of the thermochamber atmosphere in order to obtain a uniform temperature distribution. The tags were shielded by the baffle from direct radiant heat and liquid nitrogen injection. The choice of load cell was done in accordance with the required tensile forces (100 N load cell) and compressive forces (10 kN load cell). Prior to tag programming *via* tensile deformation-determinated functionalization (TDDF) or compressive deformation-determinated functionalization (CDDF), a first check of QR code decodability was done.

For TDDF, the tags were clamped into the tensile testing machine with a clamping force of 620 N at a clamping distance of a_0 = 30 mm. When using PEU as the basic material, the tag was heated to T_{high} = 60 °C and stretched with a deformation rate of 30 mm min^{-1} to a maximum elongation $\Delta a/a_0$ of 50%, 100%, 150% and 200%, respectively. After 5 min, the imposed shape was stabilized by keeping the clamping distance constant and cooling the tag to T_{low} = −15 °C, which constituted the shape fixity temperature. After keeping the tag 5 min at that temperature, it was unloaded at a rate of 10 N min^{-1} and the freshly functionalized, temporarily fixed tag with a strongly distorted QR code was then heated to 23 °C in order to reassess the decodability of the QR code. This step marked the end of the TDDF process. Adjacently, reheating of the tag to 60 °C was carried out to trigger the SME. The tag was allowed to respond with spontaneous length contraction (shape recovery into the almost permanent shape) and the associated surface reconversion. To ensure an almost complete recovery of the tag, it was kept for 15 min at 60 °C before it was cooled to 23 °C. Finally, a last QR code reading took place. For those tags composed of EBP, the programming process mostly differed in the selection of T_{high} (80 °C) and the maintenance of the residual force as detected 5 min after tensile deformation until the tag was unloaded at the shape fixity temperature T_{low} (23 °C).

For CDDF, the squarish tags were directly placed inside the center of two plane steel plates, which were used as compressive unit. The steel plates with the dimensioning of 80 × 80 mm^2 were in turn connected to compression rods. The contact area between the polymer surfaces and the pressure unit was defined by the size of the tag, inter alia, covering the entire surface with the engraved QR code. In order to ensure the direct contact between the steel plates and the polymer surface, a permanent load of −10 N was applied at the beginning of the functionalization process. At the maximum temperature (60 °C in case of PEU and 80 °C for EBP), the tags were loaded at a crosshead displacement speed of 0.5 mm min^{-1} to a maximum compressive force F_{max}. After 5 min, the residual force was kept constant during cooling the tags to −15 °C (in case of PEU) or 23 °C (in case of EBP). The unloading at a rate of 500 N min^{-1} constituted the end of the CDDF process. Adjacently, one further assessment of QR code decodability was carried out at 23 °C. Finally, the tags were recovered as far as possible by their reheating to the maximum temperature. After keeping them 15 min at that temperature the tags were cooled to 23 °C for a final scan of the QR code.

2.2.4. Results and Discussion

Dynamic mechanical analysis (DMA) was used to characterize the mechanical and thermal properties of PEU and EBP. DMA was methodically complemented by differential scanning calorimetry (DSC), which was used to monitor the phase transitions as a function of temperature. **Figure 2.3** provides an overview of the obtained measurement results.

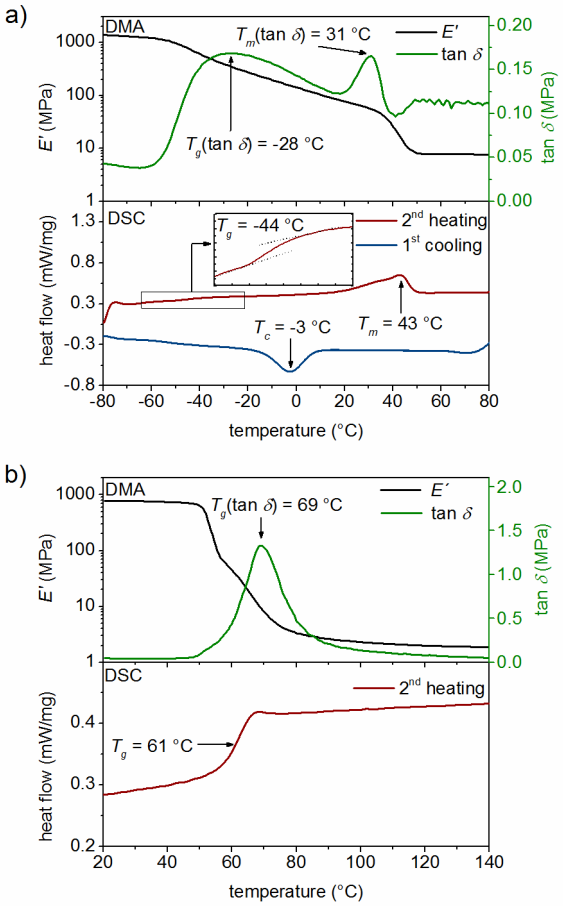

Figure 2.3 Thermal and mechanical properties of neat PEU (a) and EBP (b) as determined by DMA and DSC. For both polymers, the temperature-dependence of E' (black curve) and tan δ (green curve) is plotted above. The DSC thermograms are given below; they include the 1st cooling scan (blue curve) and 2nd heating scan (red curve with enlarged glass transition region provided by the inset) for PEU and the 2nd heating scan for EBP.

For neat PEU, the DMA and DSC heating traces showed the presence of two successive soft segmental phase transitions, corresponding to the T_g and T_m of PBA (DMA: 28 and 31 °C; DSC: 44 and 43 °C).[33,38,39] Concomitantly, the DSC signal located at −3 °C was attributed to T_c of PBA. In similar PEUs, the crystallization of the soft segment was found to depend on a variety of parameters, such as the hard to soft segment ratio, the length of the soft segment and the total molecular mass of the polymer.[40] The DMA plots

of PEU were consistent with those obtained by Chen *et al.*,[41,42] whose PEUs were composed of the same hard segments (MDI–BDO), but slightly longer soft segments (poly(hexylene adipate) 4000).

The DMA curve for neat EBP exhibited a pronounced tan δ peak associated with a broad glass transition around 69 °C as confirmed by the DSC measurement (T_g = 61 °C). The glass transition temperature of EBPs is known to depend, *inter alia*, on curing conditions and the type of curing agent.[43-45] Both of the investigated polymers unveiled a characteristic drop in E' above room temperature, when passing T_m of PBA (PEU) and T_g (EBP). With about three orders of magnitude, the drop in E' was more accentuated for EBP, which is characteristic for such polymers,[46] indicating pronounced shape memory properties.

Due to the different analysis methods (DMA and DSC) and the associated sample geometries and testing conditions, the obtained phase transition data were not identical. Indeed, we noticed that the DMA-related T_g values (tan δ peaks) were consistently higher for PEU and EBP than those determined by the DSC. The finding is in good accordance with those for similar PEUs,[47] epoxy-based copolymer thermoset systems[46] and for EBP composites with non-woven fibers of poly-(ε-caprolactone).[48]

In order to address the challenge of lacking surface contrast, we applied "guest diffusion" to the polymers. **Figure 2.4** exhibits the visible absorption spectra for the pure dye solution and solid samples of non-dyed and dyed PEU and EBP.

We found that the cationic dye *Victoria Blue B* displayed an absorption band in dilute acetone/ethanol solution with a λ_{max} of 612 nm (8×10^{-5} mol l^{-1}). At the same time, no comparable absorbances were observed in the visible absorption spectra for neat PEU and EBP. We assume that the absorption band of *Victoria Blue B* is related to the formation of an excited state as usually found in triarylmethane dyes, which structurally resemble a three-bladed propeller.[49] In the ground state, the planes of the aromatic rings of *Victoria Blue B*, including two phenyl rings and one naphthyl ring, are twisted out of the plane, defined by the central carbon atom and its three bonds. In the excited state, two aromatic rings are assumed to share the same plane against steric repulsion among two *ortho*-hydrogen atoms (for the combinations phenyl/phenyl and naphthyl/phenyl) or among the neighboring *ortho*- and *meta*-hydrogen atom (phenyl/naphthyl) (**Scheme 2.2**).

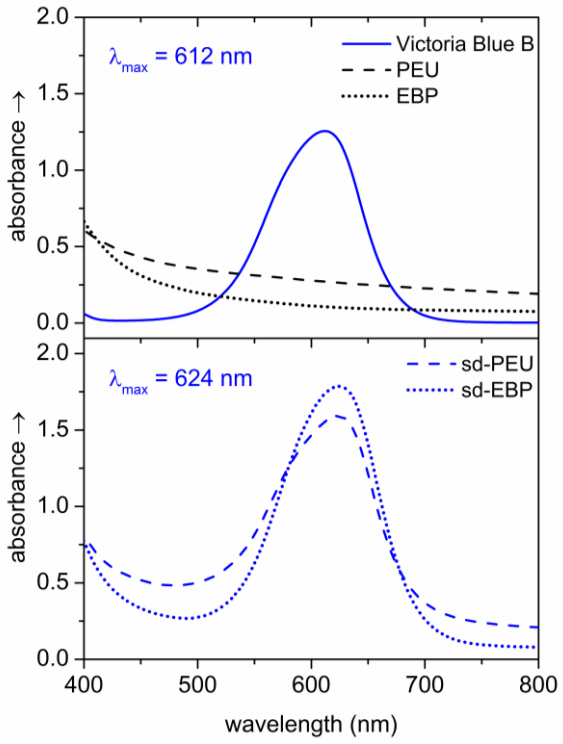

Figure 2.4 Visible absorption spectra for acetone/ethanol (50:50) solution with a *Victoria Blue B* concentration of 8×10^{-5} mol l^{-1} (pH value = 5.7, blue curve) and for neat samples of PEU (dashed line) and EBP (dotted line) (above). Visible absorption spectra for surface-dyed (sd) polymer samples of PEU with *Victoria Blue B* (dashed blue line, sd-PEU) and of EBP with *Victoria Blue B* (dotted blue line, sd-EBP) (below). In the surface-loaded polymer samples, the sorption percentages of *Victoria Blue B* were 0.08 wt% (with PEU) and 0.11 wt% (with EBP), respectively. All spectra were recorded at 23 °C.

Due to "guest diffusion", a strong absorption band could be detected in the visible absorption spectra of PEU/*Victoria Blue B* and EBP/*Victoria Blue B* (shown in ESI† **Figure 2.8**). The lowering of the dye concentration in solution from 3.2×10^{-2} to 7.8×10^{-3} mol l^{-1} and the associated limitation of dye uptake enabled the exact determination of λ_{max} for our surface-dyed polymer samples, which exhibited a uniform bathochromic shift (λ_{max} = 624 nm) towards the pure dye solution (**Figure 2.4** and ESI† **Figure 2.8**). It is worthwhile noting that in contrast to solvent-dye interactions, the dye molecules get immobilized inside a solid matrix. Various attractive forces can play a role in the retention of a dye within a polymer surface, depending on the underlying chemical or physical interactions. We assume that the dye molecules were incorporated into the host polymers as supported by hydrogen-bonding, van der Waals forces and salt formation.[50] Possible molecular interactions include the aggregation of the π-conjugated dye molecules and their interplay with the surrounding polymer chains (*e.g.* polar groups), residual solvent and dye counterions.

Upon evaporation of the solvents, self-assembly of the dye molecules inside the polymer surfaces occurred. Approximately 30 min after surface-specific dyeing with *Victoria Blue B*, PEU and EBP were CO_2-laser treated. **Figure 2.5** provides representative microscopic images of the PEU surface (**Figure 2.5**a and b) and includes the images of two cryomicrotome sections (PEU, **Figure 2.5**c and EBP, **Figure 2.5**d).

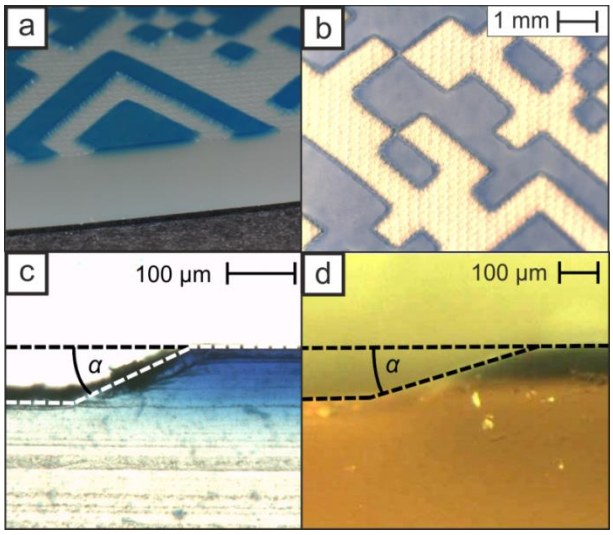

Figure 2.5 Microscopic profiles of the CO_2-laser ablation zones of intensely surface-colored and CO_2-laser engraved PEU (a–c) and EBP (d), provided in different optical resolutions. The images of the PEU tag are given in diagonal view (a) and top view (b). Cryomicrotome section profiles of the transition zones between CO_2-laser ablated regions (left part) and intensely surface-colored regions (right part) of PEU (c) and EBP (d). The removal of polymeric material (including dye) by means of CO_2-laser ablation is indicated by the dashed lines in (c) and (d), which enabled the determination of the inclination angle *α*.

The images reveal that complete removal of the dye component occurred in the CO_2-laser-ablated regions, leading to strong surface contrast. A color penetration depth of about 100 µm could be detected for both polymers (**Figure 2.5**c and d), demonstrating the high affinity shown by the guest molecules for the polymeric host materials. The optical changes towards deeper polymeric layers could be readily discerned visually. The microscopic investigation of the cross-section of the laser ablation zones within the QR code region unveiled that the CO_2-laser ablation depths were around 110 µm (PEU, **Figure 2.5**c) or rather 140 µm (EBP, **Figure 2.5**d). The contours in the sidewalls of the cavities exhibited an inclination angle of 26° (PEU) and 19° (EBP). In the ablated regions, heat-induced scission of polymer chains and the volatilization of small molecular fragments (including the ablation of dye molecules) were expected to happen.[51] The microstructures within the polymer surfaces unveiled an engraving depth, which was exceeding the penetration depth of the dye, assuring a sufficiently high surface contrast for easy decoding of QR codes from tag surfaces by means of the scanning and decoding

device. As expected from the relatively low sorption percentages of *Victoria Blue B* with the polymer matrices (< 0.2 wt%), surface-dyeing exerted a not remarkable influence on the morphology of the polymer chains as evidenced by the almost unaffected phase transition temperatures in the second DSC heating scans (shown in ESI† **Figure 2.9**). However, what might have been affected are the micro-morphological properties such as local diffusivity and polymer chain orientation.[36] Interestingly, the dye sorption capacities of the polymers were quite similar, despite fundamental discrepancies in chemical composition, nature of cross-links, phase morphologies, *etc.* We like to point out that our dye sorption experiments started strongly above T_g of neat PEU and well below T_g of neat EBP. Not surprisingly, we observed that semi-crystalline PEU was able to retain its mechanical integrity in course of surface-dyeing,[52] representing a certain technological advantage over the glassy amorphous EBP, whose surface became tacky and therefore had to be treated cautiously. For the latter we assumed a sporadic lowering of T_g due to the uptake of solvents, which enabled EBP to serve as host material. However, due to restriction in network chain mobility at the end of the solvent evaporation process, we could imagine that glassy amorphous polymers are able to better kinetically trap dye molecules in the long term.

In principal, various deformation techniques can be considered as essential part of the programming process for an SMP, including stretching, compression, denting, bending and twisting.[34,53-57] For convenience, our application oriented approach focused on TDDF and CDDF. In line with the inherently different thermal properties of the polymers, the concept involved the use of two distinct shape fixing and actuation mechanisms. Upon deformation at an elevated temperature T_d well above the switching temperature T_{switch}, the polymer chains received a higher degree of orientation compared to the initial state. The stabilization of the imposed shape and the associated immobilization of constituent polymer chains were achieved by cooling the polymer to the shape fixity temperature T_{fix}, which resulted for PEU in the crystallization of the switching segment ($T_{fix} < T_c$ of PBA). In case of EBP, the vitrification of the switching segment took place ($T_{fix} < T_g$). When triggering the SME on functionalized, semi-crystalline PEU, the recovery into the almost undeformed, as processed shape at an opposite direction to the deformation direction was due to soft segment melting ($T_{switch} = T_m$ of PBA). By contrast, for EBP the conversion of vitrified into devitrified constituent polymer chains occurred in course of switching ($T_{switch} = T_g$). In parallel, each polymer passed from higher to much lower tensile storage modulus as evidenced by the abovementioned DMA results. The reason

behind is a significant regain in polymer chain configurational entropy with rising temperature as consistent with Flory's theory.[58]

At the macroscopic level, our two polymeric tag candidates were stabilized in a temporarily fixed state at varying degrees of elongation (**Figure 2.6**) and compression (**Figure 2.7**), respectively.

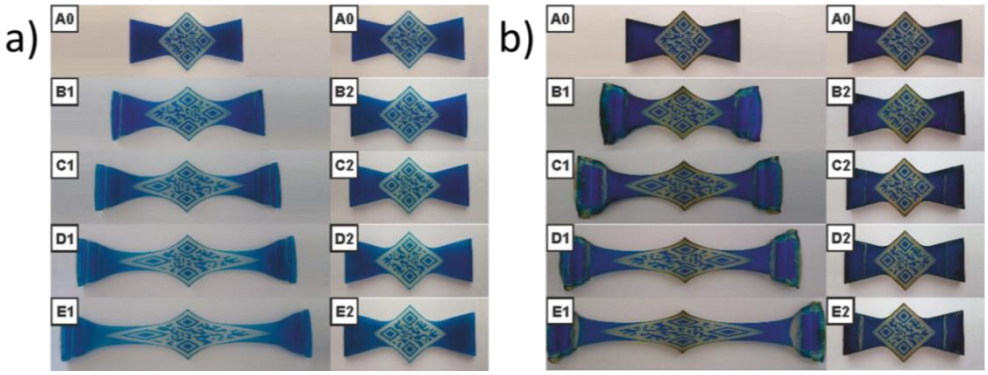

Figure 2.6 Tags having PEU (a) and EBP (b) as basic material, containing the information "BAM QRM-Label". The undeformed tags (A_0) were subjected to stretching to $\Delta a/a_0$ of 50% (B), 100% (C), 150% (D) and 200%. All functionalized (thermo-mechanically programmed) PEU tags (1) were non-decodable with the scanning and decoding device; same as the functionalized EBP tags (C1, D1 and E1). The recovered states (2) enabled the precise decoding of the QR codes. The lower material stiffness of EBP at the deformation temperature caused a higher deformation in the clamping region (compared to PEU).

Table 2.1 and **Table 2.2** give an overview on the commensurate deformation parameters and the mostly surface-(because QR-code) related shape memory characteristics of the tags.

The imposed shapes were tightly controlled by the applied deformation forces. In this regard, the relative change in length of the QR code diagonals can be expressed for the longitudinal direction ($\Delta b/b_0$) and for the transverse direction ($\Delta c/c_0$), as defined in **Figure 2.2**. The relative change of the QR code area $\Delta A/A_0$ was taken as further criterion to quantify QR code distortions within the polymer surfaces.

Almost all of the applied functionalization approaches had in common that they produced non-affine QR code distortions, which were appropriate to avoid the decoding of the stored tag information in the deformed temporarily fixed state. The only exception was the EBP tag with the lowest tensile elongation ($\Delta a/a_0 = 50\%$). In this case, the associated QR code distortion level ($\Delta b/b_0 = 46\%$; $\Delta c/c_0 = -10\%$) seemed to be close to the verge of compensability by the deskewing and decoding algorithms of the scanning and decoding device. Stronger QR code distortions ($\Delta b/b_0 = 54\%$; $\Delta c/c_0 = -11\%$) as detected for

the PEU tag with the same elongation level were accompanied by a drastic increase in QR code area from $\Delta A/A_0 = 23\%$ (EBP) to 30% (PEU). As a result, the decodability of the QR code was rendered impossible. However, major discrepancies in local deformation behavior can be explained with the individual tag thickness and the different thermo-viscoelastic properties of PEU and EBP, respectively. In general, programmed EBP tags showed lower QR code distortions than PEU tags for the same tensile elongation, as evidenced by the deformation-dependent $\Delta A/A_0$ ratio. Conversely, CDDF gave much lower levels of distortion for functionalized EBP tags compared with PEU tags.

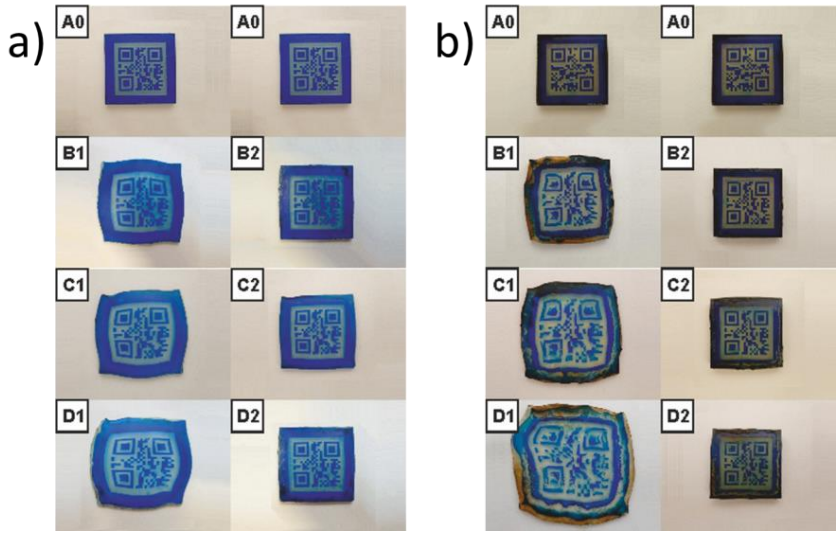

Figure 2.7 Tags having PEU (a) and EBP (b) as basic material, containing the information BAM QRM-Label'. The undeformed PEU tags (A_0) were subjected to a maximum compressive force $|F_{max}|$ of 3000 N (B), 4750 N (C) and 7000 N (D) and the undeformed EBP tags (A_0) to a maximum compressive force $|F_{max}|$ of 1000 N (B), 1800 N (C) and 4000 N (D). All functional zed (thermo-mechanically programmed) tags (B1, C1 and D1) were non-decodable with the scanning and decoding device. The recovered states (2) enabled the precise decoding of the QR codes. The brownish edges of the EBP tags (B1, C1, D1) derived from CO_2-laser cutting.

Once the SME was triggered, the recovered states of the tags enabled the unexceptional decoding of the QR code (**Figure 2.6** and **Figure 2.7**). Astonishingly, even relatively high residual QR code distortions ($\Delta b/b_0 = 27\%$, $\Delta c/c_0 = -7\%$) as evidenced for PEU turned out to be no hindrance. As pointed out above, the QR code distortion level ($\Delta b/b_0 = 46\%$; $\Delta c/c_0 = -10\%$) constituted a critical barrier for enabling QR code readability. Accordingly, QR codes which were previously functionalized *via* severe TDDF (*e.g.* $\Delta a/a_0 \geq 100\%$) were rendered machine-readable again, as soon as the ratios $\Delta b/b_0$ and $\Delta c/c_0$ fell below the threshold value given above (independent of the selected type of polymer). Thus, the two explored tag prototypes fulfilled two major requirements, consisting of an adequate QR code recoverability at any distortion level investigated and

a sufficiently high surface contrast as prerequisite for successful scanning and decoding. From quantitative point of view, the residual QR code distortions were consistently lower in EBP tags, regardless of which functionalization technique was applied (**Table 2.1** and **Table 2.2**).

It is worth mentioning that functionalizing EBP tags *via* CDDF gave some slight surface layer damage on the QR code patterned site of the tag, which seemed to become more dominant with growing compressive force; in contrast no obvious sign for similar effects could be detected for the PEU tags (**Figure 2.7**). We attributed the EBP-related effect to the adhesion between the polymer itself and the steel plate used as programming tool. The observation suggests that our "pretreated" EBPs behaved similarly as other pristine EBPs, which display reversible dry adhesion on polymeric surfaces,[11] thus unveiling a certain level of substrate tolerance (in our case towards stainless steel). In this context further investigations will be necessary. Most importantly, the effect did not impart the decodability of the QR code after triggering the SME.

In order to find out in how far thermo-mechanical treatment influenced the color penetration depth in our tags, we microscopically investigated recovered PEU tags, which were programmed before *via* TDDF under severe conditions ($\Delta a/a_0 = 200\%$). The results have shown that obviously no diffusion of the dye inside deeper layers of the polymer matrix occurred, ensuring the maintenance of the contrast between the engraved and colored domains. In a progressive approach, we investigated the impact of programming on the optical properties of the tags. We found that even heat treatment as part of severe TDDF ($\Delta a/a_0 = 200\%$) resulted in only modest changes of the visible absorption characteristics both for PEU and EBP tags (not shown herein).

With the overall concept of switchable information carriers in mind, we see in particular advantageous effects in tunable deformation conditions. For instance, the maximum elongation applied to PEUs can be varied in a broad range of up to several 100%,[33,34] which predestines them as useful information carries as long as shape recoverability remains sufficiently high. Keeping functionalized tags at temperatures below T_{switch} allows for their secure handling without any change of shape, so that they can be used *e.g.* during shipment of products, whose identity should later be verified. Upon heating above T_{switch}, the recovery of the decodable surface profile sets in, thus making the QR codes precisely readable "on demand". Another point is that the employment of adequate fillers inside SMP matrices leaves much room for effectively tuning shape memory

properties[59-61] and indirect triggering of the thermally induced SME, e.g. upon application of an electrical current[62,63] or a magnetic field.[64-66]

Table 2.1 Tensile deformation parameters for different tag elongations (A to E) and QR code related shape memory characteristics of PEU and EBP tags as indicated in **Figure 2.6**. The decodability of the QR code was explored for the temporarily fixed state "1" and recovered state "2". The relevant dimensions a, b, c and the QR code area A are defined in **Figure 2.2**

	Tensile deformation		Temporarily fixed state (1)				Recovered state (2)			
	Max. force	Tag elongation	QR code distortion			QR code readability	QR code distortion			QR code readability
	F_{max} [N]	$\Delta a/a_0$ [%]	$\Delta b/b_0$ [%]	$\Delta c/c_0$ [%]	$\Delta A/A_0$ [%]		$\Delta b/b_0$ [%]	$\Delta c/c_0$ [%]	$\Delta A/A_0$ [%]	
PEU tags										
A	0	0	0	0	0	yes	0.0	0.0	0.0	yes
B	48	50	54	−11	30	no	6.0	−2.8	3.1	yes
C	59	100	99	−14	39	no	13.0	−5.9	3.3	yes
D	65	150	143	−18	61	no	20.8	−6.8	11.8	yes
E	71	200	182	−21	78	no	27.2	−7.1	15.1	yes
EBP tags										
A	0	0	0	0	0	yes	0.0	0.0	0.0	yes
B	19	50	46	−10	23	yes	1.3	−3.1	4.2	yes
C	22	100	93	−20	46	no	2.8	−4.0	2.2	yes
D	24	150	141	−26	56	no	4.7	−4.2	5.7	yes
E	33	200	182	−31	67	no	6.8	−5.5	6.5	yes

Table 2.2 Compressive deformation parameters for different tag compressions (A to D) and QR code related shape memory characteristics of PEU and EBP tags as indicated in **Figure 2.7**. The decodability of the QR code was explored for the temporarily fixed state "1" and recovered state "2". The relevant dimensions *a*, *b*, *c* and the QR code area *A* are defined in **Figure 2.2**.

	Compressive deformation		Temporarily fixed state (1)		Recovered state (2)	
	Maximum compr. Force	Tag compression	QR code distortion	QR code readability	QR code distortion	QR code readability
	$\lvert F_{max} \rvert$ [N]	$\Delta t/t_0$ [%]	$\Delta A/A_0$ [%]		$\Delta A/A_0$ [%]	
PEU tags						
A	0	0	0	yes	0	yes
B	3000	−27	33	no	9.5	yes
C	4750	−41	48	no	10.4	yes
D	7000	−50	66	no	15.1	yes
EBP tags						
A	0	0	0	yes	0	yes
B	1000	−25	44	no	0.7	yes
C	1800	−32	93	no	4.9	yes
D	4000	−48	133	no	6.8	yes

2.2.5. Conclusion

On the basis of our experimental results, we can summarize that shape memory polymers could serve as a new technology platform for a safe way of information storage and release. Gratifyingly, the introduced concept of "guest diffusion" was easily applicable to surface layers of two structurally totally different SMPs. Preliminary investigations unveiled that the concept is transferable to a series of other SMP matrices, in particular to some chemically cross-linked network structures. Due to the fact that a lack in contrast necessitated surface dyeing, the integration of small amounts of dye molecules into SMP surfaces can be considered as the key to the applicability of SMPs as switchable QR code carriers. Advanced tag geometries and programming strategies, *inter alia*, both offer conceptual extensibility and tremendous potential, but also a possible response to the development of strongly improved reading software for QR codes. For a start, two different routes of shape programming turned out to be easily applicable to render QR codes temporarily non-decodable. The applied programming techniques can be considered as a functional security feature, which is rather difficult to copy without a specialist's knowledge. Once thermally switched, the programmed tag recovers large parts of its permanent shape, thus facilitating the error-free decoding of the QR code by means of a scanning and decoding device. Therefore, we consider the idea of switchable machine-readability of QR codes as a highly promising one and assume appreciable technological potential. The attractiveness of the overall information carrier concept relies on the fact that it is not restricted to QR codes; it can easily be expanded to Data Matrix codes, other codes, alphanumeric characters, logos, schematic diagrams, etc. However, what remains is a formidable challenge to establish the presented technical concept alongside well established technologies in this field.

2.2.6. Acknowledgements

The authors gratefully acknowledge financial support from the German Federal Ministry of Education and Research (BMBF, project funding reference number 16V0043), and fruitful discussions with Professor Gerhard Wegner (Max Planck Institute for Polymer Research) and their colleagues Dr Werner Müller, Dr Volker Wachtendorf, Dr Ulrike Braun, Dr Wolfgang Stark and Dr Martin Böhning. Mrs Edelgard Lorenz is acknowledged for conducting microtome sections, Mrs Petra Fengler for running the DMA measurements, Mrs Tina Garchow for carrying out the DSC measurements and

Mr Jan Hüttig for programming and recovering “smart tags”. The authors thank Bayer MaterialScience AG for kindly providing the PEUs.

2.2.7. References

1 A. Lendlein and S. Kelch, Shape-memory polymers, *Angew. Chem., Int. Ed*., 2002, **41**, 2034-2057.

2 T. Xie, Recent advances in polymer shape memory, *Polymer*, 2011, **52**, 4985-5000.

3 C. Liu, H. Qin and P. T. Mather, Review of progress in shape memory polymers, *J. Mater. Chem*., 2007, **17**, 1543-1558.

4 H. R.Mattila, *Intelligent Textiles and Clothing*, Woodhead Publishing Limited and CRC Press LLC, 2006.

5 J. Hu, *Shape Memory Polymers and Textiles*, Woodhead Publishing Limited and CRC Press LLC, 2007.

6 W. Sokolowski, S. Tan, P. Willis and M. Pryor, Shape memory selfdeployable structures for solar sails, *Proc. SPIE-Int. Soc. Opt. Eng*., 2008, **7267**, art. no. 72670K.

7 K. Kratz, S. A. Madbouly, W. Wagermaier and A. Lendlein, Temperature-memory polymer networks with crystallizable controlling units, *Adv. Mater*., 2011, **23**, 4058-4062.

8 C.-C. Hong and J.-C. Chen, Pre-programmable polymer transformers as on-chip microfluidic vacuum generators, *Microfluid. Nanofluid*., 2011, **11**, 385-393.

9 E. Kinkin-Gil, US Pat. 2010/0295820 A1, filed 2009, published 2010.

10 S. Reddy, E. Arzt and A. Campo, Bioinspired surfaces with switchable adhesion, *Adv. Mater*., 2007, **19**, 3833-3837.

11 T. Xie and X. Xiao, Self-peeling reversible dry adhesive system, *Chem. Mater*., 2008, **20**, 2866-2868.

12 R. Wang and T. Xie, Shape memory- and hydrogen bonding-based strong reversible adhesive system, *Langmuir,* 2010, **26**, 2999-3002.

13 A. DiOrio, X. Luo, K. M. Leec and P. T. Mather, A functionally graded shape memory polymer, *Soft Matter*, 2011, **7**, 68-74.

14 A. Lendlein and M. Behl, Shape-Memory Polymers for Biomedical Applications, in *CIMTEC 2008-Proceedings of the 3rd International Conference on Smart Materials, Structures and Systems–Smart Materials and Micro/Nanosystems*, 2008, vol. 54, pp. 96-102.

15 J. F. Mano, Stimuli-responsive polymeric systems for biomedical applications, *Adv. Eng. Mater*., 2008, **10**, 515-527.

16 W. M. Huang, Thermo-moisture responsive polyurethane shape memory polymer for biomedical devices, *Open Med. Dev. J*., 2010, **2**, 11-19.

17 A. Lendlein, M. Behl, B. Hiebl and C. Wischke, Shape-memory polymers as a technology platform for biomedical applications, *Expert Rev. Med. Dev*., 2010, **7**, 357-379.

18 W. Small, P. Singhal, T. S. Wilson and D. J. Maitland, Biomedical applications of thermally activated shape memory polymers, *J. Mater. Chem*., 2010, **20**, 3356-3366.

19 L. Sun and W. M. Huang, Thermo/moisture responsive shapememory polymer for possible surgery/operation inside living cells in future, *Mater. Des*., 2010, **31**, 2684-2689.

20 L. Xue, S. Dai and Z. Li, Biodegradable shape-memory block copolymers for fast self-expandable stents, *Biomaterials*, 2010, **31**, 8132-8140.

21 I. M. Pereira, F. Axisa, R. L. Oréfice, J. Vanfleteren and H. P. Neves, Shape-memory anchoring system for bladder sensors, *J. Biomed. Mater. Res., Part B*, 2011, **96**, 369-375.

22 K. Hearon, K. Gall, T. Ware, D. J. Maitland, J. P. Bearinger and T. S. Wilson, Post-polymerization crosslinked polyurethane shape memory polymers, *J. Appl. Polym. Sci.*, 2011, **121**, 144-153.

23 S. Kim, M. Sitti, T. Xie and X. Xiao, Reversible dry micro-fibrillar adhesives with thermally controllable adhesion, *Soft Matter*, 2009, **5**, 3689-3693.

24 L. F. Boesel, C. Greiner, E. Arzt and A. Campo, Gecko-inspired surfaces: a path to strong and reversible dry adhesives, *Adv. Mater*., 2010, **22**, 2125-2137.

25 N. Liu, W. M. Huang, S. J. Phee, H. Fan and K. L. Chew, A generic approach for producing various protrusive shapes on different size scales using shape-memory polymer, *Smart Mater. Struct*., 2007, **16**, N47-N50.

26 N. Liu, W. M. Huang, S. J. Phee and T. H. Tong, The formation of micro-protrusions atop a thermo-responsive shape memory polymer, *Smart Mater. Struct.*, 2008, **17**, art. no. 057001.

27 N. Liu, Q. Xie, W. M. Huang, S. J. Phee and N. Q. Guo, Formation of micro protrusion arrays atop shape memory polymer, *J. Micromech. Microeng*., 2008, **18**, art. no. 027001.

28 C. C. Fu, A. Grimes, M. Long, C. G. L. Ferri, B. D. Rich, S. Ghosh, S. Ghosh, L. P. Lee, A. Gopinathan and M. Khine, Tunable nanowrinkles on shape memory polymer sheets, *Adv. Mater*., 2009, **21**, 4472-4476.

29 Y. Zou, A. Lam, D. E. Brooks, A. S. Phani and J. N. Kizhakkedathu, Bending and stretching actuation of soft materials through surfaceinitiated polymerization, *Angew. Chem., Int. Ed*., 2011, **50**, 1-5.

30 W. M. Huang, Z. Ding, C. C. Wang, J. Wei, Y. Zhao and H. Purnawali, Shape memory materials, *Mater. Today*, 2010, **13**, 54-61.

31 W. M. Huang, B. Yang, Y. Zhao and Z. Ding, Thermo-moisture responsive polyurethane shape-memory polymer and composites: a review, *J. Mater. Chem*., 2010, **20**, 3367-3381.

32 C. Schmidt, K. Neuking and G. Eggeler, Functional fatigue of shape memory polymers, *Adv. Eng. Mater*., 2008, **10**, 922-927.

33 T. Pretsch, I. Jakob and W. Müller, Hydrolytic degradation and functional stability of a segmented shape memory poly(ester urethane), *Polym. Degrad. Stab*., 2009, **94**, 61-73.

34 T. Pretsch and W. Müller, Shape memory poly(ester urethane) with improved hydrolytic stability, *Polym. Degrad. Stab*., 2010, **95**, 880-888.

35 W. Müller and T. Pretsch, Hydrolytic aging of crystallizable shape memory poly(ester urethane): effects on the thermo-mechanical properties and visco-elastic modeling, *Eur. Polym.* J., 2010, **46**, 1745-1758.

36 J. Kunzelman, T. Chung, P. T. Mather and C. Weder, Shape memory polymers with built-in threshold temperature sensors, *J. Mater. Chem.*, 2008, **18**, 1082-1086.

37 http://code.google.com/p/zxing.

38 T. Zorba, K. Chrissafis, K. M. Paraskevopoulos and D. N. Bikiaris, Synthesis, characterization and thermal degradation mechanism of three poly(alkylene adipate)s: comparative study, *Polym. Degrad. Stab.*, 2007, **92**, 222-230.

39 T. Pretsch, Triple-shape properties of a thermoresponsive poly(ester urethane), *Smart Mater. Struct.*, 2010, **19**, art. no. 015006.

40 B. Bogdanov, V. Toncheva and E. Schacht, Thermal properties and morphology of poly(ester-urethanes) prepared from polycaprolactone-diol, *J. Therm. Anal. Calorim.*, 1999, **56**, 1115-1121.

41 S. J. Chen, J. L. Hu, S. G. Chen and C. L. Zhang, Study on the structure and morphology of supramolecular shape memory polyurethane containing pyridine moieties, *Smart Mater. Struct.*, 2011, **20**, art. no. 065003.

42 S. Chen, J. Hu, Y. Liu, H. Liem, Y. Zhu and Y. Liu, Effect of SSL and HSC on morphology and properties of PHA based SMPU synthesized by bulk polymerization method, *J. Polym. Sci., Part B: Polym. Phys.*, 2007, **45**, 444-454.

43 I. A. Rousseau and T. Xie, Shape memory epoxy: composition, structure, properties and shape memory performances, *J. Mater. Chem.*, 2010, **20**, 3431-3441.

44 F. Castro, K. W. Westbrook, J. Hermiller, D. U. Ahn, Y. Ding and H. J. Qi, Time and temperature dependent recovery of epoxy-based shape memory polymers, *J. Eng. Mater. Technol.*, 2011, **133**, art. no. 021025.

45 W. B. Song, L. Y. Wang and Z. D. Wang, Synthesis and thermomechanical research of shape memory epoxy systems, *Mater. Sci. Eng., A*, 2011, **529**, 29-34.

46 T. Xie and I. A. Rousseau, Facile tailoring of thermal transition temperatures of epoxy shape memory polymers, *Polymer*, 2009, **50**, 1852-1856.

47 M. Furukawa, T. Shiiba and S. Murata, Mechanical properties and hydrolytic stability of polyester urethane elastomers with alkyl side groups, *Polymer*, 1999, **40**, 1791-1798.

48 X. Luo and P. T. Mather, Triple-shape polymeric composites (TSPCs), *Adv. Funct. Mater.*, 2010, **20**, 2649-2656.

49 D. F. Duxbury, The photochemistry and photophysics of triphenylmethane dyes in solid and liquid media, *Chem. Rev.*, 1993, **93**, 381-433.

50 G. S. Egerton, Action of light on dyes in polymer materials, *Br. Polym. J.*, 1971, **3**, 63-67.

51 S. Kakac, B. Kosoy, D. Li and A. Pramuanjaroenkij, Microfluidics Based Microsystems, Proceedings of the NATO Advanced Study Institute on Microfluidics Based Microsystems: Fundamentals and Applications, 2009, p. 440.

52 J. Kunzelman, B. R. Crenshaw, M. Kinami and C. Weder, Selfassembly and dispersion of chromogenic molecules: a versatile and general approach for self-assessing polymers, *Macromol. Rapid Commun.*, 2006, **27**, 1981-1987.

53 C. Liu and P. T. Mather, Thermomechanical characterization of a tailored series of shape memory polymers, *J. Appl. Med. Polym.*, 2002, **6**, 47-52.

54 B. Atli, F. Gandhi and G. Kars, Thermomechanical characterization of shape memory polymers, *J. Intell. Mater. Syst. Struct.*, 2009, **20**, 87-89.

55 T. Pretsch, Review on the functional determinants and durability of shape memory polymers, *Polymers*, 2010, **2**, 120-158.

56 J. Diani, C. Fr_edy, P. Gilormini, Y. Merckel, G. R_egnier and I. Rousseau, A torsion test for the study of the large deformation recovery of shape memory polymers, *Polym. Test.*, 2011, **30**, 335-341.

57 K. Y. Mya, H. B. Gose, T. Pretsch, M. Bothe and C. He, Star-shaped POSS-polycaprolactone polyurethanes and their shape memory performance, *J. Mater. Chem.*, 2011, **21**, 4827-4836.

58 P. J. Flory, *Principles of Polymer Chemistry*, Cornell University Press, Ithaca, New York, 1953.

59 Q. Meng and J. Hu, A review of shape memory polymer composites and blends, *Composites, Part A*, 2009, **40**, 1661-1672.

60 M. Behl, J. Zotzmann and A. Lendlein, Shape-memory polymers and shape-changing polymers, *Adv. Polym. Sci.*, 2010, 1-40.

61 J. Leng, X. Lan, Y. Liu and S. Du, Shape-memory polymers and their composites: stimulus methods and applications, *Prog. Mater. Sci.*, 2011, **56**, 1077-1135.

62 J. S. Leng, X. Lan, Y. J. Liu, S. Y. Du, W. M. Huang, N. Liu, S. J. Phee and Q. Yuan, Electrical conductivity of thermoresponsive shape-memory polymer with embedded micron sized Ni powder chains, *Appl. Phys. Lett.*, 2008, **92**, art. no. 014104.

63 L. Sun, W. M. Huang, Z. Ding, Y. Zhao, C. C. Wang, H. Purnawali and C. Tang, Stimulus-responsive shape memory materials: a review, *Mater. Des.,* 2012, **33**, 577-640.

64 R. Mohr, K. Kraftz, T. Weigel, M. Lucka-Gabor, M. Moneke and A. Lendlein, Initiation of shape-memory effect by inductiveheating of magnetic nanoparticles in thermoplastic polymers, *Proc. Natl. Acad. Sci. U. S. A.*, 2006, **103**, 3540-3545.

65 P. R. Buckley, G. H. McKinley, T. S. Wilson, W. Small, W. J. Benett, J. P. Bearinger, M. W. McElfresh and D. J. Maitland, Inductively heated shape memory polymer for the magnetic actuation of medical devices, *IEEE Trans. Biomed. Eng.*, 2006, **53**, 2075-2083.

66 A. M. Schmidt, Electromagnetic activation of shape memory polymer networks containing magnetic nanoparticles, *Macromol. Rapid Commun.*, 2006, **27**, 1168-1172.

2.3. SUPPLEMENTAL INFORMATION

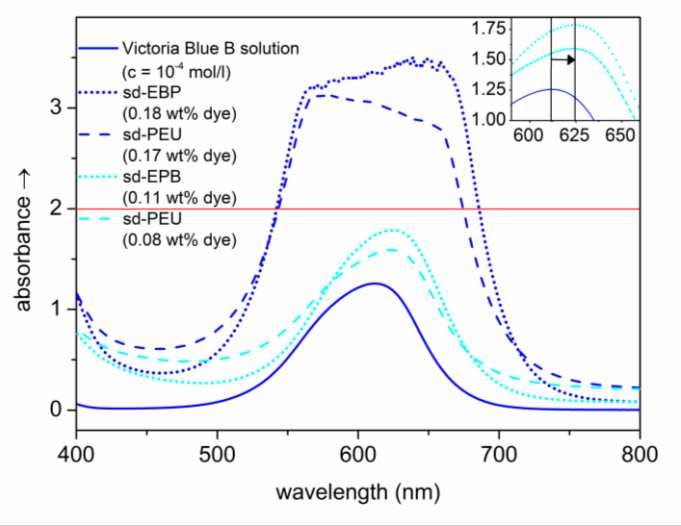

Figure 2.8 Visible absorption spectra for acetone/ethanol (50:50) solution with *Victoria Blue B* concentration of 8×10^{-5} mol l^{-1} (blue line, pH value = 5.7) and surface-dyed polymer samples of PEU with *Victoria Blue B* (sd-PEU) and EBP with *Victoria Blue B* (sd-EBP). Surface treatment with a lower concentration of dye (7.8×10^{-3} mol l^{-1}) gave sorption percentages of 0.08 wt% (sd-PEU, dashed cyan line) and 0.11 wt% (sd-EBP, dotted cyan line); a higher concentration of dye (3.2×10^{2} mol l^{-1}) resulted in *Victoria Blue B* sorption percentages of 0.17 wt% (sd-PEU, dashed blue line) and 0.18 wt% (sd-EBP, dotted blue line), at which absorbances exceeded the absorption edge (red line). The inset (top right) illustrates the bathochromic shift in sd-PEU and sd-EBP towards *Victoria Blue B* solution. All spectra were recorded at 23 °C.

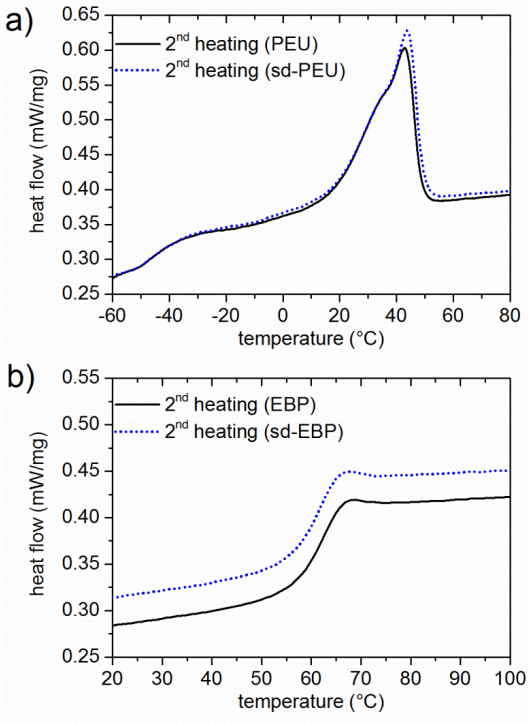

Figure 2.9 DSC thermograms of the 2nd heating scan for neat PEU (black line) and surface-dyed PEU (sd-PEU, dotted blue line) (a), and for neat EBP (black line) and surface-dyed EBP (sd-EBP, dotted blue line) (b). The sorption percentages of *Victoria Blue B* were 0.17 wt% with PEU and 0.18 wt% with EBP, respectively.

3. DURABILITY OF SWITCHABLE QR CODE CARRIERS UNDER HYDROLYTIC AND PHOTOLYTIC CONDITIONS

The article: M. Ecker and T. Pretsch, *Smart Mater. Struct.*, **2013**, *22* (9), art. no. 094005 is reproduced by permission of IOP science. The original article is online available at: http://stacks.iop.org/0964-1726/22/i=9/a=094005

3.1. EXPERIMENTAL CONTRIBUTION

My contribution for this manuscript comprises:

Experimental investigations, data analysis, preparation of the figures and writing an early version of the manuscript.

Contributions of co-author:

T. Pretsch: Conception and writing of the manuscript.

3.2. PUBLICATION

3.2.1. Abstract

Following a guest diffusion approach, the surface of a shape memory poly(ester urethane) (PEU) was either black or blue colored. Bowtie-shaped quick response (QR) code carriers were then obtained from laser engraving and cutting, before thermo-mechanical functionalization (programming) was applied to stabilize the PEU in a thermo-responsive (switchable) state. The stability of the dye within the polymer surface and long-term functionality of the polymer were investigated against UVA and hydrolytic ageing. Spectrophotometric investigations verified UVA ageing-related color shifts from black to yellow-brownish and blue to petrol-greenish whereas hydrolytically aged samples changed from black to greenish and blue to light blue. In the case of UVA ageing, color changes were accompanied by dye decolorization, whereas hydrolytic ageing led to contrast declines due to dye diffusion. The Michelson contrast could be identified as an effective tool to follow ageing-related contrast changes between surface-dyed and laser-ablated (undyed) polymer regions. As soon as the Michelson contrast fell below a crucial value of 0.1 due to ageing, the QR code was no longer decipherable with a scanning device. Remarkably, the PEU information carrier base material could even

then be adequately fixed and recovered. Hence, the surface contrast turned out to be the decisive parameter for QR code carrier applicability.

3.2.2. Introduction

Shape memory polymers (SMPs) are stimuli-responsive materials.[1-7] They can be stabilized in a temporary shape, which may significantly differ from the original shape and keep that shape until the shape memory effect is triggered. Ideally, the programming (functionalization) of an SMP comprises the application of a deformation in the viscoelastic state of the polymer and the systematic blocking of the restoring force by the subsequent crystallization or vitrification of the switching segment. As a result, the imposed new shape remains stable as long as the polymer is stored at temperatures below the transition temperature T_{trans}. Upon heating, devitrification or melting of the switching segment initiates the recovery into the original shape, which is an entropically driven process. The growing economic interest in this emerging class of materials is reflected by a variety of potential applications, ranging from medical ones such as pressure bandages,[8] to SMP emulsions as finishing agents for textiles to achieve wrinkle-free effects,[9] to active disassembly concepts[10] and morphing structure technologies such as skeletal structural components.[11]

Recently, we reported the results of a comprehensive proof-of-concept study for using SMPs as base material for the preparation of switchable information carriers.[12] In this connection, phase-segregated poly(ester urethane) (PEU) with poly(1,4-butylene adipate) (PBA) as switching segment qualified as reliable multi-block copolymer due to easy colorability, good CO_2-laser engravability and distinct shape memory properties. Hence, we decided to extend our investigations onto the durability of PEU "tags" with characteristically dyed surface and engraved quick-response (QR) code patterns. Therefore, we selected bowtie-shaped tags, since their QR code-related shape memory properties can be more easily quantified compared with tags of cuboid shape, whose profiles may display more random QR code distortions due to programming.

In accordance with our recent study,[12] we selected the triarylmethane dye *Victoria Blue B*[13] for blue coloring the PEU surface. As alternative, a mixture of *Victoria Blue B* and two further dyes, with one of them belonging to the same class of triarylmethane dyes (*Basic Green 1*)[13] and the other one to the family of hemicyanine dyes (*Basic Red 28*),[14] was used for black coloring. Subsequently, the either blue or black colored side of the PEU surface was laser engraved with a machine-readable QR code,

containing the information “BAM QRM-Label”. The subsequent cutting of the samples into tag size was followed by stability investigations against different environmental impacts. Motivated by the question whether the limiting factor in regard of tag durability was QR code readability as strongly depending on the surface contrast or the QR code-related shape memory functionality, two degradation scenarios were considered, consisting of exposure to UVA light at different levels of humidity and hydrolytic ageing. In both cases, surface-dyed PEU was aged with PBA, being either in a semi-crystalline state (ageing at 23 °C and thus below $T_{trans} = T_m = 37$ °C)[15] or in an amorphous state (ageing at 60 °C and thus above T_m). For tag durability we defined dye-related assessment criteria such as the QR code readability by means of a smartphone used as a scanning and decoding device, changes in color intensity within surface-dyed regions (including reflection properties) and the Michelson contrast.[16] Also, we studied the stability of PEU as tag base material with respect to shape memory functionality and thermal properties. Hydrolytic ageing is known to significantly alter the phase morphology of poly(ester urethanes),[17, 18] but also to strongly affect shape memory properties such as the recovery temperature, which increases in the course of degradation.[15, 19] In the case of UVA ageing, artificial ageing conditions may initiate oxidative degradation in polyurethane elastomers.[20, 21] However, in any ageing scenario investigated, regular checks of QR code readability and shape memory functionality were carried out to identify the maximum applicability of the tags.

3.2.3. Experimental Section

3.2.3.1. Materials

Desmopan DP 2795A SMP is a poly(ester urethane) (PEU) from Bayer MaterialScience AG and was used as received. The hard segment was composed of 4,4′-methylenediphenyl diisocyanate and a 1,4-butanediol chain extender. The soft segment was based on poly(1,4-butylene adipate) (PBA). Further information regarding the thermal and mechanical properties of pristine and hydrolytically aged PEU is given in previous publications.[15, 19, 22] The raw material was supplied as rectangular injection molded plaque samples with dimensions of 126 × 52 × 2 mm^3.

3.2.3.2. Sample preparation

The PEU plaques were surface-dyed with a blue or black colored dye solution. For blue coloring, 2 wt% of *N*-[4-[[4-(dimethylamino)phenyl][4-(phenylamino)-1-naphthyl]methylene]-2,5-cyclohexadien-1-ylidene]-*N*-methyl-methanaminium chloride

(*Victoria Blue B*; C.I. 44045; CAS 2580-56-5; Sigma Aldrich) was completely dissolved in a 1:1 mixture of ethanol (96%, Merck) and acetone (98%, AppliChem), resulting in a dye solution with a concentration of 3.9×10^{-2} mol l^{-1}. The same solvent mixture was taken to prepare the respective solution for black coloring, but the individual components consisted in 2 wt% of *Victoria Blue B*, 5.5 wt% of [4-[4-(Diethylamino)benzhydrylene]cyclohexa-2,5-dien-1-ylidene]diethylammonium hydrogen sulfate (*Basic Green 1*; C.I. 42040; CAS 633-03-4) and 5.5 wt% of 3-[1,3-dihydro-1,3,3-trimethyl-2H-indol-2-(ylene)ethylidene]-9-ethyl-3H-carbazolium chloride (*Basic Red 28*; CAS 72828-91-2), resulting in a solution with a dye concentration of 27.9×10^{-2} mol l^{-1}. The chemical structure of the employed dyes is given in Scheme 3.1.

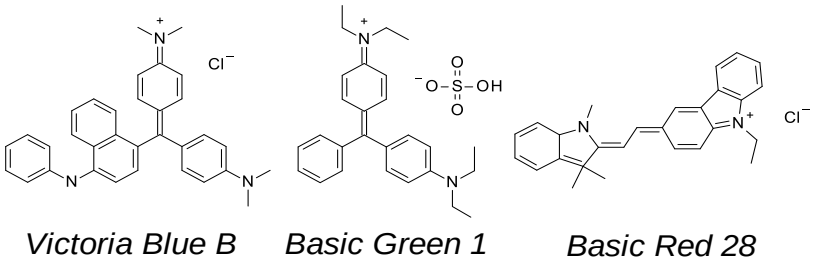

Scheme 3.1 Chemical structure of dyes used for PEU surface-specific coloring.

For specific blue or black coloring, the PEU surface was cleaned with lint-free cloth, before it was pretreated with acetone and exposed to the above-mentioned dye solutions, which were pipetted onto the surface and uniformly distributed by means of a brush. After an exposure time of 30 s, the residues of the dye solution were completely removed with lint-free cloth. In a last step, QR codes containing the arbitrarily selected information "BAM QRM-Label" were engraved into the colored PEU surface and the polymer was cut into information carrier size (**Figure 3.1**). For engraving and cutting bowtie-shaped samples, a 30 W CO_2-laser (spot size: 0.0762–0.127 mm; wavelength λ = 10.6 µm) was used. The prepared blue and black colored information carriers were termed "tags". At the end, the QR code of every PEU tag was readable with a smartphone used as a scanning and decoding device. In order to microscopically explore the influence of guest diffusion upon the PEU matrix and characterize the laser-ablation depth, the polymer was cut perpendicular to its surface by means of a cryomicrotome CM1950 from Leica. The approximately 100 µm thick slices were prepared at −20 °C and studied with a Leica DM EP microscope at a ten times optical zoom. The diffusion depth of the dye was determined with the Dietermann and Heuser Solution GmbH (dhs) software (version 13) and the graphical program ImageJ. Therefore, a microscopic image

of the cryomicrotome section was considered and the darkest point at the surface set as the standard. The intensity decline down to a loss of 70% was measured; the corresponding distance to the surface was defined as the color diffusion depth.

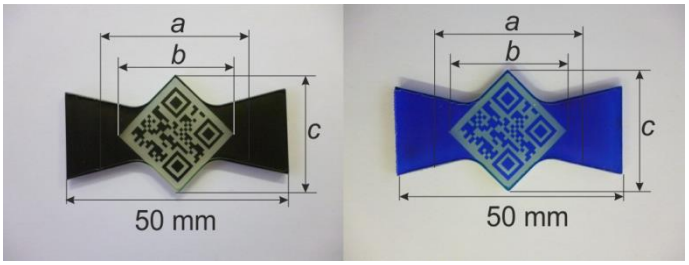

Figure 3.1 Bowtie-shaped PEU tags in black (left) and blue color (right) with identical dimensioning (tag thickness of 2 mm), drawn in a QR code-related longitudinal and transversal length ($b_0 = c_0 = 25.3$ mm) and functionalization-related clamping distance $a_0 = 30$ mm. The QR code contains the information "BAM QRM-Label".

3.2.3.3. QR code scanning and decoding

A Samsung Galaxy S I9000 smartphone equipped with the software "Barcode Scanner" version 4.0 from Zxing was used as a QR code scanning and decoding device. The QR codes of the tags were directly scanned after fabrication and at regular time intervals during ageing. After QR code scanning of artificially aged tags, the same tags were again subjected to the ageing scenarios. Tags, whose functionality was investigated, were additionally scanned in their temporarily fixed state and after triggering the shape memory effect.

3.2.3.4. Spectroscopy and spectrophotometry

Visible absorption spectra were recorded on rectangular, undyed and surface-colored samples with a cuboidal dimension of $10 \times 10 \times 2$ mm^3. The samples were investigated with a Cary 300 Scan spectrophotometer from Varian, which was equipped with a Czerny-Turner pre-monochromator, a high-performance R928 photomultiplier tube and a tungsten halogen visible source containing a quartz window. During the wavelength scan, the uncolored back side of the samples pointed toward the light source and the colored surface toward the detector. A Labsphere DRA–CA–30I was used as an integrating sphere to collect the lost light and direct it onto the detector. All visible absorption spectra were recorded at 23 °C with a scan rate of 60 nm min^{-1} at wavelengths λ from 800 to 400 nm. A CM–2600d spectrophotometer from Minolta was used to quantitatively determine the reflection properties of unaged and aged, black and blue surface-colored samples as a function of wavelength. The samples had the same dimensioning as for the visible absorption analysis. During all measurements, a circular

illumination area of 28.3 mm^2 inside the center of each sample was investigated. Therefore, a wavelength scan range from 740 to 360 nm was selected. Three xenon flashlights were used as the light source, simulating the standard illuminant D65, which corresponds with a color temperature of around 6500 K to the average daylight in Western Europe.[23] In every ageing series, the measurements were conducted on the same samples in specular component excluded (SCE) mode. For the differently aged samples, the reflectivity was determined as a function of wavelength.

3.2.3.5. Determination of surface contrast

For the evaluation of surface contrast, the surface-colored and undyed regions within the QR code area of the tags were closely considered. The color of the undyed regions was mostly dominated by the semi-crystalline PBA phase, whose crystals rendered the polymer whitish. The applied procedure of blue or black coloring and the choice of dye components drastically influenced the contrast toward the undyed (laser-ablated) regions. For contrast determination, the Michelson contrast C_M – as defined in equation (1) – was used:[16]

$$C_M = \frac{L_{max} - L_{min}}{L_{max} + L_{min}} \quad (1)$$

Herein, the relation between the difference and the sum of the highest and lowest luminance L_{max} and L_{min}, differing in grayscale value, is considered. The grayscale varies from black at the weakest intensity to white at the strongest intensity. Accordingly, in an 8 bit per pixel grayscale, black has the lowest value (0), whereas white has the highest (255). In a standard approach, the color image of a tag was converted into a grayscale histogram by using the image analysis program ImageJ. The Michelson contrast C_M was determined for five different subzones within the QR code area (top left, top right, center, bottom left and bottom right) and subsequently averaged. The maximum deviation from the mean value was determined and set as the error. In order to assure stable experimental conditions, under which the pictures of the QR code were taken, the camera Panasonic DMC–FS16 was kept perpendicular to the polymer surface at a constant distance of 50 mm. The pictures were recorded in macromode.

3.2.3.6. UVA weathering

The PEU tags shown in **Figure 3.1** and black or blue surface-dyed PEU samples with a cuboidal dimension of 10 × 10 × 2 mm^3 were exposed to UVA irradiation at 23 °C and a

relative air humidity of 50%. Alternatively, the tags and samples were irradiated with UVA light at 60 °C and an air humidity of 16%. The employed weathering device was a UV200 Weiss "Global UV Test" climate chamber. For UVA ageing, a setup was used in which 18 type 1A fluorescent UVA lamps (DIN EN ISO 4892–3:2006), having a maximum wavelength of 340 nm each and a broad operating wavelength ranging from 400 to 290 nm, were directly placed into the door of the climate chamber. In order to simulate the photochemical active spectrum as an integral part of natural sunlight in Central Europe, a UVA irradiance of 38–40 W m^{-2} was chosen, representing the maximal irradiance at noon. The tags and samples were clamped inside the climate chamber with the surface-colored sites pointing toward the fluorescent lamps. The distance between the UVA lamps and the PEU was about 30 cm. Upon ageing, the QR codes of the tags were regularly scanned with the scanning and decoding device, the dye diffusion behavior was microscopically investigated, the surface contrast determined, calorimetric studies were conducted and the QR code-related shape memory properties quantified. Also, the reflectance of the purely surface-colored samples was spectrophotometrically studied.

3.2.3.7. Hydrolytic ageing

For hydrolytic ageing, PEU tags or either black or blue surface-dyed PEU samples with a cuboidal dimension of 10 × 10 × 2 mm^3 were put into glass laboratory bottles having a volume of 100 ml each, which were then filled with 60 ml of de-ionized water. The bottles were sealed and placed in a convection oven, where ageing was simulated at 60 °C. Alternatively, the tags were stored in water at 23 °C. The tags and the either black or blue surface-dyed PEU samples were removed from the bottles and surface-dried with lint-free cloth for regular investigations. Tag examinations included QR code scanning, microscopic investigations, the determination of surface contrast, calorimetric studies and the analysis of the QR code-related shape memory functionality. The other samples were spectrophotometrically investigated.

3.2.3.8. Functionalization and recovering

The programming (functionalization) of the bowtie-shaped PEU tags was realized with an electromechanical testing system (MTS Insight 10), which was equipped with a thermochamber (Thermcraft). Heating of the tags was achieved through two electrical heating elements, which were placed in the back of the thermochamber. For cooling, liquid nitrogen was injected from a Dewar vessel into the chamber.

In the course of functionalization, a tag was heated to 60 °C and stretched to a maximum elongation $\Delta a/a_0$ (**Figure 3.1**) of either 100 or 200%, which assured the strong distortion of the QR code within the PEU surface. The new shape with unreadable QR code was fixed by cooling the tag to −15 °C, while keeping the clamping distance constant. After 5 min at −15 °C, the tag was heated to 23 °C, whereupon the readability of the QR code was investigated. Programming-related heating rates of 15 °C min^{-1} from 23 to 60 °C and 17 °C min^{-1} from −15 to 23 °C and a cooling rate of 26 °C min^{-1} from 60 to −15 °C were employed. As a result of programming, the tag was stabilized in a room-temperature-stable, QR-code-unreadable state. This state was characterized by longitudinal ($\Delta b/b_0$) and transversal ($\Delta c/c_0$) changes (**Figure 3.1**) toward the initial state of the QR code. In a final step, the temporarily fixed (functionalized) tag was heated to 60 °C at the same rate as employed during programming to trigger the shape memory effect. To ensure an almost complete recovering of the permanent shape, the tag was kept for 5 min at 60 °C, before it was cooled to 23 °C at a rate of 20 °C min^{-1}. Finally, the QR code readability of the recovered tag was examined and one further time $\Delta b/b_0$ and $\Delta c/c_0$ were determined.

3.2.4. Results and Discussion

At first, we investigated the influence of surface-specific dyeing on PEU as base material for tag preparation. The microscopic profiles of intensely black or blue surface-colored PEU showed homogeneous dye diffusion depths of around (95 ± 5) µm for the blue color and (100 ± 5) µm for the black color (shown in ESI, **Figure 3.10**). **Figure 3.2** exhibits the visible absorption spectra of pristine PEU and black and blue surface-dyed (sd) PEU.

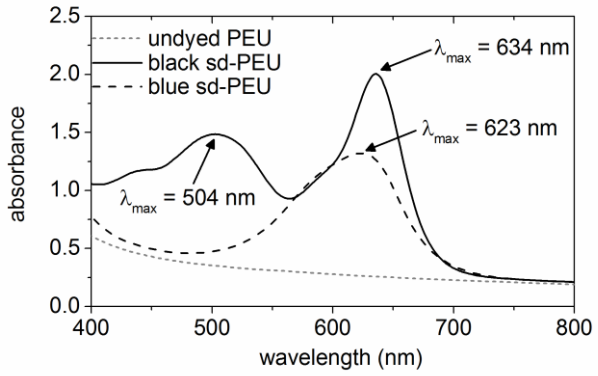

Figure 3.2 Visible absorption spectra of pristine (undyed) PEU and black and blue surface-dyed (sd) PEU.

Between 800 and 400 nm, no significant absorbance could be detected for pristine PEU. By contrast, the two surface-colored samples exhibited strong absorptions, as evidenced

by λ_{max} = 623 nm for PEU when blue-dyed with *Victoria Blue B*, and two characteristic absorptions for black-dyed PEU.

Since the black dye solution consisted of a three-component dye mixture, including blue, green and red dye (individual spectra of black, blue, green and red surface-dyed PEU are included in ESI, **Figure 3.11**), overlapping absorptions at λ_{max} = 634 nm, attributable to *Victoria Blue B* and *Brilliant Green 1*, and at 504 nm, assignable to *Basic Red 28*, were detected for the black surface-colored PEU. The absorbance proved the distinct PEU colorability by means of guest diffusion.

Independent of the used dye solution, a fairly small amount of dye was taken up by the polymer matrix. In detail, the polymer weight increased by (0.12 ± 0.02) wt% upon black coloring and by (0.09 ± 0.02) wt% upon blue coloring. As shown by calorimetric measurements on undyed and black or blue surface-dyed PEU samples, the fairly small amount of dye inside the polymer surface had a rather weak influence on the melting and crystallization behavior of the soft segment poly(1,4-butylene adipate) (PBA) (shown in ESI, **Figure 3.12**). In fact, the PBA crystallization and melting transitions were close to those which were recently reported.[15, 24] In our present concept, PBA crystallization served to fix the temporary shape of an elongated tag with an unreadable QR code, whereas PBA melting initiated the entropically driven shape recovery process and thus the return of the tag into the almost permanent, QR code readable shape.

Inside the PEU surface, the laser-engraved QR code region showed a maximum ablation depth of about (105 ± 5) µm, as evidenced by microscopic images (not shown herein). Thus, the maximum laser-ablation depth did slightly exceed the color penetration depths. The sufficiently high surface contrast enabled the reading of the QR code with a scanning and decoding device. In general, blue colored tags had a lower Michelson contrast C_M of (0.31 ± 0.03) compared to black colored tags (0.75 ± 0.05).

The concept of using shape memory polymers such as PEU as information carriers, and in particular as QR code carriers, necessitates an adequate long-term surface contrast in the QR code region. After tag exposure to artificial ageing, a scanning and decoding device was used to verify the QR code readability. The result of UVA ageing, applied to black and blue tags at 23 and 60 °C, is shown in **Figure 3.3**.

As general trend, all blue and black tags lost their QR code readability with proceeding ageing time due to dye decolorization. Under UVA irradiation at 23 °C (**Figure 3.3**a),

the black color changed to yellow-brownish while blue tags went petrol-greenish. As visible to the naked eye, the color intensity of the blue colored tags increased first before decolorization occurred. During ageing, the QR code could be read from black and blue tags for up to 11 d, corresponding to a UV radiant exposure of 49 MJ m^{-2}. Under more severe UVA ageing conditions (at 60 °C, **Figure 3.3**b), a similar color evolution could be detected. In this case, the QR code could be read from black tags for up to 17 h at a UV radiant exposure of 2.5 MJ m^{-2} and from blue tags for 75 h at a UV radiant exposure of 10.2 MJ m^{-2}.

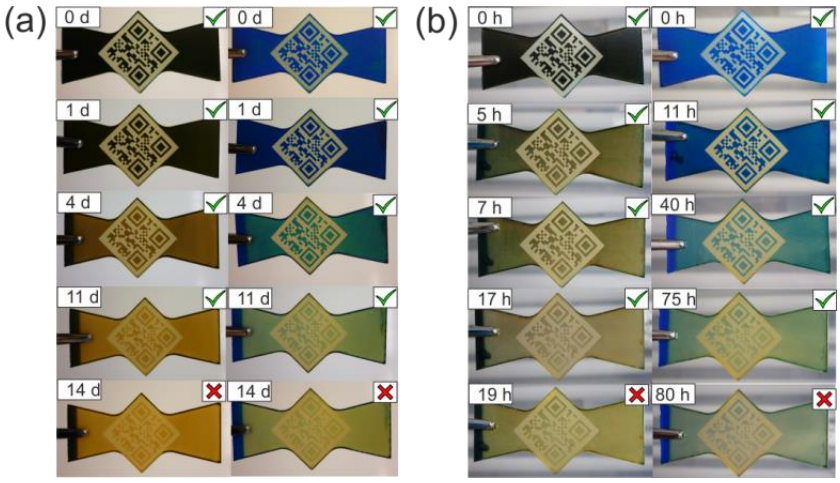

Figure 3.3 Tags after different exposure times to UVA irradiation at 23 °C and 50% air humidity (a) and 60 °C and 16% air humidity (b), respectively. In the ageing series, black tags are shown left and blue tags right. The tags consistently exhibited a vertical color stripe on the left, which was not exposed to UVA light due to clamping. The QR code could be read from all tags with a check mark (top right in the individual images).

In the second degradation scenario, the QR code readability was investigated on hydrolytically aged PEU tags (**Figure 3.4**).

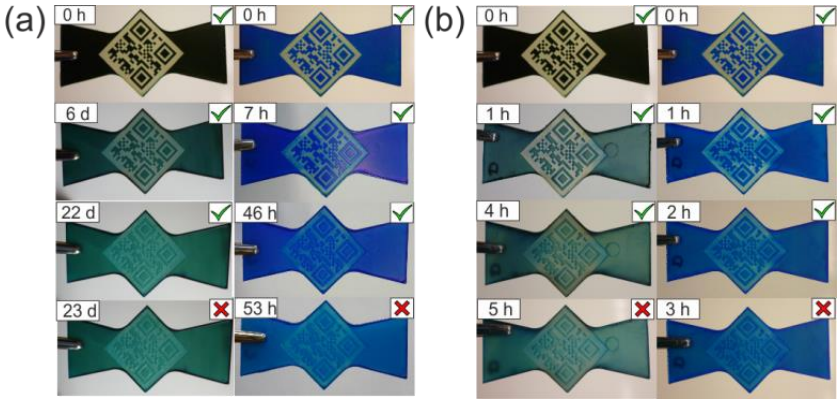

Figure 3.4 Tags after different time intervals of water immersion at 23 °C (a) and 60 °C (b). In the ageing series, black tags are shown left and blue tags right. The QR code could be read from all tags with a check mark (top right in single images).

Here, the results were fundamentally different. The black colored regions within the tags turned greenish, whereas the blue colored ones brightened. However, dye decolorization played a minor role and instead a coloring of undyed regions took place. Upon water immersion at 23 °C (pH value = 7.0), the QR codes could be decoded for up to 22 d from black tags and thus much longer than from blue tags (46 h) (**Figure 3.4**a). In the case of water immersion at 60 °C (pH value = 7.0, **Figure 3.4**b), the QR code could be read for 4 h from black tags and 2 h from blue tags, respectively.

A series of microtome sections was prepared to follow changes in dye diffusion depth in the respective tag exposure scenarios (**Figure 2.5**). Remarkably, the diffusion depth of *Victoria Blue B* decreased inside the PEU surface by 25 µm within 24 h of UVA irradiation at 23 °C (**Figure 2.5**a and b), which resulted in enhanced surface contrast.

A totally different trend was found for tags aged in water. Here, either diffusion of dye molecules from surface-colored to undyed regions or a second coloring through the surrounding aqueous solution, which took up staining agent by eluting parts of the dye from the polymer surface, occurred (**Figure 2.5**c). In the laser-ablated regions, the dye diffused at 60 °C within 5 h down to a depth of 170 µm (**Figure 2.5**c). As a consequence, hydrolytic ageing led to decreased color contrast in the QR code area. With ongoing immersion, the dye molecules diffused even deeper inside the PEU matrix. For instance, after 16 h of water immersion at 60 °C, approximate dye diffusion depths of about 500 µm (black tag, not shown herein) and 600 µm (blue tag, **Figure 2.5**d) were detected.

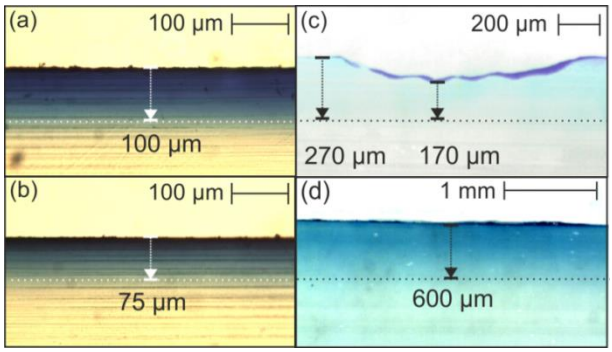

Figure 3.5 Microscopic images of cryomicrotome sections as taken from a blue colored PEU tag before (a) and after exposure to 24 h UVA irradiation at 23 °C and 50% air humidity (b) and from a second blue colored PEU tag after 5 h ((c), focusing on a laser-ablated region) and 16 h (d) immersion in water at 60 °C. The dotted horizontal lines were drawn in to illustrate the dye diffusion depth.

To follow ageing-related color changes, we spectrophotometrically investigated surface-dyed, non-laser-ablated polymer samples. The rectangular, either black or blue colored PEU samples, with identical dye diffusion depth as for the above-mentioned tags, were

UVA aged at 23 and 60 °C and the reflectivity of the employed D65 standard illuminant determined (**Figure 3.6**).

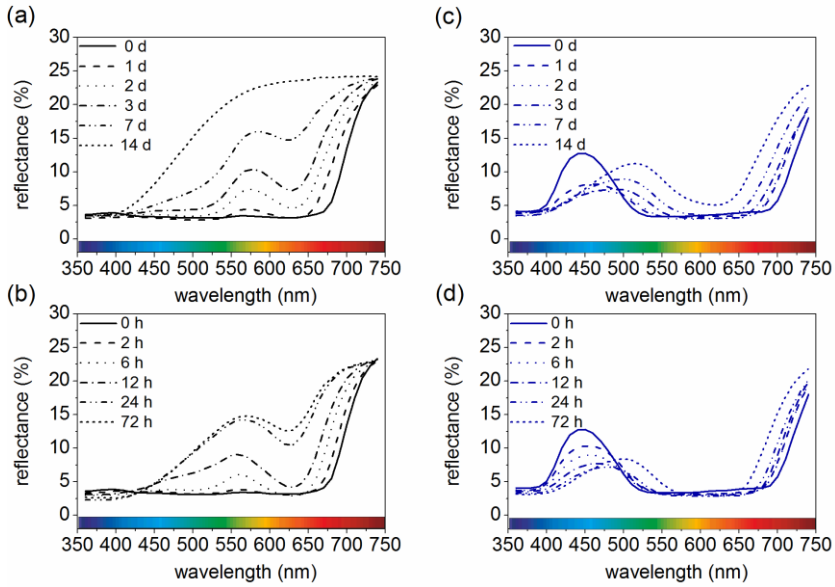

Figure 3.6 Reflectance as a function of wavelength λ for black ((a) and (b)) and blue ((c) and (d)) surface-colored PEU samples after different UVA ageing periods at 23 °C ((a) and (c)) and 60 °C ((b) and (d)), 73on-tinutively.

We found that unaged, black samples (continuous black lines in **Figure 3.6**a and b) exhibited reflectances between 745 and 680 nm, culminating in maxima at the highest wavelength (745 nm). Upon UVA ageing, the reflectance of the pure black surface started to increase strongly at about 575 nm. This is in accordance with the findings above, that dye fading occurred together with a color change from black to yellow-brownish (**Figure 3.3**). The unaged blue colored sample (continuous blue lines in **Figure 3.6**c and d) exhibited reflectances in the wavelength range between 518 and 397 nm, with a maximum of about 12% at 445 nm. With ongoing ageing, the peak decreased first, before it shifted toward higher wavelengths with a coincidental increase of reflectance. This finding is in accordance with the tag color changes deducible from **Figure 3.3**, namely that the color intensity increased first, before decolorization and a shift from blue toward petrol-greenish took place. In the case of hydrolytically aged samples, black colored PEU samples exhibited a steadily increasing peak at 500 nm in the green color region with a shoulder at 420 nm (not shown herein). By contrast, the peak maximum of blue colored PEU samples was slightly shifted toward higher wavelengths (from 445 to 460 nm), corresponding to a brightening effect, and at the same time the peak width and maximum increased (not shown herein). In any case, an acceleration of the observed effects could be found at the higher ageing temperature.

In a next step, grayscale histograms were generated from the spot color photographs (**Figure 3.3**b and **Figure 3.4**a) in order to get a better understanding of the ageing-dependent changes in QR code contrast of our tags. For this purpose, five different subzones within the QR code area were considered. The selected regions were found to be representative for the whole QR code area of the tag. The grayscale histograms for the different ageing scenarios looked quite similar; one typical grayscale histogram series is shown in **Figure 3.7** for UVA ageing of blue tags at 60 °C and hydrolytic ageing of black tags at 23 °C, respectively.

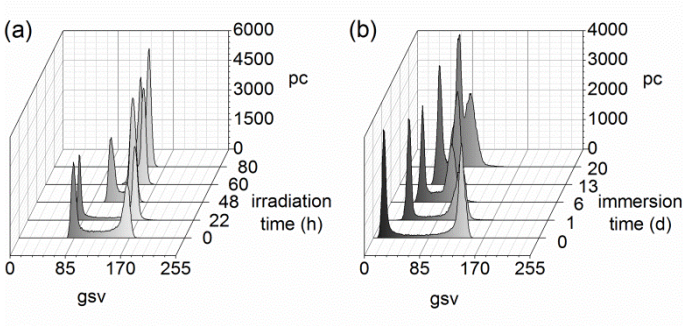

Figure 3.7 Grayscale histograms: ageing-dependent changes in grayscale value (gsv) and pixel counts (pc) of a blue tag, UVA irradiated at 60 °C and 16% air humidity (a), and a black tag, hydrolytically aged at 23 °C (b).

In the grayscale histograms two peaks are omnipresent, which correspond to the grayscale values of the undyed areas (L_{max}, the peak at higher grayscale value) and the surface-dyed areas (L_{min}, the peak at lower grayscale value). Upon UVA irradiation at 60 °C, L_{min} shifted for blue tags with proceeding ageing time to a higher grayscale value, whereas L_{max} did not alter position. As a result, the two peaks came closer to each other (**Figure 3.7**a), corresponding to a loss in contrast. The grayscale histogram series for black tags (water-immersed at 23 °C, **Figure 3.7**b) showed a different behavior. Here, the peaks also came closer to each other in the course of ageing, but in parallel the width of the individual peaks increased strongly. This increase was most pronounced for L_{max}, which shifted toward lower grayscale values. The finding is in agreement with those of the image series provided by **Figure 3.4**. The uncolored areas took up dye from solution or from the colored regions and turned darker in the course of ageing.

For all ageing scenarios investigated, the Michelson contrast C_M was directly determined (**Figure 3.8**).

Upon UVA ageing, the QR code-related C_M of black tags decreased, whereas blue tags at first showed a strong increase in C_M by 71% (after 24 h at 23 °C and a UV radiant

exposure of 3.4 MJ m^{-2}) and 49% (after 5 h at 60 °C and a UV radiant exposure of 0.7 MJ m^{-2}), before the contrast also decreased (**Figure 3.8**a and b).

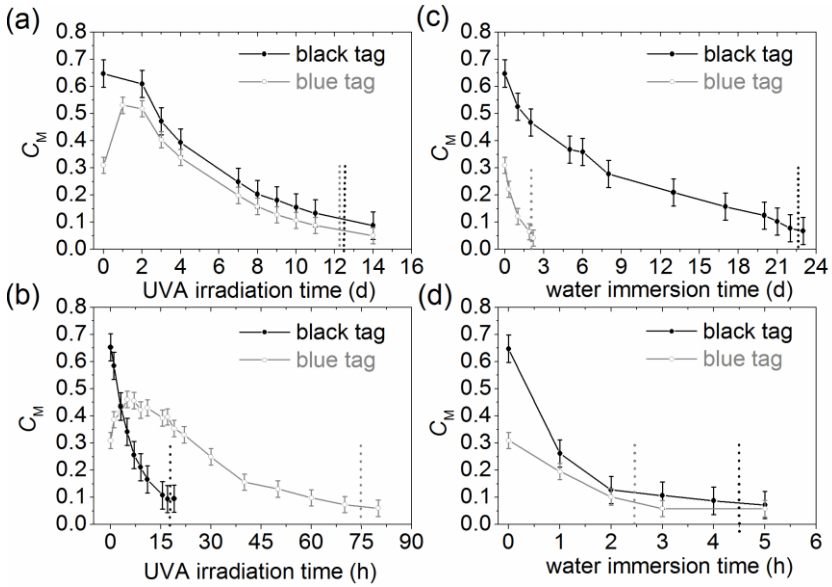

Figure 3.8 Ageing-related changes in Michelson contrast C_M within the QR code area of black and blue PEU tags. Tags were considered after UVA irradiation at 23 °C and 50% air humidity (a) and at 60 °C and 16% air humidity (b) and water immersion at 23 °C (c) and 60 °C (d). Dotted vertical lines are drawn in for every ageing study to illustrate when QR codes became unreadable (at about a C_M threshold of 0.1).

The initial increase in surface contrast can be explained with an increase in dye concentration close to the PEU surface, as indicated by our microscopic investigations (**Figure 3.5**b). For the subsequent period of C_M decline, we assume in line with earlier interpretations of dye fading mostly related to textiles, that in a two-step reaction first a breakdown of dye aggregates took place, before degradation processes started.[25] Presumably, photochemical degradation of the employed triarylmethane dyes, and thus decolorization, were initiated by photoxidation or photoreduction and underwent three main reactions, consisting of *N*-demethylation, hydroxylation and cleavage of the conjugated structure, thus forming benzophenone derivates.[13, 26]

Toward the end, C_M decreased to values below 0.1, at which the QR code was no longer machine-readable. In the case of water immersion, C_M of black tags gradually decreased over a period of 23 d (ageing at 23 °C, **Figure 3.8**c) and over 5 h (ageing at 60 °C, **Figure 3.8**d), respectively. A more rapid decline in C_M was found for blue tags. Once again, the QR code was consistently decodable above a minimum C_M value of 0.1. In this way, C_M proved to be a beneficial indicator for machine-readability of QR codes.

Next, we were interested in finding out to what extent the maximum ageing conditions, which led to the malfunction of QR code readability, influenced the thermal properties of PEU. In detail, these conditions included 14 d of UVA irradiation at 23 °C and 50% air humidity (black tag), 80 h of UVA irradiation at 60 °C and 16% air humidity (blue tag), 23 d of water immersion at 23 °C (black tag) and 5 h of water immersion at 60 °C (black tag). The respective DSC thermograms (shown in ESI, **Figure 3.13**) revealed that the thermal properties of PEU were virtually unaffected by UVA irradiation and hydrolysis, since the PBA melting and crystallization enthalpies remained almost constant and the respective signals (peaks) did not shift by more than 2 °C. Moreover, we found that the surface-colored and laser-engraved side of every tag exposed to UVA light showed calorimetric properties comparable with the uncolored back side, which was not directly exposed to UVA irradiation.

Subsequently, we investigated the QR code-related functionality of the tags for an arbitrarily selected tag elongation of $\Delta a/a_0 = 100\%$, which subsequently was temporarily stabilized by PBA crystallization and recovered by PBA melting. In this connection, the QR code-related longitudinal changes $\Delta b/b_0$ and transversal changes $\Delta c/c_0$ (as defined in **Figure 3.1**) were examined for the temporarily fixed and recovered state. As expected, the dye itself did not influence the thermo-mechanical properties of the polymer. This was evidenced by the fact that both unaged and black or blue colored tags consistently exhibited a longitudinal QR code distortion of +98% and a transversal shortening of −14% in the temporary shape with an unreadable QR code. Upon triggering the shape memory effect, the differently colored tags revealed QR codes with longitudinal residues of $\Delta b/b_0 = +15\%$ and transversal residues of $\Delta c/c_0 = -1\%$. As prerequisite for successful scanning and decoding of recovered tags, we selected the error correction level "M" when generating the QR codes. This allowed restoring up to 15% of the symbol codewords in a distorted code area. For this reason, QR codes with minor (residual) distortions were decipherable.

Next, the shape fixity of an elongation $\Delta a/a_0 = 100\%$ and the corresponding tag recoverability were analyzed after exposure to the above-mentioned ageing scenarios. In every single case, tags were investigated whose QR code was on the verge of becoming unreadable (approaching a Michelson contrast of 0.1). For 14 d of UVA irradiation at 23 °C and 50% air humidity, 23 d of water immersion at 23 °C and 5 h of water immersion at 60 °C, no change of the QR code-related shape memory characteristics was found for both the fixed and recovered state. These findings were in agreement with the

calorimetric data of the respective samples (shown in ESI, **Figure 3.13**) and with the material behavior in the initial phase of hydrolytic ageing, as recently investigated on the same polymer.[15, 19] An exception was the result of tag irradiance for 80 h with UVA light at 60 °C and 16% air humidity. In this case, a deterioration of the QR code-related shape fixity was evidenced by $\Delta b/b_0 = 83\%$ and $\Delta c/c_0 = -12\%$. However, the tag could still be fixed at an elongation of $\Delta a/a_0 = 95\%$ and recovered to $\Delta a/a_0 = 3\%$. In return, the QR code-related shape recoverability remained high, as documented by $\Delta b/b_0 = 8\%$ and $\Delta c/c_0 = -1\%$.

In a further experiment, temporarily fixed tags (tensile deformed to $\Delta a/a_0 = 200\%$ and stabilized by PBA crystallization) were subjected to two ageing scenarios, consisting of 9 d ageing in water at 23 °C (black colored tag) and irradiation with UVA light for 9 d at 23 °C (blue colored tag) (**Figure 3.9**).

In both cases, the selected ageing scenarios had no considerable influence on the temporarily fixed state, as evidenced by the ratios $\Delta b/b_0 = 174\%$ and $\Delta c/c_0 = -20\%$, which remained almost constant compared with the unaged tags. In the strongly distorted states, the QR codes of the aged tags stayed non-decodable. Due to the initiation of shape recovery through heating to 60 °C, the QR codes switched to readable, while the QR code distortion ($\Delta b/b_0 = 32\%$ and $\Delta c/c_0 = -3\%$) did not significantly alter in comparison with the unaged tags. This shows that even storage of programmed tags under severe environmental conditions does not constitute a limiting factor to the technological applicability.

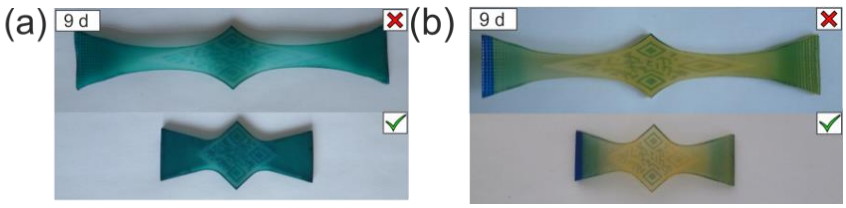

Figure 3.9 Black colored, functionalized ($\Delta a/a_0 = 200\%$) tag after 9 d of water immersion at 23 °C (a) and blue colored, functionalized ($\Delta a/a_0 = 200\%$) tag after 9 d exposure to UVA light at 23 °C and 50% air humidity (b). The tags could be switched from QR code unreadable (above) to decipherable (bottom) through heating to 60 °C.

3.2.5. Conclusion

QR code carriers based on shape memory poly(ester urethane) exhibited staining agent-dependent stabilities against UVA and hydrolytic ageing. From the results of our ageing series we deduce that tags should be black colored due to the higher Michelson contrast

in the QR code region and the longer UVA stability at 23 °C. In such cases, where tags are meant to be exposed to UVA conditions at elevated temperatures, blue tags may constitute the better candidates. Interestingly, 24 h UVA irradiance of blue tags at 23 °C even proved useful to enhance the Michelson contrast by 71% (UV radiant exposure of 3.4 MJ m^{-2}). Independent of the selected ageing conditions, the Michelson contrast turned out to be a reliable indicator for QR code readability; QR codes could be deciphered until C_M dropped below a crucial value of 0.1. Under the most drastic experimental conditions, which led to the malfunction of QR code readability, the thermal and shape memory functionality of PEU remained almost unaffected. As a matter of fact, we conclude that, when handling tags, dye-related ageing effects should be minimized by storing and transporting them in a dry environment with ideally no long exposure to UVA light. With these findings in mind, switchable information carriers can be used for product and brand protection applications.

3.2.6. Acknowledgments

The authors gratefully acknowledge financial support from the German Federal Ministry of Education and Research (BMBF, project funding reference number 03V0043). The authors thank Dr Volker Wachtendorf for fruitful discussions and for providing the setup for artificial UV weathering, Mr Dietmar Neubert for conducting the DSC measurements, Mr Jan Hüttig for tag programming and recovering, and Bayer MaterialScience AG for kindly providing the PEU.

3.2.7. References

1. A. Lendlein and S. Kelch, *Angew Chem Int Ed*, 2002, **41**, 2034-2057.
2. B. Dietsch and T. Tong, *J Adv Mater*, 2007, **39**, 3-12.
3. C. Liu, H. Qin and P. T. Mather, *J Mater Chem*, 2007, **17**, 1543-1558.
4. I. A. Rousseau, *Polym Eng Sci*, 2008, **48**, 2075–2089.
5. J. Leng, X. Lan, Y. Liu and S. Du, *Prog Mater Sci*, 2011, **56**, 1077-1135.
6. L. Sun, W. M. Huang, Z. Ding, Y. Zhao, C. C. Wang, H. Purnawali and C. Tang, *Mater Des*, 2012, **33**, 577-640.
7. K. K. Julich-Gruner, C. Löwenberg, A. T. Neffe, M. Behl and A. Lendlein, *Macromol Chem Phys*, 2013, **214**, 527-536
8. M. Ahmad, J. Luo and M. Miraftab, *Sci Technol Adv Mater*, 2012, **13**, art. no. 015006.
9. J. Hu, M. Harper, L. Guoqiang and S. I. Ibekwe, *Smart Mater Struct*, 2012, **21**, art. no. 053001.

10. H. Purnawali, W. W. Xu, Y. Zhao, Z. Ding, C. C. Wang, W. M. Huang and H. Fan, *Smart Mater Struct*, 2012, **21**, art. no. 075006.

11. S. Wang and J. C. Brigham, *Smart Mater Struct*, 2012, **21**, art. no. 105016.

12. T. Pretsch, M. Ecker, M. Schildhauer and M. Maskos, *J Mater Chem*, 2012, **22**, 7757-7766.

13. D. F. Duxbury, *Chem Rev*, 1993, **93**, 381-433.

14. L. Strekowski, *Heterocyclic Polymethine Dyes*, Springer, Berlin, Heidelberg, 2008.

15. T. Pretsch, I. Jakob and W. Müller, *Polym Degrad Stab*, 2009, **94**, 61-73.

16. A. A. Michelson, *Studies in Optics*, The University of Chicago Press, Chicago, Illinois, 1927.

17. C. S. Schollenberger and F. D. Stewart, *J Elastoplast*, 1971, **3**, 28-56.

18. D. G. Thompson, J. C. Osborn, E. M. Kober and J. R. Schoonover, *Polym Degrad Stab*, 2006, **91**, 3360-3370.

19. W. Müller and T. Pretsch, *Eur Polym J*, 2010, **46**, 1745-1758.

20. K. M. Zia, M. Zuber, M. Barikani, I. A. Bhatti and M. A. Sheikh, *J Appl Polym Sci*, 2009, **113**, 2843-2850.

21. V. Rek and M. Bravar, *Journal of Elastomers and Plastics*, 1983, **15**, 33-42.

22. T. Pretsch, *Polym Degrad Stab*, 2010, **95**, 2515-2524.

23. in Commission Internationale de l'Eclairage [CIE], 1999.

24. T. Pretsch, *Smart Mater Struct*, 2010, **19**, art. no. 015006.

25. C. H. Giles, D. P. Johari and C. D. Shah, *Text Res J*, 1968, **38**, 1048-1056.

26. L. A. Pérez-Estrada, A. Agüera, M. D. Hernando, S. Malato and A. R. Fernández-Alba, *Chemosphere*, 2008, **70**, 2068-2075.

3.3. SUPPLEMENTAL INFORMATION

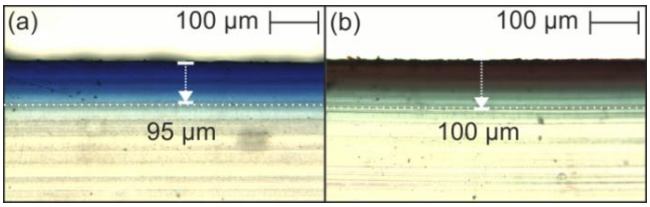

Figure 3.10 Microscopic images of cryomicrotome section profiles of blue (a) and black (b) surface-dyed PEU samples.

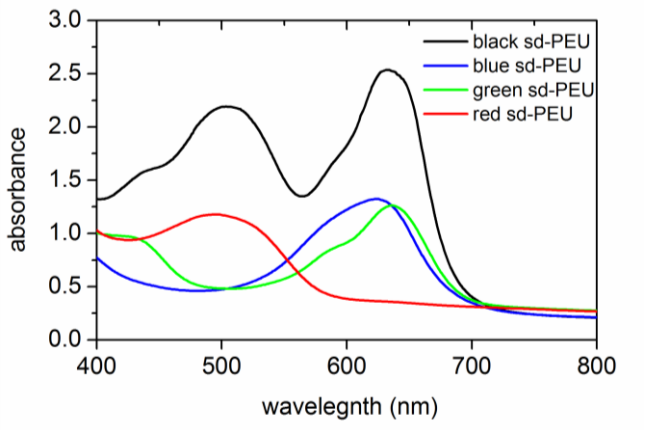

Figure 3.11 Visible absorption spectra of purely black (composed of a *Victoria Blue B*, *Basic Green 1* and *Basic Red 28* mixture), blue (*Victoria Blue B*), green (*Basic Green 1*) and red (*Basic Red 28*) surface-dyed PEU.

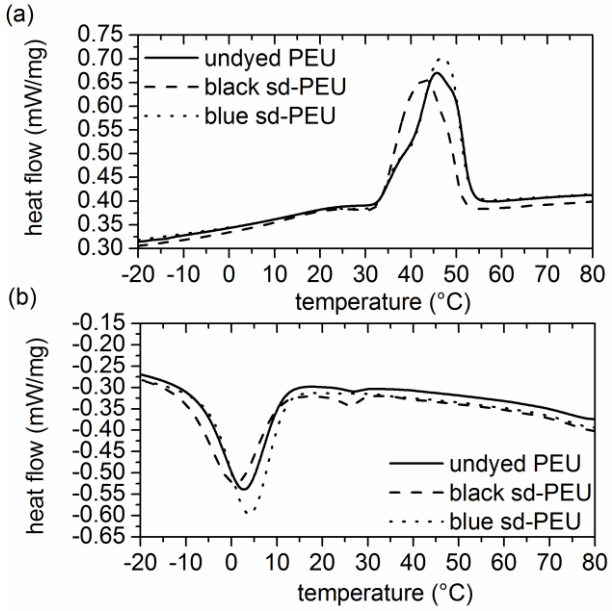

Figure 3.12 DSC thermograms of undyed and black or blue surface-dyed PEU (first heating (a) and cooling (b) scans). The thermograms were obtained from differential scanning calorimetry (DSC) and recorded with a DSC 7020 from Seiko. A specimen, weighing approximately 10 mg, was sealed in a DSC aluminum pan, before it was placed inside the calorimeter. At first, the sample was cooled down to −80 °C, before it was heated to 90 °C. Subsequently, the sample was cooled to −80 °C and heated for a second time to 90 °C. For all measurements, temperature holding times of 5 min at −80 and 90 °C were established and uniform heating and cooling rates of 10 °C min^{-1} selected.

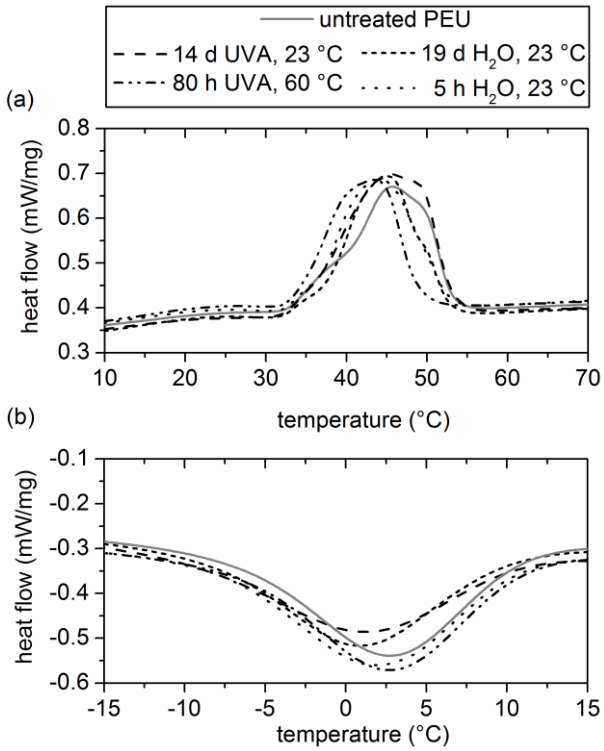

Figure 3.13 . DSC thermograms of differently aged PEU samples. First heating gave broad PBA melting temperatures (a). During first cooling, a characteristic PBA crystallization peak appeared (b). The thermograms were obtained from differential scanning calorimetry (DSC) and recorded with a DSC 7020 from Seiko. A specimen, weighing approximately 10 mg, was sealed in a DSC aluminum pan, before it was placed inside the calorimeter. At first, the sample was cooled down to −80 °C, before it was heated to 90 °C. Subsequently, the sample was cooled to −80 °C and heated for a second time to 90 °C. For all measurements, temperature holding times of 5 min at −80 and 90 °C were established and uniform heating and cooling rates of 10 °C min^{-1} selected.

4. FREELY CONFIGURABLE FUNCTIONALIZATION TOOL FOR SWITCHABLE INFORMATION CARRIERS

The conference proceeding is published as a book section and is reproduced with kind permission from Springer Science+Business Media: M. Ecker and T. Pretsch, In *Materials Challenges and Testing for Manufacturing, Mobility, Biomedical Applications and Climate*, Udomkichdecha, W.; Böllinghaus, T.; Manonukul, A.; Lexow, J., Eds. Springer Berlin Heidelberg, **2014**, ch. 3, pp. 25-35. The original article is online available at: http://dx.doi.org/10.1007/978-3-319-11340-1_3

4.1. EXPERIMENTAL CONTRIBUTION

My contribution for this manuscript comprises:

Conducting the experiments and data analysis, preparation of all figures and writing an early version of the manuscript.

Contributions of co-author:

T. Pretsch: Conception and writing of the manuscript.

4.2. PUBLICATION

4.2.1. Abstract

The selective compression of quick response (QR) and Data Matrix code carriers based on shape memory polymer (SMP) with a freely configurable steel ball type indenter and adjacent thermo-mechanical shape fixing gave notched, room temperature (23 °C) stable, temporary shapes with non-decipherable codes. The microscopic investigation of cryomicrotome sections unveiled indentation-related shape fixities of about 90%. Independent of the selected two-dimensional code, the triggering of the SM effect resulted in sufficient shape recoveries to restore the code readability so that a maximum number of characters including 122 for a QR code (version 7) and 112 in case of a Data Matrix code (version 12) could be read with a scanning and decoding device. Due to the large number of difficult to copy shapes with on demand releasable information, SMPs may serve as viable information carriers for product and brand protection applications.

4.2.2. Introduction

Shape memory polymers (SMPs) are stimuli-responsive materials,[1-4] which can be stabilized in a temporary shape by means of thermo-mechanical treatment (also denoted as “programming” or “functionalization”). The temporary shape is kept by the SMP until the SM effect is triggered by heating the polymer above the switching temperature. As a result, the SMP returns almost completely into the original (permanent) shape. One excellent example for an SMP is phase-segregated poly(ester urethane) (PEU) based on poly(1,4-butylene adipate) (PBA) as soft segment. The physically cross-linked block copolymer combines the advantages of distinct shape memory properties[5-7] with facile surface structuring.[8]

In surface-colored SMPs, two-dimensional (2D) codes like quick response (QR) codes are affine towards distortions, which inhibit their deciphering with a scanning and decoding device.[8] Having this in mind, we prepared switchable information carriers (hereafter also called tags), by laser engraving either a QR or Data Matrix code into a dyed SMP surface and thermo-mechanically functionalized the tags to render the 2D codes temporarily non-readable. Both types of codes are widely-used and decodable in a non-distorted state with a standard scanning and decoding device (smartphone). In contrast to earlier functionalization routes, in which for instance PEU-based QR code carriers were compressed with plane steel plates to randomly distort the overall QR code (version 1) with the aim of rendering it temporarily non-readable, we herein used a freely configurable steel ball type indenter as exclusively developed for a more selective code distortion. Beyond that, we employed QR code version 7 with a much higher data capacity and analyzed the compatibility of the overall SMP Tagnologies™ concept with two versions of Data Matrix codes. In any case, the shape memory effect was finally triggered to efficiently recover the permanent shape and investigate the code readability.

4.2.3. Experiments

4.2.3.1. Materials

Desmopan DP 2795A SMP, which is a poly(ester urethane) (PEU) from Bayer MaterialScience AG, was specially developed for shape memory applications and used as received. The hard segment was composed of 4,4’-methylenediphenyl diisocyanate and a 1,4-butanediol chain extender. The soft segment was based on poly(1,4-butylene adipate) (PBA). The raw material was supplied as cuboidal, injection molded plaques with dimensions of 126 × 52 × 2 mm^3.

4.2.3.2. Sample preparation

The cuboidal PEU plaques were surface-dyed with a black-colored dye solution, consisting of 2 wt% of *N*-[4-[[4-(dimethylamino)phenyl][4-(phenylamino)-1-naphthyl] methylene]-2,5-cyclohexadien-1-ylidene]-*N*-methyl-methanaminium chloride (*Victoria Blue B*; C.I. 44045; CAS 2580-56-5; Sigma Aldrich), 5.5 wt% of [4-[4-(Diethylamino) benzhydrylene]cyclohexa-2,5-dien-1-ylidene]diethylammonium hydrogen sulphate (*Basic Green 1*; C.I. 42040; CAS 633-03-4) and 5.5 wt% of 3-[1,3-dihydro-1,3,3-trimethyl-2H-indol-2-ylene)ethylidene]-9-ethyl-3H-carbazolium chloride (*Basic Red 28*; CAS 72828-91-2), which were completely dissolved in a 1:1 mixture of ethanol (96%, Merck) and acetone (98%, AppliChem). The obtained solution had a dye concentration of 27.9×10^{-2} mol l^{-1}.

The surface-specific dyeing procedure was based on guest diffusion. In the first step, the PEU surface was cleaned with lint-free cloth, before it was pretreated with acetone for about 30 s. Adjacently the black dye solution was pipetted onto the PEU surface and uniformly distributed by means of a brush. After 30 s, the residue of the dye solution was completely removed with another lint-free cloth. In a next step, either a QR or Data Matrix code was engraved into the colored PEU surface. Basically, both code types may hold different numbers of characters, depending on the employed version. For instance, QR code version 1 may hold a maximum of 34 numeric, 20 alphanumeric (consisting of the Latin letters "A to Z" and the Arabic digits "0 to 9") or 14 (8-bit) characters (alphanumeric characters and special characters; each character is encoded as an 8-bit byte), whereas QR code version 7 may store up to 293 numeric, 178 alphanumeric or 122 (8-bit) characters.[9] Likewise, Data Matrix code version 5 may hold a maximum of 36 numeric, 25 alphanumeric or 16 (8-bit) characters, whereas Data Matrix code version 12 is able to store up to 228 numeric, 169 alphanumeric or 112 (8-bit) characters.[10] The engraved, codified information was "BAM QRM-Label" (version 1) and "BAM QRM-Label 123456789 followed by webpage URL[11]" (version 7) for QR codes and "BAM DM-Label" (version 5) same as "BAM DM-Label followed by webpage URL[11] " (version 12) for Data Matrix codes. The QR codes were generated by means of the free application accessible through the website "http://goQR.me" by selecting the error correction level "M" and the Data Matrix codes *via* "http://www.barcode-generator.org". For engraving the black-and-white inverted 2D codes into the colored PEU surface and cutting plaques into squarish (25×25 mm^2) samples, an Epilog Zing 16 laser engraver and cutting machine was used. In order to guarantee a sufficiently high surface contrast, the laser ablation depth was set to exceed the dye diffusion depth.

4.2.3.3. Functionalization and recovering

The programming (functionalization) and recovering of samples was conducted with an electromechanical testing system (MTS Insight 10), which was equipped with a thermochamber (Thermcraft). The heating of the samples was accomplished by two electrical heating elements in the back of the thermochamber. The cooling was achieved by injecting liquid nitrogen from a Dewar vessel into the thermochamber.

For compressive deformation-determined functionalization (CDDF), a freely configurable stainless steel ball type indenter was developed (Figure 4.1).

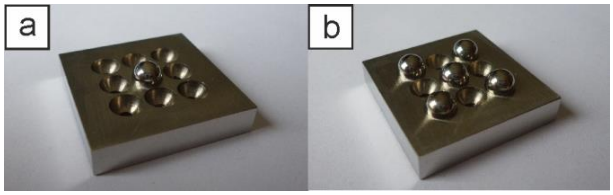

Figure 4.1 Freely configurable stainless steel ball type indenter, occupied by one (a, center position) and five metal balls (b, arranged in an X-shape similar to the five pip side of a Western-style die).

In the stainless steel indenter with a dimensioning of 25 × 25 mm², nine indentations of identical 5 mm diameter and 2.5 mm depth were arranged in a 3 × 3 matrix, so that every indentation could be filled with one stainless steel ball maximum (having a radius of 2.5 mm). The horizontal and vertical distance between the maximum depths of nearby indentations was 5.5 mm. Mathematically speaking, when allocating k balls n positions, the overall number of possible indenter configurations corresponds to the binominal coefficient, indexed by n and k (equation 1):

$$\binom{n}{k} = \frac{n!}{k!(n-k)!} \tag{1}$$

Accordingly, a maximum number of 126 configurations is obtainable both for $k = 4$ and 5 (at $n = 9$). Herein, we focused on two out of 511 possible indenter configurations. In the first one, the center position was occupied by one steel ball, whereas in the second configuration, five steel balls were arranged in an X-shape similar to the five pip side of a Western-style die (**Figure 4.1**). In this regard, we would like emphasizing that the indenter dimensioning was selected in compliance with the tag size and thus with the QR and Data Matrix code areas.

In the given setup, the deformable areas of the PEU were thus predetermined by the selected number of steel balls and their positions. The PEU sample was always placed exactly in the same way atop the configurable indenter with the steel ball(s) pointing towards the colored PEU surface (**Figure 4.2**). In this connection, aluminum foil was used for a proper adjustment. The indenter and PEU sample were positioned between the upper and lower steel plates, which in turn were connected to the rods of the electromechanical testing system.

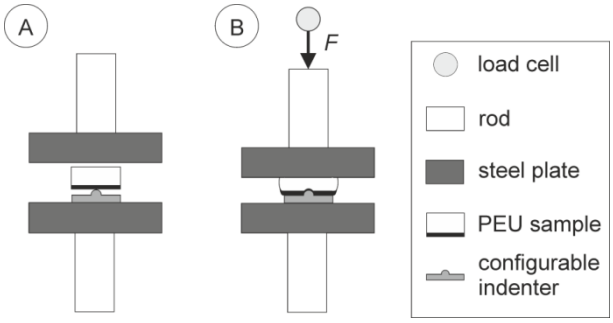

Figure 4.2 Schematic setup for CDDF of PEU samples: (A) before and (B) after loading.

In order to assure that the PEU sample and the indenter did not alter position, an initial force of 10 N was applied prior to heating the polymer with a rate of 4.3 °C min^{-1} to 80 °C and thus above the PBA melting transition (which was close to 40 °C[8]). After 5 min at 80 °C, the sample was compressed with a rate of 100 N min^{-1} to the maximum force F_{max}, which was chosen in accordance with the selected indenter configuration (one ball: F_{max} = 60 N; five balls: F_{max} = 300 N). In order to fix the polymer in the temporary shape, F_{max} was maintained during cooling the PEU sample with a rate of 5.3 °C min^{-1} to −20 °C and thus below the PBA crystallization temperature (around 0 °C[8]). After 5 min at −20 °C, the steel ball indented (notched) PEU sample was unloaded with a rate of 500 N min^{-1} to finalize shape programming, before it was heated to 23 °C. In order to trigger the shape memory effect and recover the original shape, the PEU was reheated to 80 °C and kept at that temperature for 5 min. Finally, the sample was cooled to 23 °C.

4.2.3.4. Scanning and decoding

A Samsung Galaxy S I9000 smartphone equipped with the software "Barcode Scanner" version 4.1 from Zxing Team was used as scanning and decoding device. The 2D codes were scanned after the preparation, functionalization and recovering of the information carriers (tags).

4.2.3.5. Indentation-related shape memory properties

Microscopic investigations were carried out on cryomicrotome sections (prepared at −20 °C) of black surface-dyed PEU, both after the functionalization and recovering of the sample. For a first microscopic image, the steel ball indented (notched), programmed polymer was cut perpendicular to the dyed surface and exactly through the indentation maximum with a cryomicrotome CM1950 from Leica. Then, the polymer was heated to 80 °C and kept at that temperature for 5 min to recover the permanent shape, before one further microscopic image was taken. In any case, a Wild M5A stereo microscope with 6 times optical zoom and the associated Dietermann and Heuser Solution GmbH (dha) software (version 13) were used. From the obtained photographs the steel ball indentation depth and the dye diffusion depth were determined with the graphical program ImageJ (developed at the National Institutes of Health, USA). For latter, the darkest point at the surface was set as standard and the intensity decline down to a loss of 70% was measured. The corresponding distance to the surface was defined as dye diffusion depth.

Independent of the employed one or five steel ball type indenter, the indentation-related shape memory properties of the PEU were quantified. In the initial state, the PEU was characterized by a sample height h_0 of 2 mm. The steel ball penetration depth h_p as directly determined from crosshead displacement, the maximum indentation depth ($h_0 - h_t$), corresponding to the lowest sample height in the temporary state, the extent of indentation recovery ($h_r - h_t$) and the maximum height of protrusive bumps ($h_b - h_0$) in the temporary and recovered state were determined (**Figure 4.3**).

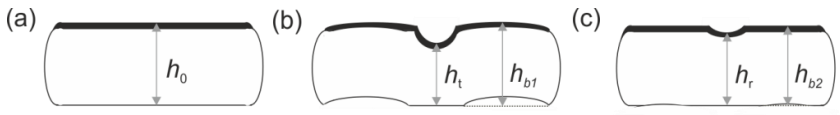

Figure 4.3 Side view of a schematic cross-section through the permanent (a), the temporarily fixed (b, as characterized by one indentation surrounded by a protrusive bump) and recovered shape (c) of a PEU sample.

Accordingly, we defined the indentation depth-related ratios of shape fixity R_f and shape recoverability R_r in equations 2 and 3:

$$R_f = \frac{h_0 - h_t}{h_p} \cdot 100 \qquad (2)$$

$$R_r = \frac{h_r - h_t}{h_0 - h_t} \cdot 100 \quad (3)$$

4.2.4. Results and Discussion

First of all, the PEU surface was colored with the three-component black dye solution, consisting of two triarylmethane dyes (*Victoria Blue B* and *Basic Green 1*) and the hemicyanine dye *Basic Red 28*. As verified by cryomicrotome sections (not shown herein), the black-coloring of the PEU resulted in homogenous dye diffusion depths of around (95 ± 5) µm. The amount of dye inside the polymer surface was (0.13 ± 3) wt%.

To elucidate the indentation-related shape memory properties of the black surface-dyed PEU, a cryomicrotome section was microscopically investigated in the steel ball indented, temporarily fixed state and after the almost complete return of the polymer into the permanent shape due to triggering the shape memory effect. When using a one steel ball type indenter, the functionalized state was characterized by one spherical indentation with a depth ($h_0 - h_t$) = (1.50 ± 0.02) mm (**Figure 4.4**), which was close to the steel ball penetration depth of (1.67 ± 0.05) mm. Accordingly, the shape fixity ratio R_f was (90 ± 3)%.

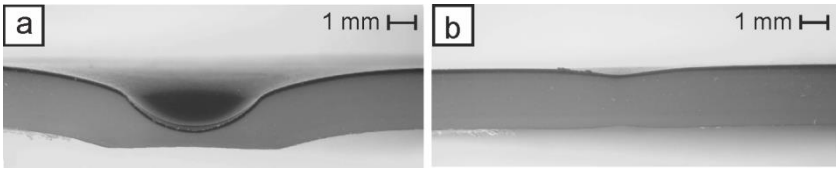

Figure 4.4 Microscopic image of a cryomicrotome section of black surface-dyed PEU, showing the polymer in the temporary shape (a, functionalized *via* the one steel ball type indenter) and recovered shape (b).

In parallel, a homogenous circular protrusive bump formed around the indentation with a maximum height ($h_{b1} - h_0$) = 0.5 mm. The indentation-related phenomenon of protrusive bump formation is fairly well known from shape memory polymers like styrene-based block copolymer.[12-14] The triggering of the shape memory effect mostly led to the recovery of the indentation together with the almost complete disappearance of the protrusive bump as evidenced by a negligible residue of ($h_{b2} - h_0$) = (0.01 ± 0.02) mm. Beyond that, an R_r ratio of (79 ± 2)% could be detected. Latter is in accordance with the tensile-related shape memory properties of the PEU (R_r = 77%[6]). In agreement with the findings obtained from the one steel ball type indenter, using five steel balls instead at a fivefold compressive force gave similar indentation geometries (**Figure 4.5**).

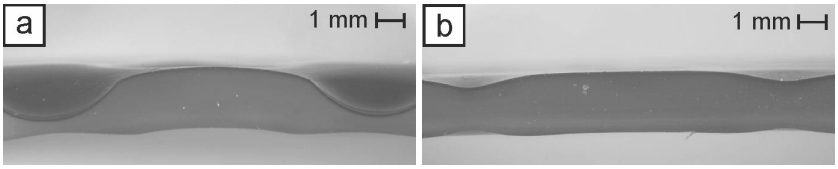

Figure 4.5 Microscopic image of a cryomicrotome section of black surface-dyed PEU, showing the polymer in the temporary shape (a, functionalized *via* the five steel ball type indenter) and recovered shape (b).

The averaged data per indentation included a depth ($h_0 - h_t$) = (1.50 ± 0.03) mm and an R_f ratio of (89 ± 3)%. Upon triggering the shape memory effect, the protrusive bumps also disappeared almost completely, giving small averaged residues of ($h_{b2} - h_0$) = (0.01 ± 0.02) mm and an R_r value of (71 ± 2)%.

One further finding included that functionalizations with the freely configurable steel ball type indenter resulted in puncture, when the applied compressive force exceeded a crucial value of 200 N per indentation. For instance, transferring 1000 N *via* the five steel ball type indenter onto the PEU favored the formation of five holes equal in diameter (1.1 mm) and located in the non-dyed backside of the polymer sample. Once heated to 80 °C, a distinctive shape recovering of the PEU took place, which was accompanied by the shrinkage of the voids to an averaged diameter of 0.4 mm (not shown herein).

The above presented results undoubtfully document the distinct shape memory properties of PEU and imply that the material is an appropriate candidate for discrete surface modifications. Therefore we functionalized switchable information carriers (tags) *via* the freely configurable steel ball type indenter. The employed 2D codes included in each case two QR and Data Matrix codes of different versions (**Figure 4.6**).

At first, the tags were programmed with the one steel ball type indenter as described above for the solely surface-colored PEU. We found that in case of QR codes, the exact position of indentation played a major role. Here, the QR codes could be rendered temporarily non-readable through the deformation of one of the three position detection patterns, which had a dimensioning of 5.0 × 5.0 mm² (QR code version 1) and constituted distortion-sensitive areas. In all other scenarios, arbitrary deformations were applied with the one steel ball type indenter and fixed, but the QR codes remained decipherable.

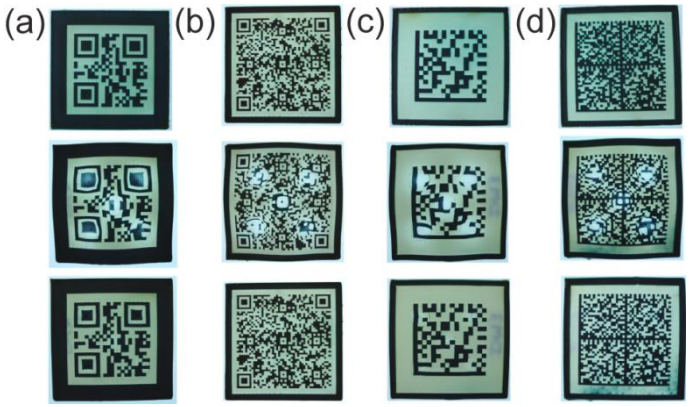

Figure 4.6 Smart tags with QR (a and b) and Data Matrix codes (c and d). The respective 2D codes include version 1 (a), 7 (b), 4 (c) and 12 (d). Each of the tags is exhibited in the original (top), temporarily fixed (center) and recovered state (bottom).

By contrast, the position detection pattern in Data Matrix codes is composed of two so-called "search lines", which could not be strongly enough distorted by the one steel ball type indenter. Thus, Data Matrix codes remained decipherable, independent of which code area was indented. Neglecting the presence of protrusive bumps atop, the overall deformed code areas were within the high error tolerance of the different 2D code versions (**Table 4.1**).

Finally, we investigated the programming efficiency of our five steel ball type indenter. As a result of functionalization, every single code turned non-readable even though the position detection patterns of QR code version 7 were only slightly distorted. Both in case of QR and Data Matrix codes, the distorted area exceeded the error tolerance values of the employed codes (**Table 4.1**). Finally, the shape memory effect was triggered, which coincided with the restoration of the 2D code machine-readability.

Table 4.1 Error tolerance of QR and Data Matrix codes towards real code distortion (the data were taken from Ref.[9,10]) and relative deformation of the code areas through the employed one and five steel ball type indenter.

Code type	Code version	Code area in the permanent shape [mm²]	Error tolerance [%]	Overall code deformation by one indentation [%]	Overall code deformation by five indentations [%]
QR-M	1	15 × 15	15	9	44
QR-M	7	20 × 20	15	5	25
Data Matrix	5	15 × 15	43.8	9	44
Data Matrix	12	18 × 18	29.6	6	30

4.2.5. Conclusions

The freely configurable steel ball type indenter turned out to be an appropriate tool to obtain selectively modified temporary shapes in information carries based on poly(ester urethane) as shape memory polymer. In particular, the deformation of the QR code position detection pattern in code version 1 and 7 as simply achievable with a one steel ball type indenter and the more general approach of exceeding the deformation-compensable barrier in both QR and Data matrix codes gave notched, room temperature (23 °C) stable, temporary shapes with non-readable 2D codes. In parallel, the formation of protrusive bumps may have additionally contributed to render the 2D codes temporarily non-readable. Once functionalized *via* the five steel ball type indenter, the information carriers could reliably be switched from non-readable to readable, independent of the investigated code type and version. The use of SMP Tagnologies™ in manifold ways illustrates the huge potential for product and brand protection applications.

4.2.6. Acknowledgments

The authors gratefully acknowledge financial support from the German Federal Ministry of Education and Research (BMBF, project funding reference number 16V0043). Mr. Miteshkumar Patel is acknowledged for programming and recovering the information carriers. The authors thank Bayer MaterialScience AG for kindly providing the PEUs.

4.2.7. References

1. J. Leng, H. Lu, Y. Liu, W. M. Huang and S. Du, *MRS Bull.*, 2009, **34**, 848-855.
2. W. M. Huang, Z. Ding, C. C. Wang, J. Wei, Y. Zhao and H. Purnawali, *materialstoday*, 2010, **13**, 54-61.
3. T. Pretsch, *Polymers*, 2010, **2**, 120-158.
4. M. Behl, J. Zotzmann and A. Lendlein, *Adv Polym Sci*, 2010, 1-40.
5. T. Pretsch, Proceedings of the 1st Workshop for Young Materials Scientists, Tsukuba (Japan), 2008.
6. T. Pretsch, I. Jakob and W. Müller, *Polym Degrad Stab*, 2009, **94**, 61-73.
7. W. Müller and T. Pretsch, *Eur Polym J*, 2010, **46**, 1745-1758.
8. T. Pretsch, M. Ecker, M. Schildhauer and M. Maskos, *J Mater Chem*, 2012, **22**, 7757-7766.
9. ISO, International Organization for Standardization, Geneva, Switzerland, 2000, vol. ISO/IEC 18004:2000I.

10. ISO, International Organization for Standardization, Geneva, Switzerland, 2006, vol. ISO/IEC 16022:2006I.

11. BAM - Shape Memory Polymers, *http://www.bam.de/en/kompetenzen/fachabteilungen/abteilung_6/fg65/fb65_formgedaechtnispolymere.htm*

12. N. Liu, W. M. Huang, S. J. Phee, H. Fan and K. L. Chew, *Smart Mater Struct*, 2007, **16**, N47-N50.

13. N. Liu, Q. Xie, W. M. Huang, S. J. Phee and N. Q. Guo, *J Micromech Microeng*, 2008, **18**, art. no. 027001.

14. N. Liu, W. M. Huang, S. J. Phee and T. H. Tong, *Smart Mater Struct*, 2008, **17**, art. no. 057001.

5. MULTIFUNCTIONAL POLY(ESTER URETHANE) LAMINATES WITH ENCODED INFORMATION

The article: M. Ecker and T. Pretsch, *RSC Adv.*, **2014**, *4* (1), 286-292 and the corresponding graphical abstract (**Figure 5.1**) are reproduced by permission of The Royal Society of Chemistry. The original is online available at: http://dx.doi.org/10.1039/C3RA45651J

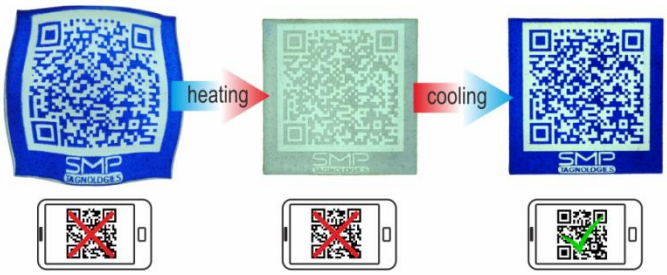

Figure 5.1 Visual summary of the main findings of the article (graphical abstract) as visible on the webpage of RSC Advances in connection with the abstract of the article.

5.1. EXPERIMENTAL CONTRIBUTION

My contribution for this manuscript comprises:

Experimental contributions, data analysis, preparation of the figures and writing an early version of the manuscript.

Contribution of co-author:

T. Pretsch: Conception and writing of the manuscript.

5.2. PUBLICATION

5.2.1. Abstract

Solvent-cast films from shape memory poly(ester urethane) (PEU) containing different weight contents of microencapsulated thermochromic pigments (T-PIGs) were prepared by drying in air. Spectrophotometric investigations unveiled that gradual loading with T-PIG black resulted in continuous darkening of the films up to filler contents of 20 wt%, accompanied by a steady enhancement of thermochromic properties. Taking this composition as standard, PEU films equipped with T-PIG black, blue and red were

deposited atop PEU plaques to obtain laminate structures. Herein, the cover layer thickness (100 ± 5 µm) and the good dispersion of T-PIGs inside the polymer matrix were verified by scanning electron microscopy. Machine-readable information carriers were prepared by laser engraving quick response (QR) codes into the cover layer of the laminates and subsequently cutting cuboidal samples therefrom. Finally, thermo-mechanical programming of the QR code carriers was applied to randomly distort the code patterns, thus rendering them unreadable. Upon heating, surface decolorization and shape recovering occurred; during the ensuing cooling, the surface color and contrast reappeared whereupon the QR codes could be read out. Spectrophotometric, calorimetric and thermo-mechanical investigations gave evidence that the color switching temperature of the T-PIGs roughly coincided with the melting temperature of the ester-based switching segment and thus with the activation temperature of the shape memory effect. Apart from that unique functionality, manifold design concepts may render information carriers difficult-to-copy. Therefore, we anticipate tremendous potential as anti-counterfeiting technology.

5.2.2. Introduction

Shape memory polymers (SMPs) belong to the class of smart materials. Once thermo-mechanically programmed (functionalized), a temporary shape is maintained until the shape memory effect (SME) is thermally triggered, which usually results in the almost complete recovering of the permanent shape. When equipped with appropriate fillers, exposure to an alternating magnetic field or the application of an electrical current even enable an indirect triggering of the thermally induced SME.[1-4] Further stimuli include light (in case of photoresponsive SMPs)[5] and the diffusion of low molecular weight plasticizers into SMPs.[6,7] Shape memory polymers and their composites have become increasingly important in the past few years;[8-14] various examples of use indicate a blurring of the borderline between research and applications.[15-24]

Physically cross-linked block copolymers like poly(ester urethane) (PEU) may have distinct shape memory properties. In such phase segregated systems, hard segments act as netpoints whereas soft segments serve as mobile phase.[25,26] Depending on the underlying thermal transition and programming conditions like deformation and shape fixity temperature, PEU can change shape as a result of soft segment devitrification and melting.[27] One further advantage of PEU consists in a chemically tunable soft segmental

melting transition, which can be set *e.g.* at around 40 °C and thus slightly above room temperature.[28]

Recently, Desmopan DP 2795A SMP, a PEU from Bayer MaterialScience AG, proved to be particularly suitable as base material for switchable information carriers.[29] For instance, two-dimensional (2D) codes like quick response (QR), Data Matrix and Aztec can be engraved into surface-dyed PEU plates. When subsequently programmed, these codes become unreadable and keep that state until the SME is triggered by heating, whereupon the encoded information can be easily read out with a scanning and decoding device. So far, reliable shape change behavior grants access to hitherto hidden or distorted information, which qualifies information carriers as useful technology for anti-counterfeit product verification and identification.[30]

In search of one further, thermo-responsive security feature, fitting well to our information carrier concept, we became aware of thermochromic dyes.[31,32] Microencapsulated thermochromic pigments (T-PIGs) may turn colorless when heated above the color switching temperature (CST) and regain color upon cooling below that temperature.[33] When utilizing melamine resin as polymeric shell material, the coloring components may include an electron-donating, chromogenic organic compound (color former, in our case leuco dye) and an electron-accepting agent (developer, commonly a weak organic acid like hexa- or octadecanol); in addition, a solvent (long chain alkyl alcohol, ester or acid) is used as matrix component (**Figure 5.2**).[34,35]

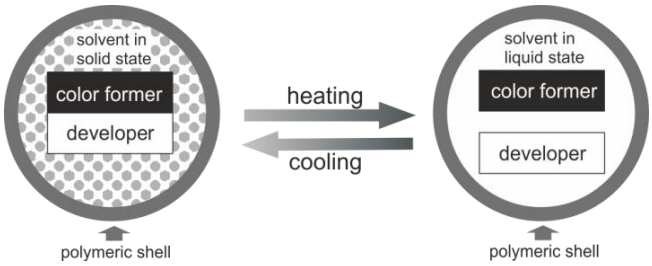

Figure 5.2 Simplified working principle of thermoreversible color changes in microencapsulated T-PIGs: The polymeric microcapsules remain in a colored state as long as the solvent does not inhibit electronic interaction between color former and developer.

Since the thermochromic mixture usually contains about 75–95 mol% solvent (only low concentrations of color former, usually about 1 mol%, are needed due to the high extinction coefficient of the dye), the melting and crystallization points of the solvent largely control that of the mixture.[36] Below the solvent melting temperature, the coloring components of thermochromic leuco dye-developer-solvent systems electronically

interact, forming an extended conjugated π-electron system.[37] Upon a temperature increase above the solvent melting transition, the color-forming components get separated from each other, whereupon electronic interaction is inhibited, thus rendering the microcapsules achromatic.[38,39] Reliable color switch functionality is ensured as long as the protective polymeric microcapsules remain undamaged.

In this contribution, we aimed at bringing together both functionalities in one and the same system – shape memory behavior and thermochromism. Therefore, we developed pastes, containing PEU as SMP, T-PIGs and a solvent for PEU. In contrast to recent research efforts by Jinlian Hu and her colleagues, who elegantly took advantage of the adhesiveness of (achromatic) urethanebased solutions by connecting two layers of urethane-based SMP, one programmed the other one in permanent shape,[40,41] we will demonstrate that paste preparation is a useful technique to obtain thermochromic films, which may even be tightly connected to PEU plaques, forming structurally stable laminates. These polymer bilayer structures were taken as basis to produce QR code carriers therefrom, characterized by an exceptional combination of shape memory and color switch functionality.

5.2.3. Experimental Section

5.2.3.1. Fabrication methods

Desmopan DP 2795A SMP, a poly(ester urethane) (PEU) from Bayer MaterialScience AG, was used as base material for the fabrication of multifunctional information carriers. The hard segments were composed of 4,4′-methylenediphenyl diisocyanate and 1,4-butanediol as chain extender. The soft segments were based on poly(1,4-butylene adipate) (PBA). The raw material was supplied both as pellets and cuboidal, injection molded plaques with dimensions of 126 mm × 52 mm × 2 mm.

At first, different PEU pastes, containing microencapsulated thermochromic pigment powder (T-PIG, Sintal Chemie GmbH) of black, blue or red room temperature color, were prepared. The mass densities of the T-PIGs were 0.26 g cm^{-3}. For paste preparation, 5 g of PEU were dissolved in 15 ml of *N*-methyl-2-pyrrolidone (NMP), before 1.25 g of T-PIG was added to the viscous solution. The obtained liquid paste was well stirred for 5 min to homogenously disperse the T-PIG. Following a solvent casting approach, the paste was either layered atop glass plates to prepare PEU films filled with T-PIG black, blue and red or layered atop PEU plaques to fabricate laminate structures. Here, an applicator

was used to homogeneously distribute the liquid paste on the upper PEU surface, before drying on air at 23 °C was carried out for about 18 h. A CO_2 laser was used to fabricate information carriers therefrom. The main steps included engraving a QR code into the pigment-containing PEU layer and cutting cuboid samples with a dimensioning of 25 mm × 25 mm × 2 mm. In order to ensure sufficiently high surface contrast in the obtained QR code carriers at room temperature, the laser ablation depth was set to exceed the deposition height of the cover layer. In all cases, the QR codes carried the encoded information http://www.bam.de/en/kompetenzen/fachabteilungen/abteilung_6/fg65/fb65_formgedaechtnispolymere.htm.

5.2.3.2. Characterization methods

A scanning electron microscope (SEM) was used to study both the shape and size distribution of the T-PIGs and the surface morphology of the laminates. For this purpose, a Zeiss Gemini Supra 40 device, operating at an extra high tension of 10 kV, was employed. By means of a sputtering system, powdery T-PIGs were coated with a few nanometers thin carbon layer, whereas the laminates were coated with a thin layer of gold. Cross-sections of the laminates were prepared at −20 °C using a Leica CM1950 device. The size distribution of the T-PIGs was determined from scanning electron micrographs. By standard, 500 particles were analyzed with the program ImageJ.

Spectrophotometric investigations were conducted with the modular spectrometer system MultiSpec UV–VIS–NIR from tec5. The experimental setup is provided by **Figure 5.10**, ESI†. The spectrometer operated in the wavelength scan range between 730 and 360 nm. The reflection properties of PEU films loaded with T-PIG black, blue and red were determined at different temperatures, 50% air humidity and a measuring geometry of 45°/0°. Inside the climate chamber (VCL 4006, Vötsch Industrietechnik GmbH), the loaded films were heated from 23 to 55 °C with rates of 0.4 °C min^{-1}, before they were cooled to 23 °C with rates of 0.3 °C min^{-1}. The sample temperature was followed with a Pt100 temperature sensing device, which was connected to the backside of each sample. To ensure efficient heat transfer, a heat-conductive paste (Keratherm KP12) was used at the contact areas. The D65 standard illuminant and 2° standard observer were selected to determine the colorimetric properties of the samples from the reflectance data by using the mathematically defined CIE 1976 $L^*a^*b^*$ (CIELAB) color

space.[42-44] From the CIELAB values, the temperature-dependent color difference ΔE as defined in eqn (1) was calculated for PEU films loaded with T-PIG black, blue and red.

$$\Delta E = \sqrt{(L^* - L^*_0)^2 + (a^* - a^*_0)^2 + (b^* - b^*_0)^2} \qquad (1)$$

The ΔE values were determined with reference to the CIELAB values at the respective starting temperatures, which were 23 °C on heating and 55 °C on cooling. The color switching temperature (CST) was defined as that temperature, at which the strongest change in ΔE occurred, coinciding with the peak maximum in the $\Delta E/\mathrm{d}T$ derivative.

The mechanical properties of solvent-cast, non-loaded PEU films and solvent-cast PEU films loaded with 20 wt% of T-PIG black were investigated with an MTS Insight 10 electromechanical testing system. The studied films had a dimensioning of 50 mm × 5 mm × 0.1 mm. The tensile tests were carried out 72 h after film preparation. The films were clamped, using a clamping distance of 10 mm, and stretched at 23 °C with a deformation rate of 30 mm min^{-1} until failure occurred. The tensile data was averaged from three independent measurements.

Differential scanning calorimetry (DSC) was used to characterize both as-received powdery T-PIGs and solvent-cast films of PEU and PEU loaded with T-PIGs, respectively. The measurements were carried out with a DSC 7020 from Seiko. Initially, a sample, weighing approximately 5 mg, was sealed in a DSC aluminum pan, before it was placed inside the calorimeter. The sample was cooled down to −80 °C, before it was heated to 90 °C. Subsequently, the sample was cooled to −80 °C and heated for a second time to 90 °C. For all measurements, temperature holding times of 5 min at −80 and 90 °C were selected and uniform heating and cooling rates of 10 °C min^{-1} chosen.

To determine the surface contrast in multifunctional QR code carriers, color images were taken and converted into grayscale histograms by using the image analysis program ImageJ.[45] From these results, the Michelson contrast C_M between surface-colored regions (containing T-PIG) and laser-ablated regions (PEU substrate) was determined at 23 and 60 °C. For this purpose, C_M was defined as relation between the difference and the sum of the highest and lowest luminance L_{max} and L_{min}, differing in grayscale value (GSV).[46]

The programming of multifunctional QR code carriers was carried out with an MTS Insight 10 electromechanical testing system, which was equipped with a Thermcraft

thermochamber. Heating of the information carriers was accomplished by two electrical heating elements in the back of the thermochamber, whereas cooling was achieved by injecting liquid nitrogen from a Dewar vessel into the thermochamber. For simplicity a recently introduced programming method (compressive deformation-determinated functionalization[29]) was used. In the experimental setup, the multifunctional QR code carrier was positioned in the center of an unmovable pressure plate with its laser engraved site pointing toward a second pressure plate, which was connected over steel rods to the above moveable crosshead. After applying an initial force of −10 N, the information carrier was heated from 23 to 80 °C with a rate of 4.3 °C min^{-1} and thus above the DSC melting peak offset of the PBA phase (which was close to 50 °C).[47] After 5 min at 80 °C, the QR code carrier was loaded with a crosshead displacement rate of 0.5 mm min^{-1} up to a maximum force F_{max} of 3 kN. In order to fix the temporary shape, characterized by a strongly distorted QR code pattern, F_{max} was maintained during cooling with a rate of 5.3 °C min^{-1} to −20 °C and thus below the DSC crystallization offset temperature of the PBA phase transition (around −10 °C).[47] After 5 min at −20 °C, the QR code carrier was unloaded with a rate of 500 N min^{-1}, before it was heated to 23 °C. In order to trigger the shape memory effect and recover the original shape, the PEU was reheated to 80 °C and kept there for 5 min. Finally, the QR code carrier was cooled to 23 °C.

The machine-readability of freshly prepared, programmed and recovered multifunctional QR code carriers was investigated with a Samsung Galaxy S I9000 smartphone, equipped with the software “Barcode Scanner” version 4.2 from Zxing. Most often, the QR codes were scanned at 23 and 60 °C, thus at temperatures below and above the CST of the T-PIG.

5.2.4. Results and Discussion

First of all, we investigated the shape and size distribution of as received powdery T-PIGs, which we later used as filler materials for PEU. A detailed view on the surface morphology of the polymeric microcapsules is provided by **Figure 5.3**.

The SEM image clearly reveals microcapsules of spherical geometries, characterized by a polydisperse size distribution, spreading from 0.3 to 10 mm. The mean particle size was about 1.8 mm. A similar size distribution could be detected for as-received T-PIG blue; in case of T-PIG red, the average particle size was lowest (**Figure 5.11**, ESI†).

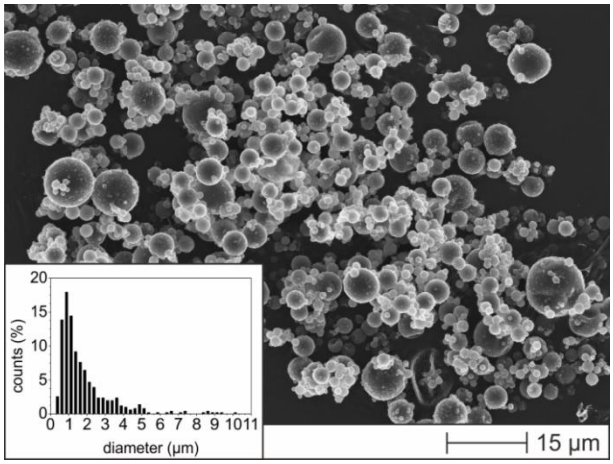

Figure 5.3 SEM image of as-received powdery T-PIG black; the inset gives the size distribution of the microcapsules.

In a next step, PEU pastes with various contents of T-PIG black were prepared and layered atop glass plates. Evaporation of the solvent NMP resulted in the formation of homogenously colored films, whose room temperature color intensity grew with rising filler contents. All films had in common, that uniform discoloration was detected upon heating to 60 °C (**Figure 5.4**).

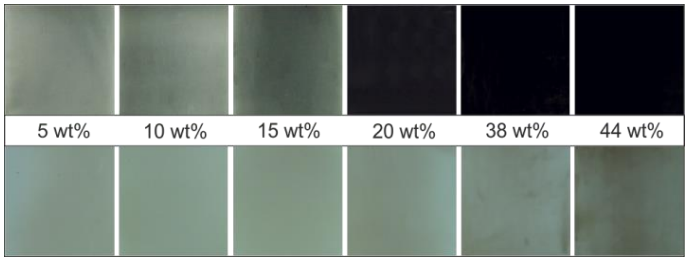

Figure 5.4 Thermochromic PEU films with different weight contents of T-PIG black at 23 °C (image series above) and at 60 °C (image series below). The films were deposited on a glass substrate and had uniform thicknesses of (95 ± 10) µm.

The reversible nature of color switching between the black and colorless dye forms was proven in ten successive thermal cycles.

In a subsequent step, the thermochromic films were spectrophotometrically investigated at 23 °C. As evidenced by the evolution of CIELAB lightness L^* (**Figure 5.12**, ESI†), gradual loading with T-PIG black resulted in a continuous darkening of the films up to filler contents of 20 wt%. Here, the difference in lightness was strongest, tantamount to highest contrast between the unloaded and loaded PEU forms. This finding suggests a promising composition to realize distinct thermochromic effects. Therefore, we decided to prepare PEU films, containing 20 wt% of T-PIG black, blue and red, and to investigate

them in continuative studies. Before concentrating on the functional performance of the employed fillers, we carried out tensile tests on solvent-cast PEU films. As expected, adding 20 wt% of T-PIG black to the PEU matrix resulted in a substantial enhancement in mechanical properties. Compared to non-loaded PEU film, increases in Young's modulus (from 2.7 ± 1.1 to 44.7 ± 9.0 MPa), ultimate tensile strength (from 4.6 ± 1.2 to 16.1 ± 2.2 MPa) and toughness (from 32.3 ± 8.4 to 138.2 ± 17.4 MJ m^{-3}) could be detected. Thus, the above selected composition proved also useful from a mechanical point of view. Next, we investigated the temperature-dependent colorimetric properties of our loaded PEU films (**Figure 5.13**, ESI† and **Table 5.1**).

Table 5.1 Color switching temperatures (CSTs) of PEU films, loaded with 20 wt% T-PIG black, blue or red (thickness = (95 ± 10) µm). The onset, peak maximum and offset CSTs are given for heating and cooling.

T-PIG	CST (heating)			CST (cooling)		
	onset (°C)	max. (°C)	offset (°C)	onset (°C)	max. (°C)	offset (°C)
black	31	38	43	40	32	30
blue	26	40	45	40	34	30
red	29	42	47	40	33	24

As effectively controlled by the solvent melting and crystallization behavior inside the polymeric microcapsules, the films decolorized upon heating at temperatures between 43 and 47 °C and regained their original color on cooling at temperatures between 30 and 24 °C.

Another important aspect in the investigation of functional polymer films is their calorimetric properties, which have been determined by DSC (**Figure 5.5**).

In the DSC thermograms, the peak positions of the endo- and exothermic signals of PEU film exemplarily loaded with 20 wt% of T-PIG black only slightly deviated from those taken from solvent-cast, non-loaded PEU film and as-received powdery T-PIG black. Similarly characteristic melting and crystallization patterns were detected in the respective thermograms of PEU loaded with T-PIG blue and red (**Table 5.2**, ESI†).

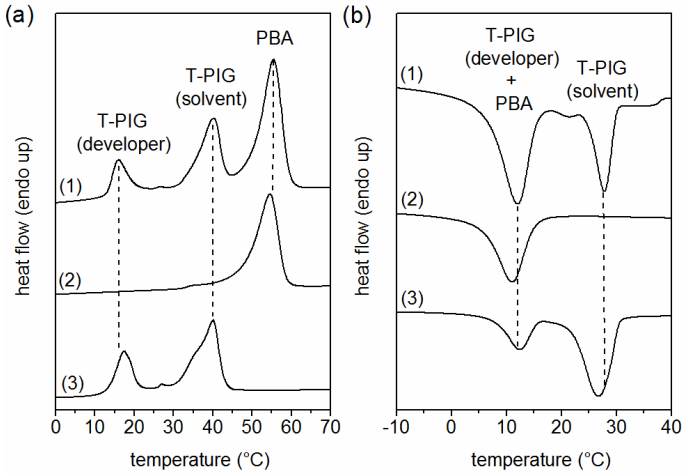

Figure 5.5 First DSC heating (a) and cooling (b) of solvent casted PEU film loaded with 20 wt% of T-PIG black (1). For comparison, DSC data is also provided for solvent casted, non-loaded PEU film (2) and as-received powdery T-PIG black (3).

In detail, the DSC melting and crystallization peak temperatures of the PBA phase were detected at around 55 and 11 °C. Compared to the phase transition temperatures of injection molded PEU plaques,[47] the values were slightly raised, suggesting that processing affected the thermal stability of the PBA phase. Independent of the filler content, loading PEU films with T-PIG black resulted in slightly decreased PBA melting enthalpies and therefore reduced PBA crystallinities (**Table 5.2**, ESI†). Obviously, the interaction of the melamine microcapsules with PBA chains restricted segmental motions and therefore promoted non-crystalline PBA conformations. It is reasonable to expect that physical adsorption of PBA chains to the melamine shell of the microcapsules can slow down the polymer dynamics, which might also result in an increase in the PBA glass transition temperature.[48] Nevertheless, there was no clear hint therefore, since T_g (PBA) was approximately −44 °C for both loaded and unloaded PEU. In the DSC thermograms, the remaining signals were attributed to solvent phase changes inside the thermochromic microcapsules. Herein, the solvent melted at 40 °C and crystallized at 28 °C as indispensable for the reliable color switch functionality of the T-PIGs and in pretty good agreement with our colorimetric results (**Table 5.1**). The mean size of the microcapsules is known to affect the crystallization behavior of solvents like *n*-octane in DSC studies.[49] However, in our case the absolute difference in average particle size was 0.6 µm (**Figure 5.11**, ESI†) and appeared to be too small to influence the phase transition behavior of the solvent in T-PIG black, blue and red (**Table 5.2**, ESI†). Beyond that, heating- and cooling-related signals at 19 and 13 °C were attributed to the melting and crystallization of the weak organic acid (developer).

To fabricate laminate structures, PEU plaques were coated with thermochromic PEU pastes containing 20 wt% of micron-size fillers. A representative SEM image of the cover layer and its transition zone with the PEU substrate is provided by **Figure 5.6**.

The cover layer thickness was about (100 ± 5) µm. On closer consideration, almost spherical and randomly distributed cavities are visible, which we assigned to those volumes filled with T-PIGs (SEM images of solvent-cast PEU did not exhibit cavities at all). In other words, the applied solvent casting technique and the selected filler/matrix ratio ensured a fairly good dispersion of functional dye inside the PEU matrix. The diameters of the cavities spread from 1 to 8 µm and were thus in the same range as the size distribution of the microcapsules (**Figure 5.3**). At a higher resolution, even the walls of the microcapsules, which were cut open in course of cryomicrotome sectioning, could be visualized (marked by arrows in **Figure 5.6**). It is remarkable that no sharp interface between the PEU substrate and the cover layer could be detected, implying that a tightly connected bilayer structure was formed.

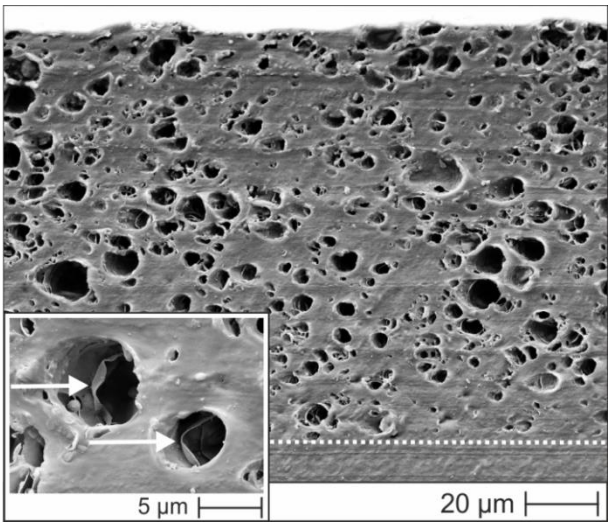

Figure 5.6 SEM image showing the cryomicrotome section profile of a PEU cover layer filled with T-PIG black (~ upper 100 µm cutout, above the dotted line) atop PEU plaque (~ lower 10 µm cutout, below the dotted line). The inset shows highly resolved cavities.

Finally, we prepared multifunctional information carriers by laser engraving QR codes into the thermochromic PEU cover layers of our laminates (**Figure 5.7**). Therefore, the laser ablation depth was set to exceed the height of the cover layer by (10 ± 5) µm.

Since the PEU base material was semi-crystalline at room temperature and therefore whitish, an adequate surface contrast was assured between opaque regions, which "laid open" after laser ablation, and non-laser ablated (colorful) regions. As a consequence, the

QR codes were consistently machine-readable at 23 °C (**Figure 5.7**a and c). In equal measure, color fading and an associated contrast decline gave non-decodable states above CST (**Figure 5.7**b). In this sense, the cover layer exhibited reliable thermochromic properties.

Figure 5.7 Multifunctional QR code carriers at 23 °C (a), 60 °C (b) and 23 °C (c). The QR codes were consistently machine-readable below CST (a and c) and unreadable above CST (b).

As illustrated in the grayscale histograms, pronounced contrast changes could be verified for multifunctional QR code carriers when heated from 23 to 60 °C (**Figure 5.8**).

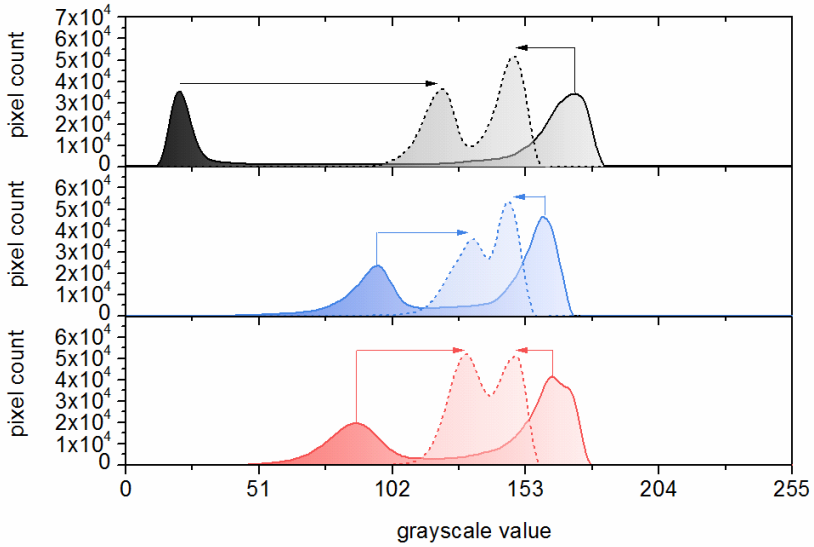

Figure 5.8 Grayscale histograms of multifunctional QR code carriers in black, blue and red color at 23 °C (below CST, continuous lines) and 60 °C (above CST, dashed lines). Heating-induced signal shifts are illustrated by arrows.

Two characteristic signal shifts took place in the grayscale histograms when heating information carriers with black and white QR code patterns above CST. In terms of the black areas, decolorization occurred as evidenced by a shift in GSV from 20 to 121. In parallel, a slight darkening of whitish regions, illustrated by a shift from 172 to 148, could be detected. While the former is attributable to the separation of color-forming components, culminating in decolorization of T-PIG black, latter is due to PBA melting. Similarly characteristic, but less pronounced shifts in GSV were found for QR code carriers, whose surfaces were loaded with T-PIG blue and red. Independent of the employed fillers, the Michelson contrast in black, blue and red QR code carriers was much higher below CST (C_M = 0.25–0.80) compared to above CST (C_M = 0.04–0.09). In agreement with recent investigations on artificially aged information carriers surface-loaded with nonfunctional dye,[45] a drop below C_M = 0.1 led to the malfunction of QR code readability.

For convenience, programming of those multifunctional QR code carriers shown in **Figure 5.7** was carried out *via* compressive deformation-determinated functionalization.[29] Hence, the QR codes became non-decipherable, since the deskewing and decoding algorithms of the scanning and decoding device could not compensate the random distortion patterns (not shown in **Figure 5.7**). For all investigated QR code carriers, the characteristic surface coloring did not change compared to their pre-programmed states, which implies that the microcapsules did not burst in course of mechanical loading and were therefore sufficiently mechanical stable.[50] The processes of shape recovering and surface decolorization are exemplified in **Figure 5.9** for a blue QR code carrier, same as the ensuing cooling-initiated return of surface contrast.

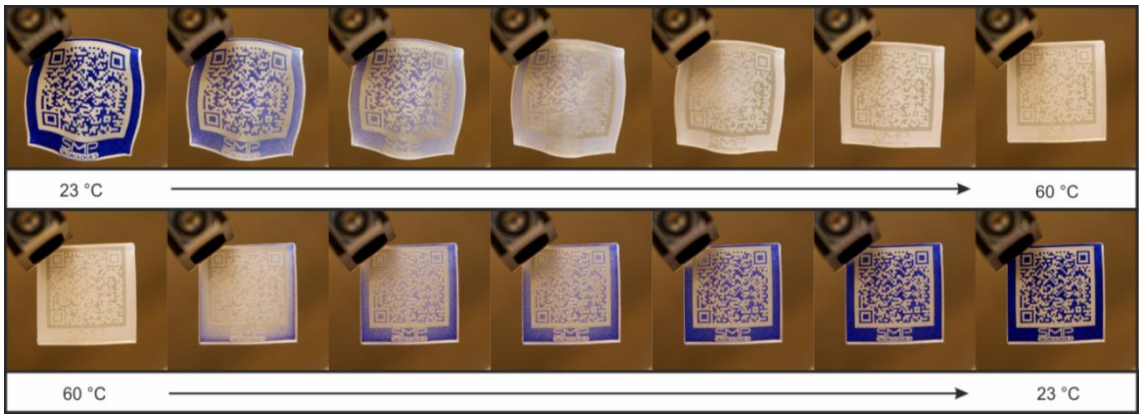

Figure 5.9 Thermo-responsiveness of a multifunctional QR code carrier. Starting with the programmed state, the information carrier was heated from 23 to 60 °C and cooled to 23 °C, at which the QR code became machine-readable. Uniform heating and cooling rates of ±4 °C min^{-1} were selected.

As visible to the naked eye, decolorization of those surface regions containing T-PIG blue set in slightly before shape recovering. This finding is in line with our DSC results where solvent melting inside the thermochromic microcapsules was detected below the PBA melting transition, which herein corresponds to the shape recovery temperature. At 60 °C, the original shape was completely recovered, suggesting that the influence of thermochromic additives, counteracting the entropy elastic behavior of polymer chains, was negligible. However, at that temperature the QR code was still machine-unreadable due to a lack of surface contrast. Once cooled below CST, the contrast returned and the encoded information could be released. Finally, it is noteworthy that multifunctional QR code carries were characterized by fairly good structural stabilities; the cover layers containing the microcapsules even did not peel off, when keeping the QR code carriers for more than one week at 60 °C.

5.2.5. Conclusions

In summary, the deposition of thermochromic PEU films atop PEU plaques is a convenient way to obtain polymer laminate structures, which can be used to fabricate multifunctional QR code carriers therefrom. Advantageously, the concepts of thermochromism and shape memory behavior complemented one another due to an excellent switching behavior. While significant advances have been made in developing information carriers with combinatorial thermo-responsiveness, there are still numerous challenges ahead to bring this promising technology from the bench into applications. One of them is integrating information carriers into existing systems. For applications mandating programmed information carriers that are precisely the same size and shape, this challenge may actually be a limitation. However with the introduction of the first generation of multifunctional information carriers, a significant number of fundamental and practical challenges could be solved, which makes us optimistic that in practice, the full potential of this remarkable technology can be realized one day.

5.2.6. Acknowledgements

The authors gratefully acknowledge financial support from the German Federal Ministry of Education and Research (BMBF, project funding reference number 03V0043). Daffne Pilger Vaca is acknowledged for programming and recovering the information carriers, Sigrid Benemann for conducting SEM and Sebastian Chruscicki for colorimetric measurements. The authors thank Bayer MaterialScience AG for kindly providing the PEU.

5.2.7. References

1. Y. Liu, H. Lv, X. Lan, J. S. Leng and S. Du, *Compos Sci Technol*, 2009, **69**, 2064-2068.
2. S. A. Madbouly and A. Lendlein, *Adv Polym Sci*, 2010, **226**, 41-95.
3. Q. Meng and J. Hu, *Composites A*, 2009, **40**, 1661-1672.
4. J. Leng, X. Lan, Y. Liu and S. Du, *Prog Mater Sci*, 2011, **56**, 1077-1135.
5. A. Lendlein, H. Jiang, O. Jünger and R. Langer, *Nature*, 2005, **434**, 879-882.
6. W. M. Huang, B. Yang, Y. Zhao and Z. Ding, *J Mater Chem*, 2010, **20**, 3367-3381.
7. X. Wu, W. M. Huang, Y. Zhao, Z. Ding, C. Tang and J. Zhang, *Polymers*, 2013, **5**, 1169-1202.
8. P. T. Mather, X. Luo and I. A. Rousseau, *Annu Rev Mater Res*, 2009, **39**, 445-471.
9. M. Behl, J. Zotzmann and A. Lendlein, *Adv Polym Sci*, 2010, 1-40.
10. T. Pretsch, *Polymers*, 2010, **2**, 120-158.
11. L. Sun, W. M. Huang, Z. Ding, Y. Zhao, C. C. Wang, H. Purnawali and C. Tang, *Mater Des*, 2012, **33**, 577-640.
12. K. K. Julich-Gruner, C. Löwenberg, A. T. Neffe, M. Behl and A. Lendlein, *Macromol Chem Phys*, 2013, **214**, 527-536.
13. H. Meng and G. Li, *Polymer*, 2013, **54**, 2199-2221.
14. H. Meng, H. Mohamadian, M. Stubblefield, D. Jerro, S. Ibekwe, S.-S. Pang and G. Li, *Smart Mater Struct*, 2013, **22**, art. no. 093001.
15. A. Lendlein, M. Behl, B. Hiebl and C. Wischke, *Expert Rev Med Devices*, 2010, **7**, 357-379.
16. J. Hu and S. Chen, *J Mater Chem*, 2010, **20**, 3346-3355.
17. W. Small, P. Singhal, T. S. Wilson and D. J. Maitland, *J Mater Chem*, 2010, **20**, 3356-3366.
18. M. Ebara, K. Uto, N. Idota, J. M. Hoffmann and T. Aoyagi, *Adv Mater*, 2012, **24**, 273-278.
19. J. Hu, H. Meng, L. Guoqiang and S. I. Ibekwe, *Smart Mater Struct*, 2012, **21**, art. no. 053001.
20. Y. Liu, J. K. Boyles, J. Genzer and M. D. Dickey, *Soft Matter*, 2012, **8**, 1764-1769.
21. M. C. Serrano and G. A. Ameer, *Macromol Biosci*, 2012, **12**, 1156-1171.
22. S. Wang and J. C. Brigham, *Smart Mater Struct*, 2012, **21**, art. no. 105016.
23. M. Anthamatten, S. Roddecha and J. Li, *Macromolecules*, 2013, **46**, 4230-4234.
24. A. Gugliuzza and E. Drioli, *J Membrane Sci*, 2013, **446**, 350-375.
25. B. K. Kim, S. Y. Lee and M. Xu, *Polymer*, 1996, **37**, 5781-5793.
26. F. L. Ji, J. L. Hu, T. C. Li and Y. W. Wong, *Polymer*, 2007, **48**, 5133-5145.
27. T. Pretsch, *Smart Mater Struct*, 2010, **19**, art. no. 015006.
28. M. Bothe, F. Emmerling and T. Pretsch, *Macromol Chem Phys*, 2014, **214**, 2683-2693.

29. T. Pretsch, M. Ecker, M. Schildhauer and M. Maskos, *J Mater Chem*, 2012, **22**, 7757-7766.

30. J. Hättig, W. Bräuer and T. Pretsch, *Kunststoffe international*, 2013, **1**, 39-41.

31. A. Seeboth and D. Lötzsch, *Thermochromic Phenomena in Polymers*, Smithers Rapra, Shawbury, Shrewsbury, Shropshire, 2008.

32. A. Seeboth, R. Ruhmann and O. Mühling, *Materials*, 2010, **3**, 5143-5168.

33. R. Kulčar, M. Friškovec, N. Hauptman, A. Vesel and M. Klanjšek Gunde, *Dyes and Pigments*, 2010, **86**, 271-277.

34. S. Lakio, J. Heinämäki and J. Yliruusi, *AAPS PharmSciTech*, 2010, **11**, 46-53.

35. R. Kulčar, M. Friškovec, M. Klanjšek Gunde and N. Knešaurek, *Color Technol*, 2011, **127**, 411-417.

36. D. C. MacLaren and M. A. White, *J Mater Chem* 2003, **13**, 1695-1700.

37. C. F. Zhu and A. B. Wu, *Thermochimica Acta*, 2005, **425**, 7-12.

38. A. Seeboth, D. Lötzsch, E. Potechius and R. Vetter, *Chinese J Polym Sci*, 2006, **24**, 363-368.

39. A. Seeboth, A. Klukowska, R. Ruhmann and D. Lötzsch, *Chinese J Polym Sci*, 2007, **25**, 123-135.

40. S. Chen, J. Hu, H. Zhuo and Y. Zhu, *Mater Lett*, 2008, **62**, 4088-4090.

41. S. Chen, J. Hu and H. Zhuo, *Compos Sci Tech*, 2010, **70**, 1437-1443.

42. DIN: Measuring conditions for object colors, German Institute for Standardization, Berlin, Germany, 1983, vol. DIN 5033-7

43. CIE, in 3rd Edition, Commission Internationale de l'Eclairage, Vienna, Austria, 2004, vol. CIE 15.3:2004

44. CIE, Commission Internationale de l'Eclairage, Vienna, Austria, vol. CIE S 017/E:2011

45. M. Ecker and T. Pretsch, *Smart Mater Struct*, 2013, **22**, art. no. 094005.

46. A. A. Michelson, *Studies in Optics*, The University of Chicago Press, Chicago, Illinois, 1927.

47. T. Pretsch, I. Jakob and W. Müller, *Polym Degrad Stab*, 2009, **94**, 61-73.

48. C. G. Robertson, C. J. Lin, M. Rackaitis and C. M. Roland, *Macromolecules*, 2008, **41**, 2727-2731.

49. X.-X. Zhang, Y.-F. Fan, X.-M. Tao and K.-L. Yick, *J Colloid Interface Sci*, 2005, **281**, 299-306.

50. G. Sun and Z. Zhang, *J Microencapsulation*, 2001, **18**, 593-602.

5.3. SUPPLEMENTAL INFORMATION

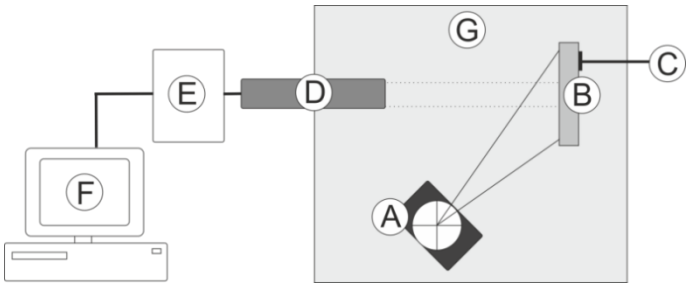

Figure 5.10 Experimental setup for spectral analysis including light source (A), sample (B), thermo-sensing element (C), collector (D), modular spectrometer system I, computer (F) and climate chamber (G). The used measuring geometry was 45°/0°. Therefore, the sample (B) was illuminated with a light beam (A) at an angle of 45° and the light-collecting lense system (D) was placed *vis-à-vis* to the sample. The whole setup was arranged in a climate chamber VCL 4006 from Vötsch Industrietechnik GmbH (G). The sample temperature was measured with a thermo-sensing element (C). The used spectrometer (MultiSpec from tec5; I operated in a wavelength scan range from 730 to 360 nm; the used software was tec5 AdminTool (F).

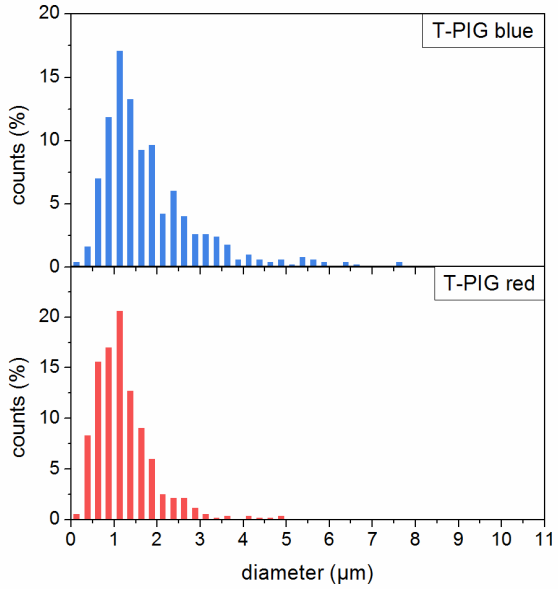

Figure 5.11 Size distribution of as-received powdery T-PIG blue and red as determined from SEM images. The mean particle size was about 1.8 µm for T-PIG blue and 1.2 µm for T-PIG red.

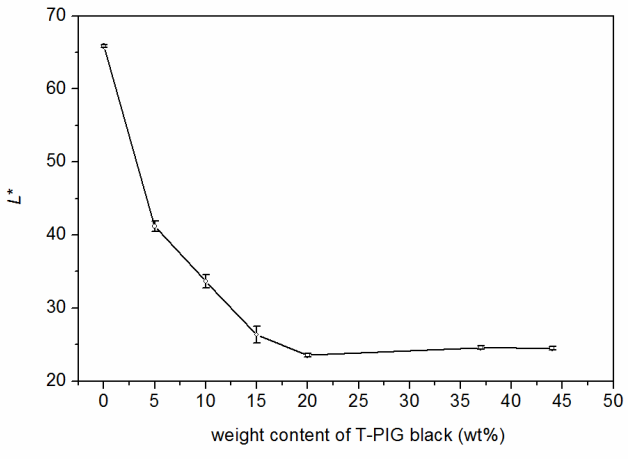

Figure 5.12 CIELAB lightness L^* of PEU films loaded with different weight contents of T-PIG black. The films were investigated at 23 °C and characterized by a thickness of (95 ± 10) µm.

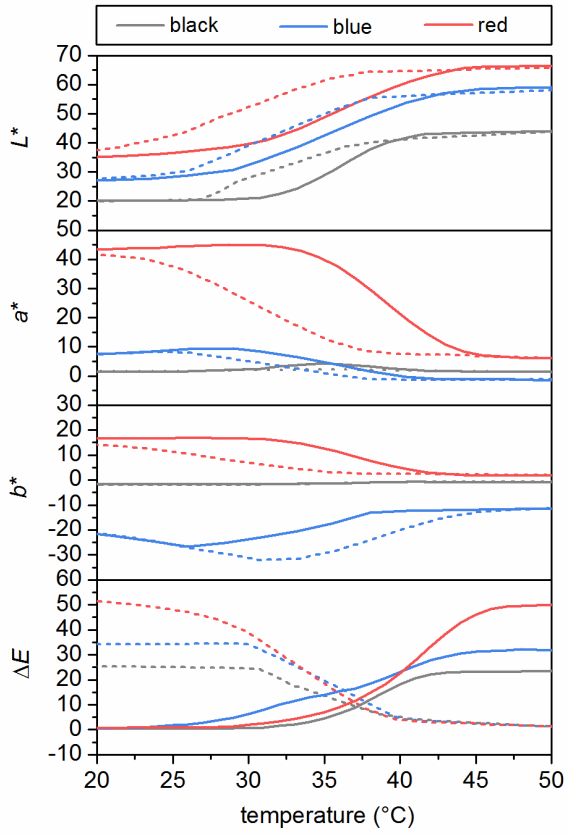

Figure 5.13 Temperature-dependence of the colorimetric properties of PEU films, containing either 20 wt% of T-PIG black, blue or red. The thickness of the films was (95 ± 10) µm. The temperature evolution in lightness L^*, the opponent color values a^* and b^* and the color difference ΔE is given during heating (continuous lines) and cooling (dashed lines).

Table 5.2 Calorimetric properties of solvent-cast PEU films with and without fillers during first heating (melting peak temperatures T_m and enthalpies ΔH_m) and cooling (crystallization peak temperatures T_c).

Sample	T_m (°C) [PBA]	ΔH_m (J/g) [PBA]	T_m (°C) [T-PIG solvent]	T_c (°C) [T-PIG solvent]
PEU film	54.5	38.7	n/a	n/a
PEU film loaded with 5 wt% T-PIG black	56.0	35.7	39.6	26.2
PEU film loaded with 20 wt% T-PIG black	55.5	34.8	41.0	27.8
PEU film loaded with 20 wt% T-PIG blue	53.5	n/a	43.0	28.9
PEU film loaded with 20 wt% T-PIG red	53.5	n/a	45.9	27.6

6. NOVEL DESIGN APPROACHES FOR MULTIFUNCTIONAL INFORMATION CARRIERS

The article: M. Ecker and T. Pretsch, *RSC Adv.*, **2014**, *4* (87), 46680-46688 and the corresponding graphical abstract (**Figure 6.1**) are reproduced by permission of The Royal Society of Chemistry. The original article is online available at: http://dx.doi.org/10.1039/C4RA08977D

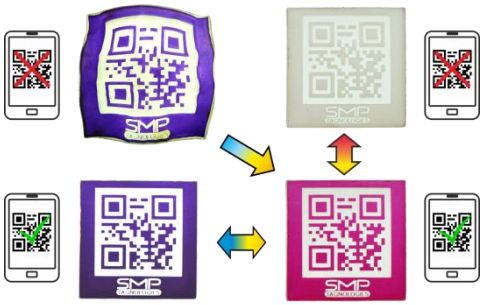

Figure 6.1 Visual summary of the main findings of the article (graphical abstract) as visible on the webpage of RSC Advances in connection with the abstract of the article.

6.1. EXPERIMENTAL CONTRIBUTION

My contribution for this manuscript comprises:

Experimental investigations, data analysis, preparation of the figures and writing an early version of the manuscript.

Contribution of co-author:

T. Pretsch: Conception and writing of the manuscript.

6.2. PUBLICATION

6.2.1. Abstract

Two design approaches for multifunctional information carriers are introduced. In the first one, quick response (QR) code carriers, which were composed of poly(ester urethane) (PEU) and microencapsulated thermochromic pigments (T-PIGs), differing in color and color switching temperature (CST), were prepared. The obtained material systems exhibited machine-readable QR codes at 23 °C and a two-stage decolorization when heated, culminating in unreadable QR codes at temperatures above the highest CST of

the employed T-PIGs. In the second scenario, information carriers were sealed with a dark, thermochromic PEU layer. As a result, the QR codes were hidden at 23 °C and became readable upon heating due to color fading. Beyond the characterization of the employed components, preparation methods, functionality analyses and durability investigations are reported. When heated after thermo-mechanical programming, pronounced shape memory properties could be verified. The thermo-responsiveness of such multifunctional material systems may qualify them for usage in anti-counterfeiting applications.

6.2.2. Introduction

After being quasi plastically distorted, shape memory polymers (SMPs) are able to recover their original shape when an appropriate external stimulus is applied.[1-3] Conventionally, the process of transferring a polymer in a temporary shape is called "programming". Therefore, the SMP is heated above a characteristic phase transition temperature T_{trans}, deformed and cooled under constraint conditions to the shape fixity temperature. As a result, the polymer chains are stabilized in a state of low conformational entropy.[4,5] Once heated again above T_{trans}, the gain in entropy drives shape recovering.

The structural prerequisite for shape memory behavior is a network architecture based on netpoints which are interconnected by switching segments. Usually, the netpoints are formed by chemical or physical cross-links and determine the permanent shape of the polymer. In turn, the switching segments are sensitive to external stimuli and serve as a mobile phase.

Physically cross-linked, phase segregated block copolymers like poly(ester urethanes) (PEUs) belong to the most promising SMP families.[6-12] Depending on the applied programming route, switching can be accomplished when passing the glass transition ($T_{trans} = T_g$) or the melting transition ($T_{trans} = T_m$) of the polyester soft segment.[13,14] Advantageously, T_{trans} can be synthetically adjusted in a wide temperature range by changing the molecular weight of the soft segment and thereby the cross-link density.[15-19] Post-polymerization cross-linking of structural motifs, which are part of the polymer repeat units, by curing[20] or electron beam irradiation[21] is another promising way to control the thermal and mechanical properties of polyurethane SMP systems. Besides that, temperature-memory effects open the door to precisely set transition temperatures within a phase transition region without the need of structural modification.[22, 23]

Inspired by potential applications for SMPs such as textiles[24, 25] and medical devices,[26-28] fundamental research started focusing on multifunctional polymers and their composites, which are characterized by the coexistence of shape memory properties and at least one further functionality.[29, 30] Fruitful examples of such polymer systems are electroactive[31-38] or magnetoactive[39-41] SMP composites same as biodegradable SMPs[42-49] and color-changing SMPs.[50, 51] In terms of latter, multifunctionality was verified by Wu *et al.* who reported on the synthesis and characterization of a PEU, in which chromic dye units of tetraphenylethylene were covalently attached to poly(*ε*-caprolactone), serving as soft segment. As a result of aggregation and disaggregation phenomena, a memory chromic behavior could be realized.[51] Kunzelman *et al.* performed pioneering work by integrating excimer-forming fluorescent chromophores *via* guest diffusion into a chemically cross-linked poly(cyclooctene) (PCO) matrix.[50] In the obtained phase-separated blends, color changes of the chromogenic dye resulted from self-assembly or dispersion of dye molecules. Another way to obtain SMP systems with thermoreversible color changes is to integrate functional microcapsules containing color-forming components in a polymer matrix. Following this approach, our group recently used a two-step process to obtain quick response (QR) code carriers, characterized by mutually complementing thermochromic and shape memory properties.[52] Therefore, laminate structures were prepared by solvent casting of thin polymer films doped with thermochromic pigments (T-PIGs) atop a PEU substrate. After drying on air, machine-readable QR codes were engraved in the cover layer. The employed T-PIGs were built up by a mixture of leuco-dye, a color-developer and a solvent; the coloring components were microencapsulated in a polymeric shell. Such systems are known to change their color thermoreversibly due to electronic interaction between the dye and dye-developer, which is inhibited upon melting and allowed upon crystallization of the solvent.[53-57]

Herein, we introduce information carriers, which contain two sorts of T-PIGs, differing in room temperature color and color switching temperature (CST). Depending on the preparation method, a mixture of T-PIGs was distributed in the same PEU matrix atop PEU substrate before QR code carriers were prepared by laser engraving and cutting or T-PIGs were separately embedded in different layers atop PEU substrate at which a QR code carrying bottom layer was completely covered by a continuous layer. The aim of this work is to investigate their functionality. Here, one focus was on the thermoreversibility of color changes and the associated changes in surface contrast, which were directly affecting the machine-readability of the QR codes. In a further step, programming was

applied and the shape memory behavior investigated. Against this background, a discussion of the obtained results is provided.

6.2.3. Experimental Section

6.2.3.1. Preparation methods

Desmopan DP 2795A SMP, which is a PEU from Bayer MaterialScience AG, was used as received. The hard segments were composed of 4,4'-methylenediphenyl diisocyanate and 1,4-butanediol as chain extender, whereas the soft segments were based on poly(1,4-butylene adipate) (PBA). Detailed information regarding the two-step synthesis process is given in a patent.[58] The raw material was supplied both as pellets, foil[59] and injection molded plaques, latter with dimensions of 126 mm × 52 mm × 2 mm.

Microencapsulated thermochromic pigments (T-PIGs) were purchased as powder from Sintal Chemie GmbH. The obtained T-PIGs varied in room temperature color and CST. The T-PIGs were black, blue and magenta (CST = 43 °C) and orange, green and magenta (CST = 65 °C). Accordingly, they were termed "T-PIG black-43", "T-PIG blue-43", "T-PIG magenta-43", "T-PIG organge-65", "T-PIG green-65" and "T-PIG magenta-65". The preparation of thermochromic polymer pastes was carried out as follows. At first, either 1.25 g of T-PIG or 2.5 g of a 1:1 mixture of two T-PIGs was suspended in 5 ml of *N*-methyl-2-pyrrolidone (NMP). After sonication for about 10 min at 23 °C, the dispersed T-PIGs were added to a solution, in which 5 g of PEU pellets or foil were dissolved in 15 ml of NMP. The resulting pastes were stirred for 5 min at 23 °C in order to obtain homogenous dispersions of the T-PIGs. This way, pastes containing different T-PIG mixtures were prepared, and their colors at 23 °C could be set by varying the combination of the individual components (**Table 6.1**).

Table 6.1 T-PIG mixtures, which were used for paste preparation, and the associated colors of the pastes.

First component	Second component	T-PIG mixture	color at 23 °C
T-PIG black-43	T-PIG orange-65	#1	brown
T-PIG blue-43	T-PIG green-65	#2	petrol green
T-PIG magenta-43	T-PIG orange-65	#3	red
T-PIG blue-43	T-PIG magenta-65	#4	purple

Following a solvent cast approach, thin thermochromic polymer films were prepared by layering the pastes atop glass plates. Subsequently, a custom-built doctor blade[60]

(**Figure 6.2**) was used to remove the excess paste and obtain a homogenous layer thickness.

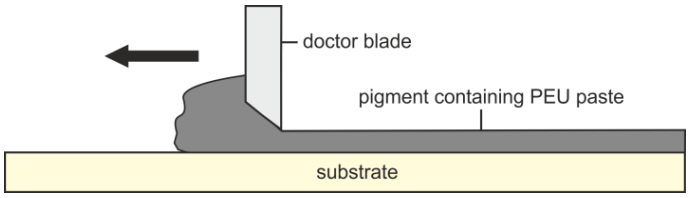

Figure 6.2 Schematic setup and functional principle of a doctor blade. The employed substrate was either glass or PEU.

After solvent evaporation, the thermal and colorimetric properties of the films were studied. Depending on the selected paste, the content of T-PIGs inside the PEU films was 20 wt% in case of pastes containing one sort of T-PIG and 33 wt% when T-PIG mixtures were used.

The preparation of multifunctional information carriers was either carried out in two or three steps; accordingly, the obtained information carriers were denoted as "type 1" or "type 2" QR code carriers (**Figure 6.3**). In both cases, a solvent cast approach was followed. This time, the above-mentioned pastes were distributed by means of a doctor blade (**Figure 6.2**) atop a 2 mm thick PEU plate, which served as a substrate (step 1 in **Figure 6.3**). After solvent evaporation for about 18 h at 23 °C, tightly connected laminate structures were obtained.

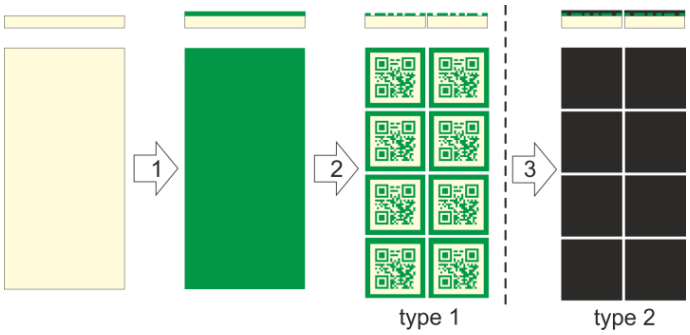

Figure 6.3 Preparation scheme for QR code carriers (side view above and top view below). Type 1 QR code carriers were prepared by solvent casting of a first T-PIG containing PEU layer atop pristine PEU (step 1), laser engraving of a QR code pattern and cutting (step 2). To prepare type 2 QR code carriers, the aforementioned steps were applied and a surface-sealing layer containing T-PIG black-43 was deposited before cutting (step 3).

In a second step, a QR code (version 1, error correction level L)[61] carrying the encoded information "http://www.bam.de" was generated,[62] engraved in the pigment-containing PEU layer and type 1 QR code carriers were prepared by laser ablation and cutting with

a 30 W CO_2 laser (step 2 in **Figure 6.3**). By standard, the edge length of the QR code symbols was 14 mm at a quiet zone width of 1 mm. In order to ensure a sufficiently high surface contrast at 23 °C between the pigment-containing regions and the PEU substrate, a laser ablation depth of (120 ± 5) µm was selected.

The preparation of type 2 QR code carriers was realized in three steps (**Figure 6.3**). In contrast to the above-described route, PEU pastes containing only one sort of T-PIG (CST = 65 °C) were selected in step 1 (**Figure 6.3**). After laser engraving a QR code pattern into the cover layer (step 2 in **Figure 6.3**), an information carrier with a machine-readable QR code was obtained as an intermediate form. Adjacently, the QR code carrying site of the information carrier was sealed with a paste containing T-PIG black-43 (step 3 in **Figure 6.3**). In a final step, QR code carriers were cut out and dried on air for 36 h at 23 °C.

6.2.3.2. Characterization methods

The shape and size distribution of the T-PIGs was studied with a scanning electron microscope (SEM). The employed Zeiss Gemini Supra 40 device operated at an extra high tension of 10 kV. In order to ensure that the surface of T-PIGs was electrically conductive, a few nanometers thin carbon layer was deposited atop the microcapsules by means of a sputtering system. The size distribution of the T-PIGs was determined from scanning electron micrographs using the software program ImageJ.[63]

Differential scanning calorimetry (DSC) was used to study solvent cast PEU films. The films had a uniform thickness of (65 ± 5) µm and were either composed of PEU or PEU, which was loaded with one sort of T-PIG or mixtures therefrom. The measurements were conducted three days after film preparation with a DSC 7020 from Seiko Instruments. Initially, a sample, weighing approximately 5 mg, was sealed in an aluminum pan, before it was placed inside the calorimeter. The sample was cooled down to −90 °C and heated to 90 °C, before cooling and heating were repeated. All measurements were carried out with cooling and heating rates of 10 °C min^{-1}. For some of the obtained thermograms, a melting peak deconvolution was carried out with the Lorentz fit function of Origin 8.5.1 software.

The surface contrast of the QR code carriers was determined at different temperatures. Therefore, heating was applied and color photos were taken. Later, the pictures were converted into grayscale histograms by using the analysis program ImageJ. From these

images the Michelson contrast C_M,[64] which is defined as the relation between the difference and the sum of the highest and lowest luminance L_{max} and L_{min}, differing in grayscale value, was calculated. For this purpose, the T-PIG containing areas and laser-ablated regions (PEU substrate) of the QR code carriers were considered. In detail, C_M was determined for five different subzones within the QR code area (top left, top right, center, bottom left and bottom right) and adjacently averaged. The maximum deviation from the mean value was determined and set as error.

The programming of information carriers was carried out with an MTS Insight 10 electromechanical testing system, which was equipped with a Thermcraft thermochamber. In accordance with the geometry of the QR code carriers, the recently introduced compressive deformation-determinated functionalization method was selected.[65] In the course of programming, a QR code carrier was positioned in the center between two pressure plates and an initial force of −10 N was applied to assure that the sample did not change position. Adjacently, the information carrier was heated with 4.3 °C min^{-1} to 80 °C and thus above the DSC melting peak offset temperature of the PBA phase, which was close to 50 °C.[65] After 5 min at 80 °C, the QR code carrier was loaded with a crosshead displacement rate of 0.5 mm min^{-1} until a maximum force F_{max} of 2.25 kN was achieved. In order to fix the temporary shape, F_{max} was maintained during cooling with 5.3 °C min^{-1} to −20 °C and thus below the DSC crystallization offset temperature of the PBA phase transition (≈ −10 °C).[65] After 5 min at −20 °C, programming was finalized by unloading with a rate of 0.5 kN min^{-1}. In a last step, the QR code carrier was heated to 23 °C.

To follow the thermoreversibility of color changes and to investigate the shape recovery behavior, programmed information carriers were gradually heated in the thermochamber from 23 to 70 °C, before they were cooled to 23 °C. In those temperature regions, in which distinct changes in color and shape occurred, namely around the CST of the T-PIGs and the melting transition of the PBA phase, heating and cooling steps of 2 °C were implemented. In the other regions, temperature intervals of 3 °C were chosen. In every case, the holding time at the different temperatures was 5 min. In parallel to temperature variation, color photos were taken using a Nikon D90 with macro objective. In order to ensure comparable conditions, the distance between the camera and the information carrier, the aperture, exposure time, focal length, ISO settings and white balance were set to be constant during the whole picture series. During shape recovering, the evolution of distorted QR code areas was followed with the image

analysis program ImageJ. In scaled photographs, which were taken at different temperatures, the areas of the QR codes were obtained through manually fitting polygons to their boundary edges (**Figure 6.4**). Temperature-dependent changes in QR code area were calculated as the difference $\Delta A = A_1 - A_0$ with A_0 being 256 mm². For error determination, the standard deviation was calculated for three measurements, which were carried out on the same QR code carrier.

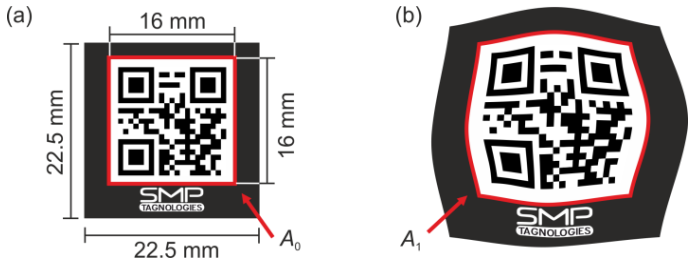

Figure 6.4 Schematic illustration of a QR code carrier in the permanent shape (a) and after programming (b). The red lines surround those surface areas, which were considered when investigating shape memory properties. The state of the QR code carrier on the left largely corresponds to the recovered state.

The machine-readability of freshly prepared, programmed and recovered QR code carriers was investigated with a Samsung Galaxy S I9300 smartphone, equipped with the software "Barcode Scanner" version 4.7.0 from Zxing.[66] Commonly, the QR codes were scanned at 23, 50 and 70 °C. Thus, temperatures below, between and above the CSTs of the employed T-PIGs were selected.

For durability investigations, type 1 and type 2 QR code carriers were prepared and temperature cycled in a Thermcraft thermochamber for $N = 100$ times between 23 and 70 °C. The selected heating and cooling rates were 20 °C min^{-1}.

6.2.4. Results and Discussion

Initially, the T-PIGs, which were differing in color at 23 °C and in color switching temperature (CST), were examined. As suggested by ATR-FTIR investigations, their polymeric shells were composed of melamine resin (**Figure 6.12**). Subsequently, scanning electron microscopy was used to further examine the T-PIGs. Here, all T-PIGs were characterized by similar size distributions and mean particle sizes; two sorts of T-PIGs are exemplarily shown in **Figure 6.5**.

Due to the similarities in shape and chemical structure, homogenous mixtures of two T-PIGs could be easily formed and a good dispersion be realized in polymer pastes, which were then used to prepare solvent cast PEU films (ESI, **Figure 6.13**). The thickness of

films, containing either one sort of T-PIG or mixtures of two T-PIGs, could be set in between (30 ± 5) and (150 ± 5) µm (ESI, **Figure 6.14**) by means of a doctor blade (**Figure 6.2**). By varying the mixtures of the T-PIGs (**Table 6.1**), polymer systems with different room temperature colors (brownish, petrol greenish, reddish and purplish) could be obtained (ESI, **Figure 6.13**).

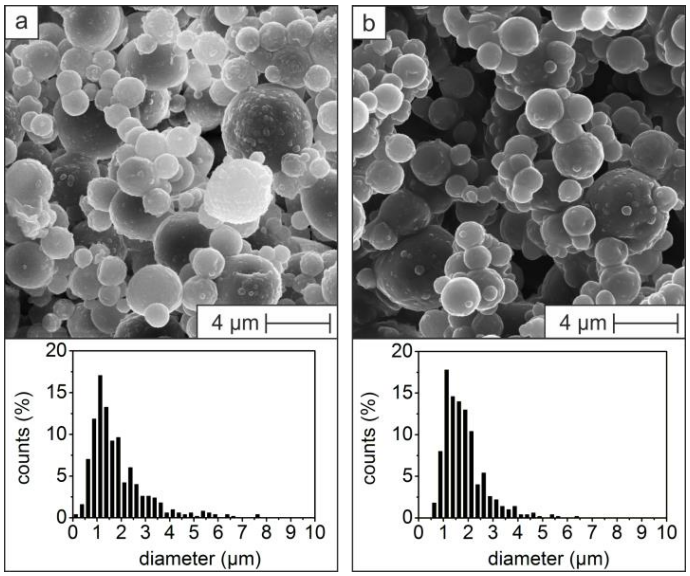

Figure 6.5 Scanning electron micrographs of T-PIG blue-43 (a) and T-PIG magenta-65 (b) and the corresponding size distributions of the microcapsules.

In a next step, the thermal properties of the films were examined with the aid of differential scanning calorimetry (**Figure 6.6**).

When investigating PEU films without fillers, broad endothermic and exothermic signals with peak temperatures at 54 and 11 °C were detected and assigned to the melting and crystallization of poly(1,4-butylene adipate) (PBA).[52, 65, 67] Upon integrating T-PIG in the PEU matrix, the position of the melting signal nearly did not change, but the crystallization peak temperature decreased from 11 to about 8 °C. Apparently, the pretty high filler contents retarded the crystallization process by hindering the diffusion of polymer chains to the growing crystallites. Under isothermal conditions, a similar behavior is known from other aliphatic polyesters like poly(*ε*-caprolactone) (PCL), which in the presence of organically modified clay shows delayed crystallization at higher filler contents.[68] In turn, under non-isothermal conditions, crystal growth is also retarded in Nylon 6 nanocomposites with high clay contents.[69]

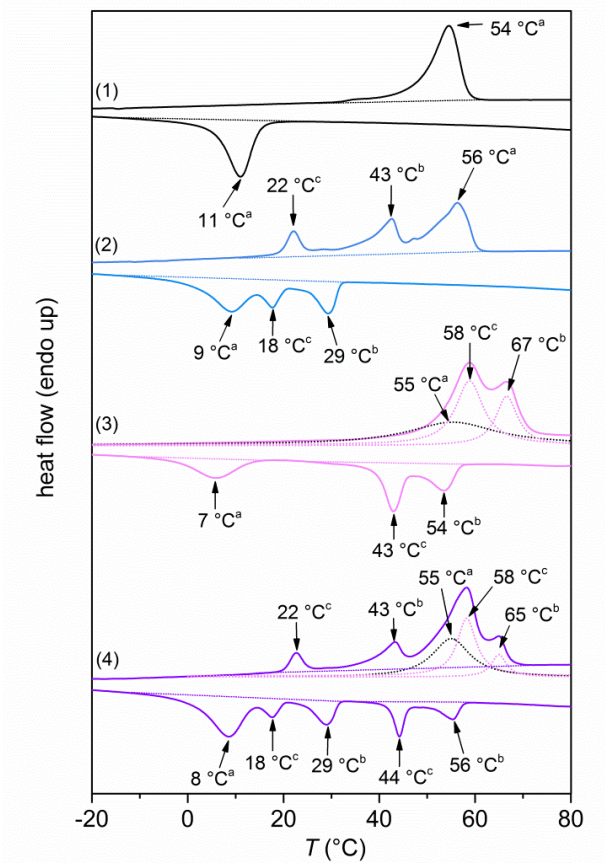

Figure 6.6 DSC thermograms of a solvent cast PEU film (1) and solvent cast PEU films containing 20 wt% of T-PIG blue-43 (2), 20 wt% of T-PIG magenta-65 (3) and T-PIG mixture #4 (4, also see Table 1). In every single measurement, the first heating is plotted above the first cooling run. The signals were denoted as "a" (PBA phase

The remaining DSC signals – some of them were obtained from peak deconvolution – could be attributed to the melting and crystallization of the color-developer and the solvent inside the polymeric microcapsules (**Figure 6.6**). Independent of the employed T-PIGs, the melting of the solvent occurred at higher temperatures compared with the corresponding crystallization event. Indeed, both peak temperatures were separated by 14 °C (T-PIG blue-43) and 13 °C (T-PIG magenta-65), respectively. The reason is that the formation of crystal nuclei is hindered in polymeric microcapsules; among others, solvent crystallization is known to be dictated by the size of the microcapsules.[70] It is noteworthy that PEU containing two sorts of T-PIGs shows a thermal behavior, which was expected from the individually loaded PEU films, thus qualifying T-PIG mixtures in a PEU matrix for consecutive color changes.

Hereafter, two types of QR code carriers are introduced. Both of them were characterized by two-step color change capabilities, but were mostly differing in those temperature regions, in which their QR codes were decipherable. Type 1 QR code carriers were

prepared by solvent casting of PEU pastes containing T-PIG mixtures atop PEU plates, followed by QR code engraving and laser cutting (**Figure 6.3**). In contrast to an earlier preparation route, in which the pigment-containing PEU paste was manually distributed atop the substrate,[52] the layer thickness could precisely be set with the doctor blade (**Figure 6.2**). From the viewpoint of color saturation, layer thicknesses of (65 ± 5) µm turned out to be useful and were selected therefor (ESI, **Figure 6.15**).

The thermochromic behavior of the obtained type 1 QR code carriers was elucidated by heating from 23 to 70 °C. The selected T-PIG mixtures exhibited a similar thermochromic behavior in all QR code carriers investigated (**Figure 6.7**).

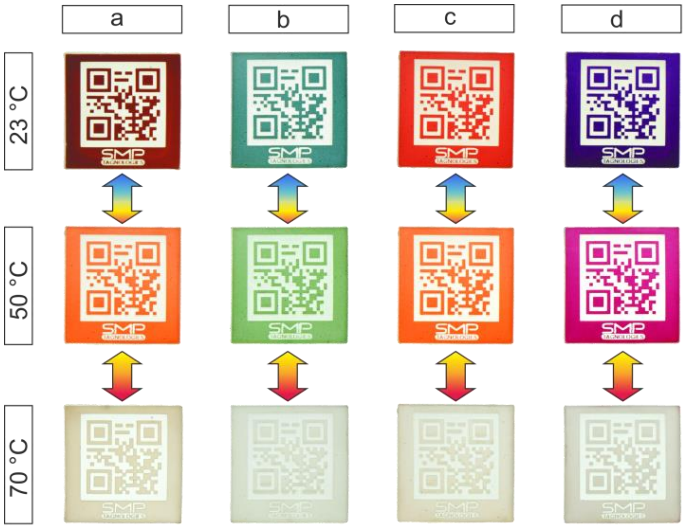

Figure 6.7 Thermochromic 123ontinuou of permanent-shaped type 1 QR code carriers, which were surface-colored with T-PIG mixture #1 (a), #2 (b), #3 (c) and #4 (d). Due to the semi-crystalline nature of the PBA phase at 23 °C, laser-ablated regions were whitish and contrasting the intensely colored T-PIG containing regions.

Typically, two-step color changes occurred, the first one at around 33 °C and the second one at about 60 °C. It is noteworthy that at temperatures above 57 °C, the QR codes became machine-unreadable. During an ensuing cooling, the colors returned at around 54 and 30 °C, respectively. A discrepancy between the temperatures of color fading and return is commonly detected in T-PIGs[71, 72] and associated with the above-mentioned distinctions in solvent melting and crystallization behavior.

Moreover, contrast determinations were carried out at 23, 50 and 70 °C to follow the temperature-dependence of Michelson contrast C_M, which, among others, is an adequate tool to gain information on the machine-readability of QR codes.[73] At ambient temperature, the comparatively highest C_M values could be detected (**Table 6.2**). Upon

heating to 50 °C, the T-PIG with the lower CST completely decolorized and the residual color was determined by the T-PIG with the higher CST. In this stage, the surface contrast was still strong enough to read out the QR codes ($C_M \geq 0.22$). Further heating to 70 °C resulted in a complete discoloration of the T-PIG containing regions. Concomitantly, C_M dropped below a value of 0.1 and the QR codes became indecipherable. This interrelationship is in accordance with recent investigations on information carriers containing non-functional dye.[73] The thermoreversibility of contrast changes and the return of QR code readability could be verified when cooling the information carriers back to 23 °C. In so far, selective contrast change capabilities could be detected.

Table 6.2 Temperature-dependence of Michelson contrast C_M of those thermochromic QR code carriers, which are exhibited in **Figure 6.7**.

	C_M (a)	C_M (b)	C_M (c)	C_M (d)
23 °C	0.79 ± 0.01	0.36 ± 0.02	0.34 ± 0.02	0.62 ± 0.05
50 °C	0.25 ± 0.02	0.26 ± 0.02	0.22 ± 0.01	0.31 ± 0.04
70 °C	0.09 ± 0.01	0.04 ± 0.01	0.04 ± 0.01	0.07 ± 0.01

In a next step, the shape memory behavior was investigated. First of all, type 1 QR code carriers were programmed. The selected programming method was based on compressive deformation and recently applied to other information carriers.[65] As a result, the information carriers could be stabilized in thermo-responsive states and their QR codes were randomly distorted and therefore indecipherable. A more detailed consideration gave that the QR code areas were enlarged by about 50% (schematically indicated in **Figure 6.4**) and the thickness of the information carriers was reduced from (2.25 ± 0.02) to (1.78 ± 0.02) mm. Subsequently, the thermo-responsiveness was investigated as exemplified in **Figure 6.8** for a purplish type 1 QR code carrier. The corresponding changes in QR code area and Michelson contrast are given in **Figure 6.9**.

As deducible from the image series, heating initiated color fading of the blue component (T-PIG blue-43) before shape recovering set in. Apparently, the solvent inside the microcapsules of T-PIG blue-43 started melting at 32 °C (**Figure 6.6**). In turn, shape recovering was initiated at 42 °C. Since this value was on the outermost region of the PBA melting signal as detected for solvent cast PEU film (**Figure 6.6**), shape recovering must have been dominated by the thermal behaviour of the programmed PEU substrate. In fact, this could be proven by means of a further DSC heating scan on a sample of a

programmed type 1 QR code carrier. In the respective thermogram, PBA melting was characterized by a broad endothermic signal, spreading from 30 to 53 °C (ESI **Figure 6.16**). At the activation temperature of the shape memory effect (42 °C), approximately 45% of the PBA crystallites were molten.

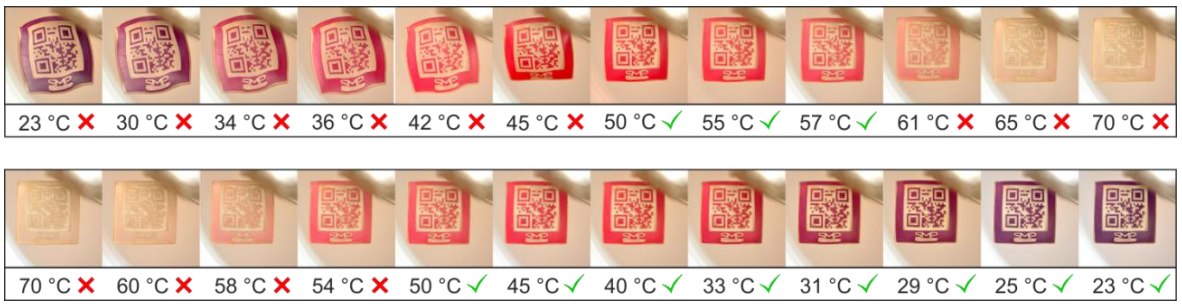

Figure 6.8 Thermo-responsiveness of a type 1 QR code carrier which was surface-colored with T-PIG mixture #4. Starting with the programmed state, the information carrier was heated from 23 to 70 °C (image series above) and cooled to 23 °C (image series below). The symbols on the right side of the temperature values indicate, whether the QR codes were machine-readable or not

Upon further heating, the QR code pattern rectified and the QR code became decipherable at 50 °C. Above 60 °C, the magenta component decolorized. In parallel, the surface contrast decreased (C_M dropped below a value of 0.1, **Figure 6.9**), which rendered the QR code unreadable. In the overall heating process, the QR code area decreased from 50.4% at 23 °C to 11.5% at 70 °C (**Figure 6.9**).

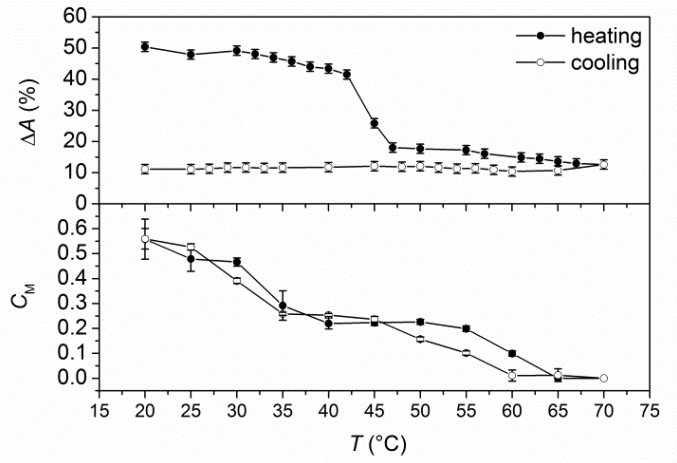

Figure 6.9 Changes in QR code area ΔA (top) and Michelson contrast C_M (bottom), when heating and cooling a programmed type 1 QR code carrier, which was surface-colored with T-PIG mixture #4.

Upon cooling, the magenta color reappeared at 52 °C, which was accompanied by a return in surface contrast and QR code readability. Finally, the purple color reappeared at about 30 °C. As expected, no significant changes occurred during cooling in the QR code area. The evolution in surface color was confirmed by temperature-dependent

colorimetric measurements (ESI, **Figure 6.17**). As evident in discrepancies regarding the evolution of all CIELAB values and color differences,[74, 75] the color of the T-PIGs depended on whether heating or cooling was applied.[76] This behaviour is in line with our DSC results, where the melting peaks of the solvent inside the microcapsules of the T-PIGs were found at higher temperatures compared with the respective crystallization signals.

To extend our concept of multifunctional information carriers, we followed one further design approach. For this purpose, a (119 ± 6) µm thick PEU layer containing 20 wt% of T-PIG green-65 was solvent cast atop a PEU plate, before a QR code was engraved and the QR code side sealed with a PEU layer containing T-PIG black-43 (**Figure 6.3**). The resulting type 2 QR code carrier was microscopically investigated. The cover layer thickness was (211 ± 6) µm above laser ablated regions and (152 ± 6) µm in the remaining regions (ESI, **Figure 6.18**). In a next step, the thermochromic behavior was examined (**Figure 6.10**).

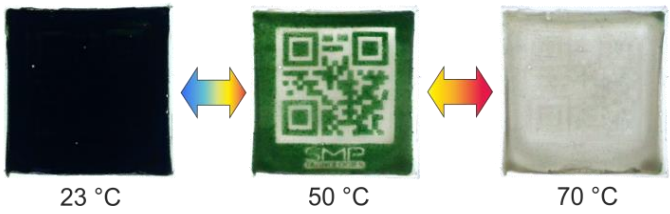

Figure 6.10 Thermo-responsiveness of a permanent-shaped type 2 QR code carrier, containing a 126ontinuous layer of T-PIG black-43 atop a laser-engraved layer of T-PIG green-65.

In contrast to the information carriers shown in **Figure 6.7**, the QR code was hidden at 23 °C by the dark sealing layer. Upon heating to 70 °C, a machine-readable QR code appeared at 44 °C and disappeared at 62 °C. Upon cooling, the QR code was readable in between 58 and 32 °C.

In order to find out in how far programming affected the thermo-responsiveness, a type 2 QR code carrier was investigated. It can be clearly seen that heating initiated color fading of the cover layer (T-PIG black-43) whereupon a distorted QR code became visible before shape recovering set in (**Figure 6.11**).

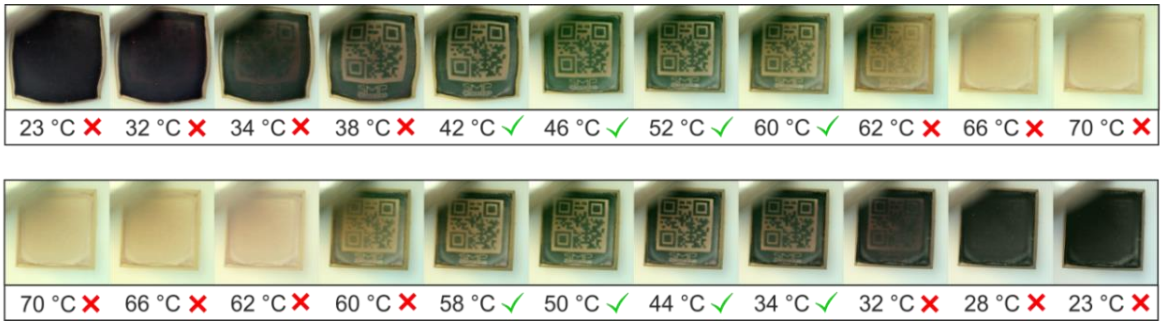

Figure 6.11 Thermo-responsiveness of a type 2 QR code carrier containing T-PIG green-65 in a laser-engraved bottom layer and T-PIG black-43 in a cover layer. Starting with the programmed state, the information carrier was heated from 23 to 70 °C (image series above) and cooled to 23 °C (image series below). The symbols on the right side of the temperature values indicate, whether the QR codes were machine-readable or not.

At temperatures in between 42 and 60 °C, the QR code was in a machine-readable state. Upon further heating, the green layer decolorized and the QR code disappeared. During an ensuing cooling, a machine-readable QR code reappeared at 52 °C and was completely hidden at temperatures below 28 °C. It is noteworthy, that for type 2 QR code carriers the Michelson contrast was in general pretty low with maximum values of about 0.2 (ESI, **Figure 6.19**). Obviously, the thermochromic top layer was not completely transparent above the CST of T-PIG black-43, which can be explained with a sensitivity toward light scattering on the employed microcapsules.[77]

Finally, we investigated the durability of our QR code carriers. Therefore, they were heated to 70 °C and adjacently cooled to 23 °C, before further 99 heating-cooling cycles were carried out (ESI, **Figure 6.20**). As evidenced by spectrophotometric measurements, the temperature colors at 23 and 50 °C remained almost unaffected by thermal cycling (ESI, Table 6.3). Apart from that, color fading and regaining was found in the same temperature regions as for freshly prepared information carriers. This demonstrates that reliable color switching could be accomplished, which assured that those temperature areas, in which the QR codes were readable, could be retained.

6.2.5. Conclusions

Mixing of different sorts of T-PIGs in a PEU matrix established a fruitful basis to obtain multifunctional material systems with two-stage, thermoreversible color change capabilities. When studying the thermo-responsiveness of type 1 QR code carriers, their codes were visible at ambient temperature and became unreadable at temperatures above the highest decolorization temperature of the employed T-PIGs. Following another design approach, type 2 QR code carriers could be obtained. This time, QR codes were

concealed at room temperature and became decipherable upon heating in a small temperature region. It is remarkable that after 100 heating-cooling cycles, no significant change in thermochromic behavior could be detected for both systems.

The verified functionalities add well to our existing portfolio of security features, which could render information carriers more difficult-to-copy, thus qualifying them as promising technology for product authentication and identification. The introduced QR code carriers can be used in a permanent or programmed state. Both could act as a deterrent to potential counterfeiters have to overcome. In particular, changes in the choice of programming instruments may offer a broad spectrum of modification possibilities.[78] Beyond that, the incorporation of more than two T-PIGs in one and the same polymer matrix or in multilayer polymer films may enhance the spectrum of color changes and could be a key to obtain highly functional information carriers.

6.2.6. Acknowledgement

The authors gratefully acknowledge financial support from the German Federal Ministry of Education and Research (BMBF, project funding reference number 03V0043). Sigrid Benemann is acknowledged for conducting SEM, Dietmar Neubert for DSC measurements and Josefine Buschke for taking the series of photographs. The authors thank Bayer MaterialScience AG (BMS) for kindly providing the PEU, Jürgen Hättig (BMS) for thoughtful discussions and Michael Maskos (Fraunhofer ICT-IMM) and Gerhard Wegner (Max Planck Institute for Polymer Research) for the support of this project and suggestions for future work.

6.2.7. References

1. A. Lendlein and S. Kelch, *Angew. Chem. Int. Ed.*, 2002, **41**, 2034-2057.
2. B. Dietsch and T. Tong, *J. Adv. Mater.*, 2007, **39**, 3-12.
3. C. Liu, H. Qin and P. T. Mather, *J. Mater. Chem.*, 2007, **17**, 1543-1558.
4. P. J. Flory, in *Principles of Polymer Chemistry*, Cornell University Press Ithaca, New York, 1953, pp. 541-594.
5. L. R. G. Treloar, in *The Physics of Rubber Elasticity*, Oxford University Press, Oxford, 1975, pp. 24-41.
6. F. K. Li, X. Zhang, J. N. Hou, M. Xu, X. L. Lu, D. Z. Ma and B. K. Kim, *J. Appl. Polym. Sci.*, 1997, **64**, 1511-1516.
7. H. M. Jeong, S. Y. Lee and B. K. Kim, *J. Mater. Sci.*, 2000, **35**, 1579-1583.
8. S. J. Chen, J. L. Hu, C. W. M. Yuen, L. K. Chan and H. T. Zhuo, *Polym. Adv. Technol.*, 2010, **21**, 377-380.

9. Y.-C. Chung, D. K. Nguyen, J. W. Choi and B. C. Chun, *J. Appl. Polym. Sci.*, 2010, **120**, 2063-2073.
10. T. Pretsch and W. W. Müller, *Polym. Degrad. Stab.*, 2010, **95**, 880-888.
11. W. Wang, Y. Jin, P. Ping, X. S. Chen, X. B. Jing and Z. H. Su, *Macromolecules*, 2010, **43**, 2942-2947.
12. K. K. Julich-Gruner, C. Löwenberg, A. T. Neffe, M. Behl and A. Lendlein, *Macromol. Chem. Phys.*, 2013, **214**, 527-536.
13. F. L. Ji, J. L. Hu, T. C. Li and Y. W. Wong, *Polymer*, 2007, **48**, 5133-5145.
14. T. Pretsch, *Smart Mater. Struct.*, 2010, **19**, art. no. 015006.
15. P. Ping, W. Wang, X. Chen and X. Jing, *Biomacromolecules*, 2005, **6**, 587-592.
16. S. J. Chen, J. L. Hu, Y. Q. Liu, H. M. Liem, Y. Zhu and Q. H. Meng, *Polym. Int.*, 2007, **56**, 1128-1134.
17. S. Mondal and J. L. Hu, *J. Elastomers Plast.*, 2007, **39**, 81-91.
18. D. Ratna and J. Karger-Kocsis, *J. Mater. Sci.*, 2008, **43**, 254-269.
19. M. Bothe, F. Emmerling and T. Pretsch, *Macromol. Chem. Phys.*, 2013, **214**, 2683-2693.
20. K. Hearon, K. Gall, T. Ware, D. J. Maitland, J. P. Bearinger and T. S. Wilson, *J. Appl. Polym. Sci.*, 2011, **121**, 144-153.
21. K. Hearon, C. J. Besset, A. T. Lonnecker, T. Ware, W. E. Voit, T. S. Wilson, K. L. Wooley and D. J. Maitland, *Macromolecules*, 2013, **46**, 8905-8916.
22. K. Kratz, U. Voigt and A. Lendlein, *Adv. Funct. Mater.*, 2012, **22**, 3057-3065.
23. N. Fritzsche and T. Pretsch, *Macromolecules*, 2014, **47**, 5952-5959.
24. J. Hu, in *Shape-Memory Polymers and Multifunctional Composites*, eds. J. Leng and S. Du, CRC Press, 2010, pp. 293-313.
25. J. Hu, H. Meng, G. Li and S. I. Ibekwe, *Smart Mater. Struct.*, 2012, **21**, art. no. 053001.
26. F. E. Feninat, G. Laroche, M. Fiset and D. Mantovani, *Adv. Eng. Mater.*, 2002, **4**, 91-104.
27. K. Gall, C. M. Yakacki, Y. P. Liu, R. Shandas, N. Willett and K. S. Anseth, *J. Biomed. Mater. Res. Part A*, 2005, **73A**, 339-348.
28. W. Sokolowski, A. Metcalfe, S. Hayashi, L. Yahia and J. Raymond, *Biomed. Mater.*, 2007, **2**, 23-27.
29. M. Behl, M. Y. Razzaq and A. Lendlein, *Adv. Mater.*, 2010, **22**, 3388-3410.
30. J. Leng, H. Lu and S. Du, in *Shape-Memory Polymers and Multifunctional Composites*, eds. J. Leng and S. Du, CRC Press, 2010, pp. 133-201.
31. H. Koerner, G. Price, N. A. Pearce, M. Alexander and R. A. Vaia, *Nature Mater.*, 2004, **3**, 115-120.
32. J. W. Cho, J. W. Kim, Y. C. Jung and N. S. Goo, *Macromol. Rapid Commun.*, 2005, **26**, 412-416.
33. N. G. Sahoo, Y. C. Jung, H. J. Yoo and J. W. Cho, *Compos. Sci. Technol.*, 2007, **67**, 1920-1929.

34. Y. J. Liu, H. B. Lv, X. Lan, J. S. Leng and S. Y. Du, *Compos. Sci. Technol.*, 2009, **69**, 2064-2068.

35. S. A. Madbouly and A. Lendlein, in *Adv. Polym. Sci.*, ed. A. Lendlein, Springer Berlin Heidelberg, 2010, vol. 226, pp. 41-95.

36. J. Leng, X. Lan, Y. Liu and S. Du, *Prog. Mater Sci.*, 2011, **56**, 1077-1135.

37. H. Meng and G. Li, *Polymer*, 2013, **54**, 2199-2221.

38. G. Fei, C. Tuinea-Bobe, D. Li, G. Li, B. Whiteside, P. Coates and H. Xia, *RSC Adv.*, 2013, **3**, 24132-24139.

39. A. M. Schmidt, *Macromol. Rapid Commun.*, 2006, **27**, 1168-1172.

40. T. Weigel, R. Mohr and A. Lendlein, *Smart Mater. Struct.*, 2009, **18**, art. no. 025011.

41. M. Y. Razzaq, M. Behl and A. Lendlein, *Adv. Funct. Mater.*, 2012, **22**, 184-191.

42. A. Lendlein and R. Langer, *Science*, 2002, **296**, 1673-1676.

43. A. Lendlein and S. Kelch, *Mater. Sci. Forum*, 2005, **492-493**, 219-224.

44. N. Y. Choi, S. Kelch and A. Lendlein, *Adv. Eng. Mater.*, 2006, **8**, 439-445.

45. Y. S. Wong, Y. Xiong, S. S. Venkatraman and F. Y. C. Boey, *J. Biomater. Sci.-Polym. Ed.*, 2008, **19**, 175-191.

46. Y. L. Wang, Y. G. Li, Y. F. Luo, M. N. Huang and Z. Q. Liang, *Mater. Lett.*, 2009, **63**, 347-349.

47. K. Nagahama, Y. Ueda, T. Ouchi and Y. Ohya, *Biomacromolecules*, 2009, **10**, 1789-1794.

48. L. L. Liu and W. Cai, *Mater. Lett.*, 2009, **63**, 1656-1658.

49. L. Xue, S. Dai and Z. Li, *Biomaterials*, 2010, **31**, 8132-8140.

50. J. Kunzelman, T. Chung, P. T. Mather and C. Weder, *J. Mater. Chem.*, 2008, **18**, 1082-1086.

51. Y. Wu, J. Hu, H. Huang, J. Li, Y. Zhu, B. Tang, J. Han and L. Li, *J. Polym. Sci., Part B: Polym. Phys.*, 2014, **52**, 104-110.

52. M. Ecker and T. Pretsch, *RSC Adv.*, 2014, **4**, 286-292.

53. D. C. MacLaren and M. A. White, *J. Mater. Chem.*, 2003, **13**, 1695-1700.

54. D. C. MacLaren and M. A. White, *J. Mater. Chem.*, 2003, **13**, 1701-1704.

55. D. C. MacLaren and M. A. White, *J. Mater. Sci.*, 2005, **40**, 669-676.

56. A. Seeboth and D. Lötzsch, in *Thermochromic phenomena in polymers*, Smithers Rapra Technology Limited, Shrewsbury, England, 2008, pp. 17-21.

57. A. Seeboth and D. Lötzsch, in *Thermochromic and Thermotropic Materials*, Pan Stanford Publishing Pte. Ltd., Singapore, 2014, pp. 67-77.

58. Müller, F., Bräuer, W., Ott, K.H., Hoppe, H.G.,*EP Pat.*, EP0571830B1, 1993.

59. N. Fritzsche and T. Pretsch, in *Proceedings of the ASME Conference on Smart Materials, Adaptive Structures and Intelligent Systems*, 2012, vol. 1, pp. 81-88.

60. U. Siemann, in *Scattering Methods and the Properties of Polymer Materials*, Springer Berlin Heidelberg, 2005, vol. 130, pp. 1-14.

61. ISO/IEC 18004:2000I, *Information technology – Automatic identification and data capture techniques – Bar code symbology – QR Code*, Geneva, Switzerland.

62. Barcode Generator, *http://www.barcode-generator.org*

63. ImageJ, *http://rsbweb.nih.gov/ij/*

64. A. A. Michelson, in *Studies in Optics*, The University of Chicago Press, Chicago, Illinois, 1927, pp. 36-41.

65. T. Pretsch, M. Ecker, M. Schildhauer and M. Maskos, *J. Mater. Chem.*, 2012, **22**, 7757-7766.

66. Zxing, *http://code.google.com/p/zxing/*

67. T. Pretsch, I. Jakob and W. Müller, *Polym. Degrad. Stab.*, 2009, **94**, 61-73.

68. G. Jimenez, N. Ogata, H. Kawai and T. Ogihara, *J. Appl. Polym. Sci.*, 1997, **64**, 2211-2220.

69. T. D. Fornes and D. R. Paul, *Polymer*, 2003, **44**, 3945-3961.

70. X. X. Zhang, Y. F. Fan, X. M. Tao and K. L. Yick, *J. Colloid Interface Sci.*, 2005, **281**, 299-306.

71. R. Kulčar, M. Friškovec, N. Hauptman, A. Vesel and M. K. Gunde, *Dyes and Pigments*, 2010, **86**, 271-277.

72. S. Lakio, J. Heinamaki and J. Yliruusi, *AAPS PharmSciTech*, 2010, **11**, 46-53.

73. M. Ecker and T. Pretsch, *Smart Mater. Struct.*, 2013, **22**, art. no. 094005.

74. CIE 15.3:2004, *Colorimetry*, Vienna, Austria, 2004.

75. DIN 5033-1:2009-05, *Basic terms of colorimetry*, Berlin, Germany, 2009.

76. R. Kulčar, M. Friškovec, M. K. Gunde and N. Knešaurek, *Coloration Technology*, 2011, **127**, 411-417.

77. G. Mie, *Annalen der Physik*, 1908, **25**, 377-445.

78. M. Ecker and T. Pretsch, in *Materials Challenges and Testing for Manufacturing, Mobility, Biomedical Applications and Climate*, eds. W. Udomkichdecha, T. Böllinghaus, A. Manonukul and J. Lexow, Springer Berlin Heidelberg, 2014, pp 25-35.

6.3. SUPPLEMENTAL INFORMATION

6.3.1. Experimental Section

Attenuated Total Reflectance (ATR) Fourier Transform Infrared Spectroscopy (FTIR) measurements were performed with a Thermo Nicolet 6700 spectrometer using a DTGS detector. The ATR cell was equipped with a ZnSe crystal. The spectra were recorded from 4000 to 400 cm^{-1} as the average of 32 scans at a resolution of 2 cm^{-1}.

In order to determine layer thicknesses of solvent cast PEU films, cryomicrotome sections of the samples were prepared and microscopically investigated. The samples

were prepared at −20 °C with a cryomicrotome CM1950 from Leica and were characterized by a thickness of 20 µm. The slices were studied with a Leica DM EP microscope at a 10 times optical zoom.

The CIE 1976 $L^*a^*b^*$ (CIELAB) values were determined with the image editing program CorelDraw X6. Therefore, QR code carriers were temperature cycled between 20 and 70 °C and photographs were regularly taken. For all temperatures investigated, the values were determined as an average of three measurements at different subzones (at the position detection pattern) within the QR codes and the standard deviation was calculated. The temperature-dependent color difference ΔE was calculated from the CIELAB values as defined in Eq. 1 with reference to the values at 20 °C on heating and on cooling.

$$\Delta E = \sqrt{(L^* - L^*_0)^2 + (a^* - a^*_0)^2 + (b^* - b^*_0)^2} \quad (1)$$

Scanning electron micrographs of cross-sections of type 1 QR code carriers were recorded with a Zeiss Gemini Supra 40 device, which operated at an extra high tension of 10 kV. The sample was coated with a few nanometers thin gold layer by means of a sputtering system.

A DSC measurement was conducted on a programmed type 1 QR code carrier whose PEU surface layer contained T-PIG mixture #4. For sample preparation, a piece of the information carrier weighing approximately 5 mg was cut. The sample was placed in an aluminum pan with the substrate pointing toward the bottom of the pan. The sample was cooled to −90 °C before it was heated to 90 °C with cooling and heating rates of 10 °C min^{-1}.

6.3.2. Supporting Figures

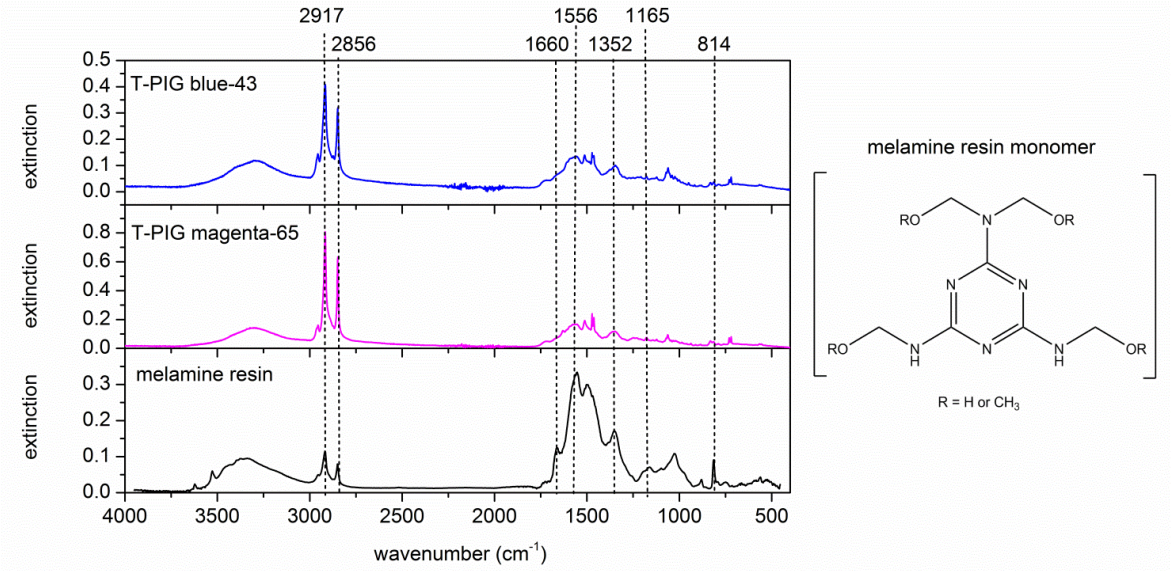

Figure 6.12 ATR-FTIR spectra of powdery T-PIG blue-43 and T-PIG magenta-65 and of melamine resin (reference data were taken from HR Thermo Nicolet Sample Library). The strong absorptions at 2917 and 2856 cm^{-1} represent the asymmetric and symmetric stretching vibration ν(CH) of the methylene group of melamine resin. The peak at 1660 cm^{-1} can be assigned to the δ(NH_2), the signals at 1556 and 1352 cm^{-1} to the in-plane stretching vibration ν(C=N) of the 1, 3, 5-triazine ring, the band at 1165 cm^{-1} to the deformation vibration δ(C-O) of the melamine resin and the signal at 814 cm^{-1} to the out-of-plane deformation vibration of the triazine ring.

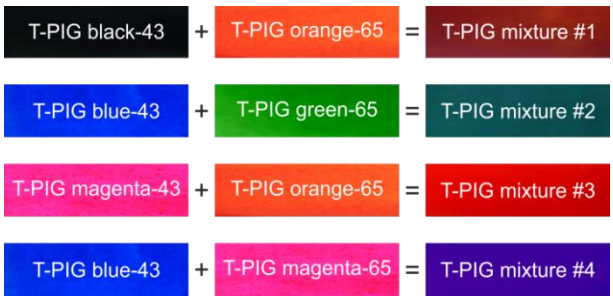

Figure 6.13 Solvent cast PEU films containing 20 wt% of one sort of T-PIG with a CST of 43 °C (left column), 20 wt% of another sort of T-PIG with a CST of 65 °C (column in the middle) and 1:1 mixtures of both (right column). The films had uniform thicknesses of (65 ± 5) µm. The images were recorded at 23 °C.

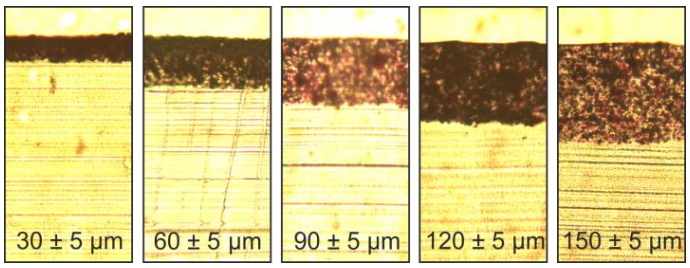

Figure 6.14 Microscopic images of solvent cast PEU films containing T-PIG mixture #4 atop PEU substrate. The thickness of the films could be controlled by means of a doctor blade.

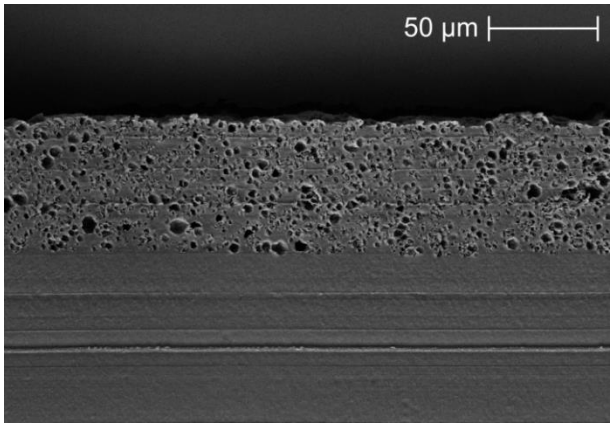

Figure 6.15 Scanning electron micrograph of a PEU surface layer containing T-PIG mixture #4 atop PEU substrate.

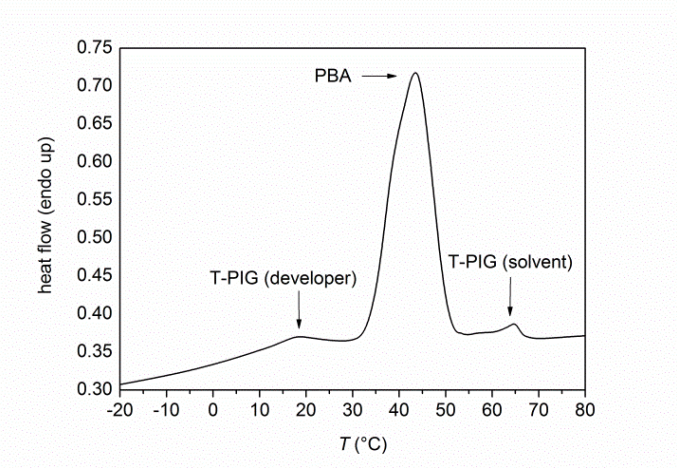

Figure 6.16 First DSC heating scan of a sample of programmed type 1 QR code carrier whose PEU surface layer contained T-PIG mixture #4. The PEU substrate was in direct contact with the aluminum pan.

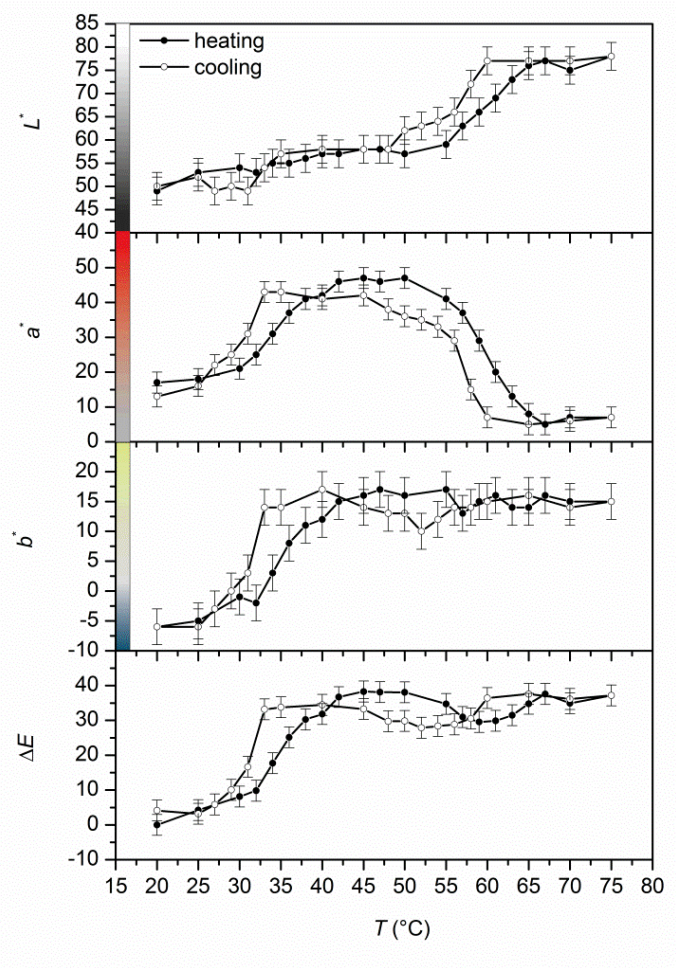

Figure 6.17 Temperature-dependence of CIELAB values and color differences Δ*E* of a type 1 QR code carrier whose PEU surface layer contained T-PIG mixture #4.

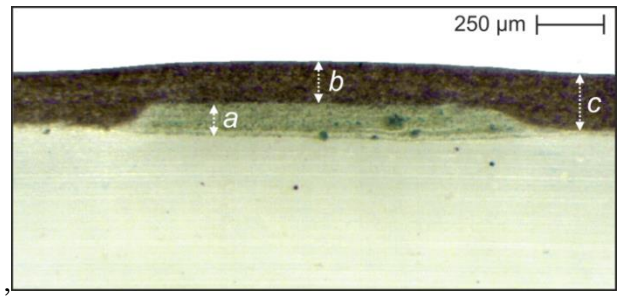

Figure 6.18 Microscopic image of a type 2 QR code carrier containing T-PIG green-65 in a laser-engraved bottom layer and T-PIG black-43 in a continuous cover layer. Layer thicknesses of a = (119 ± 6) µm, b = (152 ± 6) µm and c = (211 ± 6) µm were determined.

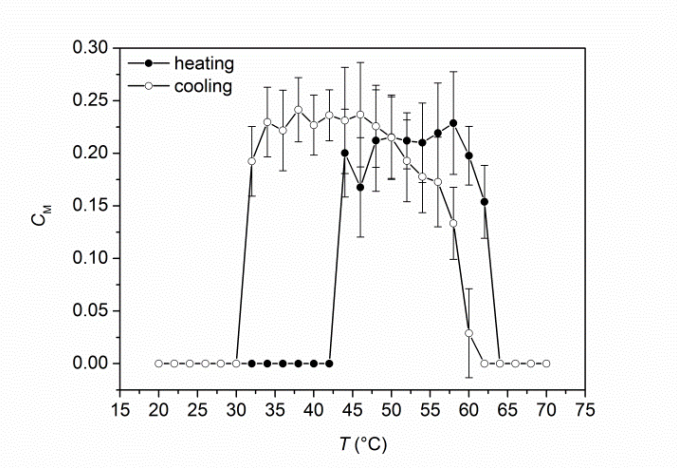

Figure 6.19 Temperature-dependent evolution of Michelson contrast C_M of a permanent-shaped type 2 QR code carrier containing T-PIG green-65 in a bottom layer and T-PIG black-43 in a cover layer.

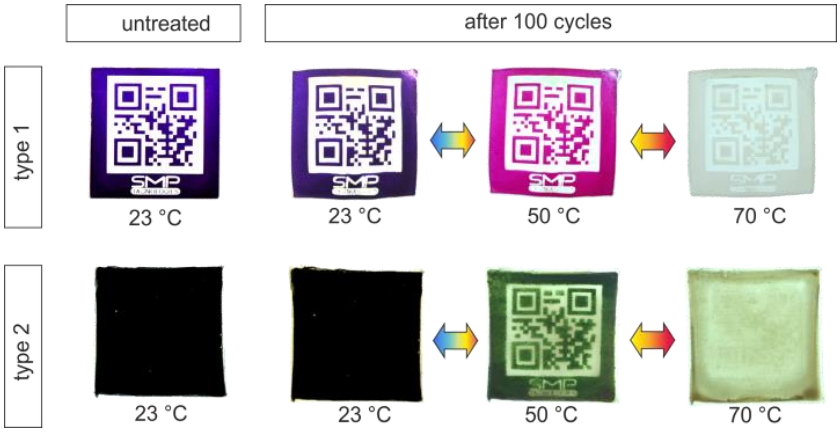

Figure 6.20 Durability of thermochromic behavior in permanent-shaped type 1 and type2 QR code carriers. The untreated states (left) are compared with the states at 23, 50 and 70 °C after running 100 heating-cooling cycles (right).

Table 6.3 CIELAB values and color differences ΔE of a type 1 QR code carrier whose PEU surface layer contained T-PIG mixture #4. The values are provided for the untreated state and for the state after running 100 heating-cooling cycles between 23 and 70 °C.

sample	T [°C]	L^*	a^*	b^*	ΔE
untreated	23	22.8 ± 1.0	8.7 ± 1.0	−7.7 ± 1.0	-
after 1 cycle	23	24.2 ± 1.0	8.4 ± 1.0	−5.0 ± 1.0	3.6 ± 1.0
after 100 cycles	23	22.3 ± 1.0	10.1 ± 1.0	−8.3 ± 1.0	2.1 ± 0.8
untreated	50	26.4 ± 1.0	26.4 ± 1.0	−1.0 ± 1.0	-
after 1 cycle	50	29.9 ± 1.0	25.4 ± 1.0	1.1 ± 1.0	4.8 ± 1.0
after 100 cycles	50	27.8 ± 1.0	28.8 ± 1.0	−0.2 ± 1.0	3.2 ± 1.7

7. DISCUSSION

7.1. SECURITY FEATURES

One aim of this work was the development of a new kind of security label based on an SMP for anti-counterfeiting applications. In order to enhance the protection against forgery of such labels, it is reasonable to combine various strategies like visible (overt), hidden (covert), forensic as well as track and trace features in one system. With increasing complexity of such labels it becomes more difficult to copy them.

By employing SMPs with distinct but adjustable switching temperatures as base material, an overt security feature was introduced. Thermoset as well as thermoplastic SMPs turned out to be applicable as substrate for the fabrication of switchable information carriers. Both base polymer materials were able to undergo distinct changes in shape upon triggering the SME.

The usage of organic dyes for the surface-specific coloring is initially an overt feature, too. But due to the ability to absorb/emit specific wavelengths (like a finger print), dyes may be regarded as a forensic feature as well. The spectral lines are not visible with the naked eye, but can be detected using spectrometers. In addition, UV or IR active dyes may be suitable for the introduction of a covert security feature.

On the contrary, using T-PIGs for the surface-specific coloring of information carriers may employ both, overt and covert security features. The CST of the T-PIGs is adjustable by the variation of the solvent inside the microcapsules. Hence, the pigments allow the fabrication of information carriers with color changes at defined temperatures. When combining several T-PIGs having different colors and CSTs, it is even possible to obtain surfaces with multiple and unique temperature-dependent changes in color. Besides that, information carriers with temporarily concealed QR codes can be obtained by covering a QR code with an additional layer doped with T-PIG.

In contrast to the organic dyes, which were previously used for the surface-specific coloring of SMPs, the T-PIGs were not able to diffuse into the polymeric matrix. One reason might be that the microcapsules are too large in comparison with the meshes of the polymeric network. That is why another technique for the surface-specific coloring based on solution mixing and solvent casting was applied in order to obtain thermochromic polymer surfaces with defined thicknesses.

Generally, as soon as the temperature exceeds the CST of the employed T-PIGs, the information carriers become unreadable due to a lack in contrast. Hence, information carriers, whose readability is given only over a distinct temperature range by the targeted use of the SMP and one or more T-PIGs having appropriate switching temperatures, are available.

The solvent cast technique could also be applied for a surface-specific coloring of PEU plaques with pigments, which are not thermochromic. A variety of organic and inorganic pigments may be suitable for that purpose. One condition has to be fulfilled: the pigments have to be insoluble but dispersible in solvents like NMP, which was used in the course of paste preparation. Further studies revealed, that the addition of pigments, such as Igrazin® red DPP BO (*pigment red 254*), cobalt chromite green (*pigment green 26*), ultramarine blue (*pigment blue 29*) or graphite powder to a PEU paste resulted in homogenously distributed pigments. After solvent casting, thin films with even color distribution could be obtained (**Figure 7.1**).

Figure 7.1 Left: PEU plaques solvent cast with PEU pastes containing 20 wt% of Igrazin-red DPP BO, Cobalt chromite green, ultramarine blue and graphite powder (*pigment green 26*); right: QR code carriers prepared from the blue and black colored PEU plates shown next to it.

Another possibility to use the solvent cast technique is to integrate forensic markers into polymeric surfaces. This way, it might be possible to incorporate additional covert security features like artificial DNA fragments or other taggants to the PEU pastes. After deposition on top of the polymeric substrate, information carriers may be more complex and difficult to copy.

Applying different programming procedures, based either on tensile or on compressive-deformation, information carriers could be stabilized in temporary shapes with distorted and indecipherable barcodes. More selective distortions, for example at the position detection pattern of QR codes, could be achieved by the usage of steel ball type indenters during compressive deformation. The use of indenters had another useful advantage compared to the compressions without indenter: lower compressive forces were required (300 instead of 3,000 N) for sufficient code distortions. Beyond that, it was possible to use

indenters to pattern the surface of the information carriers with unique designs, text, symbols or logos, as depicted in **Figure 7.2**.

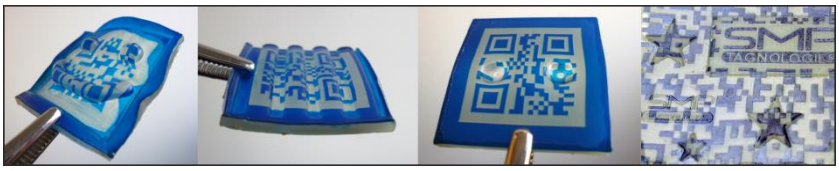

Figure 7.2 Information carriers surface-patterned by means of various indenters.

Interesting in this connection is also the possibility to introduce tunable microstructure topography to the material. Such micro-patterns may be in a µm range and thus invisible to the naked eye. Different concepts for micro-patterning are currently under investigation.[271,272,282,283] These approaches are not only interesting for anti-counterfeit purposes, but also for medical applications, such as tunable micro-channels.[284] On the one hand, a micro-structured permanent shape of the polymer is feasible. Thus, the patterns are integrated during the processing or by means of laser ablation. On the other hand, the microstructure can be integrated during a programming step, similar to the herein displayed procedure by means of an indenter.

In connection with this the enclosed manuscripts, QR and Data Matrix codes were applied for the fabrication of switchable information carriers. However, other 2D barcodes, like BeeTaggs,[285] Maxi codes and Aztec codes may also be useful for the application in switchable information carriers. Laser engraving of different code-sizes and versions into the colored surfaces of PEU and EBP resulted in machine-readable 2D barcodes. Equally to QR codes, other codes rendered also undecipherable after programming, and decipherable again after recovery as shown in preliminary studies. In addition, other barcode types, such as BeeTaggs,[285] have advantages to common barcodes. They need, for example, special commercial software in order to generate them. Thus, the hurdle for their reproduction increases.

A basic advantage of any kind of 2-D barcode is their trackability. In practice, it means that the manufacturer of the code can monitor when someone scanned the barcode and went to the linked website. In addition, one can generate any kind of access statistics with this tool.

The potential of QR codes in connection with potential anti-counterfeit applications was also exploited by Han *et al.*[275] They fabricated lithographically QR-coded micro-taggants for authentication of drugs.

7.2. DURABILITY

A second aim of this work was to investigate the durability of the introduced information carriers against different environmental impacts, such as hydrolytic aging and UVA irradiation. This is particularly important for new potential applications. Artificial aging was exemplarily conducted on black and blue colored bowtie-shaped PEU-based information carriers. It turned out, that the limiting factor for their functionality was a loss of contrast within the QR codes upon the selected aging scenarios, and thus it was basically a dye related phenomenon. By contrast, the shape memory properties were only slightly affected through the applied aging conditions. Nevertheless, for longer aging times the PEU base material was strongly affected by the artificial aging. As recently shown, hydrolytic aging of PEU specimens at elevated temperatures has a significant effect on the complex morphological structure of the PEU.[89,91] Thus, the shape memory properties, such as the recoverable strain and shape recovery temperature were also impaired in the course of aging. The proposed mechanism behind the degradation of PEU in aqueous medium is hydrolytic chain scission. At first, the ester linkages were cleaved, later the urethane linkages as well. The addition of hydrolysis-stabilizers such as carbodiimide-based compounds improved the stability of the PEU by inhibiting the autocatalytic degradation process.[53] The durability of the investigated specimens immersed in de-ionized water was increased by more than a factor of 5 towards the time of failure at 80 °C.

As previously mentioned, the applicability of information carriers was impaired by the durability of the dyes employed for the surface-specific coloring. Generally, protection against light induced degradation, or weathering, can be achieved by the addition of additives, such as UV absorbers to the polymer matrix. These light stabilizers ensure that the mechanical properties and aesthetic appearance of the end product is retained. Besides that, they protect it against color fading, discoloration and loss of gloss. As shown in preliminary studies, the addition of 5 to 10 wt% of UV stabilizer 2-hydroxy-4-methoxybenzophenone to the dyeing solution increases the durability of triarylmethane dyes toward UVA irradiation by a factor of 3. Even better results could be obtained when layering a thin PEU film containing the UV absorber on top of the colored surface of the PEU.

The durability of the information carriers colored with T-PIGs was also investigated. Therefore information carriers with overt and hidden QR codes were temperature cycled

between 70 °C and 23 °C 100 times. As expected, the functionality of the T-PIGs remained reliable after extensive temperature cycling. Their temperature-dependent colors were almost the same as before cycling as indicated by spectrophotometric measurements. In addition, DSC measurements indicated, that the melting and crystallization signals remained also unaffected by repeated heating and cooling. Thus, the information carriers might be reused for several times, which makes this technology environmentally friendly and at the same time cost efficient.

Besides that, the light and water stability of thermochromic information carriers was investigated. First studies (not shown herein) revealed that their durability against UVA irradiation and hydrolytic degradation is much higher than the durability of information carriers colored with organic dyes *via* dye diffusion. Apparently, the leuco-dyes were effectively protected by the surrounding microcapsules and by the polymeric matrix. Besides that, the microcapsules were too large to diffuse out of the polymeric bulk in the course of hydrolytic aging. Even if the PEU is in the swollen state, the T-PIGs are not able to migrate like the organic dyes.

7.3. Potential Applications

A proposed example for the application of the herein developed information carriers is displayed in **Figure 7.3**. One could add such a smart label to any product at the end of the fabrication process. The information of the QR code carrier is non-decodable during the shipping and disposal. When the product achieves its desired destination, the retailer or even the consumer can prove the originality by triggering the SME. This application example may be particularly suitable for high-quality products, such as champagne, designer purses, watches or shoes.

Figure 7.3 Proposed example of use for switchable information carriers based on SMP.

Besides that, one could use the thermo-responsiveness of programmed information carriers in order to monitor temperature abuse of food and pharmaceuticals.[286] When a

pre-defined temperature threshold is exceeded, the information carrier recovers its shape and releases the information. This might be “Attention! Threshold exceeded!” Thus, the consumer knows that the cold chain of the product was interrupted.

8. CONCLUDING REMARKS

In summary, the realization of a new technological concept was demonstrated: switchable information carriers based on SMPs. The proof of concept comprised the combination of SMPs as a functional material with various surface colors, chosen from permanent visibly inks and T-PIGs, and with traceable barcodes. Applying different programming procedures, information carriers could reliably be switched from a programmed state with indecipherable barcode to a recovered state with decipherable information.

The durability of the information carriers was limited by the employed organic dyes which were used in a first approach for the surface-specific coloring. A way to improve the light stability of colored polymers could be the implementation of pigments, which are characterized by improved light-fastness or the addition of stabilizers.

This work has also shown that T-PIGs are ideal candidates to integrate additional thermo-responsive security features to the existing system. On the one hand, tunable temperature-dependent changes in surface color were realized, on the other hand, temporarily concealed information. Besides that, the combination of various thermo-responsive components may open the door for versatile potential applications in which temperature-thresholds play a role and should be monitored.

Taken together, a significant number of fundamental and practical challenges could be solved so far. Various security features were combined in the information carriers, which make them complex and could therefore render them difficult-to-copy without a specialist's knowledge. This may qualify them as a promising technology for anti-counterfeit applications. But will the concept have commercial success?

Before the new technological concept can brought from the bench into market, one has to overcome some challenges. These include automated mass production and a proper way to attach the information carriers to the good to be protected.

Future work could also focus on the implementation of a triggering mechanism *via* joule heating. This might be achieved by integrating graphite within the tag, which was already shown to be proper for the surface coloring of SMPs by means of a solvent casting approach.

9. REFERENCES

1. A. D. Jenkins, P. Kratochvil, R. F. T. Stepto and U. W. Suter, Glossary of basic terms in polymer science, *Pure Appl. Chem.*, 1996, **68** (12), 2287-2311.
2. J. M. G. Cowie, *Polymers: Chemistry and Physics of Modern Materials, 2nd Edition*, Taylor & Francis, 1991.
3. P. C. Painter and M. M. Coleman, *Fundamentals of Polymer Science: An Introductory Text, Second Edition*, Technomic Pub. Co. , Lancaster, PA, 1997.
4. P. C. Painter and M. M. Coleman, *Essentials of Polymer Science and Engineering*, DEStech Publications, Incorporated, Lancaster, PA, 2009.
5. R. J. Young and P. A. Lovell, *Introduction to Polymers, Third Edition*, Taylor & Francis, 2011.
6. A. K. Mohanty, M. Misra and L. T. Drzal, *Natural Fibers, Biopolymers, and Biocomposites*, Taylor & Francis, 2005.
7. S. Thomas, N. Ninan, S. Mohan and E. Francis, *Natural Polymers, Biopolymers, Biomaterials, and Their Composites, Blends, and IPNs*, Apple Academic Press, 2012.
8. A. E. Barron and R. N. Zuckermann, Bioinspired polymeric materials: in-between proteins and plastics, *Curr. Opin. Chem. Biol.*, 1999, **3** (6), 681-687.
9. C. J. Hawker and K. L. Wooley, The convergence of synthetic organic and polymer chemistries, *Science*, 2005, **309** (5738), 1200-1205.
10. D. S. Achilias, C. Roupakias, P. Megalokonomos, A. A. Lappas and E. V. Antonakou, Chemical recycling of plastic wastes made from polyethylene (LDPE and HDPE) and polypropylene (PP), *J. Hazard. Mater.*, 2007, **149** (3), 536-542.
11. D. Feldman and A. Barbalata, in *Synthetic Polymers: Technology, Properties, Applications*, Springer, 1996, ch. 1, pp. 3-57.
12. D. Feldman and A. Barbalata, in *Synthetic Polymers: Technology, Properties, Applications*, Springer, 1996, ch. 2, pp. 58-132.
13. J. E. Mark, *Physical Properties of Polymers Handbook*, Springer, 2007.
14. L. Mandelkern, in *Crystallization of Polymers: Volume 1, Equilibrium Concepts*, Cambridge University Press, 2002, ch. 1.2, pp. 3-8.
15. P. C. Painter and M. M. Coleman, in *Essentials of Polymer Science and Engineering*, DEStech Publications, Incorporated, Lancaster, PA, 2009, ch. 2, pp. 23-45.
16. K. Hearon, K. Gall, T. Ware, D. J. Maitland, J. P. Bearinger and T. S. Wilson, Post-Polymerization Crosslinked Polyurethane Shape Memory Polymers, *J. Appl. Polym. Sci.*, 2011, **121** (1), 144-153.
17. K. Hearon, L. D. Nash, B. L. Volk, T. Ware, J. P. Lewicki, W. E. Voit, T. S. Wilson and D. J. Maitland, Electron Beam Crosslinked Polyurethane Shape Memory Polymers with Tunable Mechanical Properties, *Macromol. Chem. Phys.*, 2013, **214** (11), 1258-1272.
18. R. Brown, *Handbook of Polymer Testing: Physical Methods*, Taylor & Francis, 1999.

19. L. H. Sperling, *Introduction to Physical Polymer Science*, Wiley, 2005.

20. L. H. Sperling, in *Introduction to Physical Polymer Science*, Wiley, 2005, ch. 5, pp. 197-238.

21. J. D. Ferry, *Viscoelastic Properties of Polymers*, Wiley, 1980.

22. L. H. Sperling, in *Introduction to Physical Polymer Science*, Wiley, 2005, ch. 8, pp. 349-425.

23. G. Höhne, W. Hemminger and H. J. Flammersheim, *Differential Scanning Calorimetry*, Springer, 2003.

24. J. E. Mark, in *Physical Properties of Polymers Handbook*, Springer, 2007, ch. 37, pp. 611-617.

25. A. Guinier, *X-ray Diffraction in Crystals, Imperfect Crystals, and Amorphous Bodies*, Dover, 1994.

26. C. Suryanarayana and G. Norton, *X-Ray Diffraction: A Practical Approach*, Springer, 1998.

27. L. H. Sperling, in *Introduction to Physical Polymer Science*, Wiley, 2005, ch. 6, pp. 239-323.

28. L. Mandelkern, *Crystallization of polymers. Volume 1: Equilibrium Concepts*, Cambridge University Press, Cambridge,UK, 2002.

29. J. E. Mark, The Effect of Strain-Induced Crystallization on the Ultimate Properties of an Elastomeric Polymer Network, *Polymer Engineering & Science*, 1979, **19** (6), 409-413.

30. K. Sakurai and T. Takahashi, Strain-induced crystallization in polynorbornene, *J. Appl. Polym. Sci.*, 1989, **38**, 1191-1194.

31. I. J. Rao and K. R. Rajagopal, A study of strain-induced crystallization of polymers, *Int J Solid Struct*, 2001, **38**, 1149-1167.

32. Y. Zhu, J. Hu and K. Yeung, Effect of soft segment crystallization and hard segment physical crosslink on shape memory function in antibacterial segmented polyurethane ionomers, *Acta Biomater.*, 2009, **5**, 3346-3357.

33. G. Holden, N. R. Legge, R. Quirk and H. Schroeder, *Thermoplastic Elastomers*, Hanser Publishers ; Hanser/Gardner Publications, Munich; New York; Cincinnati, 1996.

34. R. Bonart and E. H. Müller, Phase separation in urethane elastomers as judged by low-angle X-ray scattering. I. Fundamentals *J Macrom Sci Part B: Phys*, 1974, **10** (1), 177-189.

35. H. S. Lee, Y. K. Wang and S. L. Hsu, Spectroscopic Analysis of Phase Separation Behaviour of Model Polyurethanes, *Macromolecules*, 1987, **20**, 2089-2095.

36. Y. Xu, Z. Petrovic, S. Das and G. L. Wilkes, Morphology and properties of thermoplastic polyurethanes with dangling chains in ricinoleate-based soft segments, *Polymer*, 2008, **49** (19), 4248-4258.

37. P. Ping, W. Wang, X. Chen and X. Jing, Poly(caprolactone) Polyurethane and Its Shape-Memory Property, *Biomacromolecules*, 2005, **6** (2), 587-592.

38. S. J. Chen, J. L. Hu, Y. Q. Liu, H. M. Liem, Y. Zhu and Q. H. Meng, Effect of molecular weight on shape memory behavior in polyurethane films, *Polym. Int.*, 2007, **56** (9), 1128-1134.

39. M. Bothe, F. Emmerling and T. Pretsch, Poly(ester urethane) with Varying Polyester Chain Length: Polymorphism and Shape-Memory Behavior, *Macromol. Chem. Phys.*, 2013, **214** (23), 2683-2693.

40. M. Momtaz, M. Razavi-Nouri and M. Barikani, Effect of block ratio and strain amplitude on thermal, structural, and shape memory properties of segmented polycaprolactone-based polyurethanes, *J. Mater. Sci.*, 2014, **49** (21), 7575-7584.

41. W. P. Chen and D. J. Kenney, Study of Phase Separation in Polyurethane Using Paramagnetic Labels. Effect of Soft Segment Molecular Weight, Structure, and Thermal History, *J. Polym. Sci., Part B: Polym. Phys.*, 1991, **29** (12), 1513-1524.

42. I. M. Pereira and R. L. Oréfice, The morphology and phase mixing studies on poly(ester–urethane) during shape memory cycle, *J. Mater. Sci.*, 2010, **45** (2), 511-522.

43. S. Mondal and J. L. Hu, Studies of shape memory property on thermoplastic segmented polyurethanes: Influence of PEG 3400, *J. Elastomers Plast.*, 2007, **39** (1), 81-91.

44. G. Oertel and L. Abele, *Polyurethane*, Hanser, 1993.

45. Q. Zhu, S. Feng and C. Zhang, Synthesis and thermal properties of polyurethane–polysiloxane crosslinked polymer networks, *J. Appl. Polym. Sci.*, 2003, **90** (1), 310-315.

46. B. Renault, T. Tassaing, E. Cloutet and H. Cramail, One-shot synthesis of high molar mass polyurethane in supercritical carbon dioxide, *J. Polym. Sci., Part A: Polym. Chem.*, 2007, **45** (23), 5649-5661.

47. M. Kashif, E. Sharmin, F. Zafar and S. Ahmad, Synthesis and Characterization of Ricinoleamide-Based Polyurethane, *J. Am. Oil Chem. Soc.*, 2011, **88** (12), 1989-1996.

48. K. Uhlig, *Polyurethan-Taschenbuch* Hanser, München, 1998.

49. C. S. Wong and K. H. Badri, Chemical Analyses of Palm Kernel Oil-Based Polyurethane Prepolymer, *Materials Sciences and Applications*, 2012, **3**, 78-86.

50. M. Szycher, in *Szycher's Handbook of Polyurethanes, Second Edition*, CRC Press Taylor & Francis Group, 2 edn., 2013, ch. 3, pp. 37-86.

51. EP0571830B1, 1993.

52. EP000001967537A1, 2008.

53. T. Pretsch and W. W. Müller, Shape memory poly(ester urethane) with improved hydrolytic stability, *Polym. Degrad. Stab.*, 2010, **95** (5), 880-888.

54. R. Chandra, B. P. Thapliyal and R. K. Soni, Stabilization of polyurethane films against thermal and photooxidative degradation, *Polym. Degrad. Stab.*, 1993, **39** (1), 93-101.

55. H. J. Jacobasch, K. Grundke, S. Schneider and F. Simon, The influence of additives on the adhesion behaviour of thermoplastic materials used in the automotive industry, *Prog. Org. Coat.*, 1995, **26** (2-4), 131-143.

56. S. V. Levchik and E. D. Weill, Thermal decomposition, combustion and fire-retardancy of polyurethanes - a review of the recent literature, *Polym. Int.*, 2004, **53** (11), 1585-1610.

57. D. K. Chattopadhyay and D. C. Webster, Thermal stability and flame retardancy of polyurethanes, *Prog. Polym. Sci.*, 2009, **34** (10), 1068-1133.

58. US4026931 A, 1977.

59. K. Gall, M. Mikulas, N. A. Munshi, F. Beavers and M. Tupper, Carbon fiber reinforced shape memory polymer composites, *J. Intell. Mater. Syst. Struct.*, 2000, **11** (11), 877-886.

60. T. Ohki, Q. Q. Ni, N. Ohsako and M. Iwamoto, Mechanical and shape memory behavior of composites with shape memory polymer, *Composites Part a-Applied Science and Manufacturing*, 2004, **35** (9), 1065-1073.

61. A. Elidrissi, O. Krim and S. Ousslimane, Effect of sequence concentrations on segmented polyurethanes properties, *Pigm. Resin. Technol.*, 2008, **37** (2), 73-79.

62. M. Szycher, in *Szycher's Handbook of Polyurethanes, Second Edition*, CRC Press Taylor & Francis Group, 2 edn., 2013, ch. 2, pp. 13-36.

63. M. S. M. Alger, *Polymer Science Dictionary*, Chapman & Hall, 1997.

64. G. Alliger and I. J. Sjothun, *Vulcanization of elastomers: principles and practice of vulcanization of commercial rubbers*, Reinhold Pub. Corp., 1964.

65. L. R. G. Treloar, in *The Physics of Rubber Elasticity*, Oxford University Press, Oxford, 1975, ch. 1, pp. 1-23.

66. L. R. G. Treloar, in *The Physics of Rubber Elasticity*, Oxford University Press, Oxford, 1975, ch. 2, pp. 24-41.

67. J. P. Pascault, H. Sautereau, J. Verdu and R. J. J. Williams, *Thermosetting Polymers*, Taylor & Francis, 2002.

68. C. May, *Epoxy Resins: Chemistry and Technology, Second Edition*, Taylor & Francis, 1987.

69. B. Ellis, *Chemistry and Technology of Epoxy Resins* Chapman & Hall, London, 1993.

70. D. Feldman and A. Barbalata, *Synthetic Polymers: Technology, Properties, Applications*, Springer, 1996.

71. I. Hamerton, *Recent Developments in Epoxy Resins*, Rapra Technology Limited, 1996.

72. B. Ellis, in *Chemistry and Technology of Epoxy Resins* Chapman & Hall, London, 1 edn., 1993, ch. 1, pp. 1-36.

73. A. Bhattacharya, Radiation and industrial polymers, *Prog. Polym. Sci.*, 2000, **25** (3), 371-401.

74. R. L. Clough, High-energy radiation and polymers: A review of commercial processes and emerging applications, *Nucl. Instr. Meth. Phys. Res. B*, 2001, **185** (1-4), 8-33.

75. C. Decker, The use of UV irradiation in polymerization, *Polym. Int.*, 1998, **45** (2), 133-141.

76. A. Lendlein and S. Kelch, Shape-Memory Polymers, *Angew. Chem. Int. Ed.*, 2002, **41** (12), 2034-2057.

77. B. Dietsch and T. Tong, A review - Features and benefits of shape memory polymers (SMPs), *J. Adv. Mater.*, 2007, **39** (2), 3-12.

78. C. Liu, H. Qin and P. T. Mather, Review of progress in shape-memory polymers, *J. Mater. Chem.*, 2007, **17** (16), 1543-1558.

79. J. Hu, Y. Zhu, H. Huang and J. Lu, Recent advances in shape memory polymers: Structure, mechanism, functionality, modeling and applications, *Prog. Polym. Sci.*, 2012, **37** (12), 1720-1763.

80. X. Lan, J. S. Leng, Y. J. Liu and S. Y. Du, in *Multi-Functional Materials and Structures, Pts 1 and 2*, eds. A. K. T. Lau, J. Lu, V. K. Varadan, F. K. Chang, J. P. Tu and P. M. Lam, Trans Tech Publications Ltd, Stafa-Zurich, 2008, vol. 47-50, pp. 714-717.

81. J. S. Leng, X. Lan, Y. J. Liu, S. Y. Du, W. M. Huang, N. Liu, S. J. Phee and Q. Yuan, Electrical conductivity of thermoresponsive shape-memory polymer with embedded micron sized Ni powder chains, *Appl. Phys. Lett.*, 2008, **92**, art. no. 014104.

82. L. Petit, B. Guiffard, L. Seveyrat and D. Guyomar, Actuating abilities of electroactive carbon nanopowder/polyurethane composite films, *Sens. Actuator A-Phys.*, 2008, **148** (1), 105-110.

83. P. R. Buckley, G. H. McKinley, T. S. Wilson, W. Small, W. J. Benett, J. P. Bearinger, M. W. McElfresh and D. J. Maitland, Inductively Heated Shape Memory Polymer for the Magnetic Actuation of Medical Devices, *IEEE Trans. Biomed. Eng.*, 2006, **53** (10), 2075-2083.

84. M. Y. Razzaq, M. Behl, K. Kratz and A. Lendlein, Multifunctional Hybrid Nanocomposites with Magnetically Controlled Reversible Shape–Memory Effect, *Adv. Mater.*, 2013, **25** (40), 5730-5733.

85. A. Lendlein, H. Jiang, O. Jünger and R. Langer, Light-induced shape-memory polymers, *Nature*, 2005, **434**, 879-882.

86. J. Leng, X. Wu and Y. Liu, Infrared light-active shape memory polymer filled with nanocarbon particles, *J. Appl. Polym. Sci.*, 2009, **114** (4), 2455-2460.

87. Y. Liu, J. K. Boyles, J. Genzer and M. D. Dickey, Self-folding of polymer sheets using local light absorption, *Soft Matter*, 2012, **8** (6), 1764-1769.

88. J. Leng, X. Lan, Y. Liu and S. Du, Shape-memory polymers and their composites: Stimulus methods and applications, *Prog. Mater Sci.*, 2011, **56** (7), 1077-1135.

89. T. Pretsch, I. Jakob and W. Müller, Hydrolytic degradation and functional stability of a segmented shape memory poly(ester urethane), *Polym. Degrad. Stab.*, 2009, **94** (1), 61-73.

90. T. Pretsch, Durability of a polymer with triple-shape properties, *Polym. Degrad. Stab.*, 2010, **95** (12), 2515-2524.

91. W. W. Müller and T. Pretsch, Hydrolytic aging of crystallizable shape memory poly(ester urethane): Effects on the thermo-mechanical properties and visco-elastic modeling, *Eur. Polym. J.*, 2010, **46** (8), 1745-1758.

92. T. Pretsch, Triple-shape properties of a thermoresponsive poly(ester urethane), *Smart Mater. Struct.*, 2010, **19** (1), art. no. 015006.

93. Cornerstone Research Group Inc., CRG Introduces Veriflex® E (Epoxy SMP), http://www.crgrp.com/news/crg-introduces-veriflex-e-epoxy-smp.

94. F. Castro, K. K. Westbrook, J. Hermiller, D. U. Ahn, Y. Ding and H. J. Qi, Time and Temperature Dependent Recovery of Epoxy-Based Shape Memory Polymers, *J. Eng. Mater. Technol.*, 2011, **133** (2), 021025-021025.

95. T. Pretsch, M. Ecker, M. Schildhauer and M. Maskos, Switchable information carriers based on shape memory polymer, *J. Mater. Chem.*, 2012, **22** (16), 7757-7766.

96. R. J. Young and P. A. Lovell, in *Introduction to Polymers, Third Edition*, Taylor & Francis, 2011, ch. 4, pp. 241-309.

97. M. Behl and A. Lendlein, Triple-shape polymers, *J. Mater. Chem.*, 2010, **20**, 3335-3345.

98. M. Bothe, K. Y. Mya, E. M. Jie Lin, C. C. Yeo, X. Lu, C. He and T. Pretsch, Triple-shape properties of star-shaped POSS-polycaprolactone polyurethane networks, *Soft Matter*, 2012, **8** (4), 965-972.

99. Q. Ge, X. Luo, C. B. Iversen, P. T. Mather, M. L. Dunn and H. J. Qi, Mechanisms of triple-shape polymeric composites due to dual thermal transitions, *Soft Matter*, 2013, **9** (7), 2212-2223.

100. X. F. Yang, L. Wang, W. X. Wang, H. M. Chen, G. Yang and S. B. Zhou, Triple Shape Memory Effect of Star-Shaped Polyurethane, *ACS Appl. Mater. Interfaces*, 2014, **6** (9), 6545-6554.

101. I. Bellin, S. Kelch, R. Langer and A. Lendlein, Polymeric triple-shape materials, *Proceedings of the National Academy of Sciences of the United States of America*, 2006, **103** (48), 18043-18047.

102. T. Xie, Tunable polymer multi-shape memory effect, *Nature*, 2010, **464** (7286), 267-270.

103. H. Meng, H. Mohamadian, M. Stubblefield, D. Jerro, S. Ibekwe, S.-S. Pang and G. Li, Various shape memory effects of stimuli-responsive shape memory polymers, *Smart Mater. Struct.*, 2013, **22** (9), 093001.

104. T. Chung, A. Romo-Uribe and P. T. Mather, Two-Way Reversible Shape Memory in a Semicrystalline Network, *Macromolecules*, 2008, **41**, 184-192.

105. S. Chen, J. Hu and H. Zhuo, Properties and mechanism of two-way shape memory polyurethane composites, *Compos. Sci. Technol.*, 2010, **70** (10), 1437-1443.

106. M. Behl, J. Zotzmann and A. Lendlein, One-way and reversible dual-shape effect of polymer networks based on polypentadecalactone segments, *Int. J. Artif. Organs*, 2011, **34** (2), 231-237.

107. J. Li, W. R. Rodgers and T. Xie, Semi-crystalline two-way shape memory elastomer, *Polymer*, 2011, **52** (23), 5320-5325.

108. M. Bothe and T. Pretsch, Two-Way Shape Changes of a Shape-Memory Poly(ester urethane), *Macromol. Chem. Phys.*, 2012, **213** (22), 2378-2385.

109. M. Behl, K. Kratz, U. Noechel, T. Sauter and A. Lendlein, Temperature-memory polymer actuators, *Proc. Natl. Acad. Sci. USA*, 2013, **110** (31), 12555-12559.

110. M. Behl, K. Kratz, J. Zotzmann, U. Nochel and A. Lendlein, Reversible bidirectional shape-memory polymers, *Adv. Mater.*, 2013, **25** (32), 4466-4469.

111. M. Bothe and T. Pretsch, Bidirectional actuation of a thermoplastic polyurethane elastomer, *J. Mater. Chem. A*, 2013, **1** (46), 14491-14497.

112. H. Tamagawa, Thermo-responsive two-way shape changeable polymeric laminate, *Mater. Lett.*, 2010, **64** (6), 749-751.

113. G. Qi, K. W. Kristofer, T. M. Patrick, L. D. Martin and H. J. Qi, Thermomechanical behavior of a two-way shape memory composite actuator, *Smart Mater. Struct.*, 2013, **22** (5), art. no. 055009.

114. S. Imai and K. Sakurai, An actuator of two-way behavior by using two kinds of shape memory polymers with different Tgs, *Precis. Eng.*, 2013, **37** (3), 572-579.

115. S. Chen, J. Hu, H. Zhuo and Y. Zhu, Two-way shape memory effect in polymer laminates, *Mater. Lett.*, 2008, **62** (25), 4088-4090.

116. K. K. Westbrook, P. T. Mather, V. Parakh, M. L. Dunn, Q. Ge, B. M. Lee and H. J. Qi, Two-way reversible shape memory effects in a free-standing polymer composite, *Smart Mater. Struct.*, 2011, **20**, art. no. 065010.

117. M. Behl, M. Y. Razzaq and A. Lendlein, Multifunctional Shape-Memory Polymers, *Adv. Mater.*, 2010, **22** (31), 3388-3410.

118. J. Leng and S. Du, *Shape-memory polymers and multifunctional composites*, CRC Press/Taylor & Francis, Boca Raton, 2010.

119. K. Gall, M. Mikulas, N. A. Munshi and M. Tupper, Carbon Fiber Reinforced Shape Memory Polymer Composites, *J. Intell. Mater. Syst. Struct.*, 2000, **11**, 877-886.

120. J. S. Leng, H. B. Lv, Y. J. Liu and S. Y. Du, Electroactive shape-memory polymer filled with nanocarbon particles and short carbon fibers, *Appl. Phys. Lett.*, 2007, **91**, art. no. 144105.

121. H. Lu, Y. Liu, J. Gou, J. Leng and S. Du, Electroactive shape-memory polymer nanocomposites incorporating carbon nanofiber paper, *International Journal of Smart and Nano Materials*, 2010, **1** (1), 2-12.

122. H. Koerner, G. Price, N. A. Pearce, M. Alexander and R. A. Vaia, Remotely actuated polymer nanocomposites - stress-recovery of carbon-nanotube-filled thermoplastic elastomers, *Nature Mater.*, 2004, **3** (2), 115-120.

123. J. W. Cho, J. W. Kim, Y. C. Jung and N. S. Goo, Electroactive shape-memory polyurethane composites incorporating carbon nanotubes, *Macromol. Rapid Commun.*, 2005, **26** (5), 412-416.

124. Q. Meng, J. Hu and L. Yeung, An electro-active shape memory fibre by incorporating multi-walled carbon nanotubes, *Smart Mater. Struct.*, 2007, **16**, 830-836.

125. J. S. Leng, W. M. Huang, X. Lan, Y. J. Liu and S. Y. Du, Significantly reducing electrical resistivity by forming conductive Ni chains in a polyurethane shape-memory polymer/carbon-black composite, *Appl. Phys. Lett.*, 2008, **92**, art. no. 204101.

126. K. Wongtimnoi, B. Guiffard, A. Bogner-Van de Moortele, L. Seveyrat, C. Gauthier and J. Y. Cavaille, Improvement of electrostrictive properties of a polyether-based polyurethane elastomer filled with conductive carbon black, *Compos. Sci. Technol.*, 2011, **71** (6), 885-892.

127. C. S. Hazelton, S. C. Arzberger, M. S. Lake and N. A. Munshi, RF actuation of a thermoset shape memory polymer with embedded magnetoelectroelastic particles, *J. Adv. Mater.*, 2007, **39** (3), 35-39.

128. P. Martins and S. Lanceros-Méndez, Polymer-Based Magnetoelectric Materials, *Adv. Funct. Mater.*, 2013, **23** (27), 3371-3385.

129. A. M. Schmidt, Electromagnetic Activation of Shape Memory Polymer Networks Containing Magnetic Nanoparticles, *Macromol. Rapid Commun.*, 2006, **27** (14), 1168-1172.

130. M. Y. Razzaq, M. Anhalt, L. Frormann and B. Weidenfeller, Mechanical spectroscopy of magnetite filled polyurethane shape memory polymers, *Mater. Sci. Eng., A*, 2007, **471** (1-2), 57-62.

131. G. Vialle, M. A. D. Prima, E. Hocking, K. Gall, H. Garmestani, T. Sanderson, S. Arzberger and D. Campbell, Remote activation of nanomagnetite reinforced shape memory polymer foam, *Smart Mater. Struct.*, 2009, **18**, art. no. 115014.

132. S. A. Madbouly and A. Lendlein, in *Adv. Polym. Sci.*, ed. A. Lendlein, Springer Berlin Heidelberg, 2010, vol. 226, ch. 28, pp. 41-95.

133. D. Yang, W. Huang, X. He and M. Xie, Electromagnetic activation of a shape memory copolymer matrix incorporating ferromagnetic nanoparticles, *Polym. Int.*, 2012, **61** (1), 38-42.

134. D. J. Maitland, M. F. Metzger, D. Schumann, A. Lee and T. S. Wilson, Photothermal properties of shape memory polymer micro-actuators for treating stroke, *Lasers Surg. Med.*, 2002, **30** (1), 1-11.

135. W. Small, T. S. Wilson, W. J. Benett, J. M. Loge and D. J. Maitland, Laser-activated shape memory polymer intravascular thrombectomy device, *Opt. Express*, 2005, **13** (20), 8204-8213.

136. H. Zhang, H. Xia and Y. Zhao, Optically triggered and spatially controllable shape-memory polymer-gold nanoparticle composite materials, *J. Mater. Chem.*, 2012, **22** (3), 845-849.

137. Q. H. Shou, K. Uto, M. Iwanaga, M. Ebara and T. Aoyagi, Near-infrared light-responsive shape-memory poly(epsilon-caprolactone) films that actuate in physiological temperature range, *Polym. J.*, 2014, **46** (8), 492-498.

138. J. S. Leng, X. L. Wu and Y. J. Liu, Infrared Light-Active Shape Memory Polymer Filled with Nanocarbon Particles, *J. Appl. Polym. Sci.*, 2009, **114** (4), 2455-2460.

139. W. M. Huang, Y. Zhao, C. C. Wang, Z. Ding, H. Purnawali, C. Tang and J. L. Zhang, Thermo/chemo-responsive shape memory effect in polymers: a sketch of working mechanisms, fundamentals and optimization, *J. Polym. Res.*, 2012, **19** (9), 1-34.

140. H. Chen, Y. Li, Y. Liu, T. Gong, L. Wang and S. Zhou, Highly pH-sensitive polyurethane exhibiting shape memory and drug release, *Polymer Chemistry*, 2014, **5** (17), 5168-5174.

141. H. Lu and W. M. Huang, A phenomenological model for the chemo-responsive shape memory effect in amorphous polymers undergoing viscoelastic transition, *Smart Mater. Struct.*, 2013, **22** (11), art. no. 115019.

142. B. Yang, W. M. Huang, C. Li, C. M. Lee and L. Li, On the effects of moisture in a polyurethane shape memory polymer, *Smart Mater. Struct.*, 2004, **13**, 191-195.

143. W. M. Huang, B. Yang, L. An, C. Li and Y. S. Chan, Water-driven programmable polyurethane shape memory polymer: Demonstration and mechanism, *Appl. Phys. Lett.*, 2005, **86** (11), art. no. 114105.

144. B. F. Pierce, K. Bellin, M. Behl and A. Lendlein, Demonstrating the influence of water on shape-memory polymer networks based on poly (rac-lactide)-co-glycolide segments in vitro, *International Journal of Artificial Organs*, 2011, **34** (2), 172-179.

145. R. W. Lenz, Biodegradable Polymers, *Adv. Polym. Sci.*, 1993, **107**, 1-40.

146. A. Lendlein and R. Langer, Biodegradable, elastic shape-memory polymers for potential biomedical applications, *Science*, 2002, **296** (5573), 1673-1676.

147. Y. L. Wang, Y. G. Li, Y. F. Luo, M. N. Huang and Z. Q. Liang, Synthesis and characterization of a novel biodegradable thermoplastic shape memory polymer, *Mater. Lett.*, 2009, **63** (3-4), 347-349.

148. H. Deka, N. Karak, R. D. Kalita and A. K. Buragohain, Biocompatible hyperbranched polyurethane/multi-walled carbon nanotube composites as shape memory materials, *Carbon*, 2010, **48** (7), 2013-2022.

149. L. Xue, S. Dai and Z. Li, Biodegradable shape-memory block co-polymers for fast self-expandable stents, *Biomaterials*, 2010, **31** (32), 8132-8140.

150. J. Kunzelman, B. R. Crenshaw, M. Kinami and C. Weder, Self-Assembly and Dispersion of Chromogenic Molecules: A Versatile and General Approach for Self-Assessing Polymers, *Macromol Rapid Commun*, 2006, **27**, 1981-1987.

151. J. Kunzelman, T. Chung, P. T. Mather and C. Weder, Shape memory polymers with built-in threshold temperature sensors, *J. Mater. Chem.*, 2008, **18** (10), 1082-1086.

152. W. Small, P. Singhal, T. S. Wilson and D. J. Maitland, Biomedical applications of thermally activated shape memory polymers, *J. Mater. Chem.*, 2010, **20**, 3356-3366.

153. M. C. Serrano and G. A. Ameer, Recent Insights Into the Biomedical Applications of Shape-memory Polymers, *Macromol. Biosci.*, 2012, **12** (9), 1156-1171.

154. J. Ishizawa, K. Imagawa, S. Minami, S. Hayashi and N. Miwa, Research on Application of Shape Memory Polymers to Space Inflatable Systems, in *Proceeding of the 7th International Symposium on Artificial Intelligence, Robotics and Automation in Space: i-SAIRAS*, Nara, Japan, 2003, pp.

155. Y. Liu and J. Leng, in *Shape-Memory Polymers and Multifunctional Composites*, eds. J. Leng and S. Du, CRC Press, 2010, pp. 233-266.

156. Y. Liu, H. Du, L. Liu and J. Leng, Shape memory polymers and their composites in aerospace applications: a review, *Smart Mater. Struct.*, 2014, **23** (2), art. no. 023001.

157. H. R. Matilla, *Intelligent textiles and clothing*, Woodhead Publishing in Textiles, 2006.

158. J. Hu, *Shape memory polymers and textiles*, Woodhead Publishing Limited and CRC Press LLC, Cambridge, Boca Raton, 2007.

159. J. Hu and S. Chen, A review of actively moving polymers in textile applications, *J. Mater. Chem.*, 2010, **20** (17), 3346-3355.

160. J. Hu, H. Meng, G. Li and S. I. Ibekwe, A review of stimuli-responsive polymers for smart textile applications, *Smart Mater. Struct.*, 2012, **21** (5), art. no. 053001.

161. C. Wischke, A. T. Neffe, S. Steuer and A. Lendlein, Evaluation of a degradable shape-memory polymer network as matrix for controlled drug release, *J. Controlled Release*, 2009, **138**, 243-250.

162. C. Wischke and A. Lendlein, Shape-Memory Polymers as Drug Carriers - A Multifunctional System, *Pharm. Res.*, 2010, **27** (4), 527-529.

163. J. N. Rodriguez, F. J. Clubb, T. S. Wilson, M. W. Miller, T. W. Fossum, J. Hartman, E. Tuzun, P. Singhal and D. J. Maitland, In vivo response to an implanted shape memory polyurethane foam in a porcine aneurysm model, *J. Biomed. Mater. Res. Part A*, 2014, **102** (5), 1231-1242.

164. M. C. Chen, H. W. Tsai, Y. Chang, W. Y. Lai, F. L. Mi, C. T. Liu, H. S. Wong and H. W. Sung, Rapidly self-expandable polymeric Stents with a shape-memory property, *Biomacromolecules*, 2007, **8** (9), 2774-2780.

165. K. E. Smith, M. Garcia, K. McAnuff, R. Lamell, C. M. Yakacki, J. Griffis, G. B. Higgs and K. Gall, Anterior cruciate ligament fixation: Is radial force a predictor of the pullout strength of soft-tissue interference devices?, *The Knee*, 2012, **19** (6), 786-792.

166. A. Nakasima, J. R. Hu, M. Ichinose and H. Shimada, Potential application of shape memory plastic as elastic material in clinical orthodontics, *Eur. J. Orthodont.*, 1991, **13**, 179-186.

167. C. M. Yakacki, R. Shandas, C. Lanning, B. Rech, A. Eckstein and K. Gall, Unconstrained recovery characterization of shape-memory polymer networks for cardiovascular applications, *Biomaterials*, 2007, **28**, 2255-2263.

168. M. S. Lake and D. Campbell, The fundamentals of designing deployable structures with elastic memory composites, *IEEE Trans Aerospace Conf Proc*, 2004, 2745-2756.

169. L. Xin, L. Yanju, L. Haibao, W. Xiaohua, L. Jinsong and D. Shanyi, Fiber reinforced shape-memory polymer composite and its application in a deployable hinge, *Smart Mater. Struct.*, 2009, **18** (2), art. no. 024002.

170. D. Campbell, R. Barrett, M. S. Lake, L. Adams, E. Abrahamson, M. R. Scherbarth, G. Freebury, N. Beidleman and J. Abbot, Development of a Novel, Passively Deployed Solar Array, *American Institute of Aeronautics and Astronautics*, 2006, 1-8.

171. W. Sokolowski, S. Tan, P. Willis and M. Pryor, Shape memory self-deployable structures for solar sails, *Proceedings of SPIE - The International Society for Optical Engineering*, 2008, **7267**, art. no. 72670K.

172. Y. Y. F. Chan Vili, Investigating Smart Textiles Based on Shape Memory Materials, *Text. Res. J.*, 2007, **77** (5), 290-300.

173. J. Hu, in *Shape-Memory Polymers and Multifunctional Composites*, eds. J. Leng and S. Du, CRC Press, 2010, pp. 293-313.

174. J. L. Hu, Y. M. Zeng and H. J. Yan, Influence of Processing Conditions on the Microstructure and Properties of Shape Memory Polyurethane Membranes, *Text. Res. J.*, 2003, **73**, 172-178.

175. A. Gugliuzza and E. Drioli, A review on membrane engineering for innovation in wearable fabrics and protective textiles, *J. Membr. Sci.*, 2013, **446**, 350-375.

176. F. H. Mahnke, *Color, Environment, and Human Response: An Interdisciplinary Understanding of Color and Its Use as a Beneficial Element in the Design of the Architectural Environment*, Wiley, 1996.

177. H. Zollinger, *Color Chemistry*, Wiley VCH, 2003.

178. R. G. Kuehni, *Color: An Introduction to Practice and Principles*, Wiley, 2004.

179. R. G. Kuehni, *Color Vision & Technology*, American Association of Textile Chemists and Colorists, 2008.

180. G. N. Lewis and M. Calvin, The Color of Organic Substances, *Chem. Rev.*, 1939, **25** (2), 273-328.

181. CIE 15.3:2004, *Colorimetry*

182. DIN 5033-1:2009-05, *Colorimetry*

183. R. G. Kuehni, *Color Space and Its Divisions: Color Order from Antiquity to the Present*, Wiley, 2003.

184. R. G. Kuehni, in *Color Vision & Technology*, American Association of Textile Chemists and Colorists, 2008, ch. 4, pp. 134-137.

185. R. G. Kuehni, in *Color Space and Its Divisions: Color Order from Antiquity to the Present*, Wiley, 2003, ch. 2.29, pp. 100-101.

186. DIN 5033-2:1992-5, *Colorimetry*

187. Quark67, Additive color mixing with RGB colors, Wikimedia Commons, licensed under CreativeCommons CC0 1.0.

188. Quark67, Subtractive color mixing with CMY colors (without black), Wikimedia Commons, licensed under CreativeCommons CC0 1.0.

189. CIE 135/1-1999, *CIE Collection 1999 - Vision and Colour - Physical Measurement of Light and Radiation*.

190. CIE S 017/E:2011, *ILV: International Lighting Vocabulary*.

191. U. Häßler, Lab: Farben vergleichen und Farbabstand, http://www.wisotop.de/farbabstand-farben-vergleichen.shtml.

192. D. F. Duxbury, The photochemistry and photophysics of triphenylmethane dyes in solid and liquid media, *Chem. Rev.*, 1993, **93** (1), 381-433.

193. Y. Mido, in *Chemistry of Colour*, Discovery Publishing House, 1995, ch. 6, pp. 92-125.

194. G. Wolfschmidt, in *Farben in Kulturgeschichte und Naturwissenschaft*, tredition, 2011, ch. 16.5, pp. 300-302.

195. A. Baeyer, Ueber eine neue Klasse von Farbstoffen, *Berichte der deutschen chemischen Gesellschaft*, 1871, **4** (2), 555-558.

196. A. Baeyer, Ueber die Phenolfarbstoffe, *Berichte der deutschen chemischen Gesellschaft*, 1871, **4** (2), 658-665.

197. O. W. Kolling and M. L. Smith, Selected Triphenylmethane Dyes as Acid-Base Indicators in Glacial Acetic Acid, *Anal. Chem.*, 1959, **31** (11), 1876-1879.

198. R. W. Sabnis, *Handbook of Acid-Base Indicators*, Taylor & Francis, 2007.

199. R. D. Combes and R. B. Havelandsmith, A review of the genotoxicity of food, drug and cosmetic colours and other azo, triphenylmethane and xanthene dyes, *Mutat. Res.*, 1982, **98** (2), 101-243.

200. EP1471116 B1, 2008.

201. H. Zollinger, in *Color Chemistry* Wiley VCH, 2003, ch. 4, pp. 101-122.

202. Magnus, Carsten Triphenylmethanfarbstoffe, http://www.ruschmidt.de/FarbSite/pages/CMagnus/CMagnus.html.

203. A. Seeboth and D. Lötzsch, in *Thermochromic and Thermotropic Materials*, Pan Stanford Publishing Pte. Ltd., Singapore, 2014, ch. 2.2 pp. 41-45.

204. M. Toba, Y. Takeoka and M. Rikukawa, Thermochromic and solvatochromic properties of poly(thiophene) derivatives with liquid crystal moiety, *Synth. Met.*, 2003, **135** (1-3), 339-340.

205. S.-J. Yoon, J. H. Kim, K. S. Kim, J. W. Chung, B. Heinrich, F. Mathevet, P. Kim, B. Donnio, A.-J. Attias, D. Kim and S. Y. Park, Mesomorphic Organization and Thermochromic Luminescence of Dicyanodistyrylbenzene-Based Phasmidic Molecular Disks: Uniaxially Aligned Hexagonal Columnar Liquid Crystals at Room Temperature with Enhanced Fluorescence Emission and Semiconductivity, *Adv. Funct. Mater.*, 2012, **22** (1), 61-69.

206. J.-W. Wang and B.-Y. Zhang, Synthesis and optical properties of cholesteric liquid-crystalline oligomers displaying reversible thermochromism, *J. Appl. Polym. Sci.*, 2013, **130** (2), 1321-1327.

207. A. Seeboth and D. Lötzsch, in *Thermochromic and Thermotropic Materials*, Pan Stanford Publishing Pte. Ltd., Singapore, 2014, ch. 1.2, pp. 3-27.

208. A. Seeboth, A. Klukowska, R. Ruhmann and D. Lötzsch, Thermochromic polymer materials, *Chin. J. Polym. Sci.*, 2007, **25** (2), 123-135.

209. A. Seeboth and D. Lötzsch, in *Thermochromic phenomena in polymers*, Smithers Rapra Technology Limited, Shrewsbury, England, 2008, ch. 3.1, pp. 17-21.

210. A. Seeboth and D. Lötzsch, in *Thermochromic and Thermotropic Materials*, Pan Stanford Publishing Pte. Ltd., Singapore, 2014, ch. 2.8 pp. 67-77.

211. M. Kronstein, K. Kriechbaum, J. Akbarzadeh, H. Peterlik and M.-A. Neouze, Irreversible thermochromism in copper chloride Imidazolium Nanoparticle Networks, *PCCP*, 2013, **15** (30), 12717-12723.

212. A. Seeboth and D. Lötzsch, *Thermochromic phenomena in polymers*, Smithers Rapra Technology Limited, Shrewsbury, England, 2008.

213. A. Seeboth and D. Lötzsch, *Thermochromic and Thermotropic Materials*, Pan Stanford Publishing Pte. Ltd., Singapore, 2014.

214. M. Gaudon, P. Deniard, L. Voisin, G. Lacombe, F. Darnat, A. Demourgues, J. L. Perillon and S. Jobic, How to mimic the thermo-induced red to green transition of ruby with control of the temperature via the use of an inorganic materials blend?, *Dyes Pigments*, 2012, **95** (2), 344-350.

215. M. Friesel, B. Baranowski and A. Lunden, Phase transitions of the system silver mercury iodide (Ag2HgI4)-copper mercury iodide (Cu2HgI4) at normal and high pressure studied by differential scanning calorimetry, *The Journal of Physical Chemistry*, 1990, **94** (3), 1113-1117.

216. A. Seeboth and D. Lötzsch, in *Thermochromic and Thermotropic Materials*, Pan Stanford Publishing Pte. Ltd., Singapore, 2014, ch. 2.3, pp. 45-51.

217. R. M. Christie and I. D. Bryant, An evaluation of thermochromic prints based on microencapsulated liquid crystals using variable temperature colour measurement, *Color. Technol.*, 2005, **121** (4), 187-192.

218. P. T. Ireland and T. V. Jones, The response time of a surface thermometer employing encapsulated thermochromic liquid crystals *Journal of Physics E-Scientific Instruments*, 1987, **20** (10), 1195-1199.

219. M. A. White and M. LeBlanc, Thermochromism in commercial products, *J. Chem. Educ.*, 1999, **76** (9), 1201-1205.

220. R. Kulčar, M. Friškovec, N. Hauptman, A. Vesel and M. K. Gunde, Colorimetric properties of reversible thermochromic printing inks, *Dyes Pigments*, 2010, **86** (3), 271-277.

221. S. Lakio, J. Heinamaki and J. Yliruusi, Colorful Drying, *AAPS PharmSciTech*, 2010, **11** (1), 46-53.

222. R. Kulčar, M. Friškovec, M. K. Gunde and N. Knešaurek, Dynamic colorimetric properties of mixed thermochromic printing inks, *Color. Technol.*, 2011, **127** (6), 411-417.

223. R. Arshady, Microspheres and microcapsules: A survey of manufacturing techniques. Part 1: Suspension cross-linking, *Polymer Engineering & Science*, 1989, **29** (24), 1746-1758.

224. H. Kage, H. Kawahara, N. Hamada, T. Kotake and H. Ogura, Operating conditions and microcapsules generated by in situ polymerization, *Adv. Powder Technol.*, 2002, **13** (3), 265-285.

225. H. Zhang and X. Wang, Fabrication and performances of microencapsulated phase change materials based on n-octadecane core and resorcinol-modified melamine–formaldehyde shell, *Colloids Surf. Physicochem. Eng. Aspects*, 2009, **332** (2-3), 129-138.

226. L. Bayés-García, L. Ventolà, R. Cordobilla, R. Benages, T. Calvet and M. A. Cuevas-Diarte, Phase Change Materials (PCM) microcapsules with different shell compositions: Preparation, characterization and thermal stability, *Sol. Energy Mater. Sol. Cells*, 2010, **94** (7), 1235-1240.

227. B. Šumiga, E. Knez, M. Vrtačnik, V. F. Savec, M. Starešinič and B. Boh, Production of Melamine-Formaldehyde PCM Microcapsules with Ammonia Scavenger used for Residual Formaldehyde Reduction, *Acta Chim. Slov.*, 2011, **58** (1), 14-25.

228. Z. Wu, X. Ma, X. Zheng, W. Yang, Q. Meng and Z. Zheng, Synthesis and characterization of thermochromic energy-storage microcapsule and application to fabric, *Journal of the Textile Institute*, 2014, **105** (4), 398-405.

229. A. Seeboth and D. Lötzsch, in *Thermochromic phenomena in polymers*, Smithers Rapra Technology Limited, Shrewsbury, England, 2008, ch. 3, pp. 17-48.

230. B. Boh, E. Knez and B. Sumiga, Microencapsulation of phase change materials by in situ polymerisation, in *XVIth International Conference on Bioencapsulation*, Dublin, Ireland, 2008, pp. 1-4.

231. S. M. Burkinshaw, J. Griffiths and A. D. Towns, Reversibly thermochromic systems based on pH-sensitive functional dyes, *J. Mater. Chem.*, 1998, **8** (12), 2677-2683.

232. C. F. Zhu and A. B. Wu, Studies on the synthesis and thermochromic properties of crystal violet lactone and its reversible thermochromic complexes, *Thermochim. Acta*, 2005, **425** (1-2), 7-12.

233. A. Seeboth, D. Lötzsch, E. Potechius and R. Vetter, Thermochromic Effects of Leuco Dyes studied in polypropylene, *Chin. J. Polym. Sci.*, 2006, **24** (04), 363-368.

234. D. C. MacLaren and M. A. White, Dye-developer interactions in the crystal violet lactone-lauryl gallate binary system: implications for thermochromism, *J. Mater. Chem.*, 2003, **13** (7), 1695-1700.

235. D. C. MacLaren and M. A. White, Competition between dye-developer and solvent-developer interactions in a reversible thermochromic system, *J. Mater. Chem.*, 2003, **13** (7), 1701-1704.

236. D. C. MacLaren and M. A. White, Design rules for reversible thermochromic mixtures, *J. Mater. Sci.*, 2005, **40** (3), 669-676.

237. J. Luthern and A. Peredes, Determination of the stoichiometry of a thermochromic color complex via Job's method, *J. Mater. Sci. Lett.*, 2000, **19** (3), 185-188.

238. D. Aitken, S. M. Burkinshaw, J. Griffiths and A. D. Towns, Textile applications of thermochromic systems, *Review of Progress in Coloration and Related Topics*, 1996, **26** (1), 1-8.

239. ISO/IEC 15420:2009-12, *Information technology - Automatic identification and data capture techniques - EAN/UPC bar code symbology specification*.

240. A. Q. Morton, Packaging history: The emergence of the uniform product code (UPC) in the United States, 1970–75, *History and Technology*, 1994, **11** (1), 101-111.

241. ISO/IEC 18004:2000(E), *Information technology - Automatic identification and data capture techniques - Bar code symbology - QR Code*.

242. ISO/IEC 16022:2006(E), *Information technology - Automatic identification and data capture techniques - Data Matrix bar code symbology specification*.

243. ISO/IEC 16023:2000-05 *Information technology - International symbology specification - MaxiCode*.

244. ISO/IEC 24778:2008-02, *Information technology - Automatic identification and data capture techniques - Aztec Code bar code symbology specification*.

245. Deutsche Bahn, The Online-Ticket in a few steps - Step 11, http://www.bahn.de/hilfe/view/pk/en/ticketbuchung/ot-schritt11.shtml.

246. S. C. D. J. Lin, *Error control coding : fundamentals and applications*, Prentice-Hall, Englewood Cliffs, N.J., 1983.

247. I. S. Reed and G. Solomon, Polynomial codes over certain finite fields, *Journal of the Society for Industrial and Applied Mathematics*, 1960, **8** (2), 300-304.

248. Denso Wave Inc., QR code.com Answers to your questions about the QR Code, http://www.qrcode.com/en/.

249. EP0672994 (A1) 1995.

250. Bobmath, QR Character Placement, Wikimedia Commons, licensed under CreativeCommons CC0 1.0.

251. T. Staake, F. Thiesse and E. Fleisch, The emergence of counterfeit trade: a literature review, *European Journal of Marketing*, 2009, **43** (3), 320-349.

252. European Union, *Report on EU customs enforcement of intellectual property rights. Results at the EU border 2012*, Luxembourg, 2013.

253. P. Aldhous, Counterfeit pharmaceuticals: Murder by medicine, *Nature*, 2005, **434** (7030), 132-136.

254. A. K. Deisingh, Pharmaceutical counterfeiting, *Analyst*, 2005, **130** (3), 271-279.

255. F. M. Fernandez, M. D. Green and P. N. Newton, Prevalence and Detection of Counterfeit Pharmaceuticals: A Mini Review, *Industrial & Engineering Chemistry Research*, 2008, **47** (3), 585-590.

256. B. Yoon, J. Lee, I. S. Park, S. Jeon, J. Lee and J.-M. Kim, Recent functional material based approaches to preventing and detecting counterfeiting, *J. Mater. Chem. C*, 2013, **1** (13), 2388-2403.

257. B. Hardwick, W. Jackson, G. Wilson and A. W. H. Mau, Advanced Materials for Banknote Applications, *Adv. Mater.*, 2001, **13** (12-13), 980-984.

258. R. Y. Shah, P. N. Prajapati and Y. K. Agrawal, Anticounterfeit packaging technologies, *J Adv Pharm Tech Res*, 2010, **1** (4), 368-373.

259. F. Been, Y. Roggo, K. Degardin, P. Esseiva and P. Margot, Profiling of counterfeit medicines by vibrational spectroscopy, *Forensic Sci. Int.*, 2011, **211** (1-3), 83-100.

260. T. Staake, F. Thiesse and E. Fleisch, Business strategies in the counterfeit market, *Journal of Business Research*, 2012, **65** (5), 658-665.

261. Y. Qian, Brand Management and Strategies Against Counterfeits, *Journal of Economics & Management Strategy*, 2014, **23** (2), 317-343.

262. L. Jacobs, A. C. Samli and T. Jedlik, The Nightmare of International Product Piracy: Exploring Defensive Strategies, *Industrial Marketing Management*, 2001, **30** (6), 499-509.

263. G. Power, in *Facts|Activities|Documents developed by the Assembly and the Working Groups of IMPACT*, ed. I.-I. M. P. A.-C. Taskforce, Italy, 2011, ch. 6.2, pp. 144-154.

264. S. P. McGrew, Hologram counterfeiting: problems and solutions, in *Proc. SPIE 1210, Optical Security and Anticounterfeiting Systems*, Los Angeles, CA, 1990, pp. 66-76.

265. Y. T. Lu and S. Chi, Compact, reliable asymmetric optical configuration for cost-effective fabrication of multiplex dot matrix hologram in anti-counterfeiting applications, *Optik*, 2003, **114** (4), 161-167.

266. R. W. Phillips and A. F. Bleikolm, Optical coatings for document security, *Appl. Opt.*, 1996, **35** (28), 5529-5534.

267. S. J. Simske and J. S. Aronoff, Qualification of a layered security print deterrent, *J. Imaging Sci. Technol.*, 2007, **51** (1), 86-95.

268. J. M. Meruga, W. M. Cross, P. S. May, Q. Luu, G. A. Crawford and J. J. Kellar, Security printing of covert quick response codes using upconverting nanoparticle inks, *Nanotechnology*, 2012, **23** (39), art. no. 395201.

269. I. J. Cox, J. Kilian, F. T. Leighton and T. Shamoon, Secure spread spectrum watermarking for multimedia, *Ieee Transactions on Image Processing*, 1997, **6** (12), 1673-1687.

270. C. T. Hsu and J. L. Wu, Hidden digital watermarks in images, *Ieee Transactions on Image Processing*, 1999, **8** (1), 58-68.

271. G. Fei, C. Tuinea-Bobe, D. Li, G. Li, B. Whiteside, P. Coates and H. Xia, Electro-activated surface micropattern tuning for microinjection molded electrically conductive shape memory polyurethane composites, *RSC Adv.*, 2013, **3** (46), 24132-24139.

272. Y. Martelé, K. Naessens, P. Van Daele, R. Baets, K. Callewaert and E. Schacht, Micropatterning polyurethane surfaces with lasers, *Polym. Int.*, 2003, **52** (10), 1641-1646.

273. R. Cowburn, Laser surface authentication - reading Nature's own security code, *Contemp. Phys.*, 2008, **49** (5), 331-342.

274. Y. Cui, R. S. Hegde, I. Y. Phang, H. K. Lee and X. Y. Ling, Encoding molecular information in plasmonic nanostructures for anti-counterfeiting applications, *Nanoscale*, 2014, **6** (1), 282-288.

275. S. Han, H. J. Bae, J. Kim, S. Shin, S.-E. Choi, S. H. Lee, S. Kwon and W. Park, Lithographically Encoded Polymer Microtaggant Using High-Capacity and Error-Correctable QR Code for Anti-Counterfeiting of Drugs, *Adv. Mater.*, 2012, **24** (44), 5924-5929.

276. U. Bussy, C. Thibaudeau, F. Thomas, J.-R. Desmurs, E. Jamin, G. S. Remaud, V. Silvestre and S. Akoka, Isotopic finger-printing of active pharmaceutical ingredients by C-13 NMR and polarization transfer techniques as a tool to fight against counterfeiting, *Talanta*, 2011, **85** (4), 1909-1914.

277. V. M. Thomas, A universal code for environmental management of products, *Resour Conserv Recy*, 2009, **53** (7), 400-408.

278. M. Dodge and R. Kitchin, in *Globalization in Practice*, eds. N. Thrift, A. Tickell and S. Woolgar, Oxford Univerity Press, Oxford, UK, 1 edn., 2014, ch. 49, pp. 269-271.

279. A. Juels, RFID security and privacy: a research survey, *IEEE Journal on Selected Areas in Communications*, 2006, **24** (2), 381-394.

280. R. Want, An introduction to RFID technology, *Pervasive Computing, IEEE*, 2006, **5** (1), 25-33.

281. E. W. T. Ngai, K. K. L. Moon, F. J. Riggins and C. Y. Yi, RFID research: An academic literature review (1995-2005) and future research directions, *Int. J. Prod. Econ.*, 2008, **112** (2), 510-520.

282. S. A. Turner, J. Zhou, S. S. Sheiko and V. S. Ashby, Switchable Micropatterned Surface Topographies Mediated by Reversible Shape Memory, *ACS Appl. Mater. Interfaces*, 2014, **6** (11), 8017-8021.

283. W. Li, T. Gong, H. Chen, L. Wang, J. Li and S. Zhou, Tuning surface micropattern features using a shape memory functional polymer, *RSC Adv.*, 2013, **3** (25), 9865-9874.

284. M. Ebara, K. Uto, N. Idota, J. M. Hoffman and T. Aoyagi, Rewritable and shape-memory soft matter with dynamically tunable microchannel geometry in a biological temperature range, *Soft Matter*, 2013, **9** (11), 3074-3080.

285. connvision Ltd., BeeTagg, http://www.beetagg.com.

286. N. Fritzsche and T. Pretsch, Programming of Temperature-Memory Onsets in a Semicrystalline Polyurethane Elastomer, *Macromolecules*, 2014, **47** (17), 5952-5959.

10. APPENDIX

10.1. LIST OF FURTHER PUBLICATIONS

CONFERENCE PAPER

I. M. Ecker and T. Pretsch, Durability of QR code carriers based on shape memory polymer, In *Proceedings of the ASME Conference on Smart Materials, Adaptive Structures and Intelligent Systems, Vol 1*; Ed. Amer. Soc. Mechanical Engineers: New York, **2013**; pp 89-96

PRESENTATIONS (presenting author is underlined)

I. 2012/05/14: T. Pretsch and M. Ecker, Deformable QR codes with shape memory functionality, *E-MRS 2012 Spring Meeting*, *Symposium Q,* Straßburg, France.

II. 2012/08/28: M. Ecker and T. Pretsch, Freely configurable functionalization tool for switchable information carriers, *3rd WMRIF International Workshop for Young Materials Scientists*, National Metal and Materials Technology Center (MTEC), Pathum Thani, Thailand.

III. 2012/09/21: M. Ecker and T. Pretsch; Durability of QR code carriers based on shape memory polymer, *ASME Conference on Smart Materials, Adaptive Structures and Intelligent Systems*, Stone Mountain, GA.

IV. 2014/05/26: M. Ecker and T. Pretsch, Multifunctional information carriers with concealed quick response codes, *E-MRS 2014 Spring Meeting, Symposium L*, Lille, France.

POSTER (presenting author is underlined)

I. 2012/04/03: M. Ecker, N. Fritzsche and T. Pretsch, Smart tags carrying QR codes, *2. Berliner Chemiesymposium, Gesellschaft Deutscher Chemiker – JungChemikerForum*, Berlin, Germany.

II. 2012/08/30: M. Ecker and T. Pretsch, Freely configurable functionalization tool for switchable information carriers, *3rd WMRIF Workshop for Young Materials*

Scientists, *World Materials Research Institutes Forum WMRIF*, Pathum Thani, Thailand.

PATENT APPLICATIONS

I. DE 10 2011 054 925 A1, DE 10 2012 102 546.0, DE 10 2012 106 150.5, DE 10 2012 109 303.2; WO 00 2013 060 831 A3 Dyeing surface of polymer article comprising shape memory polymer, comprises pre-treating surface of polymer article, dyeing surface with dye solution comprising organic dye and organic solvent, and cleaning surface and drying dye solution; T. Pretsch, M. Ecker, M. Schildhauer.

10.2. NOMENCLATURE

1D	one-dimensional
2D	two-dimensional
3D	three-dimensional
ATR-FTIR	attenuated total reflectance Fourier transform infrared spectroscopy
BDO	1,4-butanediol
BPA	Bisphenol A
C.I.	color index
CAS	Chemical Abstract Service (registry number for chemicals)
CDDF	compressive deformation-determinated functionalization
CIELAB	CIE 1976 ($L^*a^*b^*$) color space
CO_2	carbon dioxide
CST	color switching temperature
CTM	cyclic thermo-mechanical measurement
CVL	crystal violet lactone
CYMK	cyan, yellow, magenta and key (black) color space
D65	standard illuminant
DMA	dynamical mechanical analysis
DNA	deoxyribonucleic acid
DSC	differential scanning calorimetry
EBP	epoxy based polymer
ECC	error code correction
ESI	electronic supplementary information
GSV/gsv	grayscale value
IR	infrared, invisible radiant energy (700 nm – 1000 μm)
ISO	International Organization for Standardization
LG	lauryl gallate
MDI	4,4′-methylene diphenyl diisocyanate
NMP	*N*-methyl-2-pyrrolidone
OVD	optically variable devices
PBA	poly(1,4-butylene adipate)
pc	pixel counts
PCO	poly(cyclooctene)
PE	polyethylene

PEU	poly(ester urethane)
pH	value for acidity/basicity of aqueous solution (hydronium ion concentration)
QR	quick response
RFID	radio-frequency identification
RGB	red, green and blue color space
RT	room temperature
SCE	specular component excluded
sd	surface-dyed
SEM	scanning electron microscopy
SME	shape memory effect
SMP	shape memory polymer
TDDF	tensile deformation-determinated functionalization
T-PIG	thermochromic pigment
TPU	thermoplastic polyurethane
UPC	Universal Product Code
URL	uniform resource locator (web address)
UV	ultraviolet (400–100 nm)
UVA	ultraviolet A, long wave radiation (400–315 nm)

10.3. SYMBOLS

a^*	opponent color value (position between red and green)
a, a_0	clamping distance, initial clamping distance
A, A_0	area, initial area
b^*	opponent color value (position between yellow and blue)
b, b_0,	longitudinal length, initial longitudinal length
c, c_0	transversal length, initial transversal length
C_M	Michelson contrast
$E´$	storage modulus
$E´´$	loss modulus
F_{max}	maximum force
L^*	lightness
L_{max}	peak maximum at highest luminance
L_{min}	peak maximum at lowest luminance
r	radius

R_f	shape fixity ratio
R_r	strain recovery ratio
$R_{r,\,tot}$	total strain recovery ratio
T	temperature
tan δ	loss factor
T_c	crystallization temperature
$T_d = T_{high}$	deformation temperature, above $T_{trans,}$
T_g	glass transition temperature
$T_{fix} = T_{low}$	shape fixity temperature, temperature below T_c/T_g
T_m	melting temperature
T_{switch}	switching temperature
T_{trans}	transition temperature (induces shape recovery)
ΔE	color difference
ΔH_m	melting enthalpy
ε	strain
ε_m	maximum deformation strain
ε_p	plastic strain after shape recovery
ε_{pre}	pre-elongation strain
ε_u	fixed strain after unloading
λ	wavelength
λ_{max}	peak maximum of wavelength
σ	stress
σ_c, σ_i	constant and initial stress